Near-Infrared Proper Motion Surveys

Author:
Leigh Charles Smith

Supervised by:
Prof. H.R.A Jones
Dr. P.W. Lucas
Prof. D.J. Pinfield

Centre for Astrophysics Research
Science and Technology Research Institute
University of Hertfordshire

Submitted to the University of Hertfordshire in partial fulfilment of the requirements of the degree of PhD.

April 2015

Abstract

I present the development of two near infrared proper motion pipelines for high resolution near infrared data from UKIDSS and the VISTA VVV survey. The UKIDSS pipeline is capable of accuracies of order $5-10$ $mas\ yr^{-1}$ for bright sources with the largest epoch baselines (~ 8 years). The VVV pipeline reaches $1-2$ $mas\ yr^{-1}$ proper motion precision at the bright end and parallax measurements at ~ 1 mas precision. It will be possible to improve upon the VVV astrometric precision due to increases in data volume and further pipeline development.

I have used the proper motion pipelines to generate three near infrared proper motion catalogues of the UKIDSS LAS and GPS and the VVV survey. The LAS proper motion catalogue covers 1500 deg^2 at high Galactic latitudes and contains approximately 15 million sources with two J band epochs. The GPS proper motion catalogue covers 1500 deg^2 of the northern Galactic plane and contains approximately 400 million sources with two K band epochs. The VVV proper motion catalogue covers 560 deg^2 of the Galactic bulge and disc and contains approximately 200 million sources with between 50 and 150 Ks band epochs. I have also produced a preliminary 5σ parallax catalogue containing 3403 VVV sources.

The LAS and GPS proper motion catalogues have been used by myself and other authors to identify and study many new examples of high proper motion stars, brown dwarfs, ultracool dwarf benchmark candidates, cool white dwarfs, substellar subdwarfs and nearby sources within < 25 pc. These catalogues remain far from fully exploited and will be a useful resource for future research by the astronomical community. Exploitation of the VVV proper motion catalogue is still in its infancy, yet it has already generated large numbers of new high proper motion sources. These include new brown dwarf candidates, important benchmark objects, and nearby sources which have previously avoided detection. Parallax results from the VVV pipeline will be useful to improve low mass star/ultracool dwarf luminosity functions, significantly increasing the numbers of brown dwarfs with known parallaxes and illustrates how general purpose multi-epoch wide area surveys can generate parallaxes.

Finally, I discuss the long term usefulness of such catalogues in the Gaia era and how they might be exploited in the future.

Declaration of Authorship

I declare that while registered as a candidate for a University Research Degree, I have not been a registered candidate or enrolled student for another award of the University or other academic or professional institution.

No substantial component of this thesis is the same as any that I have submitted or intend to submit for any other award or qualification at this or any other institution.

All the work reported in this thesis was undertaken by myself with the exception of where specifically indicated in the text.

Acknowledgements

This work would certainly not have been possible without the valued help of a number of people.

Firstly I need to thank my supervisory team. Phil Lucas, for starting this whole thing off with the idea for the proper motion final year undergraduate project, for the patient help, discussions, proofreading, etc. I will be forever grateful. Hugh Jones for the guidance and discussions, but also for making this entire process relatively straightforward, I'm sure a lot of tedious paperwork went on behind the scenes that I never knew about. Finally David Pinfield, and Ben Burningham (who technically is not a supervisor but might as well have been) for the meetings, great ideas and all the other help along the way.

I of course also need to thank mum, dad and the others, Ashleigh and friends in the world outside astronomy, without whom these last few years would have certainly driven me mad.

Contents

List of Figures

List of Tables

List of Abbreviations

2MASS	**2**(two) **M**icron **A**ll **S**ky **S**urvey
AEP	**A**ll **E**pochs **P**arallax
CASU	**C**ambridge **A**stronomy **S**urvey **U**nit
CDS	**C**entre de **D**onnées astronomiques de **S**trasbourg
CFBDS	**C**anada-**F**rance **B**rown **D**warfs **S**urvey
DENIS	**De**ep **N**ear **I**nfrared **S**urvey
ESO	**E**uropean **S**outhern **O**bservatory
FITS	**F**lexible **I**mage **T**ransport **S**ystem
FOV	**F**ield **O**f **V**iew
HPM	**H**igh **P**roper **M**otion
INT	**I**saac **N**ewton **T**elescope
IPHAS	**I**NT **P**hotometric **H**-**A**lpha Survey
IRAF	**I**mage **R**eduction and **A**nalysis **F**acility
IRTF	**I**nfra**R**ed **T**elescope **F**acility
LHS	**L**uyten **H**alf **S**econd catalogue
LPM	**L**ow **P**roper **M**otion
LQRF	**L**arge **Q**uasar **R**eference **F**rame
LSPM	**L**epine and **S**hara **P**roper **M**otion
MAD	**M**edian **A**bsolute **D**eviation
MKO	**M**auna **K**ea **O**bservatory
NIR	**N**ear **I**nfra-**R**ed
NLTT	**N**ew **L**uyten **T**wo-**T**enths catalogue
POSS	**P**alomar **O**bservatory **S**ky **S**urvey
PSF	**P**oint **S**pread **F**unction
RMS	**R**oot **M**ean **S**quared

SDSS	**S**loan **D**igital **S**ky **S**urvey
SIPS	**S**outhern **I**nfrared **P**roper Motion **S**urvey
SMP	**S**ymmetric **M**ulti**p**rocessor
SQL	**S**tructured **Q**uery **L**anguage
SSS	**S**uperCOSMOS **S**ky **S**urveys
UCD	**U**ltra**c**ool **D**warf
[U]GPS	**U**KIDSS **G**alactic **P**lane **S**urvey
UKIDSS	**UK**IRT **I**nfrared **D**eep **S**ky **S**urvey
UKIRT	**U**nited **K**ingdom **I**nfra-**R**ed **T**elescope
[U]LAS	**U**KIDSS **L**arge **A**rea **S**urvey
USNO	**U**nited **S**tates **N**avel **O**bservatory
VIRCAM	**V**ista **I**nfra**R**ed **Cam**era
VISTA	**V**isible and **I**nfrared **S**urvey **T**elescope for Astronomy
VSA	**V**ista **S**cience **A**rchive
VVV	**V**ista **V**ariables in the **V**ía Láctea
WCS	**W**orld **C**oordinate **S**ystem
WDS	**W**ashington **D**ouble **S**tar catalogue
WFCAM	**W**ide **F**ield **Cam**era
WISE	**W**ide-field **I**nfrared **S**urvey **E**xplorer
WSA	**W**FCAM **S**cience **A**rchive

List of Publications

First Author

Using the LAS proper motion catalogue, see Chapters 2 and 3.

L. Smith, P. W. Lucas, B. Burningham, H. R. A. Jones, R. L. Smart, A. H. Andrei, S. Catalán, and D. J. Pinfield.
A 1500 deg^2 near infrared proper motion catalogue from the UKIDSS Large Area Survey.
MNRAS, 437:3603–3625, February 2014a.

L. Smith, P. Lucas, B. Burningham, H. Jones, D. Pinfield, R. Smart, and A. Andrei.
A 2 epoch proper motion catalogue from the UKIDSS Large Area Survey.
In *European Physical Journal Web of Conferences*, volume 47 of *European Physical Journal Web of Conferences*, page 6006, April 2013b.

L. Smith, P. Lucas, B. Burningham, H. Jones, D. Pinfield, R. Smart, and A. Andrei.
A new UKIDSS proper motion survey and key early results, including new benchmark systems .
MemSAI, 84:976, 2013c.

L. Smith, P. Lucas, B. Burningham, H. Jones, R. Smart, D. Pinfield, F. Marocco, and J. Clarke.
The Kinematic Age of the Coolest T Dwarfs.
ArXiv e-prints: 1303.5288, March 2013a.

Using the GPS proper motion catalogue, see Chapters 2 and 4.

L. Smith, P. W. Lucas, R. Bunce, B. Burningham, H. R. A. Jones, R. L. Smart, N. Skrzypek, D. R. Rodriguez, J. Faherty, G. Barentsen, J. E. Drew, A. H. Andrei, S. Catalán, D. J. Pinfield, and D. Redburn.
High proper motion objects from the UKIDSS Galactic plane survey.
MNRAS, 443:2327–2341, September 2014b.

L. Smith, P.W. Lucas, R. Bunce, B. Burningham, H.R.A Jones, R.L. Smart, N. Skrzypek, D.R. Rodriguez, and J. Faherty.
A search for High Proper Motion Objects in the UKIDSS Galactic Plane Survey .
MemSAI, 2015c.

Co-author

Using the LAS proper motion catalogue, see Chapters 2 and 3.

S. Catalán, P.-E. Tremblay, D. J. Pinfield, **L. C. Smith**, Z. H. Zhang, R. Napiwotzki, F. Marocco, A. C. Day-Jones, J. Gomes, K. P. Forde, P. W. Lucas, and H. R. A. Jones.
The brightest pure-H ultracool white dwarf.
A&A, 546:L3, October 2012.

D. J. Pinfield, B. Burningham, N. Lodieu, S. K. Leggett, C. G. Tinney, L. van Spaandonk, F. Marocco, R. Smart, J. Gomes, **L. Smith**, P. W. Lucas, A. C. Day-Jones, D. N. Murray, A. C. Katsiyannis, S. Catalan, C. Cardoso, J. R. A. Clarke, S. Folkes, M. C. Gálvez-Ortiz, D. Homeier, J. S. Jenkins, H. R. A. Jones, and Z. H. Zhang.
Discovery of the benchmark metal-poor T8 dwarf BD +01° 2920B.
MNRAS, 422:1922–1932, May 2012.

A. Day-Jones, D. Pinfield, F. Marocco, B. Burningham, M. T. Ruiz, Z. H. Zhang, J. I. Gomes, **L. Smith**, P. W. Lucas, H. R. A. Jones, and J. S. Jenkins.
Measuring brown dwarf properties from deep surveys .
MemSAI, 84:968, 2013.

C. V. Cardoso, B. Burningham, **L. Smith**, R. Smart, D. Pinfield, A. Magazzù, F. Ghinassi, and M. Lattanzi.

The T dwarf population in the UKIDSS LAS .
MemSAI, 84:983, 2013.

B. Burningham, C. V. Cardoso, **L. Smith**, S. K. Leggett, R. L. Smart, A. W. Mann, S. Dhital, P. W. Lucas, C. G. Tinney, D. J. Pinfield, Z. Zhang, C. Morley, D. Saumon, K. Aller, S. P. Littlefair, D. Homeier, N. Lodieu, N. Deacon, M. S. Marley, L. van Spaandonk, D. Baker, F. Allard, A. H. Andrei, J. Canty, J. Clarke, A. C. Day-Jones, T. Dupuy, J. J. Fortney, J. Gomes, M. Ishii, H. R. A. Jones, M. Liu, A. Magazzú, F. Marocco, D. N. Murray, B. Rojas-Ayala, and M. Tamura.
76 T dwarfs from the UKIDSS LAS: benchmarks, kinematics and an updated space density.
MNRAS, 433:457–497, July 2013.

D. J. Pinfield, J. Gomes, A. C. Day-Jones, S. K. Leggett, M. Gromadzki, B. Burningham, M. T. Ruiz, R. Kurtev, T. Cattermole, C. Cardoso, N. Lodieu, J. Faherty, S. Littlefair, R. Smart, M. Irwin, J. R. A. Clarke, **L. Smith**, P. W. Lucas, M. C. Gálvez-Ortiz, J. S. Jenkins, H. R. A. Jones, R. Rebolo, V. J. S. Béjar, and B. Gauza.
A deep WISE search for very late type objects and the discovery of two halo/thick-disc T dwarfs: WISE 0013+0634 and WISE 0833+0052.
MNRAS, 437:1009–1026, January 2014.

F. Marocco, A. C. Day-Jones, P. W. Lucas, H. R. A. Jones, R. L. Smart, Z. H. Zhang, J. I. Gomes, B. Burningham, D. J. Pinfield, R. Raddi, and **L. Smith**.
The extremely red L dwarf ULAS J222711-004547 - dominated by dust.
MNRAS, 439:372–386, March 2014.

B. Burningham, **L. Smith**, C. V. Cardoso, P. W. Lucas, A. J. Burgasser, H. R. A. Jones, and R. L. Smart.
The discovery of a T6.5 subdwarf.
MNRAS, 440:359–364, May 2014.

C. V. Cardoso, B. Burningham, R. L. Smart, L. van Spaandonk, D. Baker, **L. C. Smith**, A. H. Andrei, B. Bucciarelli, S. Dhital, H. R. A. Jones, M. G. Lattanzi, A. Magazzu, D. J. Pinfield, and C. G. Tinney.
49 new T dwarfs identified using methane imaging.
ArXiv e-prints: 1502.06503, February 2015.

F. Marocco, H. R. A. Jones, A. C. Day-Jones, D. J. Pinfield, P. W. Lucas, B. Burningham, Z. H. Zhang, R. L. Smart, J. I. Gomes, and **L. Smith**.
A large spectroscopic sample of L and T dwarfs from UKIDSS LAS: peculiar objects, binaries, and space density.
ArXiv e-prints: 1503.05082, March 2015.

Additional co-author publications

R. L. Smart, C. G. Tinney, B. Bucciarelli, F. Marocco, U. Abbas, A. Andrei, G. Bernardi, B. Burningham, C. Cardoso, E. Costa, M. T. Crosta, M. Daprá, A. Day-Jones, B. Goldman, H. R. A. Jones, M. G. Lattanzi, S. K. Leggett, P. Lucas, R. Mendez, J. L. Penna, D. Pinfield, **L. Smith**, A. Sozzetti, and A. Vecchiato.
NPARSEC: NTT Parallaxes of Southern Extremely Cool objects. Goals, targets, procedures and first results.
MNRAS, 433:2054–2063, August 2013.

Chapter 1

Introduction

1.1 Proper Motion

Stellar proper motion (μ) is the apparent angular movement of a star in a given time period. All stars have some component of motion (depending on the reference frame) due to their motion around the Galaxy and 'gravitational kicks' they receive through interaction with other massive objects, usually molecular or atomic clouds. Motion perpendicular to a line between the star and the observer is the proper motion, which can be measured through careful observation of its position over two or more epochs, given sufficient time between observations dependant on instrument precision. Given its relationship with distance and tangential velocity

$$V_{tan} = 4.74\mu d$$

where:

$$V_{tan} \text{ is the velocity tangential to the line of sight in units of } km\ s^{-1} \tag{1.1}$$

$$\mu \text{ is the proper motion in units of "/yr}$$

$$d \text{ is the distance in units of } pc$$

a large proper motion is indicative of a fast moving and/or nearby source. For this reason many of the known stars in the solar neighbourhood were first identified due to their large proper motion.

This equation also allows us to estimate the size of the proper motion of an object with an approximate distance and tangential velocity. An relatively local object at $\sim 100\ pc$ might have a proper motion of $\sim 40-80\ mas\ yr^{-1}$ if it were a member of the thin disk population ($\sim 20-40\ km\ s^{-1}$ for young-old stars), $\sim 170\ mas\ yr^{-1}$ if it were a member of the Galactic thick disk population ($\sim 80\ km\ s^{-1}$, old, somewhat metal poor stars), or $\sim 400\ mas\ yr^{-1}$ if it were a member of the Galactic halo population ($\sim 200\ km\ s^{-1}$, independant of the rotation of the Galactic disk, significantly metal poor stars). At a more general Galactic distance of $\sim 10\ kpc$ their proper motions would be 100 times smaller, even a halo population star at $200\ km\ s^{-1}$ would have a proper motion of only $4.2\ mas\ yr^{-1}$.

In addition to nearby/fast moving source identification, proper motion is useful when attempting to identify members of gravitationally bound systems. Their members serve as useful benchmark objects when one or more components of their systems have measurable attributes (eg. age, metallicity). Since members of such systems can be assumed to have formed from the same molecular cloud at a similar time, these attributes can also be inferred to belong to all members of a system (Pinfield et al., 2006). This is particularly useful in cases where it is difficult to constrain these attributes observationally, when dealing with ultracool dwarfs for example (see Section 1.3.2). Well characterised main sequence stars and white dwarfs make good companions for benchmark systems. Identification of a common proper motion and common distance is usually required to link multiple stars as single, gravitationally bound systems.

1.1.1 History

Historically, proper motion was identified by comparison of two images of the same field using a device called a blink comparator (Figure 1.1). A blink comparator allows a user to flick between two carefully aligned images such that differences between them become apparent.

The invention of the high resolution photographic plate scanner meant that large scale photographic sky surveys could be digitised, which made it much easier to compare images using a computer. Source detection algorithms made automatic identification of

[1]Image obtained from wikipedia, originally Flickr user 'nivium', distributed under the generic creative commons license 2.0.

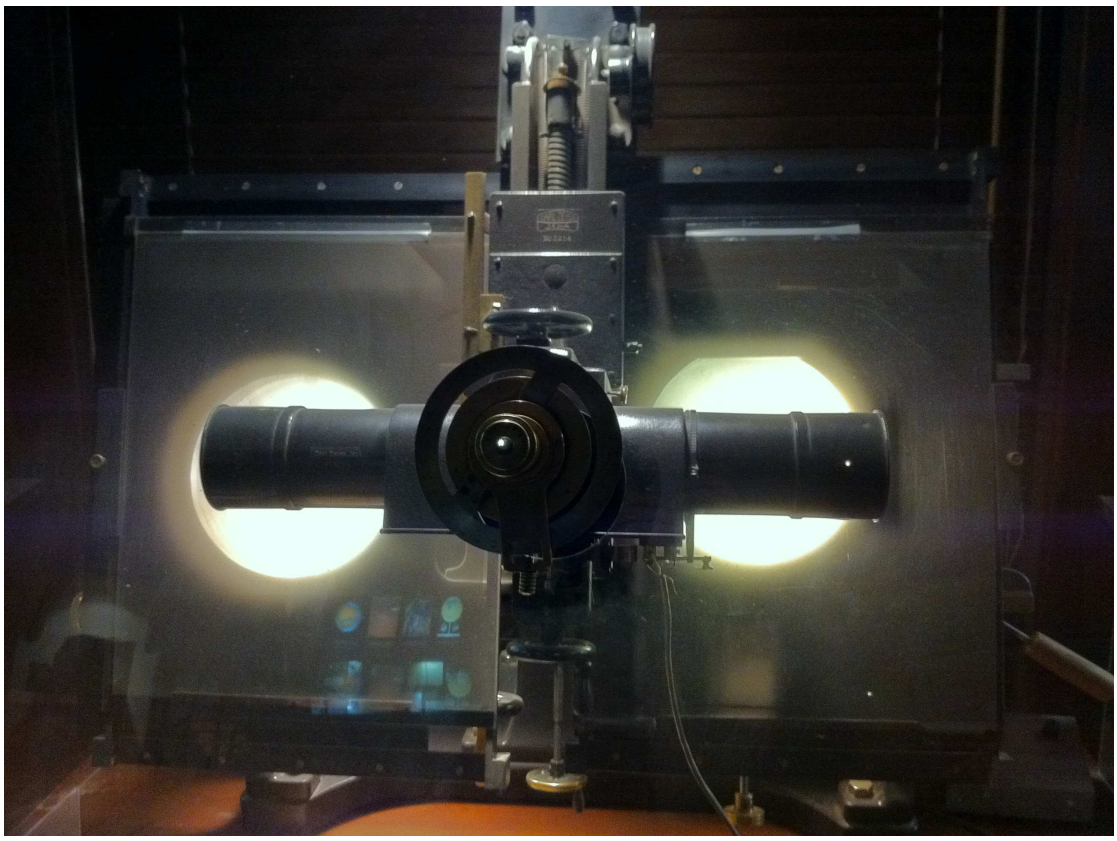

FIGURE 1.1: A blink comparator at the Lowell Observatory, Arizona. Used by Clyde Tombaugh in the discovery of the Pluto. [1]

the change in position of a star possible, and the volume of known high proper motion stars increased dramatically as a result. Large format CCDs and infrared imaging arrays provided improved astrometric precision, as well as the ability to rapidly scan large regions of the sky.

Major proper motion catalogues of the last half of the 20th century were developed using large scale surveys of Schmidt photographic plates often separated in time by many decades. As well as improving the precision of individual positional measurements, the precision of an overall proper motion measurement can be improved greatly by increasing the time difference between the first and last positional measurements. For this reason early large scale sky surveys maintain their usefulness by enabling proper motion measurements over very large time baselines.

1.1.2 Limiting Factors of Modern Proper Motion Accuracy

Atmospheric Turbulence

Atmospheric turbulence causes a varying of the refractive index of the atmosphere along a line of sight and a shift in the position of the measured centroid in exposures which are short relative to the typical timeframe of the turbulent mixing. Differences in the effect of the atmospheric turbulence are negligible over relatively small fields of view. Across larger fields of view more significant differences in the magnitude and direction of centroiding shifts become apparent. Equation 1.2 gives the approximate effect of the difference in turbulence for a modern detector at a good site as a function of the size of the FOV and the exposure time.

$$\sigma \approx 38(mas)\ (\mathrm{FOV}/30')^{\frac{1}{3}}\ T^{-\frac{1}{2}}$$

where:

$$\sigma \text{ is the rms of differential turbulence across the FOV}$$

$$T \text{ is the exposure time in seconds} \tag{1.2}$$

For an exposure time of 10 seconds the rms differential turbulence between two stars separated by 1' is approximately 4 *mas*. Consider the effect of this on the relative proper motion between them is reduced by the epoch baseline ($2-8$ years in the case of UKIDSS) it quickly reduces to $< 1\ mas\ yr^{-1}$.

Colour Dependent Effects

Atmospheric refraction alters the apparent position of objects by an angle which is a function of the apparent altitude of the object and its colour. Differences in the altitude of observations of the same field across multiple epochs are easily corrected. Differences in the intrinsic colour of the objects in the field is harder to correct for and causes varying amounts of scatter in their apparent positions relative to their true positions based on the altitude at observation. The magnitude of the differential refraction reduces with increasing wavelength and on the WFCAM was found to be negligible in the H and K bands and up to of order 1 *mas* in the J band[2].

[2] casu.ast.cam.ac.uk/documents/wfcam/astrometry/refractir.pdf

There are also colour dependent effects due to the optics, but these are minimal on modern telescopes and instruments.

Centroiding

Irwin (1985) describe the complexities involved in automatic detection and parameterization of astronomical sources on digital images. In particular, finite pixel sizes and very crowded fields can be limiting factors. Smart et al. (2010) found that the difference in the position of centroids of a field containing a cluster observed twice straddling a period where the WFCAM was removed and replaced on UKIRT (which is likely to have caused small changes in precise detector geometry) was typically at the level of 10 *mas* for sources of between mags 13 and 18 in the J band.

WCS Transformations

There can be significant uncertainty in the final WCS equatorial coordinate fit of an array due to e.g. inadequate reference stars, proper motion of reference stars, etc. The uncertainties on stellar equatorial positions can be of the order of 100 *mas* in exceptional cases. Producing proper motions from equatorial coordinates adds additional unnecessary uncertainty over simply producting proper motions on detector coordinates. Furthermore, the curvilinear shape of the detector on the equatorial coordinate grid adds additional unnecessary complexity.

Inertial Reference Frames

Typically proper motions are measured relative to a selection of nearby reference sources. If these reference sources are Galactic then they will typically have some component of proper motion themselves, which adds additional uncertainty to the measurement of an ICRF-relative (absolute) proper motion at the level of a few *mas*. If one uses very distant (e.g. extragalactic) galactic sources as references, these have essentially zero proper motion and will therefore produce essentially absolute proper motions. External galaxies can be relatively bright, are numerous (outside the Galactic plane), and can be detected by automated systems due to their extended nature. However the extended nature which makes them easy to detect also causes extra uncertainty in their centroids

and therefore a reference grid constructed using them. Quasars make ideal reference sources since they point like and have zero absolute proper motion, but they are relatively faint, and not numerous enough to be used reliably in all field with current instruments. Gaia is precise enough that it will be able to use even a sparse grid of quasars to produce a whole sky absolute reference grid to tie Galactic sources to. Once these precise positions and absolute proper motions are known they can be used to improve absolute reference grids of existing and future astrometric surveys.

1.1.3 Existing Catalogues

Notable proper motion catalogues include:

The LHS Catalogue: A catalogue of stars with proper motions exceeding 0.”5 annually (Luyten, 1979a). The LHS catalogue contains positions, proper motions and optical magnitudes for 4,470 stars with proper motions greater than 239 $mas\ yr^{-1}$ (note that a small number of sources were included, in spite of the 0.5 ” yr^{-1} lower limit). The catalogue includes data compiled from other proper motion searches and 804 hand/machine-blinked Palomar Sky Survey fields. The LHS catalogue was revised by Bakos et al. (2002). 4,323 of the original 4,470 high proper motion sources were recovered and their positions and proper motions were refined.

The NLTT Catalogue: New Luyten Catalogue of stars with proper motions larger than two tenths of an arcsecond (Luyten, 1979b). The NLTT catalogue is an extension of the LHS catalogue down to proper motions of 40 $mas\ yr^{-1}$ for 58,845 sources. Only a minority (152) have proper motion less than 180 $mas\ yr^{-1}$ however. The NLTT catalogue was revised and refined by Salim and Gould (2003), giving improved positions and proper motions for sources present in both the original POSS I frames and the second 2MASS data release.

The Hipparcos and TYCHO catalogues (Perryman and ESA, 1997) are the resultant products of the ESA-run Hipparcos mission. The aim of the Hipparcos mission was to measure precise positions, parallaxes and proper motions of around 120,000 stars. The space-based instrumentation used allowed the Hipparcos and TYCHO catalogues to measure very precise astrometric information on a large scale. The catalogues themselves contain various astrometric and photometric data including

accurate positions, proper motions and parallaxes for 118,218 and 1,058,332 (Hipparcos and TYCHO respectively) sources. van Leeuwen (2007) produced a new reduction of the Hipparcos data with accuracy improved by up to a factor of 4 for bright stars.

The TYCHO-2 Catalogue (Høg et al., 2000) is a revision of TYCHO catalogue, using the same star mapper data from the Hipparcos mission satellite. A new data reduction technique was used to improve upon the quality and quantity of the data (2,539,913 sources vs 1,058,332) over the original TYCHO catalogue.

The USNO-B1.0 Catalogue (Monet et al., 2003) contains positions, proper motions and optical magnitudes for approximately 1 billion sources. Data for the catalogue was gathered from a variety of photographic sky surveys spread across the latter half of the 20th century. The stated accuracy of the astrometry is 0."2, due in part to their widely spread, multiple epochs of observation.

The LSPM catalogue (Lépine and Shara, 2005) utilises the SUPERBLINK software (Lépine et al., 2002) to normalise the photographic differences between pairs of sub-frames from the POSS-I (Abell, 1959) and POSS-II (Reid et al., 1991) plates (usually involving a degradation in the quality of the POSS-II plate to match the POSS-I plate quality), then subtraction of one from the other to produce a residual image which maps the first and second epoch positions of sources with high proper motion. The catalogue benefits from the fact that all high proper motion sources identified by the SUPERBLINK software were manually blinked to remove any erroneous high proper motion sources, the LSPM catalogue has a minimal false detection contamination as a result. The LSPM catalogue also includes data from the TYCHO-2 (Høg et al., 2000) catalogue and the All-Sky Compiled Catalogue (Kharchenko, 2001).

The Pan-STARRS project will ultimately use an array of four telescopes (PS4) equipped with wide field imagers, giving it the capability to image the entire sky visible from Hawaii approximately once a week. Pan-STARRS will be a powerful tool for discovery and study of transient and fast moving objects. The prototype telescope, PS1, has already begun the multi-band surveys and will provide high quality proper motions and parallaxes (Liu et al., 2011).

The SuperCOSMOS Sky Survey (SSS) is an all sky catalogue based on scanned Schmidt photographic plates in B, R, and I bandpasses and includes a second epoch in R to calculate proper motions. The plate scanning is performed by the SuperCOSMOS machine with a pixel scale of 0.67" (Hambly et al., 2001c). Absolute proper motions are included with typical uncertainties of 10 $mas\ yr^{-1}$ at R ∼18 and 50 $mas\ yr^{-1}$ at R ∼21 (Hambly et al., 2001a). For a comprehensive description of SSS photometry see Hambly et al. (2001b).

A two epoch proper motion survey was conducted using 2MASS data by Kirkpatrick et al. (2010). The survey was comprised of 4030 deg^2 of the sky with multi-epoch coverage in 2MASS and led to the discovery of several new brown dwarfs.

1.1.4 Future

Considered the successor to the Hipparcos mission, ESA's space based Gaia mission will provide a wealth of astrometric and photometric information with unprecedented accuraty, invaluable in the study of nearby Galactic dynamics.

Final parallax accuracies are expected in the range of 5-11 μas (dependent on sky position) for stars from 6th to 13th magnitude in Gaia's G band. Astrometric accuracy will fall off with brightness from 13th to 20th magnitude (de Bruijne et al., 2015).

Gaia launched on December 19th, 2013, reaching its intended L_2 orbit during January 2014. The first data release, expected during 2016, will contain proper motions for approximately one hundred thousand stars in common with the Hipparcos catalogue (Michalik et al., 2014). The second data release, expected during 2017, will provide proper motions for the majority of the 10^9 objects observed. The full astrometric solution including all proper motions, parallaxes, radial velocities, exoplanet detections, etc. is not expected until around 2022.

Further ahead, the Large Synoptic Survey Telescope (LSST) is due to begin operation in 2022 from Cerro Pachón, Chile. LSST will feature an 8.4m primary mirror and a 3.2 gigapixel imager. With a 9.6 deg^2 field of view and approximately 40 seconds per pointing, LSST will be able to rapidly survey large portions of the sky. The 10 year survey mission should see roughly 800 epochs of 18,000 deg^2 of sky with a point source 5σ depth of ~ 24.5 in the r band. The final expected proper motion accuracy should be

sub-*mas* even out to $r = 24$, effectively extending the Gaia error vs. magnitude curve (Ivezic et al., 2008).

1.2 Infrared Sky Surveys

1.2.1 History

Large scale, deep, infrared sky surveys are very much a new thing as the size of infrared imaging arrays did not, until recently, permit them. The Two Micron All Sky Survey (2MASS; Skrutskie et al. 2006) and the Deep Near Infrared Survey of the Southern Sky (DENIS; Epchtein et al. 1997) are early examples of such surveys capitalising on recent improvements in infrared array technology. 2MASS and DENIS utilised 256×256 pixel mercury cadmium telluride arrays. 2MASS used a pair of automated 1.3m telescopes, one in each hemisphere, and DENIS used a single 1m telescope at La Silla observatory in Chile.

1.2.2 UKIDSS

The United Kingdom Infrared Deep Sky Survey (UKIDSS, Warren 2002, Lawrence et al. 2007) project began in 2005, and was an 8 year effort to survey approximately 7000 deg^2 using the 3.8m infrared-dedicated United Kingdom Infra-Red Telescope (UKIRT), situated at the summit of Mauna Kea, Hawaii, and the Wide Field CAMera (WFCAM, Casali et al. 2001, Casali et al. 2007). UKIDSS is comprised of 5 smaller surveys:

- The Large Area Survey (LAS) - The LAS covers 4028 square degrees (complemented in ugriz optical passbands by the SDSS) in Y, J, H, and K bands to a depth of 18.2 magnitudes in K.
- The Galactic Plane Survey (GPS) - The GPS covers 1868 square degrees in J, H, and K bands to a depth of 18.1 magnitudes in K.
- The Galactic Clusters Survey (GCS) - The GCS covers 1067 square degrees in Z, Y, J, H, and K bands to a depth of 18.2 magnitudes in K.
- The Deep Extragalactic Survey (DXS) - The DXS covers 35 square degrees in just J and K bands to a depth of 19.2-21.2 magnitudes in K.

- The Ultra Deep Survey (UDS) - The UDS covers only 0.77 square degrees in J, H, and K bands to a depth of 22.5 magnitudes in K.

NB: area data taken from Lawrence et al. (2007), bandpass and depth data retrieved from the most recent release (at the time of writing) of respective surveys from the WFCAM Science Archive (WSA[3])

1.2.3 VVV

The Vista Variables in the Vía Láctea (VVV) is a public ESO near-infrared survey of the southern Galactic plane and bulge using the wide-field VIRCAM on the VISTA telescope at Paranal observatory in Chile. The science goals of the VVV are dominated by the study of photometric variability, either intrinsic (i.e. variable stars) or simply observed (e.g. eclipsing binaries, microlensing events). Of the eleven science goals presented by Minniti et al. (2010) only two are not directly related to variability: the provision of NIR photometry to complement other surveys, and the identification of high proper motion objects. Minniti et al. (2010) describe the VVV survey and its scientific aims in detail.

1.2.4 WISE

NASA's Wide-field Infrared Survey Explorer satellite (WISE, Wright et al. (2010)), was launched in December 2009 and saw first light in January 2010. WISE was NASA's nine and a half month effort to map the sky at 4 wavelengths: 3.4, 4.6, 12 and 22 microns (WISE magnitudes W1 to W4 respectively). The mission was extended a further four months for the purpose of detecting nearby solar system objects (NEOWISE, Near Earth Object WISE). The initial WISE data were released March 2012 (Cutri et al., 2012) followed by the complete WISE + NEOWISE data set (named AllWISE), which include proper motion and parallax estimates, in 2013 (Cutri et al., 2013).

As brown dwarfs cool their spectral energy distribution shifts towards longer wavelengths; because of this WISE has been producing exciting discoveries of the coldest brown dwarfs including several new Y dwarfs (Kirkpatrick et al. (2011), Kirkpatrick et al. (2012)) with effective temperatures as low as a few hundred Kelvin. See section 1.3.2.1.

[3] http://surveys.roe.ac.uk/wsa/

Kirkpatrick et al. (2014) examined the proper motion content of the AllWISE data release and identified 3583 new high proper candidates. Of these, 3525 were confirmed using 2MASS data and the remaining 58 are retained as candidates.

Recently there have been two independent all sky proper motion searches using the WISE database by Luhman (2014a) and Luhman and Sheppard (2014). Luhman (2013, 2014b) identified WISE J104915.57-531906.1AB, a binary brown dwarf system at 2 *pc* and WISE J085510.83-071442.5, a ∼250 Kelvin Y type brown dwarf ('the snowball') respectively.

1.3 Proper Motion in the Infrared

Some proper motion catalogues have used recent near infrared data in conjunction with older optical catalogues to provide large epoch baselines, which improve the precision of the proper motion measurement, and also include accurate near infrared photometry (eg. PPMXL; Roeser et al. 2010, SIPS; Deacon et al. 2005; Folkes et al. 2007). However, for a proper motion to be measured it must be detected in both surveys, meaning that very red objects (e.g. ultracool dwarfs, distant objects in regions of high extinction) which were not detected in the optical survey are missed. It is therefore important that proper motion catalogues are provided at longer wavelengths.

To overcome the problem of poor detectability of very red objects in such proper motion catalogues it is necessary to use infrared sky surveys alone. If we consider the use of 2MASS as the first epoch in a hypothetical near infrared only proper motion catalogue, then the current maximum epoch baseline of such a survey is 15 years. The astrometric accuracy of near infrared arrays is generally better than that of the Schmidt plates, which helps to offset the reduction in proper motion measurement precision due to shorter epoch baselines. Examples of current near infrared only proper motion surveys include a 2MASS only proper motion search (Kirkpatrick et al., 2010) and a 2MASS - UKIRT Infrared Deep Sky Survey (UKIDSS) based proper motion search (Deacon et al., 2009b). Kirkpatrick et al. (2010) identified 107 proper motion candidates that lack counterparts in Digitized Sky Survey B, R and I band images. Both examples have also identified a multitude of new nearby red objects (ultracool dwarfs), very few of which are detectable in current optical based surveys.

I now consider the primary science targets for near infrared proper motion catalogues.

1.3.1 Cool White Dwarfs

Ultra cool white dwarfs are among the oldest objects in the galaxy. Their ages are often very well constrained due to their predictable cooling rate based on theoretical models (eg. Meng et al. 2010, Chen and Hansen 2011), dwarf mass to progenitor star mass relationship and main sequence progenitor lifetime. Hence, these objects are ideal tools for placing lower limits on the age of the Galaxy and can give us clues to the conditions of a young Milky Way (Kilic et al., 2006). A number of cool white dwarfs have been discovered to date, the usual method of discovery is photometric and reduced proper motion selection (Kilic et al. 2005, Leggett et al. 2011), often followed by spectroscopic confirmation. Reduced proper motion (H) substitutes proper motion in lieu of parallax in the standard absolute magnitude equation, $H = m + 5(1 + \log \mu)$. Reduced proper motion is a valid substitude for absolute magnitude of most members of the Galactic disc as they typically have similar tangential velocities. That is, within a factor of a few either side of the mean their proper motion is proportional to their parallax.

1.3.2 Ultracool Dwarfs

Ultracool dwarfs (UCDs), generally regarded as spectral type M7 or later, are very low mass stars and brown dwarfs. They are chemically very interesting since their cool atmospheres allow dust and molecules to form. Ultracool dwarfs are usually selected photometrically in the infrared, often combined with optical photometry (Pinfield et al. 2008, Burningham et al. 2010, Burgasser et al. 2011, Deacon et al. 2011, Day-Jones et al. 2011), though spectroscopic confirmation is still necessary (Pinfield et al. 2008, Day-Jones et al. 2011, Kirkpatrick et al. 2011). Proper motion is useful to discriminate between nearby ultracool dwarfs and background objects with similar colours such as high-redshift quasars and giant stars (Looper et al. 2007, Sheppard and Cushing 2009, Deacon et al. 2011). Figure 1.2 is a plot taken from Burrows et al. (2001, their figure 8) and nicely shows that for a given mass the temperature of an ultracool dwarf can vary significantly depending on its age. Metallicity also plays a reasonably significant role in determining the observational properties of ultracool dwarfs, but is itself difficult to

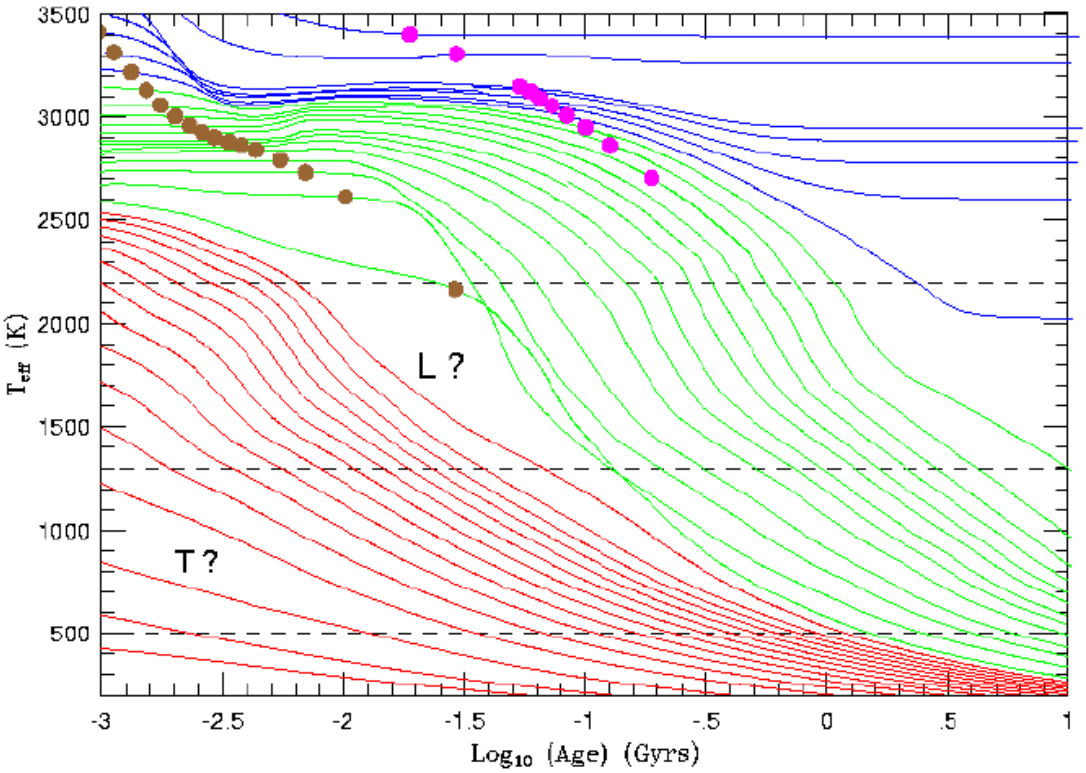

FIGURE 1.2: Figure taken from Burrows et al. (2001). Effective temperature versus age for a series of ultracool dwarfs of different masses. Blue lines are stars with masses sufficient to sustain nuclear hydrogen burning, green lines are brown dwarfs with insufficient mass to sustain nuclear hydrogen burning but $\gtrsim 13\ M_{Jup}$, red lines are objects with insufficient mass to burn deuterium ($\lesssim 13\ M_{Jup}$). All are solar metallicity objects. Nuclear burning of 50% of an objects deuterium is indicated by the brown dots, nuclear burning of 50% of an objects lithium is indicated by purple dots. Approximate L and T dwarf temperature regimes are indicated by the dashed lines.

constrain observationally due to the relatively low numbers of well studied low metallicity objects.

1.3.2.1 Brown Dwarfs

Brown dwarfs are suspected to form in a similar manner to stars, through the collapse of giant molecular clouds. Unlike stars however, they lack sufficient thermal energy to initiate and sustain nuclear hydrogen burning and hence cool through the brown dwarf sequence (see Figure 1.2, green lines). They are supported by electron degeneracy pressure, making them similar to white dwarfs and differentiating them from rocky planets (supported by the Coulomb force) and stars (supported by thermal pressure).

Observed spectroscopic/photometric variability supports theoretical predictions of variable cloud cover in brown dwarf atmospheres. Crossfield et al. (2014) produced a global cloud map using doppler imaging techniques of one of the more variable brown dwarfs, the L/T transition object WISE J104915.57-531906.1B.

The optical and infrared spectra of all brown dwarfs are dominated by various atomic and molecular absorption bands.

A census of brown dwarfs is necessary to constrain the mass function at the substellar end, filling in the gap between giant planets and low mass stars (Burgasser 2004, Pinfield et al. 2006, Kirkpatrick 2011).

M Dwarfs Late type M dwarfs can be brown dwarfs if they are relatively young ($\lesssim 1\ Gyr$, Figure 1.2). Their spectra are charactarised by TiO, VO, CO and H_2O absorption, as well as metal/alkali lines.

L Dwarfs Early L dwarfs are low mass stars (i.e. able to support nuclear hydrogen burning) if sufficiently old ($\gtrsim 1\ Gyr$, Figure 1.2). They are characterised by dusty atmospheres and show absorption in neutral alkali lines, water and metal hydrides (Kirkpatrick, 2005). They also show methane absorption in the mid infrared (Noll et al., 2000), methane also influences the K band (2.2 μm) spectra of later type L dwarfs. L dwarfs exhibit significantly redder near infrared colours than late M dwarfs as they cool.

T Dwarfs Dust, which dominates the spectra of L dwarfs, sinks below the photosphere as brown dwarfs cool into the T dwarf spectral sequence. T dwarfs are defined by the appearance of the methane absorption edge at 1.6 microns in low resolution H band spectra. T dwarfs turn bluer in near infrared colours as they cool through the sequence due to the influence of the methane absorption in the H band and water and collision-induced absorption by H_2 in the K band (Kirkpatrick, 2005). Absorption by ammonia has also been identified in their mid infrared spectra (Cushing et al., 2006).

Y Dwarfs The first identification of a new colder spectral sequence, the 'Y' dwarfs, was made using WISE data by Cushing et al. (2011) and defined by the appearance of ammonia absorption in low resolution near infrared spectra (Kirkpatrick et al., 2012).

They are characterised by the disappearance of alkali lines and appearance of atmospheric condensates of water (i.e. clouds, Morley et al. 2014). They emit essentially zero flux at optical wavelengths.

1.3.3 The Galactic Plane

The thick veil of dust in the Galactic plane is something of a benefit in identifying nearby high proper motion objects in optical surveys since it obscures more distant stars and lessens the problem of source confusion (see Boyd et al. 2011a, Figure 6; Boyd et al. 2011b, Figure 7). However, many of the nearest objects are relatively faint at optical wavelengths and we must turn to the near infrared where they are brighter. Extinction is less in the near infrared, which leads us back to a greater problem of source confusion. This has allowed many nearby objects to go unidentified until very recently.

Looper et al. (2007) reported 11 T dwarf discoveries in the 2MASS dataset (Skrutskie et al., 2006), three of which were found in a search for mid-late T dwarfs at low Galactic latitudes in the 2MASS Point Source Catalogue.

Phan-Bao et al. (2008) detected 26 new ultracool dwarfs (UCDs, generally regarded as M7 and later) in a photometric and proper motion search at low Galactic latitudes in the DEep Near-Infrared Survey of the Southern sky (DENIS, Epchtein et al. 1997).

Lucas et al. (2010) photometrically identified a very cool T dwarf in the UKIDSS Galactic Plane Survey (GPS, (Lucas et al., 2008)) and Burningham et al. (2011b) identified a further two mid-late T dwarfs in the GPS using a similar method.

Artigau et al. (2010) identified DENIS J081730.0-615520, a T6 dwarf at 4.9pc and $b \sim$ -14° in DENIS, as an unmatched source between the DENIS and 2MASS catalogues due to its high proper motion.

Gizis et al. (2011) and Castro and Gizis (2012) identified 2 L dwarfs within 10 pc of the sun at low Galactic latitudes by searching for detections in WISE with no corresponding detection in 2MASS, indicating a high proper motion.

Castro et al. (2013) identified a further 4 L dwarfs by the same method, one of which WISE J040418.01+412735.6 is close to the Galactic plane and a member of the small subclass of unusually red L dwarfs.

Folkes et al. (2012) identified 246 new UCDs due to their proper motion in a search for UCDs at low Galactic latitudes using the SUPERCOSMOS and 2MASS surveys.

Beamín et al. (2013) identified an unusually blue L5 dwarf less than 5° from the Galactic centre at 17.5 pc distance due to its high proper motion evident in the VVV survey. Mace et al. (2013a) and Cushing et al. (2014) discovered numerous late T dwarfs in the WISE survey, including WISE J192841.35+235604.9 (T6) and WISE J200050.19+362950.1 (T8) both of which are bright objects in the GPS footprint that are likely to be within 8 pc of the sun (see Section 4.4.4).
Scholz (2014) used WISE data to identify WISE J072003.20-084651.2, a relatively low proper motion ($\sim 100\ mas\ yr^{-1}$), 5-7 pc ∼M9 type dwarf in the Galactic plane. Burgasser et al. (2015) determined that WISE J072003.20-084651.2 is an M9.5+T5 binary and provide a parallax placing it at 6 pc. Mamajek et al. (2015) determined that WISE J072003.20-084651.2 likely passed within 0.25 pc of the sun approximately 70,000 years ago.

Given their relative brightness, many of the objects listed above could have been identified in previous surveys but for the effect of source confusion on both colour-based and proper motion-based searches.

1.4 Aims

Searches in the Galactic plane are currently small in number and limited in various ways. The WISE proper motion search by Kirkpatrick et al. (2014) is all sky and therefore covers the Galactic plane, but is based on low resolution data. There is an IPHAS - POSS-I proper motion survey of the Galactic plane by Deacon et al. (2009a), but this is based on optical data. The large POSS-I - IPHAS epoch baseline provided accurate motions and the IPHAS data are high resolution, but a two epoch proper motion catalogue is limited by the lowest quality observation and the POSS-I data are photographic and relatively low resolution. The large epoch baseline is something of a double edged sword in that it provides good accuracy at the expense of high proper motion sensitivity, Deacon et al. only provide proper motions for sources with $\mu < 150\ mas\ yr^{-1}$.

Proper motion surveys of the Galactic plane will prove useful in the study of clusters. They can be used to decontaminate, provide global motions for, and associate sources to globular and open clusters. Runaway stars, which are ejected from clusters at high

velocity and hypervelocity stars, which have space velocities sufficient to exit the Galaxy might also be identified.

Proper motion aids selection of objects which might otherwise be missed in traditional colour based selections due to their unusual spectral properties. It is necessary to identify low mass companions to main sequence stars or white dwarfs with known ages, distances or metallicities to test and improve model atmospheres (Pinfield et al., 2006), these properties are very difficult to accurately measure spectroscopically. It can also be used to identify objects which are members of specific kinematic populations (e.g. young moving groups, thick disc, halo) enabling us to place constraints on their ages, which are otherwise very difficult to measure. Identification of brown dwarfs which are members of the Galactic halo is of particular importance. These exhibit large space velocities and are crucial for testing the low metallicity initial mass function and atmospheric models, though few examples are currently known.

A complete census of objects in the solar neighbourhood is necessary for measurement of the initial mass function, for example. Nearby sources can often be overlooked due to source confusion (in the Galactic plane), or intrinsic faintness in the case of late type brown dwarfs and ultracool white dwarfs.

Clearly then, there is a need for proper motion surveys of the Galactic plane which are based on high resolution infrared data. The high source density in the Galactic plane necessitates high resolution data and short epoch baselines in order to maintain sensitivity to high proper motion sources. Accurate high resolution observation will also offset some of the loss of accuracy incurred when calculating motions over short time baselines. The UKIDSS GPS provides two epochs of high resolution K band data covering the northern Galactic plane, separated by between 2 and 8 years, and the VVV survey provides multiple epochs of high resolution Ks band data covering the southern Galactic plane and bulge.

The UKIDSS LAS has produced many new discoveries of nearby ultracool dwarfs, particularly late type brown dwarfs, and vastly improved our understanding of these complex objects. Despite this, at the commencement of this work there was little coverage of this region in proper motion space in the infrared.

The aim of this work is to generate and exploit new proper motion catalogues using LAS, GPS and VVV data. Due to the inherent similarity in the two epoch LAS and GPS data sets a single proper motion calculation pipeline is necessary (Chapter 2). The VVV data are multi-epoch, and require a separate dedicated pipeline (Chapter 5). I then evaluate and exploit the LAS proper motion catalogue (Chapter 3), the GPS proper motion catalogue (Chapter 4) and the VVV proper motion catalogue (Chapter 6).

Chapter 2

The UKIDSS Proper Motion Pipeline

2.1 Introduction

The United Kingdom Infrared Deep Sky Survey (UKIDSS, Warren 2002, Lawrence et al. 2007) project began in 2005, and was a 7 year effort to survey approximately 7000 deg^2 using the 3.8m infrared-dedicated United Kingdom Infra-Red Telescope (UKIRT), situated at the summit of Mauna Kea, Hawaii, and the Wide Field Camera (WFCAM, Casali et al. 2001, Casali et al. 2007).

Definitions

In this document I adopt the following terms, consistent with those used by the WSA.

Frame - An image or catalogue data from one of the four WFCAM arrays.

Frame set - A set of frames covering the same area and multiple bandpass and/or epochs.

Multi-frame - A set of four frames comprising one whole WFCAM footprint in one bandpass and epoch (excluding the guider chip).

For the purpose of this description I adopt the following terms:

Global (fit/transform) - The operation was performed using all relevant data in one frame.

Local (fit/transform) - The operation was performed using a limited area of one frame.

Target (source/frame) - Where an operation is performed on each source/frame individually, I will refer to an example as the *target* source/frame.

J1 and J2 - Refer to the first and second epoch J band images respectively.

2.2 The UKIDSS WFCAM Data

The WFCAM consists of four 2048×2048 pixel arrays (see fig. 2.1), which combined with UKIRT optics give a total viewing area of 0.21 deg^2 (0.4" per pixel, Casali et al. 2007). During observation the arrays were micro-stepped for the UKIDSS LAS J band and all GPS bands, four individual exposures are taken, each with a 0.5 pixel offset in x and/or y from the first and recombined during the Cambridge Astronomy Survey Unit (CASU) pipeline using a process called interleaving (Vick et al., 2004). Interleaving is performed using a process called *dribbling*, which corrects point spread function (PSF) mismatches caused by changes in the observing conditions between exposures, which can lead to a 'spiky' PSF [1]. This process of over-sampling improves the resolution of the WFCAM images to the limit of the seeing. The WFCAM photometric system is described in detail in Hewett et al. (2006). After the CASU pipeline the data are transferred to the WFCAM Science Archive (WSA, Hambly et al. 2008) for further processing and to make the data available for the community.

2.3 Data Acquisition

The FITS catalogue data for both UKIDSS proper motion catalogues were obtained using the WSA 'Archive Listing' tool. B. Burningham [University of Hertfordshire] obtained and matched the LAS J band catalogues using his own IDL code. For the GPS I wrote a BASH shell script to run through successive pages of Archive Listing results downloading and parsing the tables to generate an index of all GPS K band

[1] CASU, http://casu.ast.cam.ac.uk/surveys-projects/wfcam/technical/interleaving

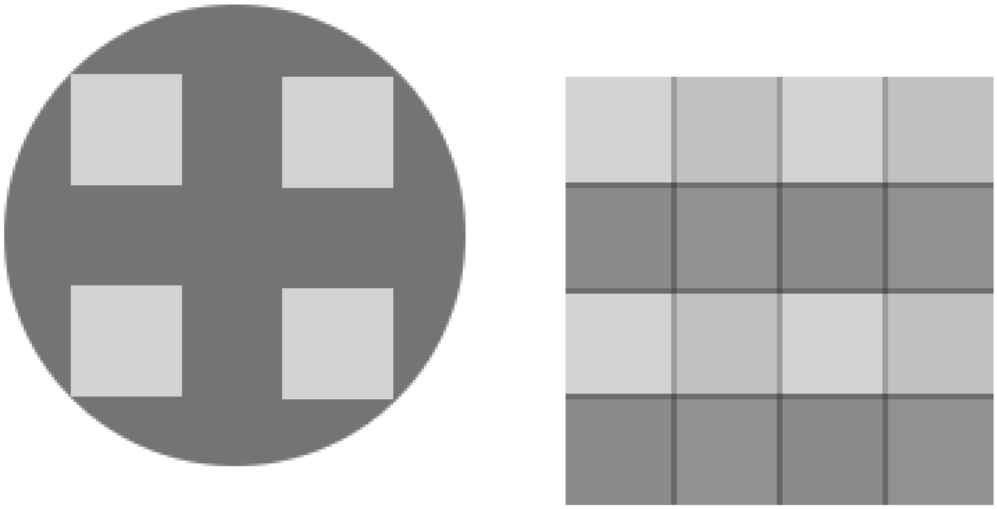

FIGURE 2.1: Left: The layout of the four 2048×2048 WFCAM arrays. Each array is 13.7' in width, the total width is 40.3'. Right: The layout of the four *macro-stepped* pointings, filling in the gaps between arrays. (Warren, 2002)

observations. The GPS observation index contained URL links to the relevant catalogue data, which were retrieved using WGET.

2.4 Epoch Matching

The catalogues were matched using their telescope pointing positions. In most cases there were two observations per pointing. In these cases I took the earlier observation as the first epoch and the later as the second epoch. In some cases where there were more than two observations per pointing, this is usually due to extra observations that had to be repeated on subsequent nights (e.g. due to low image quality). In such cases those pointing groups were separated into two further groups based on an interval of > 1.8 years between observations. The first epoch observation would then be the final observation of the earlier group, and/or the second epoch K observation would be the final observation of the latter group, since once an acceptable observation was made it would not normally be repeated.

The raw FITS file catalogues were fed through a modified fortran routine FITSIO_CAT_LIST originally provided by the CASU team [2]. The modified FITSIO_CAT_LIST unpacks the binary tables for each individual chip in the FITS file, calculates instrumental magnitudes from the fluxes given, flags saturated sources, removes columns which are surplus to my requirements and outputs the resultant tables in ascii space delimited format.

The first and second epochs catalogue pairs were cross matched using the Starlink Tables Infrastructure Library Tool Set (STILTS; Taylor 2006) two-table sky+1d match. The LAS match used a matching radius of 6" and a J band magnitude difference tolerance of 0.5 magnitudes. The GPS matching radius was increased to 24" and K band magnitude difference tolerance decreased to 0.3 magnitudes. The increased matching radius allows me to probe for higher proper motion sources, at the expense of an increase in the rate of mismatches and increased compute time, while not negatively impacting the sensitivity towards low proper motion sources. Since the source density is much greater in the GPS relative to the LAS the rate of mismatches is also much higher, the decrease in the magnitude difference tolerance is an effort to reduce the rate somewhat.

The final pipeline input catalogues are comma separated variable tables of matched pairs of sources. The LAS and GPS catalogues contain of order 17 million and 167 million sources respectively. During the initial run it was necessary to split the GPS input table into a number of smaller sections to run separately since I am limited by a 48 hour job limit on the UH cluster SMP machines. For the final GPS run I retained the multiframe structure of the files, a total of 8463 input catalogues, this overcame the job time limit and aided with parallelisation which had previously used the MATLAB Parallel Computing Toolbox but was limited to 8 cores.

2.5 Reference Star Selection

A preliminary pool of astrometric reference sources was created as a subset of the input catalogue, containing sources meeting these criteria for the LAS:

Classified as stellar at J1 & J2;

J1 & J2 between 16 & 19.6;

[2] http://casu.ast.cam.ac.uk/surveys-projects/software-release/fitsio_cat_list.f/view

J1 & J2 magnitude error < 0.1; and

J1 & J2 ellipticity < 0.3

And these criteria for the GPS:

Classified as stellar at K1 & K2;

K at both epochs between 12.25 and 17.00;

Ellipticity at both epochs < 0.3; and

K uncertainties at both epochs < 0.1.

The decrease in the upper magnitude limit for the GPS reflects a shallower 5σ detection limit in the GPS K band than the LAS J band, and limits the number of mismatches selected as reference sources since they become more common at fainter magnitudes. The GPS lower magnitude limit is a conservative cut of slightly saturated sources and also allows me to retain distant luminous stars as reference points. In the LAS and elsewhere at high Galactic latitude the brightest sources are nearby stars with large motions, owing to the small scale height of the Galactic disc. These make poor astrometric reference stars. In the Galactic plane however, the brightest sources are usually very luminous distant stars with relatively small motions which make good reference stars. Hence it was advantageous to reject bright sources as reference stars in the LAS but the opposite is true for the GPS.

I reject LAS frames containing fewer than 20 reference sources and GPS frames containing fewer than 100 reference sources. The minimum requirement for a second order polynomial fit is 6 but I adopted much larger numbers to ensure the data were well fitted across the frame.

On a frame by frame basis I fit the second epoch array (x/y) positions of the reference sources to their first epoch array positions using a second order polynomial fit and the CP2TFORM function in MATLAB to produce a preliminary global transform of the form:

$$x' = c_1 + c_2 x + c_3 y + c_4 x^2 + c_5 xy + c_6 y^2$$

where:

x' is the transformed x position.

c_i are the 6 coefficients that are fitted in each dimension.

The function is fit separately in the x' and y' dimensions producing 12 coefficients. (2.1)

I applied the inverse of this coordinate transformation (MATLAB does not allow a forward transformation for a second order polynomial) to map the first epoch reference source positions on to the second epoch positions and subtracted these from their second epoch positions to produce preliminary residuals. I measured the uncertainty on the preliminary residuals by calculating the RMS residual to the fit of all reference sources in each frame and added these in quadrature to their centroid errors.

I rejected all reference stars with significant preliminary residuals ($>1\sigma$) usually indicating motion. I then discarded all preliminary positions and motions and performed a further rejection of frames failing the minimum reference stars cuts.

Note that I use array coordinates to calculate the motions since the astrometric fit of UKIDSS frames is performed by CASU using the positions of 2MASS sources, which were observed near epoch 2000. The quality of these fits has degraded over time due to the motions of the 2MASS sources used.

2.6 Second Epoch Position Correction

Final residuals are calculated on a source by source basis. I select all reference stars (with the exception of the target source) in the same frame as the target source as a temporary pool of reference stars. I calculate a global transform by fitting the first epoch reference star array positions to the second epoch reference star array positions using a second order polynomial as before (Equation 2.1), and apply the inverse coordinate transformation to the second epoch target position to map them on to the first epoch array coordinate system. I then calculate the RMS residual to the fit of the reference

sources and add it in quadrature to the centroid error of the target at the second epoch to calculate the uncertainty on the transformed position.

Another second order polynomial fit was then calculated and applied in the same manner but using only reference stars local to the target. For the LAS I selected all reference stars within a radius sufficient to ensure that there were at least 3 in every attached circle quadrant. This radius was rounded up to the nearest 20" and I impose a minimum radius of 1'. For the GPS I increased the quadrant requirement to 5.

The use of this method ensured that there were at least 12/20 (LAS/GPS) reference stars used to calculate each fit and crucially that the reference stars were well distributed about the target source, though typically there would be several times the minimum number of reference sources. If any quadrant contained fewer than the required number of reference stars then a local polynomial was not calculated and I default to using the global polynomial to calculate a final proper motion. This was always the case for sources at the edge of frames. A 'true' value in the relavent column of the catalogue indicates that a source has a proper motion calculated using a local transform. I applied the local polynomial to the target source's second epoch position to map it on to the first epoch array coordinate system and followed the same uncertainty calculation method as before.

To calculate proper motion I used residuals calculated from the local transforms in preference to the global ones. I justify this preference by looking at the uncertainties on the total residuals for the two samples (see Figure 2.2), where the local transform produces smaller average uncertainties on the residuals than the global transform.

2.7 Conversion to Equatorial Coordinate System

In order to transform the array coordinate positions on to the tangent plane of the equatorial system, the first epoch α/δ positions underwent a tangent plane projection conversion about the centre of the frame, producing ξ/η positions (2.2a, and 2.2b). I

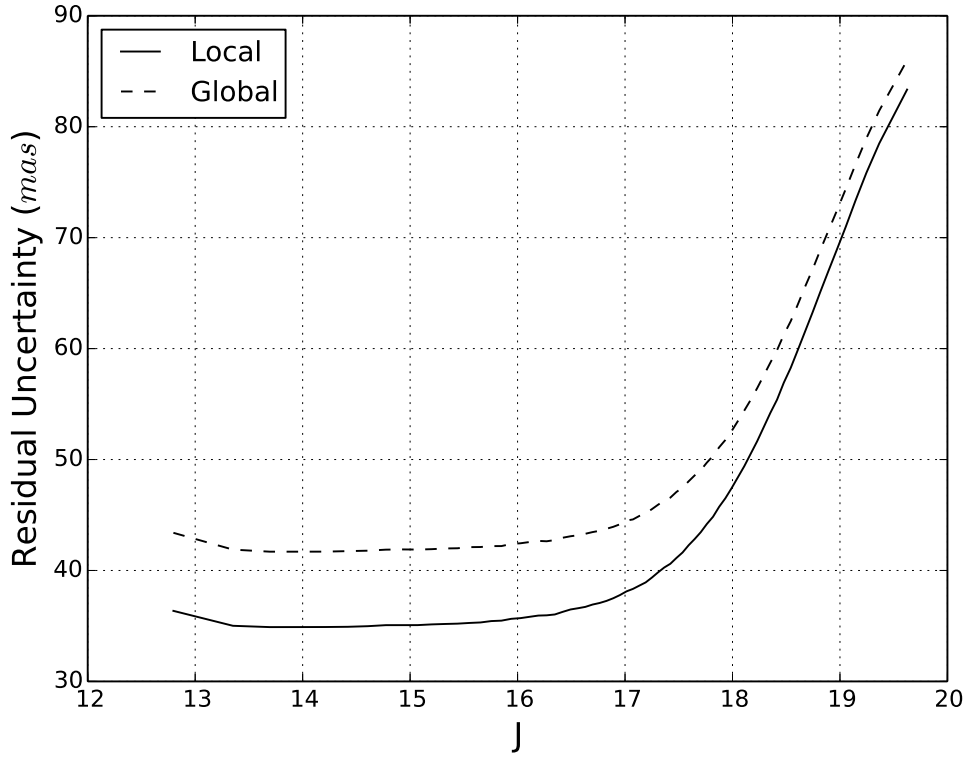

FIGURE 2.2: I selected LAS sources meeting the criteria in Section 3.4.1 with measured local and global residuals (3.5 million sources total) and split them into 70 equal sized J magnitude bins. Note that the exact width in J magnitudes of each bin was allowed to be different, giving greater resolution where the source density allowed but maintaining accuracy at the extreme ends. The mean local and global residual uncertainties in each bin are shown. The local residual uncertainties are consistently lower than the global ones.

used a starlink code S2TP translated into MATLAB to perform this projection.

$$\xi = \frac{\cos\delta \sin(\alpha - \bar{\alpha})}{\sin\delta \sin\bar{\delta} + \cos\delta \cos\bar{\delta} \cos(\alpha - \bar{\alpha})} \tag{2.2a}$$

$$\eta = \frac{\sin\delta \cos\bar{\delta} - \cos\delta \sin\bar{\delta} \cos(\alpha - \bar{\alpha})}{\sin\delta \sin\bar{\delta} + \cos\delta \cos\bar{\delta} \cos(\alpha - \bar{\alpha})} \tag{2.2b}$$

where $\bar{\alpha}, \bar{\delta}$ are the centre points of the frame in the α, δ dimensions

I then fit the first epoch ξ/η positions of all sources in the frame to their corresponding array positions using a third order polynomial:

$$x' = c_1 + c_2x + c_3y + c_4x^2 + c_5xy + c_6y^2 + c_7x^3 + c_8x^2y + c_9xy^2 + c_{10}y^3$$

where:

x' is the transformed x position.

c_i are the 10 coefficients that are fitted in each dimension.

The function is fit separately in the x' and y' dimensions producing 20 coefficients. (2.3)

I then then applied the inverse of this to the first and second epoch array positions (both now in the first epoch array coordinate system) to transform them on to first epoch tangent plane. This was simpler than applying the α, δ information in the fits headers to the second epoch data and has a precision better than 1 *mas*. I transformed the array position 1σ error box, the uncertainty being half the difference between these boundaries after the transformation was applied. Calculation of each source's proper motion was then a matter of subtracting the first epoch tangent plane positions from the second epoch tangent plane positions and dividing through by the epoch baseline. The uncertainty on the proper motion is the first and second epoch positional uncertainties added in quadrature and divided by the epoch baseline.

2.8 Relative to Absolute Proper Motion Correction

Until this stage proper motions were relative to the mean motion of the reference sources used for the fit. These were stellar sources which all have a component of proper motion due to galactic rotation and solar motion. I remove this component of proper motion and convert the relative proper motions to absolute ones, defined by selected extragalactic sources. For the GPS, Lucas et al. (2008) found that the high source density and resultant high frequency of stellar blends mean erroneous galaxy classifications based on a merge of the J, H, and K band classifications are common. In the FITS file data I use here I have morphological classifications based on a single band detection, which is even less reliable. For this reason I did not perform a relative to absolute proper motion correction on the GPS results. I calculated the median relative proper motion of LAS sources meeting the following criteria:

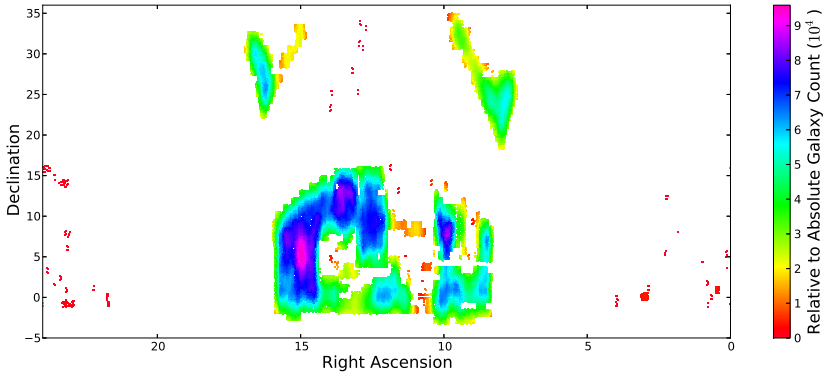

FIGURE 2.3: The distribution of the number of galaxies used to calculate the relative to absolute correction of each frame. Relatively few are used in isolated frames; the lowest value is 5. In frames central to the larger fields values can be as high as 95,000.

Classified as a galaxy in J1 & J2;

J1 & J2 between 12 & 19.6;

J1 & J2 magnitude error < 0.2; and

Total relative proper motion error < 30 $mas\ yr^{-1}$

I used sources in the target frame and those from surrounding frames within three degrees. Their median motions were then subtracted from the relative proper motions of all sources in the target frame. I found that using extragalactic sources only in the same frame or using the mean relative motion for all sources within three degrees introduces significant local scatter in the correction vectors due to inaccuracies in the centroids of extended objects. Figure 2.3 shows how the number of galaxies used varies with sky position. No correction is greater than 10 $mas\ yr^{-1}$ in $\mu_\alpha \cos\delta$ or 12 $mas\ yr^{-1}$ in μ_δ. This is typically less than the uncertainties on the motions (se Figure 2.4). Ideally quasars located in the same frame would be used to calculate the correction, however I would require a sample of confirmed quasars with several well distributed in each frame. The standard error on the median of the relative proper motion uncertainty of the selected galaxies was then added in quadrature to the uncertainties of the relative proper motions of all sources in the target frame to calculate the uncertainties on the absolute proper motions. The median contribution of the relative to absolute proper motion correction to the final proper motion uncertainty is 0.016 $mas\ yr^{-1}$ in both dimensions. See Section 3.4.6 for further discussion.

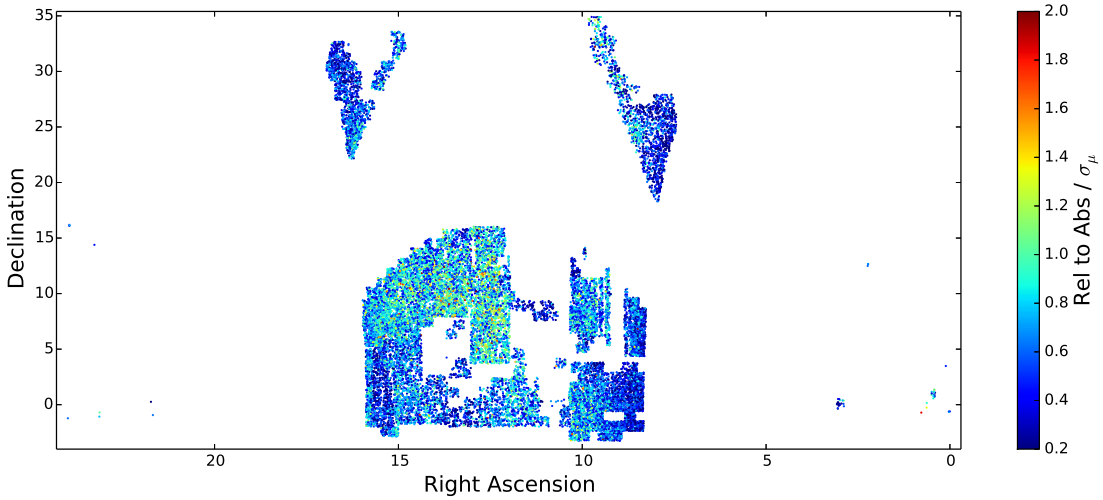

FIGURE 2.4: The distribution of the magnitude of the relative to absolute proper motion correction divided by the total uncertainty on the final absolute proper motion. These are the published 5σ proper motion catalogue data. The colour axis has been truncated at 2σ for clarity but continues to 3.4 in reality. The magnitude of the relative to absolute proper motion correction is typically less than the uncertainty on the motion.

Despite the lack of relative to absolute correction for the GPS, the relatively large distance to most reference stars and their consequently very small proper motions should provide a zero point that is fairly near to absolute. P.W. Lucas [University of Hertfordshire] calculated sample relative to absolute corrections using the Besançon models (Robin et al., 2003) and found that the correction was always ≤ 5 $mas\ yr^{-1}$, at least in the $l > 60°$ area.

Chapter 3

The UKIDSS LAS Proper Motion Catalogue

3.1 Introduction

The LAS covers 4028 deg^2 in YJHK passbands to an approximate 5σ depth of 19.6 in J and is complemented in the ugriz optical passbands by the Sloan Digital Sky Survey (SDSS). The LAS included a second epoch of observations in the J passband to calculate proper motions and investigate stellar variability. In the final months of the UKIDSS program great effort was made to observe as much of the first epoch coverage as possible at second epoch. The final second epoch coverage is around 1500 deg^2.

3.2 Data

Given the minimum epoch baseline of 1.8 years and epoch matching radius of 6", the hard upper proper motion limit of the catalogue is therefore 3."3 yr^{-1}. Though the catalogue is built from frame sets with a range of epoch baselines, giving a range of proper motion limits. Figure 3.1 shows the area distribution of the epoch baselines and the corresponding proper motion limits. Note that I performed an initial rejection of the few input sources brighter than 12^{th} or fainter than 20^{th} magnitude in the J band (see Section 3.4.6).

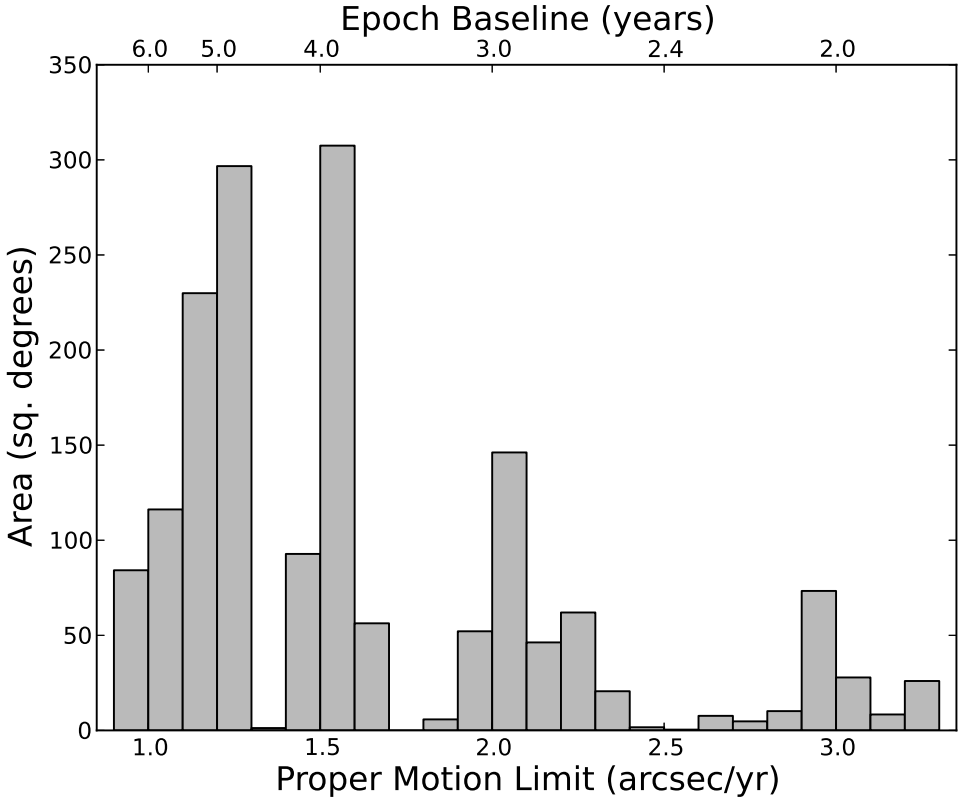

FIGURE 3.1: Plot showing the area distribution of epoch baselines and proper motion limits of the catalogue. Note that the total area represented by this plot is 1678 deg^2, this is simply the number of frames multiplied by the angular area of a frame, the catalogue is nearer to 1500 deg^2 after removal of the duplicated regions of frame overlaps.

3.3 Additional Catalogue Production Steps

3.3.1 Duplicate Source Removal

The resultant LAS catalogue contained duplicates of sources in regions of overlapping frames. I matched internally for groups of sources with separations less than 1" using the Tool for OPerations on Catalogues And Tables (TOPCAT; Taylor 2005), finding 1,614,695 initial groups containing a total of 3,380,822 sources. I found that 99.94% of groups with separations of 0."5 or less contained sources from different frames. I made the assumption that since the overlap of the frames is typically ∼24" it is very unlikely that genuine neighbouring sources would be present only on different frames. Instead, both components of a genuine group would be duplicated. I therefore remove all but the source with the lowest uncertainty on the total proper motion from groups

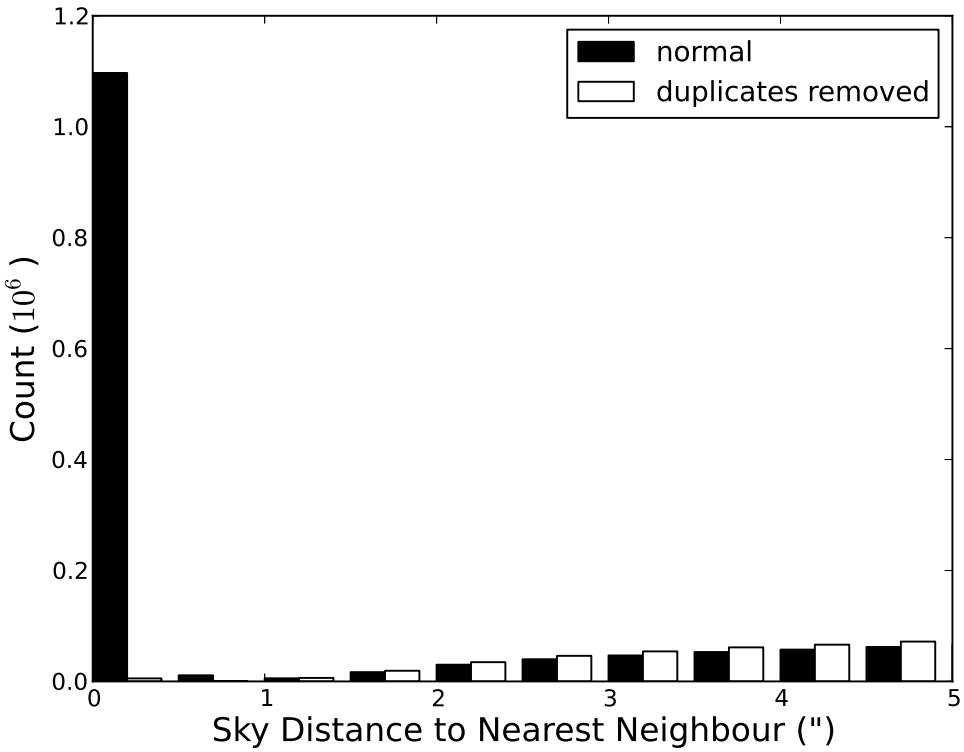

FIGURE 3.2: The distribution of distances between sources (within 10") before and after application of the duplicate removal method. The huge peak at very low separations and the fact that overwhelming majority of these pairs are in different frames is indicative of duplicate sources in frame overlap regions. After removing these duplicates using the method in section 3.3.1 the peak has been almost entirely removed. The remaining sources are close pairs in the same frame set therefore likely to be genuine.

containing sources from different frames (see Figure 3.2). This removed all but the most well measured source from each set of duplicates, a reduction in catalogue size by 10.6%.

3.3.2 YHK Retrieval and Bad Data Removal

I matched LAS DR10 first epoch J band equatorial positions and magnitudes retrieved from the WSA lasDetection tables to the LAS proper motion catalogue, providing WSA assigned source IDs and hence a method to accurately match to their source table and retrieve the data contained within. I retrieved Y, H, and K magnitudes and their associated uncertainties as well as first and second (where available) epoch J band post processing error bits (ppErrBits[1]) information. ppErrBits is a useful indicator of the quality of each detection, larger values are indicative of more severe detection quality issues. I removed from the catalogue all sources with ppErrBits values of 256 or greater

which would correspond to saturation or electronic crosstalk (Dye et al., 2006) or poor flat field region, etc.

3.3.3 Bad Pixel Sources

Approximately 20% of catalogue sources have a '−7' (bad pixel within 2" aperture) classification at either epoch. I found this has a negative effect on the precision of the astrometry, as one might expect. The median total proper motion for this selection is 50% larger than that of the rest of the catalogue, whereas the mean uncertainty is only 25% larger. The source with the median relative proper motion should have a proper motion comparable to the 1σ uncertainty (see Chapter 4, Figure 4.7). Although the proper motion uncertainties on sources with a bad pixel classification at either epoch was already slightly higher than normal sources (by this factor of about 1.25), I inflated their proper motion uncertainties by a factor of 1.2 to mirror the relative increase in median proper motion by this amount. The distribution of the final uncertainties on absolute proper motions is shown in Figure 3.3.

The flag to indicate a bad pixel within a 2" aperture is written over the morphological classification flag present in the original FITS file by FITSIO_CAT_LIST. This meant that the true classification (−1/1, stellar/extragalactic, etc) was unavailable for my purposes. To compensate for this I included the WSA merged class attribute[1] where available. Merged Class is a combination of classifications in all available bands and epochs of UKIDSS DR10 using Bayesian classification rules.

I note that since the proper motions and morphological classifications of these objects are less reliable they are not used as reference sources.

3.4 Analysis of Results

While I produced results for all LAS sources I made public only those with absolute proper motions detected at the 5σ level and above, with a morphological classification indicating a likely stellar nature. I included sources classified as stellar (class = -1) or probably stellar (class = -2) at one or more epochs and exclude sources classed as noise

[1] see http://surveys.roe.ac.uk/wsa/ppErrBits.html

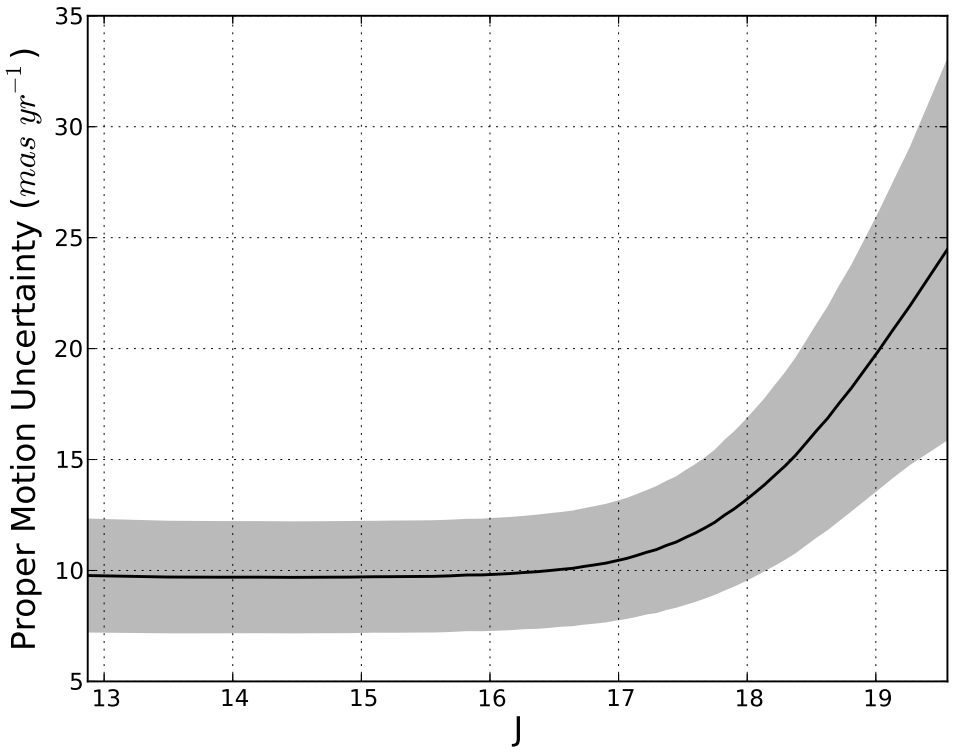

FIGURE 3.3: I selected sources meeting the same criteria as in Section 3.4.1 (5.4 million sources) and split them into 53 J magnitude bins each containing approximately 100,000 sources but having a variable width. The mean uncertainty on μ_{total} in each bin is plotted. The shaded section shows the region bound by 1 standard deviation.

(class = 0) at either epoch. I found 135,625 sources classified as stellar in both J band detections, and a further 88,324 sources with ambiguous morphological classifications. This produced a catalogue of 223,949 sources in the 1500 deg^2 area shown in Figure 2.3. Note that ellipticity and morphological classification traced genuine high proper motion detections very well at J≤19 (see Section 3.4.5). However, in the interest of not rejecting large numbers of potentially genuine sources I imposed no restriction on ellipticity. I recommended that users employ cuts on ellipticity and morphological classification if a very reliable high proper motion sample is sought. The lowest uncertainties for the brightest and faintest sources are 4 and 12 $mas\ yr^{-1}$ respectively, corresponding to the longest epoch baselines. The 5σ lower limit on absolute proper motion significance therefore corresponds to minimum proper motions of 20 to 60 $mas\ yr^{-1}$ for bright and faint sources respectively. A sample of the catalogue is presented in the appendix (Table A.1) and the full table is available online at http://star.herts.ac.uk/ lsmith/downloads.html.

I scrutinised 1/5th of the results, approximately 300 deg^2. This area corresponds to the overlap with second epoch J coverage of UKIDSS DR10.

3.4.1 Comparison to WSA Proper Motions

With the WFCAM Science Archive's 9th release of LAS data came proper motions (Collins and Hambly, 2012) to which I have compared my results (Figure 3.4). The WSA proper motions are not absolute, so here I compare using the relative proper motions calculated by the pipeline. The WSA uses a linear transform in the tangent plane across the whole frame which I have shown in Section 2.6 to be less accurate. It effectively assumes that there are no non-linear distortions in the focal plane apart from the known 3rd order radial distortion that is removed by the CASU WFCAM pipeline as part of the astrometric solution for each WFCAM array.

I calculated proper motions for a new input data set containing the most recent WSA DR10 data from the LAS detection table. Matching the two catalogues using the unique source IDs assigned by the WSA and maintained throughout the proper motion pipeline ensured there were no mismatches.

I selected sources with no post processing error flags, low ellipticity and classified as stellar in both J band images as an appropriate group of sources for comparison, a total of 1.6 million sources.

The proper motion measurements are fairly consistent between the catalogues with Pearson product-moment correlation coefficients of 0.80 and 0.82 in $\mu_\alpha \cos\delta$ and μ_δ respectively and 86% and 99% of proper motions matching within their 1σ and 2σ uncertainties respectively. The WSA proper motions are obtained using all available LAS detections in the YJHK passbands. The WSA assumes that chromatic dispersion is minimal, and hence no effort is made to correct for the effects of this. I note that where the WSA results used multi-band frames to calculate a proper motion the values differ slightly more, with Pearson's r coefficients of 0.79 and 0.82 in $\mu_\alpha \cos\delta$ and μ_δ respectively. As one might expect, for the few sources with only J band images the proper motions agree very well, with Pearson's r coefficients of 0.99 in both $\mu_\alpha \cos\delta$ and μ_δ.

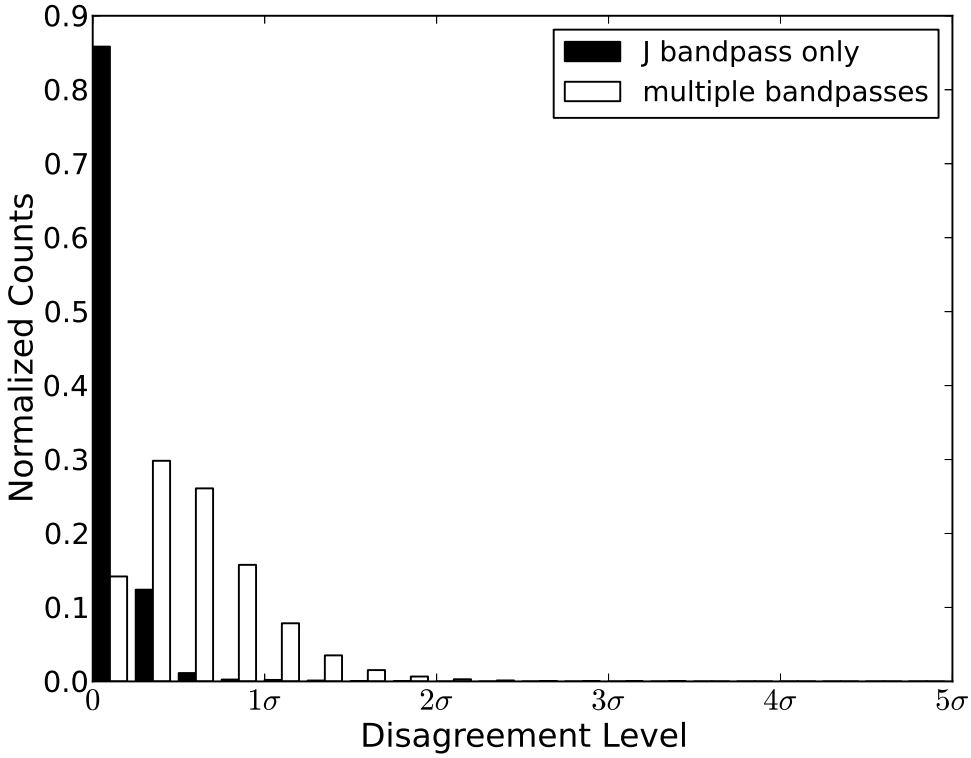

FIGURE 3.4: Histogram showing the distribution of disagreement between proper motions of stellar sources from my LAS pipeline and those from the WSA. The catalogues agree very well where the WSA has used only J bandpass data for their proper motion, and less well where they have use multiple bandpasses. Pearson product-moment correlation coefficients are 0.99 and 0.80 for J only and multiple bandpass total proper motions respectively.

3.4.2 Comparison to LSPM Catalogue

The LSPM catalogue (Lépine and Shara, 2005) utilises the SUPERBLINK software (Lépine et al., 2002) to normalise the differences between pairs of sub-frames from the POSS-I (Abell, 1959) and POSS-II (Reid et al., 1991) plates (usually involving a degradation in the quality of the POSS-II plate to match the POSS-I plate quality), then subtraction of one from the other to produce a residual image which maps the first and second epoch positions of sources with high proper motion. The catalogue benefits from the fact that all high proper motion sources identified by the SUPERBLINK software were manually blinked to remove any erroneous high proper motion sources, the LSPM catalogue has a minimal false detection contamination as a result. The LSPM catalogue also includes data from the TYCHO-2 (Høg et al., 2000) catalogue and the All-Sky Compiled Catalogue (Kharchenko, 2001).

I matched the LSPM-North catalogue to the LAS proper motion catalogue using a 3" matching radius and a 0.5 magnitude J band discrepancy tolerance. I found 381 matches and compared LSPM and my LAS proper motions, see Figure 3.5. The majority of LSPM proper motions given are derived using the author's SUPERBLINK software, there is one Tycho-2 proper motion and four from 'other' sources, these five proper motions agree well with those from the LAS catalogue. I found proper motions from both catalogues agreed within their 1σ uncertainties for 79% of sources, this rises to 98% agreement at 2σ. The LSPM proper motion uncertainties were taken as 8 $mas\ yr^{-1}$ (Lépine and Shara, 2005). The proper motions are also well correlated, with Pearson product-moment correlation coefficients of 0.994, 0.979 and 0.980 ($\mu_\alpha \cos\delta$, μ_δ and μ_{total} respectively). From a sample of 381 sources I do not expect any to have proper motions with a disagreement greater than 4σ, I found 3 of these: LSPM J1644+3203, 4.43σ; LSPM J1625+2519, 4.81σ; and LSPM J1609+2457, 27.41σ. I discuss these three outliers below, see also Section 3.4.6.

LSPM J1644+3203

In the J1 image the high proper motion source is overlapping another source to the north with a separation of 1."3. This is probably causing the centroid on the object at J1 to be skewed north causing the observed larger proper motion in declination. The proper motion in right ascension agrees comfortably. LSPM J1644+3203 is NLTT 43473 (see Section 3.4.3) which has a proper motion in agreement with the LSPM catalogue.

LSPM J1625+2519

On inspection of the 2 epochs of UKIDSS LAS J band images the source is separated by 1."7 from another source, which was unresolved in the photographic data. Plotting the positions of the centroids at both epochs shows that at the second epoch the centroids are well fitted to both sources. The first epoch image quality is slightly lower which caused the fainter target to go undetected and the centroid for LSPM J1625+2519 to be skewed towards it, altering the measured proper motion. Interestingly the source which is overlapping LSPM J1625+2519 appears to share a common proper motion with it.

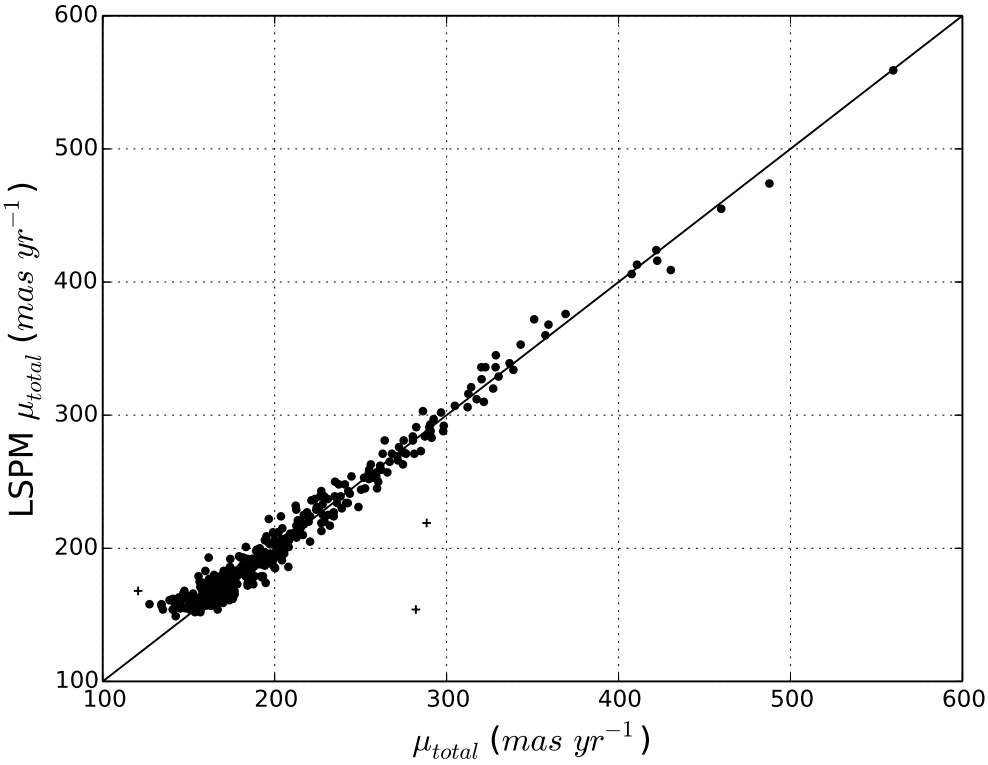

FIGURE 3.5: LSPM total proper motions (vertical axis) versus those calculated by my pipeline (horizontal axis) for the 381 matches between the two catalogues. The crosses are LSPM J1644+3203, LSPM J1625+2519, and LSPM J1609+2457 for which the total proper motions differ greater than 4σ. The data are nevertheless well correlated; the Pearson product-moment correlation coefficient is 0.980.

LSPM J1609+2457

While blinking the 2 epochs of UKIDSS LAS images the source does appear at first glance to exhibit a proper motion consistent with the LAS value, I note that the quality of the first epoch J band image is poor. Blinking of the POSS I and II images reveals a motion consistent with the value given in the LSPM catalogue. No other source with a proper motion consistent with LSPM J1609+2457 is found in the LAS proper motion catalogue within 1' of its given location. The cause of this erroneous proper motion measurement is likely the poor first epoch UKIDSS J band image and resultant centroid fit. Since the LAS proper motion is likely to be the incorrect proper motion measurement I have included this source in this comparison.

I attribute the presence of the poor quality images mentioned above to my use of data that have not yet been through the UKIDSS quality control procedures that take place prior to a formal SQL data release. I note that this has probably been the cause of two of the erroneous proper motions from this sample of 381.

In an effort to gauge the completeness of the catalogue I identified LSPM sources within the UKIDSS DR10 area and with 2MASS J magnitude > 12.5. The J magnitude cut includes null values and allows for a half a magnitude discrepancy between the UKIDSS and 2MASS J band magnitudes, this is necessary to accomodate recovery of UKIDSS objects measured up to half a magnitude brighter than in 2MASS, which would otherwise appear unrecovered due to my 12th magnitude bright limit. I identify 379 LSPM sources that should be present within this catalogue, of which I recover 375 with proper motions that agree within 4σ. A further three sources have discrepant proper motions, these are LSPM J1644+3203, LSPM J1625+2519, and LSPM J1609+2457 (see above). The final unrecovered source is LSPM J0829+2539/LHS 2015. LHS 2015 is a previously unresolved common proper motion pair originally classified by Reid and Gizis (2005) as a DQ white dwarf. The pair are unresolved in the first epoch J band image and are consequentially more than half a magnitude brighter than the resolved magnitudes at the second epoch. This caused the pair to fail this quality control cut at the epoch matching stage. If I consider sources with discrepant proper motions as unrecovered then I have an LSPM source recovery rate of 98.9%, otherwise the recovery rate is 99.7%.

Figure 3.6 compares the number of high proper motion (>150 $mas\ yr^{-1}$) sources fainter than J=12 as a function of J magnitude in the UKIDSS DR10 area from the LAS proper motion catalogue and the LSPM. I require sources in my catalogue to have ellipticity $<$ 0.3 and be classified as stellar at both epochs. This requirement means I can infer an approximate false positive rate from Figure 3.10, at the likely expense of some genuine detections. The LSPM catalogue is more complete at the bright end, where my catalogue suffers to a degree from saturation. I begin to find more high proper motion sources than the LSPM catalogue at about J=13.5. The false positive rate of LAS sources increases

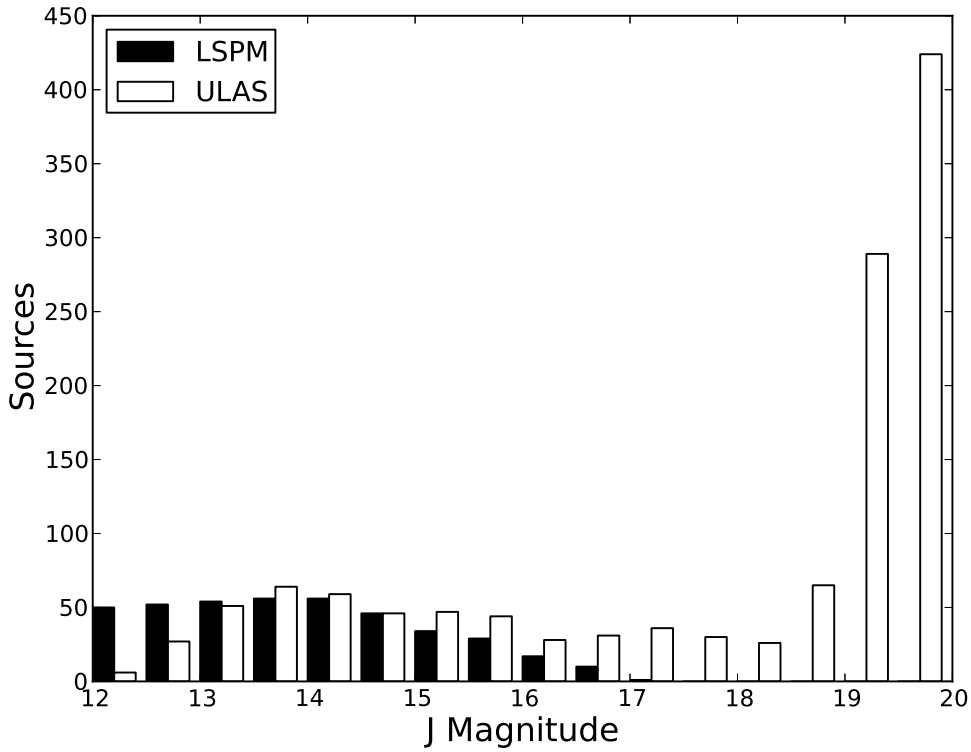

FIGURE 3.6: A comparison between the number of LSPM high proper motion stars and those from the LAS proper motion catalogue after application of ellipticity and morphological classification cuts (see text). Note that the false positive rate of the LAS high proper motion detections increases sharply at J∼19. The LAS proper motion catalogue is more complete fainter than J=13.5.

sharply at around J=19 (see Figure 3.10) which must be taken into account, and that 25 LSPM sources (6%) have null J band magnitudes and therefore could not be included in the comparison. The decline in source counts in the LAS proper motion catalogue at J≥13.5 I believe is due to the increasing average distance, and hence smaller average proper motion of these relatively faint stars.

3.4.3 Comparison to Revised NLTT Catalogue

The Luyten Half Second (LHS) Catalogue contains stars with proper motions exceeding 0."5 annually (Luyten, 1979a). The LHS catalogue contains positions, proper motions and optical magnitudes for 4,470 stars with proper motions greater than 239 $mas\ yr^{-1}$ (note that a small number of sources were included, in spite of the 0.5 " yr^{-1} lower limit). The catalogue includes data compiled from other proper motion searches and

804 hand/machine-blinked Palomar Sky Survey fields. The LHS catalogue was revised by Bakos et al. (2002). 4,323 of the original 4,470 high proper motion sources were recovered and their positions and proper motions were refined.

The NLTT (New Luyten catalogue of stars with proper motions larger than Two Tenths of an arcsecond, Luyten 1979b) catalogue is an extension of the LHS catalogue down to proper motions of 40 $mas\ yr^{-1}$ for 58,845 sources. A minority (152) have proper motion less than 180 $mas\ yr^{-1}$ however. The NLTT catalogue was revised and refined by Salim and Gould (2003), giving improved positions and proper motions for sources present in both the original POSS I frames and the second 2MASS data release.

I matched the Revised NLTT catalogue (rNLTT, Salim and Gould 2003) to the LAS proper motion catalogue using the same matching criteria as for the LSPM comparison (section 3.4.2), this time finding 115 initial matches, see Figure 3.7. I found proper motions from both catalogues agreed within their 1σ uncertainties for 70% of sources, rising to 94% agreement at 2σ. The remaining 7 sources have proper motion disagreements of greater than their 4σ uncertainties: NLTT 43473, 4.73σ; NLTT 22010, 6.22σ; NLTT 21214, 9.36σ; NLTT 20123, 10.14σ; NLTT 18649, 21.01σ; NLTT 18692, 21.52σ; and NLTT 19021 26.74σ. This represents a relatively high discrepancy rate. As a result I visually inspected the POSS I and II photographic plate scans to investigate the cause of these differences in proper motion. I found all but NLTT 43473 and NLTT 20123 to have incorrect J2000 position measurements and all but NLTT 43473 have spurious proper motion values upon comparison to other proper motion catalogues. Pearson product-moment correlation coefficients are 0.998, 0.995 and 0.988 $\mu_\alpha \cos\delta$, μ_δ and μ_{total} respectively after removal of the 6 sources as discussed below.

NLTT 43473

In the J1 image the high proper motion source is overlapping another source to the north with a separation of 1.”3, likely causing the centroid on the object at J1 to be skewed north and further causing the observed larger proper motion in declination. Proper motion in right ascension agrees comfortably. Since this is a genuine match and the rNLTT proper motion is corroborated by the LSPM catalogue I have included it in the comparison.

NLTT 22010

No high proper motion object is observed during blinking of 3' × 3' UKIDSS images, in agreement with my proper motion results. I included the 2MASS image in blinking and still no high proper motion object is evident. No source in the LAS proper motion catalogue has a similar proper motion within 1' of the given position of NLTT 22010. I can see no source with stated rNLTT 22010 proper motion when blinking 12' × 12' POSS-I and POSS-II images (which have a 42 year baseline, the total expected movement is 7.8" which should be clearly visible). Also note that this source is not present in LSPM match even though its area should be covered. This high proper motion detection is therefore questionable and has been removed from this comparison as a result.

NLTT 21214

Inspection of 1' × 1' UKIDSS images centred on the rNLTT J2000 position of NLTT 21214 reveals the UKIDSS source as clearly extended and with no proper motion, in agreement with the LAS proper motion catalogue and consistent with an extragalactic source. I located NLTT 21214 approximately 1.'25 to the north east of the Salim and Gould (2003) given J2000 position. Furthermore the magnitude of the rNLTT proper motion for this source (-75 and -174 $mas\ yr^{-1}$ in $\mu_\alpha \cos\delta$ and μ_δ respectively) is not in agreement with the LSPM catalogue (-114±8 and -217±8 $mas\ yr^{-1}$ in $\mu_\alpha \cos\delta$ and μ_δ) or my own (-123±9 and -228±8 $mas\ yr^{-1}$ in $\mu_\alpha \cos\delta$ and μ_δ). The original NLTT proper motion is closer (-104 and -195 $mas\ yr^{-1}$ in $\mu_\alpha \cos\delta$ and μ_δ). This source has been removed from the comparison due to a suspected incorrect rNLTT proper motion.

NLTT 20123

The high proper motion source is evident on blinking of UKIDSS and POSS images, the direction of proper motion is in agreement with rNLTT and the LAS proper motion catalogue. A rough centroid on the source at both epochs using the Region tool in DS9 and WCS coordinates gives proper motions of 54 and -102 $mas\ yr^{-1}$ in RA and Dec respectively, consistent with the LAS proper motion catalogue values. USNO-B1.0 and LSPM proper motion values are also consistent. No source in the LAS proper motion catalogue has a similar proper motion within 2' of the given position of NLTT 20123. I

suspect the rNLTT proper motion of this source is incorrect and have removed it from this comparison.

NLTT 18649

I blinked POSS-I (R band) and POSS-II (IR) images with an epoch baseline of 48 years and located NLTT 18649 1.'4 south south west of Salim and Gould (2003) J2000 location. I located NLTT 18649 in the LAS proper motion catalogue with a proper motion not in agreement with rNLTT but agreeing well with LSPM and USNO-B1.0 values. I suspect the rNLTT proper motion of this source is incorrect and have removed it from this comparison.

NLTT 18692

I located NLTT 18692 1.'25 south west west of Salim and Gould (2003) J2000 location. The rNLTT proper motion for NLTT 18692 is inconsistent with the USNO-B1.0 and LSPM catalogue values and has been removed from this comparison as a result. The LSPM and USNO-B1.0 proper motion values agree well with those of the LAS proper motion catalogue.

NLTT 19021

I located NLTT 19021 1.'4 south south east of Salim and Gould (2003) J2000 location. The rNLTT proper motion for NLTT 19021 is inconsistent with the USNO-B1.0 and LSPM catalogue values and has been removed from this comparison as a result. Note that the LSPM and USNO-B1.0 proper motion values agree very well with those of the LAS proper motion catalogue.

3.4.4 Testing the Relative to Absolute Correction

I produced a list of quasar candidates by matching the full LAS proper motion catalogue to the Large Quasar Reference Frame (LQRF; Andrei et al. 2009) using a 1" matching radius. I rejected quasar matches with more than one ULAS source within 3" and any that did not meet the restrictions imposed on reference stars described in Section 2.5,

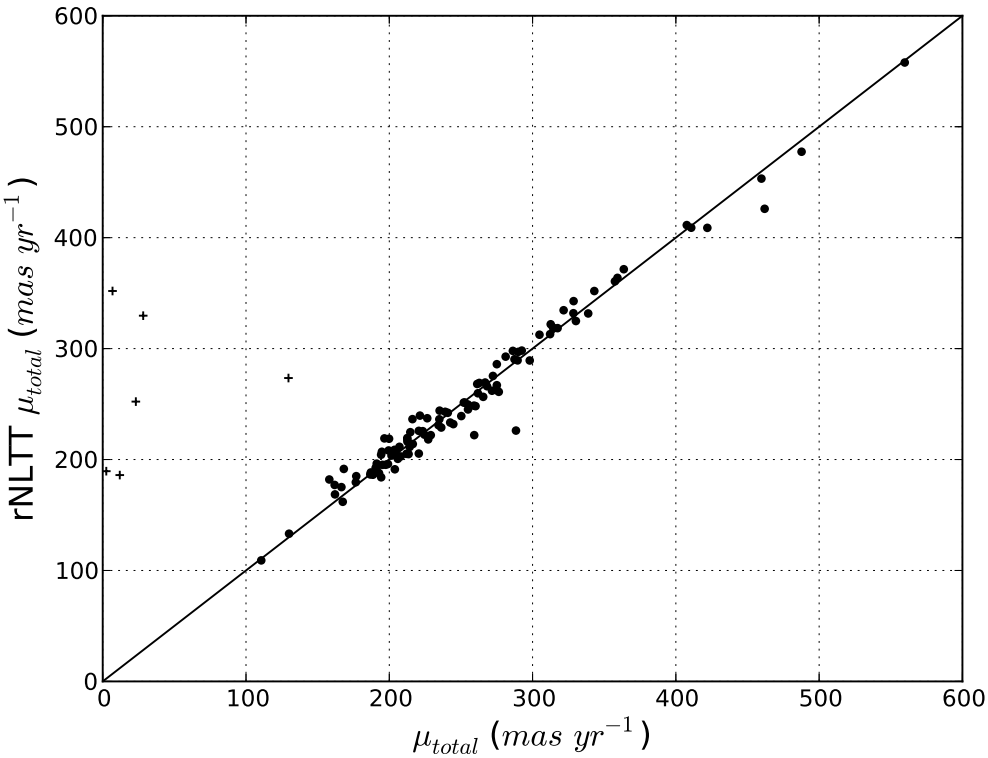

FIGURE 3.7: Comparison between proper motions from the revised NLTT catalogue (vertical axis) and those calculated by my pipeline (horizontal axis) for the 109 reliable matches between the catalogues. The 6 sources represented by crosses are those with proper motions differences greater than 2σ listed in section 3.4.3, these were removed from the comparison since they were found to have spurious rNLTT proper motion values. The Pearson product-moment correlation coefficient for the remaining data is 0.988.

leaving 4,661 quasar candidates. The mean absolute proper motion of this sample is -0.44 ± 0.16 and -0.08 ± 0.15 $mas\ yr^{-1}$ in $\alpha \cos\delta$ and δ respectively. While the mean absolute proper motion of this sample in $\alpha \cos\delta$ is significant at the 2.75σ level, I note that it is much smaller than the typical uncertainties on the proper motions (see Figure 3.3). Figure 3.8 shows that distribution of proper motion significances for this sample.

I selected a sample of 214,593 sources with which to test the direction and magnitude of the relative to absolute correction. Sources were selected in absolute proper motion space such that their motions were greater than three times their error and less than 500 $mas\ yr^{-1}$, since I wanted to exclude the nearest sources for which random velocity dispersion is the dominant factor in their proper motion, as opposed to Galactic location. I also selected only sources with $16 <$ J1 & J2 < 19.6, J1 & J2 uncertainty < 0.1, J1 & J2 ellipticity < 0.3, and classified as stellar at both epochs. I binned the sample in 13

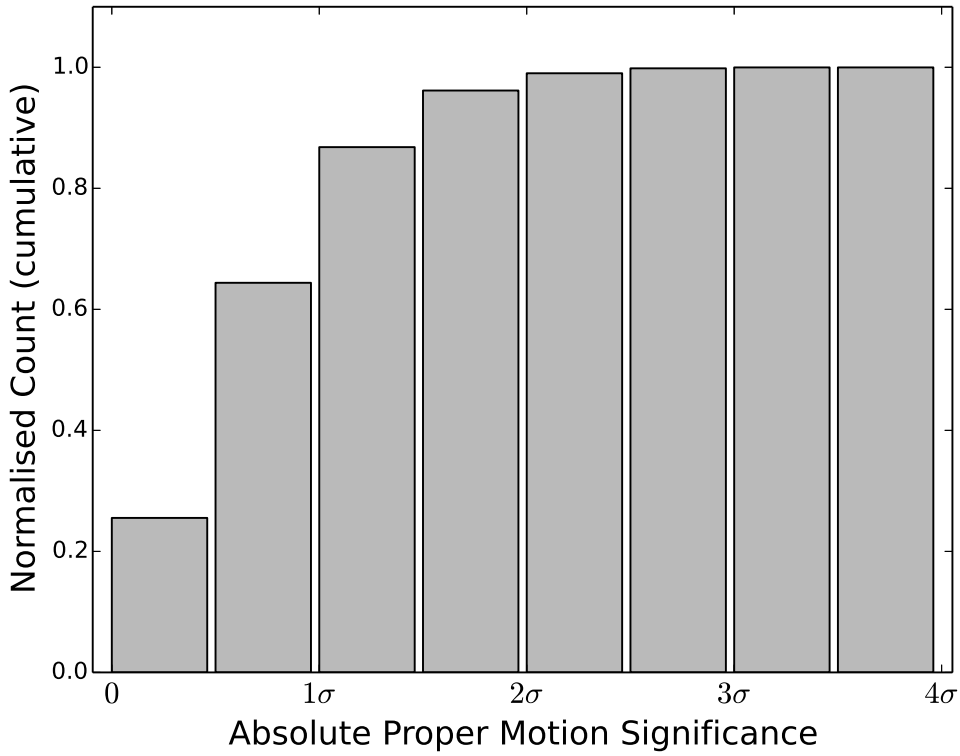

FIGURE 3.8: I identified 4,661 quasars within the LAS proper motion catalogue using a method described in Section 3.4.4. This plot shows the distribution of the proper motion significance of the quasar sample.

$\times$ 13 degree bins ($l \times b$), rejecting any bins containing fewer than five sources. Proper motions were converted into the galactic coordinate system and the median motion of each bin was calculated. Figure 3.9 shows the median motions in galactic coordinates, which agree well with an equivalent plot derived from Hipparcos measurements in Abad et al. (2003; their figure 4). The points with Galactic latitude $b < 0°$ are those of the isolated fields which have very low relative to absolute correction reference galaxy counts (see Figure 2.3). While the UKIDSS LAS and hence this catalogue were not designed to improve on the values of Oort's constants, A.H. Andrei [Observatório Nacional, Observatório do Valongo, RJ, Brazil] derived a value of $-13.79 \pm 6.58\ km\ s^{-1}\ kpc^{-1}$ for the B constant. This agrees with a value of $-12.37 \pm 0.64\ km\ s^{-1}\ kpc^{-1}$ derived from Hipparcos measurements by Feast and Whitelock (1997) and should therefore validate my relative to absolute correction. The A constant is related to radial velocity in the LAS and hence a well constrained A constant is difficult to obtain.

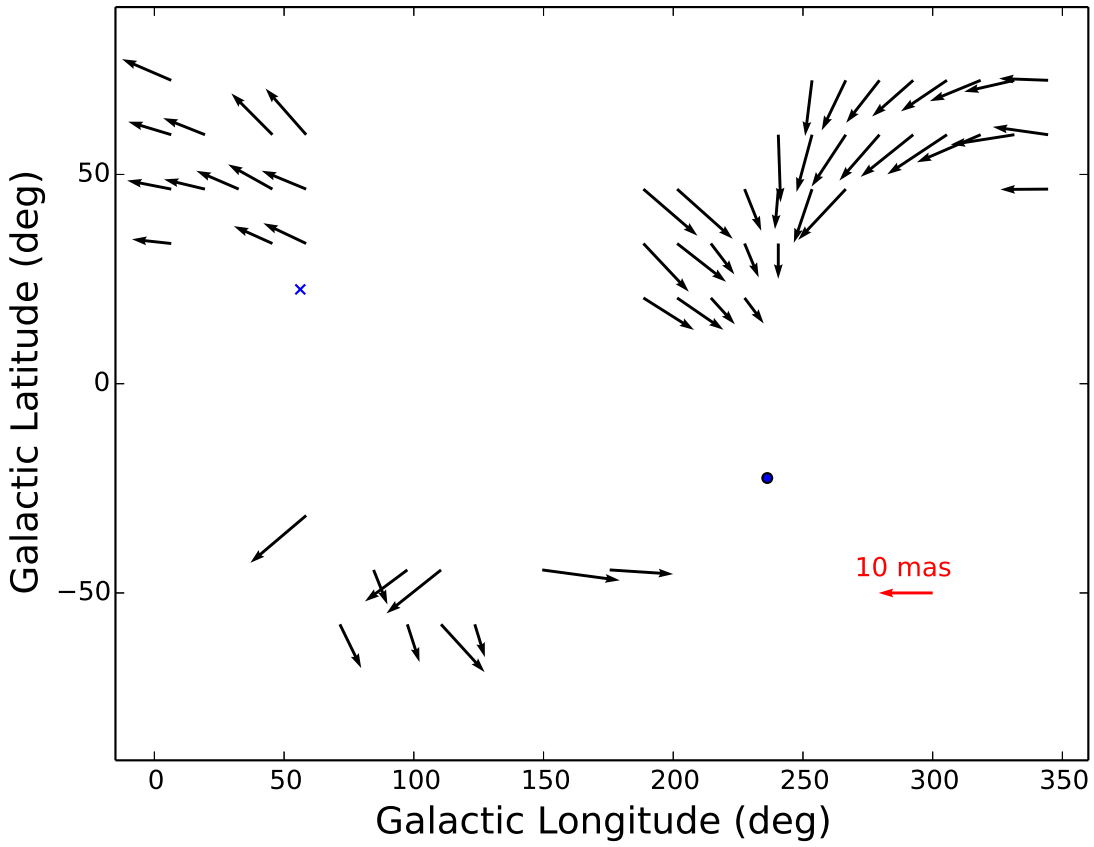

FIGURE 3.9: Median proper motions in galactic coordinates of a sample of 214,593 sources with well measured proper motions. The sample was separated into 13 × 13 degree ($l \times b$) bins. The blue cross shows the solar apex, the blue circle the solar antapex. The red arrow shows an example motion of magnitude 10 mas. The points with Galactic latitude $b < 0°$ are those of isolated fields which suffer from a relative lack of reference galaxies.

3.4.5 Investigation of Faint Limit

To attempt to quantify the reliability of catalogue proper motions and provide a reliable sample of brown dwarf candidates for binary searches (see Section 3.5.3.2) A. Wilkinson [University of Hertfordshire, work experience student] and I blinked all 980 sources with motions of 500 *mas* or more that also met the following criteria:

Y-J > 0.7

J1 & J2 ellipticity < 0.3

J1 & J2 classification −1 (stellar)

mergedClass = −1 (stellar)

We assigned classifications of genuine, false and unsure based on their calculated motion compared to their apparent motion. A further classification, interesting was applied if there appeared to be another object in the 1'×1' field with roughly the same motion vector (see Section 3.5.3.2). I chose a minimum motion between epochs of 500 *mas* since a motion of this magnitude should be detectable by eye, covering 2.5 pixels between the LAS J band images.

First epoch images were obtained using the multiGetImage tool of the WSA and I wrote Linux scripts to retrieve second epoch J band images via the WSA Archive Listing tool. A further shell script was used to automatically select pairs of images and blink them using DS9, which made visual inspection of this sample of almost one thousand images possible in under a day.

Figure 3.10 shows the distribution of genuine, false and ambiguous proper motions for this sample in proper motion and brightness. We find the catalogue to be very reliable for red sources brighter than J=19. Reliability is diminished at the faint end but there are still many genuine high proper motion sources that can be found. We found a total of 834 genuine high proper motion sources in this sample. I note that the vast majority of false high proper motions were due to mismatched sources, which is to be expected due to the 0.5 J mag variability tolerance and given the increase in source density towards the faint end.

3.4.6 Catalogue Caveats

I find that ULAS sources brighter than 12 in J are often either saturated or very close to saturation and their centroids often fall in different places at different epochs and wavebands. This causes false high proper motions and large differences between the WSA proper motion values and my own. The vast majority of saturated objects were identified and flagged by the WSA and then removed from this proper motion catalogue by myself, though further investigation showed that a few remained and as a result I elected to remove all sources brighter than 12 in the J band. I also find diffraction spikes of very bright stars as false high proper motion objects. Where these are not identified by the CASU/WSA pipelines they are usually identifiable as having large ellipticities and are easy to screen for through visual inspection, the pdf document report generated by the multiGetImage tool of the WSA in standard mode is sufficient in most cases.

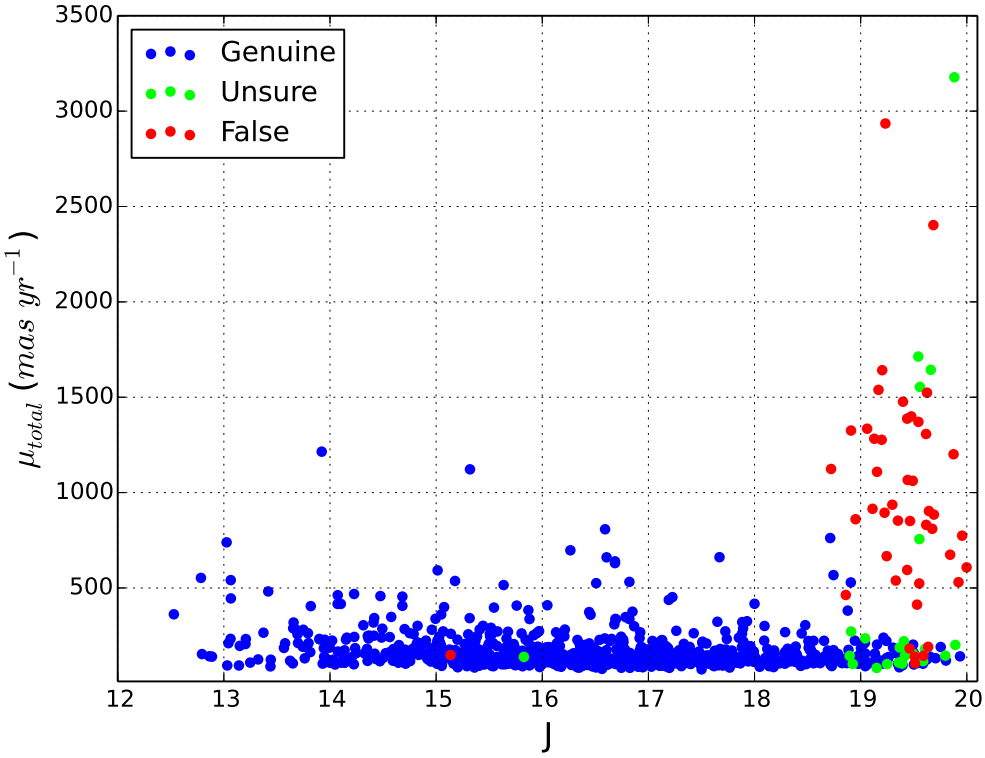

FIGURE 3.10: The distribution of *genuine*, *false* and *ambiguous* high proper motion candidates from Section 3.4.5 in proper motion and J band brightness.

Ideally quasars should be used for a relative to absolute correction but I would require several well distributed about each frame. A simple 1" match to the Large Quasar Reference Frame (LQRF; Andrei et al. 2009) yields one quasar for every two LAS frames on average which is insufficient for this purpose. Therefore I used galaxies as described in Section 2.8.

Relative proper motions are relative to the average motion of the reference stars used to compute the polynomial transform. Where a local transform is used the zero point motion is never exactly the same. This may introduce a small systematic random error into the absolute proper motion since the correction vectors are applied globally. Steps have been taken to limit this: only sources with small preliminarily measured residuals are used as reference sources in the final fit; and the requirement of at least 3 reference sources in each quadrant means that a minimum of of 12 reference sources are used. This should be sufficient to reduce any scatter in global - local mean motions. Indeed, I find that the mean difference between global and local residuals for bright stars is 13

mas on each axis, which is only 20% of the typical uncertainty on the residuals. Visual inspection of the spatial distribution of local-global variation shows no serious anomalies.

Sources LSPM J1625+2519 and LSPM J1609+2457 were found in my LAS proper motion catalogue with proper motion measurements inconsistent with those of the LSPM catalogue (see Section 3.4.2). An inspection of the J band UKIDSS images indicated that the source of these inconsistent proper motions may be a poor quality UKIDSS frame for each leading to an inaccurate centroids on the sources at those epochs. This is probably due to the inclusion of a small number of poor quality UKIDSS images because much of the second epoch data have not yet been through the UKIDSS quality control procedures. I note however that 99.5% of sources compared were unaffected by this and it is as such a minor issue.

3.5 Results

To capitalise on the availability of proper motions and a wide range of photometry for a large fraction of the LAS field I undertook several searches for new high proper motion objects which I detail here. Results of searches for new benchmark ultracool dwarfs can be found in Section 3.6. Note that unless stated otherwise Y, J, H, and K magnitudes in this section are on the MKO system and J band photometry is UKIDSS first epoch. I give first epoch J magnitude since it is most often contemporaneous with the Y band observation.

3.5.1 Initial Searches for Interesting High Proper Motion Objects

In a further effort to gauge the reliability of the catalogue to search for new high proper motion objects I selected a group of bright high proper motion objects from the 300 deg^2 of overlap with UKIDSS DR10 that also met the following restrictions:

J1 < 18

J1 & J2 ellipticity < 0.3

J1 & J2 classification -1 (stellar)

$\mu > 300\ mas\ yr^{-1}$

Note that there were no colour constraints in this selection. The selection left me with 42 sources to investigate. I retrieved their first and second epoch J band FITS images from the WSA using the multiGetImage tool and cross matched with SIMBAD to get names and alternative proper motions where available. I also cross matched to the SDSS ninth data release, which I verified visually, to retrieve ugriz optical photometry. Their images were blinked to verify their high proper motions. The values determined are given in Tables A.4 and A.5. I note that one source is false (discussed below) and is therefore not included in these tables.

Here I itemise sources of interest amongst the 41 bright, high proper motion sources.

LSR J0745+2627

This object was selected as one of the highest proper motion sources in a prototype version of this catalogue based on UKIDSS LAS DR9 data. It has previous proper motion measurements by Lépine and Shara (2005) and white dwarf identification by Reid (2003). Using this catalogue LSR J0745+2627 was re-identified by Catalán et al. (2012) as the brightest pure-H ultracool ($T_{eff} < 4000\ K$) white dwarf currently known.

LHS 6139 and ULAS J081127.84+203925.7

LHS 6139 and ULAS J081127.84+203925.7 share a common proper motion (see Figure 3.11). The difference between their measured proper motions in their measured proper motions is half the uncertainty in the difference.

ULAS J082155.56+250939.8

I re-identified the T4.5 dwarf ULAS J082155.56+250939.8. This object was identified and its spectral type confirmed spectroscopically by Burningham et al. (2013).

2MASS J07414920+2351275

The T5 dwarf (Burgasser et al., 2006) 2MASS J07414920+2351275 has a proper motion discrepancy between this catalogue ($-262 \pm 11\ mas\ yr^{-1}$ and $-212 \pm 9\ mas\ yr^{-1}$ in RA

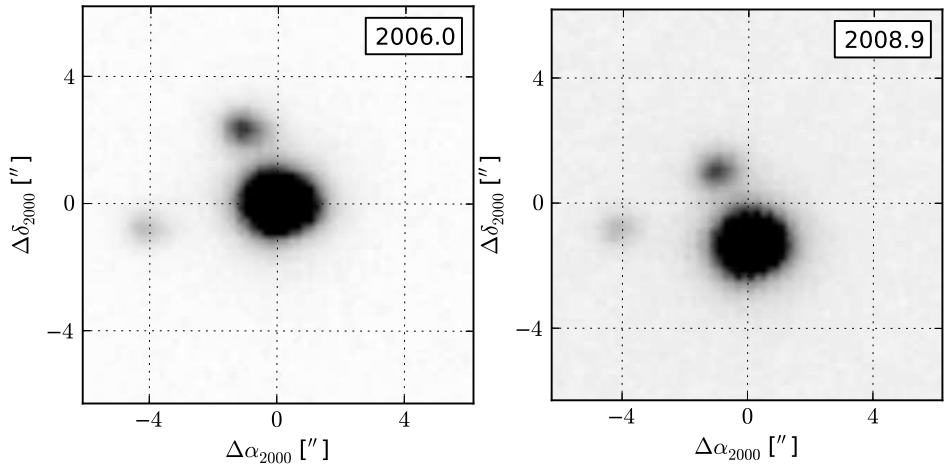

FIGURE 3.11: First and second epoch LAS J band images of LHS 6139 and ULAS J081127.84+203925.7 centred on the first epoch position of the former. Their common proper motion is evident.

and Dec respectively) and previous measurements by Casewell et al. (2008) (-250.22 ± 12.18 *mas* yr^{-1} and -116.21 ± 13.32 *mas* yr^{-1} in RA and Dec respectively) and Faherty et al. (2009) (-243 ± 13 *mas* yr^{-1} and -143 ± 14 *mas* yr^{-1} in RA and Dec respectively). Faherty et al. (2009) also provide a distance of 18 ± 2 *pc* for this object. There is no obvious defect present in the two J band images which might cause such an error in the proper motion. The relatively large parallax of the source can be ruled out as the source of proper motion error in this catalogue since the LAS epoch baseline is 11 days from a year. I also find that the WSA proper motion, derived from detections in all five bands, is consistent with my own value. The source of this discrepancy remains unknown.

2MASS J08044064+2239502 & NLTT 42650

2MASS J08044064+2239502 & NLTT 42650 are DZ and DC type white dwarfs (respectively), originally identified by Kilic et al. (2010).

EGGR 531

EGGR 531 is a well studied DA8 type white dwarf first identified by Greenstein (1980).

LP 260-3, 2MASS J15593876+2550362 & LSPM J1641+3210

The M2, M6 and M7 type dwarfs LP 260-3, LSPM J1641+3210 and 2MASS J15593876+2550362 are previously studied (separate) systems. Spectral types, photometric distances (508pc, 55.9pc and 161.9pc) and radial velocities (105$km\ s^{-1}$, $-6.1km\ s^{-1}$ and $-54.7km\ s^{-1}$) were measured by West et al. (2008) using their respective SDSS DR5 spectra.

WD 0921+315

WD 0921+315 is a $4810 \pm 60K$ DC Helium rich white dwarf identified by Sayres et al. (2012). An SDSS spectrum provided spectroscopic confirmation.

υ Geminorum Ghost

A ghosted image of υ Geminorum (see Figure 3.12) is the only false high proper motion (-224 ± 10 & -1547 ± 9 $mas\ yr^{-1}$ in $\mu_\alpha \cos\delta$ and μ_δ respectively) source to have escaped rejection by the cuts described above. Suggesting that while they are effective at removing a lot of false high proper motion sources some will remain. If a clean high proper motion sample is required then blinking the first and second epoch J band images is recommended where practical. Images may be retrieved and blinked quickly using the WSA MultiGetImage tool and an image viewer which accepts command line input such as DS9.

ULAS J075015.48+203650.0

This object was missing from the above selection due to its second J band epoch classification as a galaxy, but was identified in other searches. Based on the Hawley et al. (2002) $i - J$ colour to spectral type table and the source's SDSS DR7 i band magnitude of 21.21±0.09 (note that the source is missing from SDSS data releases 8 and 9), it is a candidate M6/M7 dwarf at a distance of between 260 and 370 pc. It has a 504 ± 18 $mas\ yr^{-1}$ proper motion. This corresponds to a range of tangential velocities between 620 and 870 $km\ s^{-1}$, above the Galactic escape velocity.

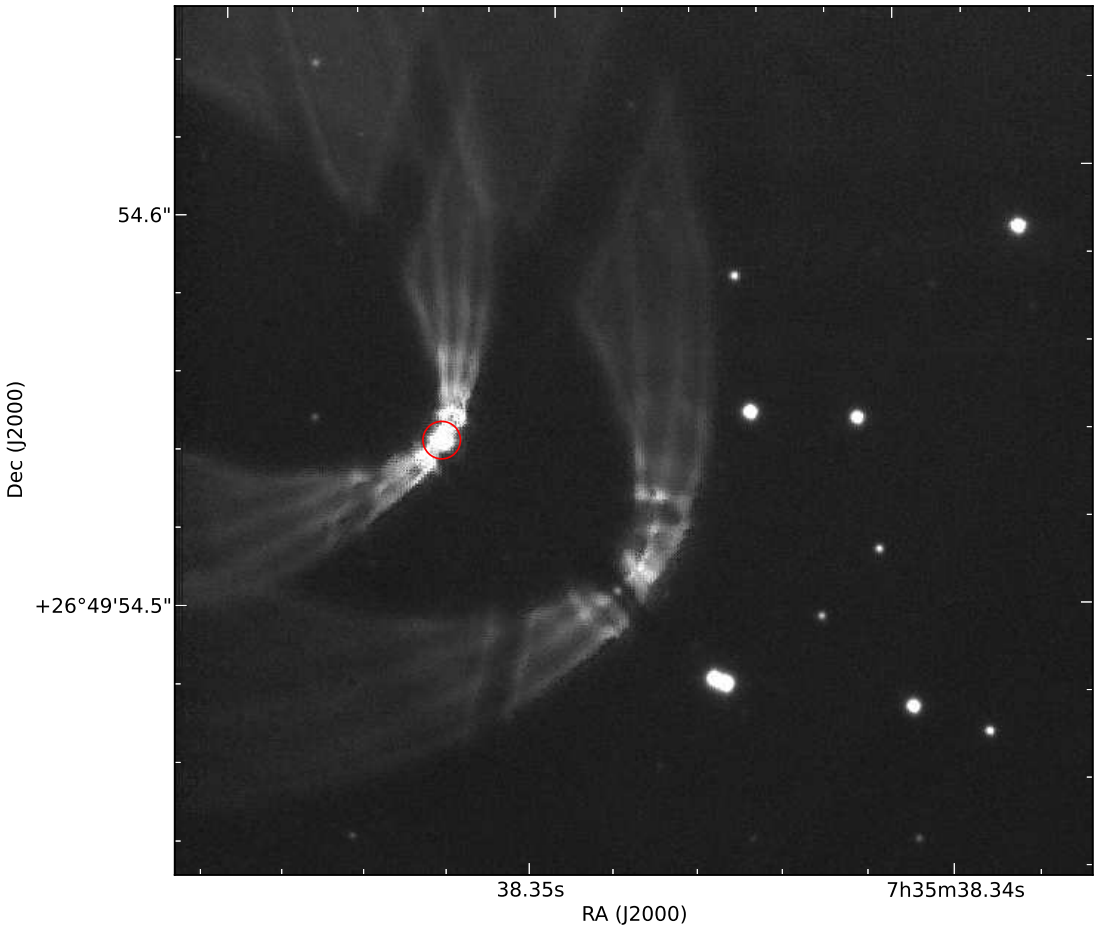

FIGURE 3.12: The first epoch J band image of the υ Geminorum ghost source, which has a different position at each epoch giving a false high proper motion. The source is indicated by the red circle.

3.5.2 T dwarfs

Burningham et al. (2013) present proper motions from this catalogue for 128 UKIDSS T dwarfs, including two new benchmark T dwarfs; LHS 6176B and HD 118865B.

I also investigated the characteristic population age of late T dwarfs (Smith et al., 2013) in response to current atmospheric models suggesting they are young and low mass (Leggett et al. 2009, 2010, 2012). For this I used tangential velocity data calculated using proper motions from this and other catalogues and spectrophotometric distances where parallax data were unavailable (Marocco et al. 2010, Andrei et al. 2011, Dupuy and Liu 2012, and Kirkpatrick et al. 2012). I concluded that the kinematic age of the population is older than that predicted by the models and, ultimately, more benchmarks are needed to anchor them.

Pinfield et al. (2012) presented a proper motion for the T8.5 dwarf WISEP J075003.84+272544.8 from a prototype version of this catalogue. I note that WISEP J075003.84+272544.8 was independently identified in this catalogue in a search for T dwarfs with high reduced proper motions shortly before its publication by the WISE team. I now provide the most up to date proper motion from this final revision of the catalogue of -736 ± 13 $mas\ yr^{-1}$ and -195 ± 15 $mas\ yr^{-1}$ in $\mu_\alpha \cos\delta$ and μ_δ respectively (the uncertainty is reduced and the proper motion difference is within the uncertainties).

Comparison of the new measured proper motion from this catalogue for the halo T dwarf candidate ULAS J1319+1209 with that reported in Murray et al. (2011) highlights a significant discrepancy. I measure a considerably lower proper motion, which suggests kinematics most consistent with membership of the Galactic disc, rather than the halo. The previous measurement by Murray et al. (2011) appears to be in error, with the likely source a dramatic underestimate of the uncertainty in the centroid in its second epoch imaging combined with a relatively short epoch baseline between the observations. This new measurement benefits from considerably higher precision thanks to deeper UKIDSS second epoch imaging, and a ∼5 year epoch baseline, compared to 0.8 years in the Murray et al. (2011) case.

3.5.3 Brown Dwarf Benchmark Searches

I undertook various searches for benchmark ultracool dwarfs, the parameters of which and known objects recovered are shown here. Given that parameters derived from atmospheric models of ultracool dwarfs are uncertain it is helpful to constrain them through associations with objects in a common system (Pinfield et al., 2006). See Section 3.6 for results.

3.5.3.1 L and Early T Dwarfs in the Full Survey

I searched the full 1500 deg^2 of data for new L and T candidates, in particular new benchmark objects, I selected sources with $Y - J > 0.8$ that were also classified as stellar in both J band images and fell into one or more of the following groups:

No H band detection, stellar merged class, and $\mu > 350$ $mas\ yr^{-1}$ (21 sources)

$J - H > 0.8$, and $\mu > 500\ mas\ yr^{-1}$ (6 sources)

$J - K > 1.4$, and $\mu > 500\ mas\ yr^{-1}$ (17 sources)

$J - H > 0.6$, $H - K > 0.5$ and $\mu > 500\ mas\ yr^{-1}$ (12 sources)

There were a further 21 sources with $Y - J > 0.8$ and $\mu > 500\ mas\ yr^{-1}$ that did not meet the other near infrared colour cuts, I elected to take a closer look at these as well since there were relatively few and sources with such large proper motions are often interesting in some way. These groups, taking into account sources in multiple groups, make 57 sources for further study.

I matched to the UKIDSS late T dwarf catalogue maintained by Ben Burningham and I found 9 matches with spectral types ranging from T5 to T9. I also matched to SIMBAD and find a further 7 L dwarfs (including one listed as an L dwarf candidate). This demonstrates the efficacy of these brown dwarf selection criteria.

I searched for benchmark candidates within this sample by retrieving a list of stars with proper motions greater than 350 $mas\ yr^{-1}$ from SIMBAD and cross matching with the list of 57 brown dwarf candidates within 5' and with proper motion difference tolerances of 50 $mas\ yr^{-1}$ independently in RA and Dec. Four potential benchmark objects have separations ranging from 64" to 111". G 62-33/2MASS J13204427+0409045 are a known K2/L3 binary (Faherty et al., 2010). Ross 458A/C (Goldman et al. 2010; Burningham et al. 2011a) and GJ 576/WISEP J150457.58+053800.1 (Scholz 2010; Murray et al. 2011) are also recovered. The fourth candidate is found to be crosstalk from the bright potential primary upon further inspection of the images.

3.5.3.2 Extended Red Search

In Section 3.4.5 A. Wilkinson and I found 834 red (Y-J > 0.7) sources with genuine large motions between the observation epochs (> 500 *mas*). This translates to genuine proper motions down to around 75 $mas\ yr^{-1}$. Note that this selection also incorporates most of the objects selected in Section 3.5.3.1. Within this sample I identified 33 sources with a possible common proper motion companion within the 1'×1' image.

In an attempt to recover common proper motion companions to these interesting sources I looked within the LAS proper motion catalogue for nearby objects (1' radius) with

proper motion differences within 1σ significance. In practice I found 1σ to be sufficient since matches above that were typically of order 5σ or greater. I recovered 13 matches meeting these criteria which produced 12 common proper motion pairs since two of the matches were both components of the same pair. I find 4 of these are known common proper motion pairs according to SIMBAD. The 12 pairs are shown in Section 3.6, Table A.2.

To expand the candidate brown dwarf binary list to include pairs with a primary too bright to be included in the LAS proper motion catalogue I used a list of SIMBAD objects with proper motions greater than 100 $mas\ yr^{-1}$. I looked for companions to the 834 red sources with genuine large motions within 10' and with $\mu_\alpha \cos\delta$ and μ_δ differences less than 30 $mas\ yr^{-1}$ independently of one another. I found 175 matches to these criteria, though I expected many to have been matched to themselves. In order to remove the self matches from the candidate list I rejected those with separation < 5" or J mag difference < 0.5, which should leave only genuine pairs, variable sources, or those with very high proper motion. Thirty one candidate pairs survived this cut. Of these I found 5 pairs had been identified in the internal search and 2 high proper motion single stars had survived the previous cut, leaving 24 systems (see Section 3.6, Table A.3).

3.6 New Candidate Benchmarks

Amongst the 36 sources in Tables A.2 and A.3 there are 29 ultracool benchmark binary candidates, of which 15 are new and survive a test for common distance. Below I discuss those for which the primary has a distance in the literature and rule out 3 candidates. All of the remainder have spectrophotometric distances consistent with binarity (see Tables 3.1 and 3.2). Note that unless stated otherwise Y, J, H, and K magnitudes in this section are on the MKO system and J band photometry is UKIDSS first epoch.

G 151-59

G 151-59 has a Hipparcos parallax of 12.63±2.21 *mas*, placing it at a distance of between 67 and 96 *pc*. Being relatively bright (2MASS J = 8.98±0.03) it is a well studied K0 type dwarf with known radial velocity (16.98±0.20$km\ s^{-1}$; Latham et al. 2002) and approximately solar metallicity. If I assume this to be a genuine common proper motion

TABLE 3.1: Upper and lower distance estimates for the components of the new binary candidates in Table A.2. Distances are calculated using LAS first epoch J band magnitude and absolute J magnitudes from Dupuy and Liu (2012) (≥M6) and Hawley et al. (2002) (<M6) and the spectral types in Table A.2 ±1 subtype where they are $i-J$ based estimates. Note that I find the SDSS and UKIDSS photometry of the secondary component of 1208+0845 fits that of a ∼5000 K H-rich white dwarf, I have used this to produce the distance estimate in this case.

α	δ	d_{min}	d_{max}	d_{min}	d_{max}
a	a	a *pc*	a *pc*	b *pc*	b *pc*
11:58:25.59	-01:22:58.9	50	139	130	130
14:04:40.20	-00:40:19.8	53	146	53	91
15:49:51.57	+08:57:29.6	56	155	99	134
14:20:16.86	+12:07:38.9	55	110	89	111
12:08:16.83	+08:45:27.6	34	34	41	41
13:25:13.86	+12:30:13.3	78	226	96	121
13:28:35.49	+08:08:19.5	84	146	105	105
14:59:41.64	+08:35:07.7	109	314	203	354

TABLE 3.2: Upper and lower distance estimates for the components of the unknown binary candidates in Table A.3. Distances to the primaries are calculated using fits of available photometry (B/V, J, H, K) to modelled spectral energy distributions of main sequence stars by S. Catalán. Missing values in the χ^2 column indicate that she was unable to fit an T_{eff} to the photometry or the photometry was unavailable. The results of solutions with a χ^2 value greater than 10 are not included as I deem them too unreliable. Upper and lower limits of ±50% are used to take into account photometric scatter and other sources of uncertainty. Note that the distance estimates calculated in this way are consistent with parallax based distances where available. Distance estimates to the secondary components are calculated using the same method as those in Table 3.1. The only binary candidate I am now able to rule out with confidence is BD+13 2724.

Name	d_{min}	d_{max}	χ^2	d_{min}	d_{max}
a	a *pc*	a *pc*	a	b *pc*	b *pc*
NLTT 21820	272	817	9.95	289	416
2MASS J14493646+0533379			193.82	137	179
2MASS J12020964+0742538				61	61
2MASS J12020933+0742477				61	61
TYC 2032-546-1	119	357	0.28	13	508
SDSS J120331.33-005332.8				74	92
2MASS J10084007+0150537			23.9	11	323
2MASS J13284331+0758378				106	106
G 151-59	45	136	0.31	118	185
G 66-40	32	96	9.25	56	63
2MASS J13284331+0758378				84	121
LP 488-31	61	182	1.49	83	144
2MASS J13272850+0916323	38	115	3.55	49	86
HD 115151	42	127	0.76	81	109
BD+13 2724	40	120	0.0	248	337
2MASS J14511622+0922464			22.18	55	79
10 Vir				52	91
2MASS J14552241+0419361	63	189	4.27	124	178

pair then the secondary (ULAS J152557.45-020456.4, J = 17.85±0.05) must be of type L4 to L6 to place it within the same distance range using the Dupuy and Liu (2012) spectral type to absolute J mag relations. Despite the estimated type of L1 given in Table A.3 this is not ruled out as a genuine pair given the inherent uncertainty in $i - J$ based spectral types of early to mid L dwarfs. To assess whether G 151-59 and the candidate companion might be a chance projection of two objects at different distances, I loosely followed the method used by Gomes et al. (2013). I calculated distances for early L dwarfs (L0-L4) using the LAS J magnitude of each candidate and the spectral type to absolute J mag (MKO) relations of Dupuy and Liu (2012). I then calculated the expected numbers of such L dwarfs in the volume between ±23% of each distance and a 46" angular radius using the early L dwarf density of 0.0019 pc^{-3} provided by Cruz et al. (2003) and the breakdown amongst subtypes provided by fig.12 of that work. The ±23% distance range is based on the typical spread of 0.3 mag in the absolute J magnitudes (approximately 15% of the distance) of early L dwarfs added in quadrature to the 17.5% uncertainty in the distance to G 151-59. I expect to find $4{\times}10^{-4}$ early L dwarfs. It is therefore clearly improbable that the candidate is present simply due to a chance alignment. When the significance of the proper motion similarity with G 151-59 is also taken into account the chance is lower still. Assuming the candidate is a genuine companion, I calculate a tangential velocity between 75 and 108 $km\ s^{-1}$ when the range of possible Hipparcos distances is taken into account. Note that a distance compatible with an L0 dwarf would imply a tangential velocity of order 200 km s^{-1}, which is larger than that of the normal disc population. At the distance range of the potential primary, the pair would have a physical separation of between 3,100 and 4,400 AU.

10 Vir

10 Vir (BD+02 2517A) has a Hipparcos parallax of 13.69±0.31 mas corresponding to a distance of between 71 and 75 pc and an USNO-B I magnitude of 4.7. Assuming this is a genuine common proper motion pair then the secondary must be of type M5 to M8, using the spectral type to MKO absolute J magnitude relation of Dupuy and Liu (2012), taking into account the uncertainties on the spectral types of those within this range of figure 25 in that work, and its UKIDSS J mag of 14.65±0.01. This spectral type range is consistent with the estimate given in Table A.3, I therefore conclude this to be a likely common proper motion companion. 10 Vir has one known close companion,

BD+02 2517B (Mason et al., 2001) though I was unable to recover this object in the LAS proper motion catalogue. Mason et al. (2001) gives a V mag of 13.4 for BD+02 2517B which should be easily visible in the UKIDSS J band image, though I find no source at the given position. This may be explained by the 1909 observation epoch and large proper motion. On inspection of the two epochs of UKIDSS J band images it is apparent that there is a close (4.5" separate) common proper motion companion to 10 Vir. This source is not detected in UKIDSS Y, J and H bands due to the close proximity of 10 Vir, the K band detection (magnitude 12.425±0.002) may be contaminated by a diffraction spike. If I am to assume that this is BD+02 2517B then I provide an updated position of 12:09:41.73 +01:53:45.28 at the UKIDSS K band epoch of 2008-05-28. I therefore conclude that the late M dwarf common proper motion companion identified here is a likely third, widely separated (10,000 *AU*) component of this system.

HD 115151

HD 115151 has a Hipparcos parallax of 10.73±1.16 *mas* corresponding to a distance of between 84 and 104 *pc* and a 2MASS J mag of 7.87±0.03. Assuming this is a genuine common proper motion pair then the secondary must be of type M6 to L1, using the spectral type to MKO absolute J magnitude relation of Dupuy and Liu (2012), taking into account the uncertainties on the spectral types of those within this range of figure 25 in that work and its UKIDSS J mag of 15.85±0.01. This spectral type range is consistent with the estimate given in Table A.3, I therefore conclude this to be a likely binary.

LP 488-31 & 2MASS J13272850+0916323

These binaries are identified in Table 3 of Deacon et al. (2009b) but not commented further upon.

BD+13 2724

The BD+13 2724 binary companion does not have a distance estimate compatible with that of the primary (see Table 3.2), I therefore rule out these two sources as being part of a common system.

SDSS J120331.33-005332.8

SDSS J120331.33-005332.8 is a G type subdwarf with a heliocentric distance of 378±35 *pc* (Dierickx et al., 2010). This pair have a weak proper motion match and the candidate secondary, a late M dwarf, would be within 100 *pc* so I rule these out as a binary pair.

2MASS J13284331+0758378

2MASS J13284331+0758378 is at first glance a widely separated (10') proper motion match to the M8.5/M6 candidate binary pair in Table A.2. When the Zhang et al. (2010) distance estimate of 118 *pc* for the M8.5 dwarf in that system is adopted, the physical separation of that system and 2MASS J13284331+0758378 works out at 70,000 *AU*. 2MASS J13284331+0758378 is likely to be an M7/8 dwarf based on its $i-J$ colour and its distance is therefore incompatible with the M6/M8.6 internal binary pair and I can safely rule it out as a third component.

3.7 Summary

I present a UKIDSS LAS derived proper motion catalogue for approximately 1500 deg^2 of northern sky. Proper motions range from 0 to a hard proper motion detection limit of 3.3" yr^{-1} with a typical 1σ uncertainties of about 10 $mas\ yr^{-1}$ for bright sources (see Figure 3.3).

I find proper motions to be largely reliable for sources brighter than about magnitude 19 in the J band, with low ellipticity and stellar morphological classification. While the reliability diminishes it is still possible to find genuine high proper motions at objects fainter than $J = 19$. Correlation of proper motions with existing optical catalogues is good, although I note a small percentage (0.5%) of motions are measured using deprecated frames and their accuracy suffers as a result.

The catalogue has already enabled the identification of a variety of high proper motion sources in particular LSR J0745+2627, WISEP J075003.84+272544.8 and two T dwarf benchmarks: LHS 6176B and HD 118865B. In addition, I identify 16 new candidate benchmark ultracool dwarfs which significantly increases the sample of benchmarks.

Chapter 4

The UKIDSS GPS Proper Motion Catalogue

4.1 Introduction

Source confusion in the Galactic plane reduces the completeness of searches for nearby stars and brown dwarfs and high proper motion sources in general. The two epochs of high resolution UKIDSS GPS data (Lawrence et al. 2007, Lucas et al. 2008) provide a new resource to search for previously missed high proper motion objects, especially brown dwarfs which would typically have been undetected in previous optical searches. It also allows for identification of new high amplitude infrared variable stars (Contreras Peña et al., 2014).
The UKIDSS GPS covers 1868 deg^2 in J, H, and K passbands to an approximate 5σ depth of 18.1 in K. It included a second epoch of K band observations two or more years after the initial epoch.

The initial search described here is limited to objects with K < 17 mag, $l > 60^\circ$ and includes only data taken up to March 31st 2013.

4.2 Data

I obtained UKIDSS GPS K band FITS file catalogues from observations taken between May 2005 (the start of UKIDSS) and March 31st 2013. The observations from this

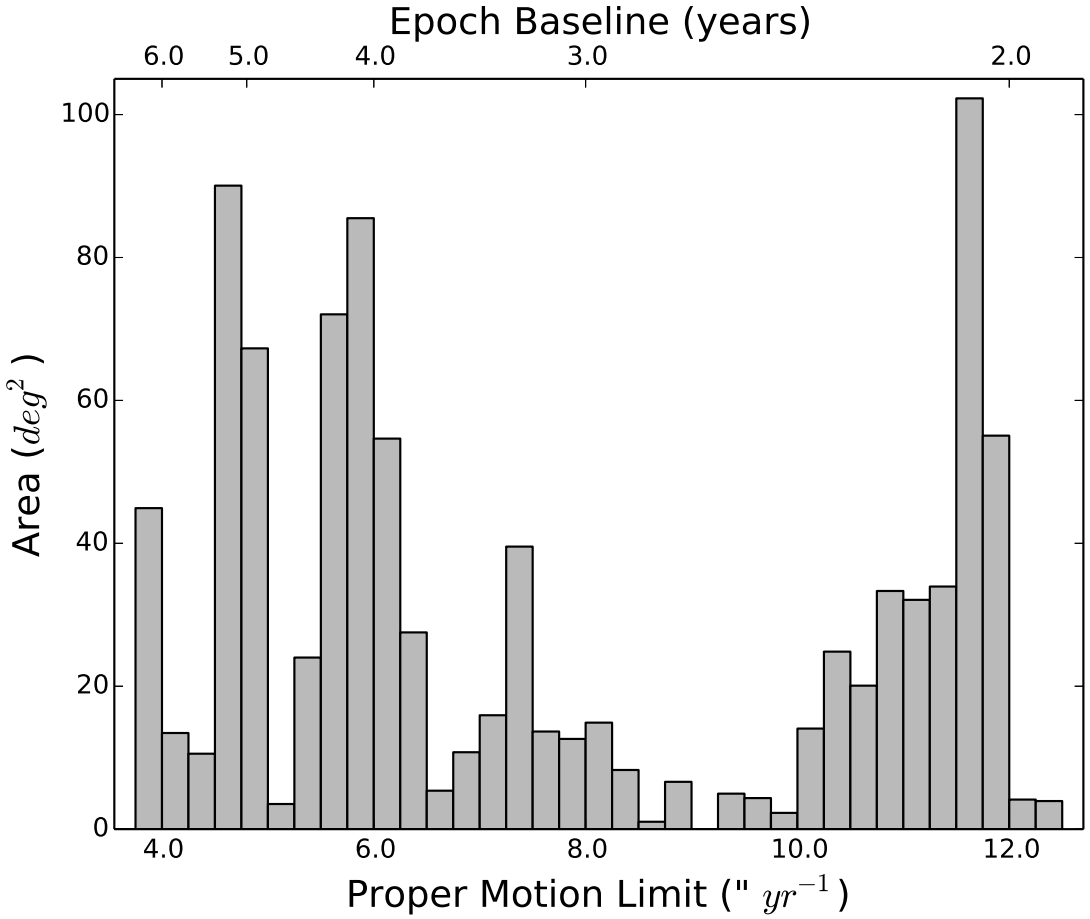

FIGURE 4.1: The area distribution of epoch baselines and maximum proper motion limits of the catalogue.

date range give epoch baselines of between 1.9 and 6.4 years (see Figure 4.1). More recent data, from March 31st 2013 to the end of 2013, take the final maximum epoch baseline to approximately 8 years. Since I used a fixed matching radius and a range of epoch baselines I also have upper proper motion detection limits of between 3.75 and 12.6 " yr^{-1}, see Figure 4.1.

Following early testing I limited the initial published search to observations with $l > 60°$, in order to keep the number of high proper motion candidates to a manageable level. The resultant pipeline input catalogue contained ∼167 million sources and covered approximately 900 deg^2, see Figure 4.2.

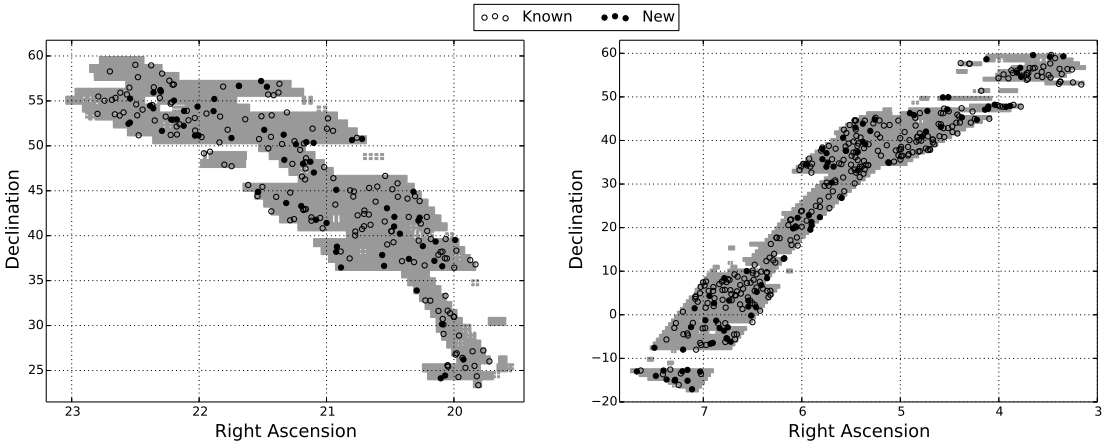

FIGURE 4.2: The coverage of the two epochs of K band data is shown here in grey. Overplotted are the visually verified high proper motion sources. Empty circles are previously identified by other authors, filled circles are new discoveries.

4.3 Results

4.3.1 Reliability

Due to the high incidence of false high proper motion detections I found visual verification to be essential. To reduce the number of candidates to a manageable quantity for visual verification I adopted the following quality criteria based on tests on a subset of the data spread throughout the plane.

l >60°;

$\mu > 200\ mas\ yr^{-1}$;

Classified as stellar at both epochs;

Ellipticity at both epochs <0.3;

K < 17 at either epoch; and

Fewer than 10 other candidates in the same 13.65' × 13.65' frame.

In a preliminary test of this selection I found no genuine high proper motion sources in any frame containing greater than 10 candidates meeting those first five criteria. This is probably due to inclusion of a small number of poor quality frames due to the use of FITS file data which has not been quality controlled. These poor quality frames

generate large numbers of spurious detections, so their identification and removal was desirable. The above selection produced 5,655 good candidates for genuine high proper motion sources.

To identify genuine high proper motion sources R. Bunce [University of Hertfordshire, summer student] and I blinked the candidates in sequence by calling DS9 from the command line specifying various display parameters. Frames were displayed in blink mode. Regions were overlaid showing the position of each source at the first epoch, the calculated position of the source at the second epoch (Fig. 4.3), and the radius of first order cross-talk. During array readout electronic cross-talk can cause fainter duplicate images of saturated or near-saturated sources at a distance of $256n$ pixels (in the case of 2×2 microstepped images with the GPS) from the bright source in either x or y depending on the readout direction. Dye et al. (2006) discuss cross-talk and other data artefacts present in WFCAM data. The overlaid regions made identification of mismatches and cross-talk, which were the dominant source of false detections, straightforward. To add to the visual cross-talk identification I also used software designed to identify possible cross-talk in WFCAM data using the positions of bright nearby 2MASS sources. This identified a small number of additional cross-talk sources that had initially been missed. R. Bunce and I identified 617 genuine high proper motion sources from within this sample which gives an overall ratio of false to genuine candidates of 9:1. Figure 4.4 shows the distribution of false and genuine high proper motion detections in Galactic coordinates. The fraction of false positives increases rapidly with decreasing Galactic longitude, the ratio of false to genuine candidates is $\sim$ 1:1 at $l = 180°$. The density of genuine high proper motion sources appears fairly uniform.

Figure 4.5 shows that the fraction of false positive proper motions is much greater at the high proper motion end. This is unsurprising since the large radius of apparent motion between the images allows for a higher incidence of mismatches. For the same reason sources with an apparent low proper motion are expected to be more reliable than those with high proper motion. At low proper motion the major source of false detections shifts to crosstalk. This can be identified and removed fairly reliably by searching for bright 2MASS sources at a ∼51" radius from the target. I found that removal of crosstalk sources in this way increased the genuine fraction amongst relatively low PM candidates (200-300 $mas\ yr^{-1}$) to ∼85%.

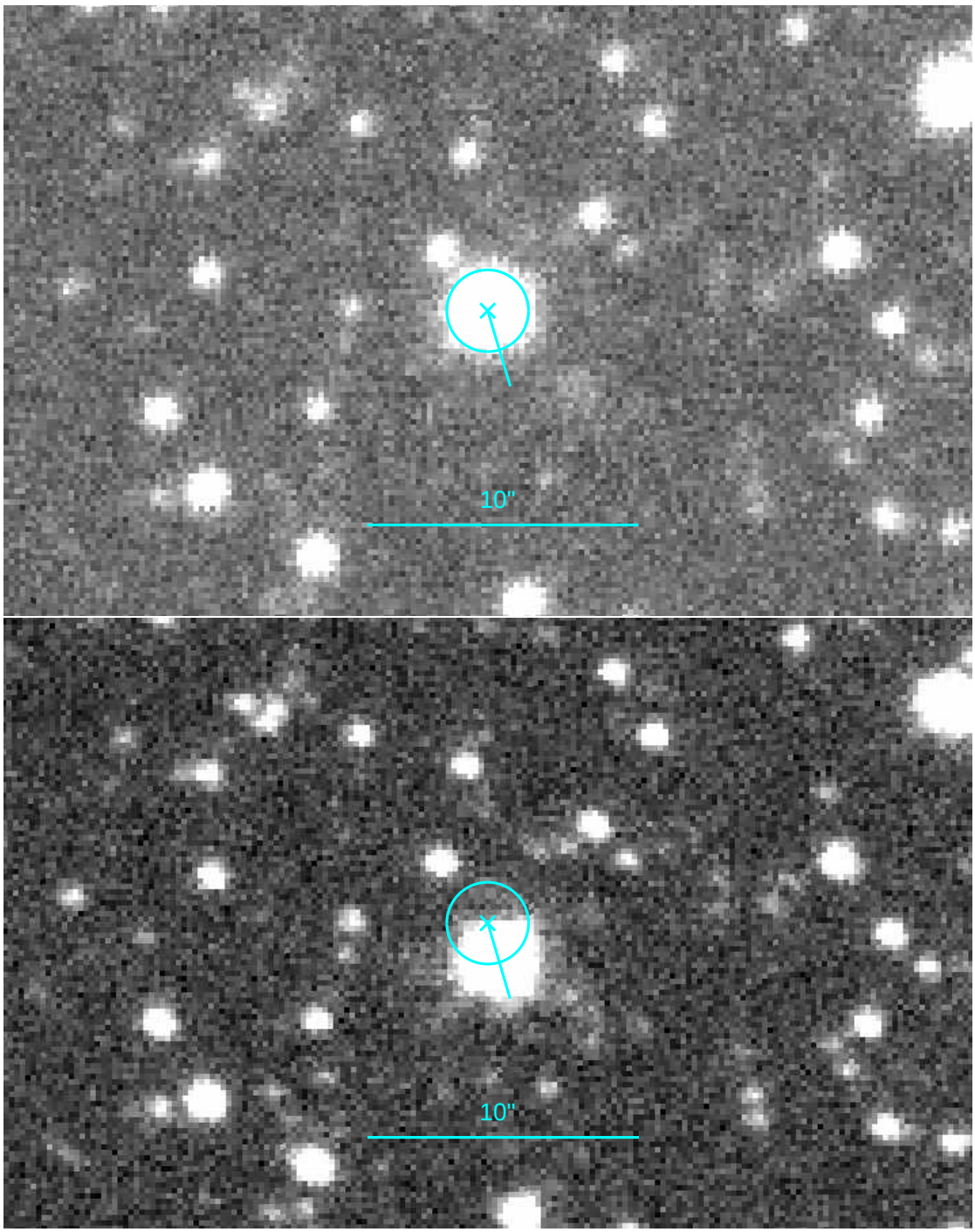

FIGURE 4.3: First epoch K (top) and second epoch K blinking images generated by DS9 for the known high proper motion object 2MASS J19483064+2321473. The GPS proper motion for this source is 295 $mas\ yr^{-1}$. The images are separated by 5.15 years. The regions are placed at the same position on both images relative to their WCS. The × shows the first epoch K band position of the source, the circle shows the radius of motion between the image epochs, the line shows the direction of travel and its length corresponds to 10 years of motion. The intersection of the circle and line therefore shows the expected position of the source at the second epoch. There is another circle with a radius of 256 pixels centred on the first epoch position of the target, which falls beyond the boundaries of these images, corresponding to the distance of a saturated or near-saturated star that could cause first order cross-talk at the target position. The bar below the source in each image shows 10" and they are oriented north-up east-left.

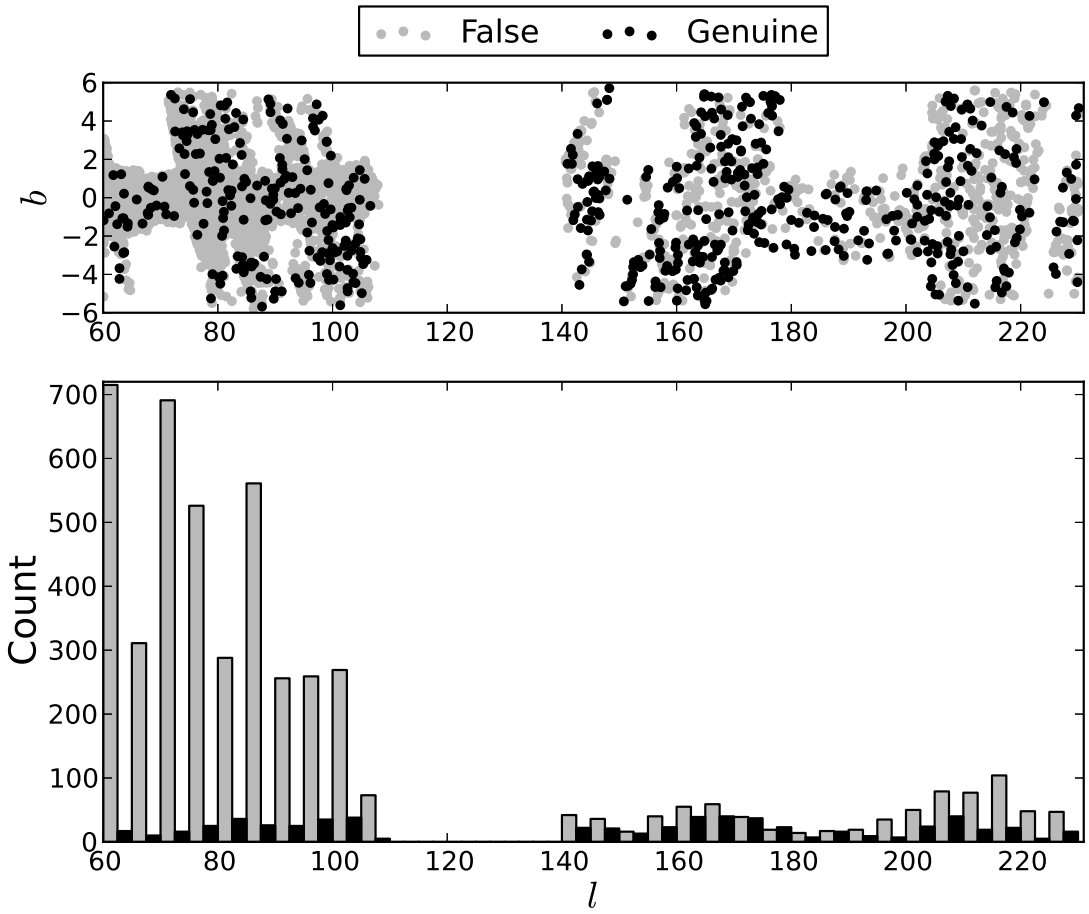

FIGURE 4.4: The distribution in Galactic coordinates of high proper motion candidates identified as false (grey) and genuine (black). The upper panel shows the coverage in Galactic coordinates and that the general distribution of genuine high proper motion objects is fairly uniform across the field, in contrast to the increase in false high proper motion objects with decreasing Galactic longitude. The lower panel shows the distribution in Galactic longitude alone. Increased coverage width in Galactic latitude corresponds to and accounts for the peaks in the distribution, which is otherwise fairly flat. The large number of false high proper motion candidates at low Galactic longitudes is driven by the large increase in source density relative to high Galactic longitudes which increases the frequency of mismatches.

4.3.2 Accuracy

To evaluate the accuracy of the proper motions I compared them to the long epoch baseline optical catalogues of Lépine and Shara (2005, LSPM; covering the north) and Boyd et al. (2011a, 2011b; covering the south). I identified 406 sources common to the LSPM catalogue and 15 common to the Boyd et al. catalogues. Figure 4.6 shows a comparison of the total proper motions of the 421 sources between the catalogues, for which Pearson's r correlation coefficient is 0.996. Of the sources in common with the LSPM, 69% of the proper motions agree within their 1σ uncertainties, I omitted the

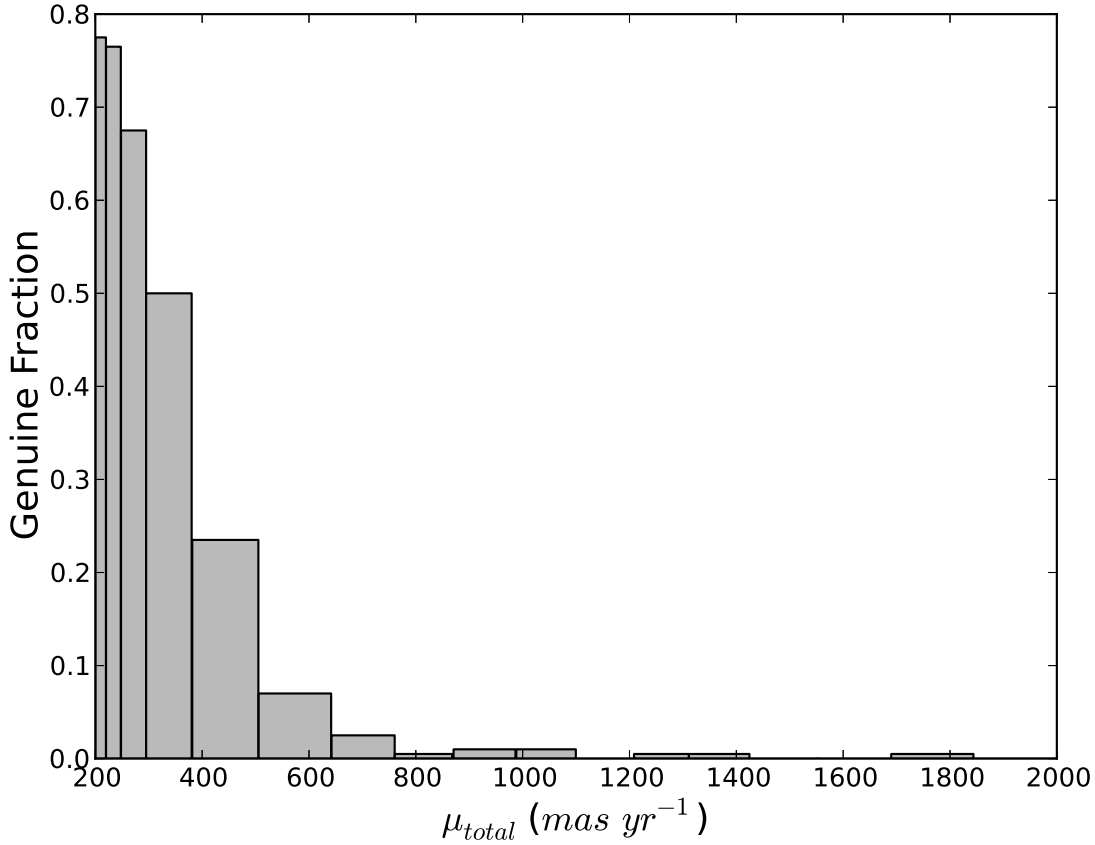

FIGURE 4.5: Histogram showing the decrease in the fraction of genuine high proper motion detections as total proper motion increases. The sample of sources described in Section 4.3.1 were sorted by total proper motion and binned into groups of 200 sources. Note that the x axis continues to 16 $arcsec\ yr^{-1}$, though the genuine fraction remains at zero past what is shown here. The fraction of genuine high proper motion sources increases rapidly with decreasing proper motion.

Boyd et al. proper motions from this calculation since the authors do not provide an estimate of their uncertainty.

To evaluate the accuracy at the lower end of the proper motion scale I selected sources with $\mu < 200\ mas\ yr^{-1}$, $l > 60°$, K magnitude at either epoch < 17, K magnitude uncertainty at both epochs < 0.1, ellipticity at both epochs < 0.3, and classified as stellar at both epochs. The distribution of total proper motions of this sample is shown in Figure 4.7. For comparison I also include a sample of low proper motion sources from the LAS (Chapter 3), with J magnitude at either epoch < 18.5. The GPS proper motion distribution is highly peaked towards $\mu < 10\ mas\ yr^{-1}$ which is expected since I am largely sampling distant main sequence stars and giants with very small proper motion. This tends to suggest that the reliability of the catalogue remains high at

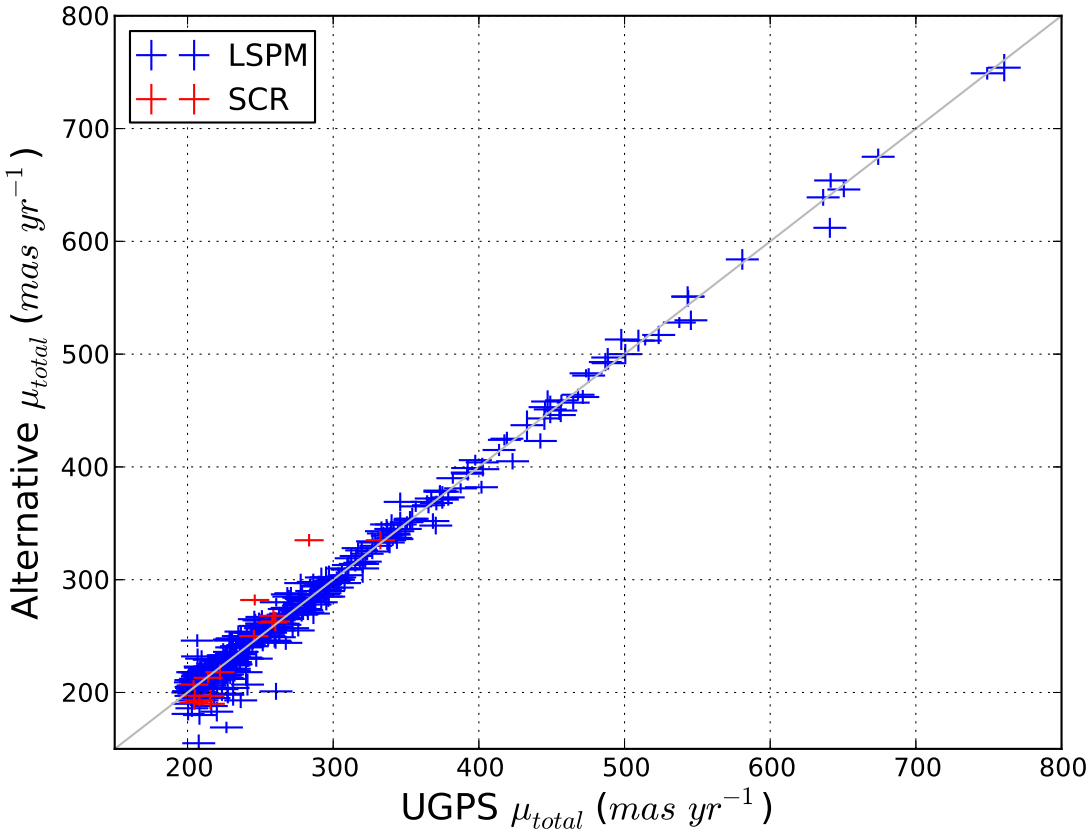

FIGURE 4.6: The GPS based total proper motions compared to those of alternative sources. The alternative sources are given by the legend. The length of the arms of the crosses indicate the uncertainty in the proper motion measurement. LSPM proper motion uncertainties are taken as 8 $mas\ yr^{-1}$ in RA and Dec. I estimate the Boyd et al. total proper motion uncertainties at 10 $mas\ yr^{-1}$. The group of sources with UGPS $\mu \sim 200 - 250\ mas\ yr^{-1}$ and alternative $\mu < 200\ mas\ yr^{-1}$ is a selection effect, the GPS proper motion sources are selected with $\mu > 200\ mas\ yr{-}1$ but there is no cut on the alternative proper motion.

$\mu < 200\ mas\ yr^{-1}$, continuing the trend indicated in Figure 4.5. By contrast, in the LAS (i.e. outside the Galactic plane) I am sampling relatively nearby stars which might be expected to have (marginally) measurable proper motions, which could explain why the distribution in Figure 4.7 is less strongly peaked towards zero. P.W. Lucas tested this by generating a catalogue sample for the same region and magnitude range as the LAS dataset using the Besançon models. He found that the typical proper motions of the model sample were in the range of 0 to 20 $mas\ yr^{-1}$ and consistent with the data in Figure 4.7 after making allowance for the uncertainties in the LAS proper motions.

Figure 4.8 shows a J-H versus H-K colour-colour diagram of a selection of 23,271 sources with $50 < \mu < 100\ mas\ yr^{-1}$; $\sigma_\mu < 10\ mas\ yr^{-1}$; $l > 60°$; J, H and K uncertainties ≤ 0.01; stellar morphological classifications and ellipticities < 0.3 in all three bandpasses;

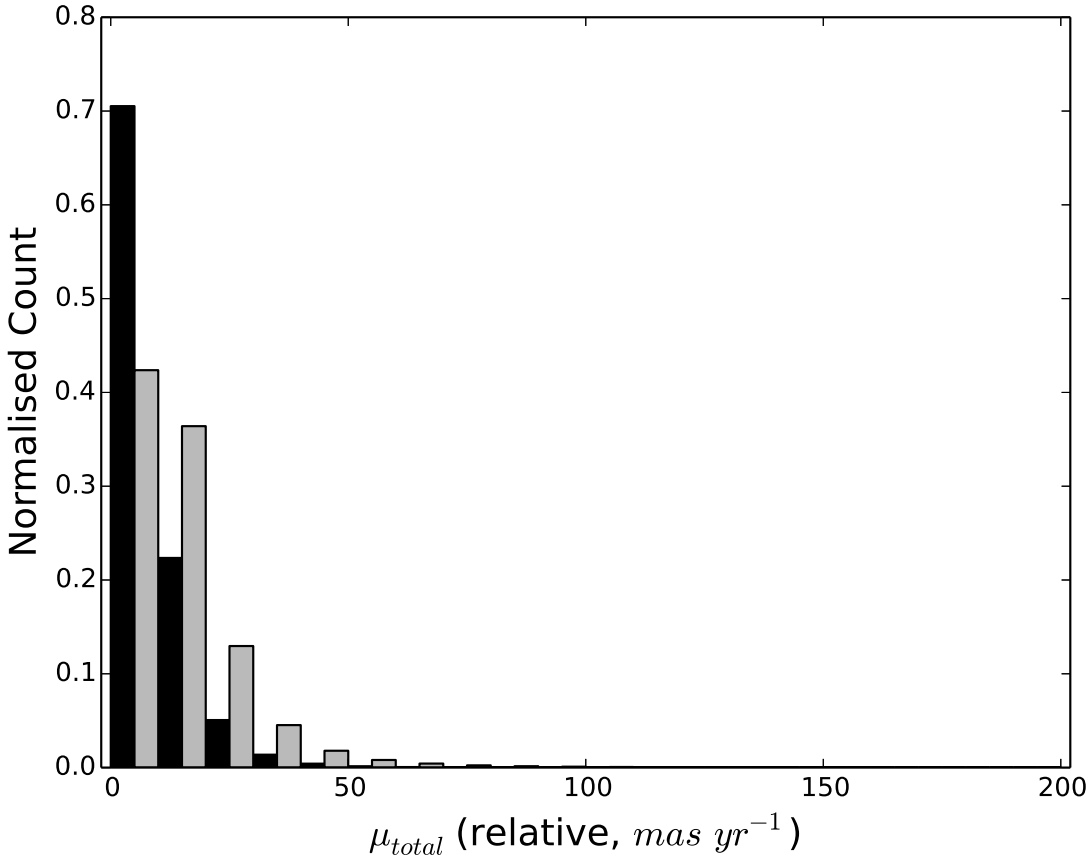

FIGURE 4.7: The distribution of a sample of low proper motion sources in the GPS (black) and the LAS (grey).

and $J > 13.25$, $H > 12.75$ and $K > 12.25$ (i.e. not saturated). Also included are the 617 visually confirmed high proper motion ($\mu > 200\ mas\ yr^{-1}$) sources.

Note that I still produced proper motions for mildly saturated objects as the morphological classification flag for saturation in the FITS catalogues is not always reliable. As a result I would encourage that proper motions for sources brighter than K∼12 be used with caution.

4.4 Discoveries

In order to characterise the new high proper motion objects I obtained r and i band photometry from the INT/WFC Photometric Hα Survey (IPHAS, Drew et al. 2005), specifically a preliminary version of the DR2 catalogue (Barentsen et al., 2014), and the J and H band photometry from either the UKIDSS DR8 GPS catalogue or their FITS

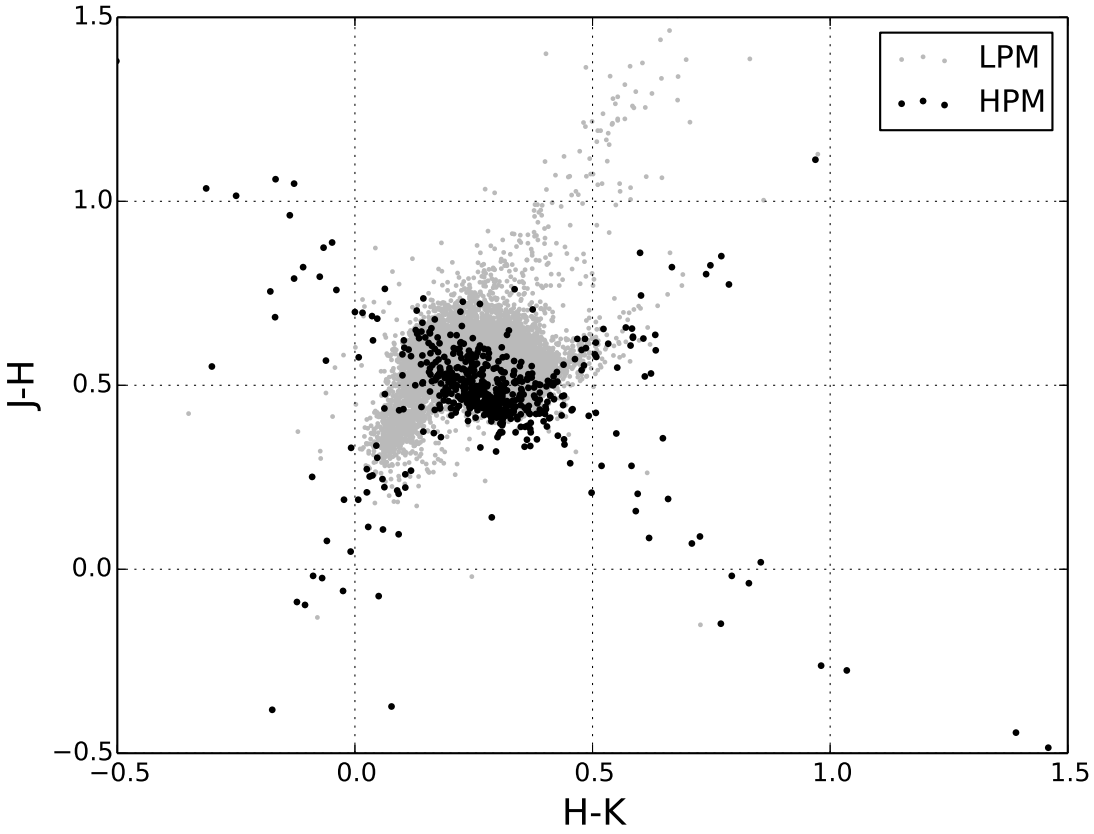

FIGURE 4.8: A J-H versus H-K colour-colour diagram for 23,271 low proper motion sources carefully selected for reliability (see text, *LPM*, grey points). Also included are the 617 visually confirmed high proper motion sources (*HPM*, black points). Note that the line of HPM sources running diagonally from the top left to the bottom right is caused by unreliable near-saturated photometry in one or more bands.

file catalogues which were retrieved from the WSA using their archive listing service. Additionally, an IPHAS detection at a third epoch allows me to safely rule out the possibility that two transient objects (e.g. solar system objects) produced an apparent proper motion of a single object.

The r and i band merged catalogues are available in the IPHAS DR2 catalogue. A small number of the high proper motion sources were in IPHAS fields observed in poor weather and for this reason are not present in the DR2 catalogue. However, the photometric uncertainties take the poor observing conditions into account and I included them where necessary. The coordinate of each IPHAS source is taken from the r band. Where an r band detection is missing the i band is used. I took the proper motion of each source into account by identifying the nearest IPHAS source to the expected position of the GPS source at the IPHAS epoch. I visually inspected all IPHAS images to ensure that the

catalogue photometry was not compromised by blending or astrometric errors. I found 17 matches located > 1" from their expected position, only one of which was a genuine IPHAS match, UGPS J211859.26+433801.3 (see Sections 4.4.2 and 4.4.3.1). The other 16 were mismatches usually due to a non-detection of the target in the i band.

I matched to the UKIDSS DR8 GPS catalogue using a radius which took into account the possibility that the position epoch (the first K band epoch), is not always the same as the epoch from which the WSA take positions. I found that 444 of the high proper motion sources were matched to only one UKIDSS DR8 source, with a further 43 instances where there were multiple matches to the same high proper motion source. I believe this to be due to missed matches in the creation of the band-merged catalogues by the WSA since these high proper motion sources almost all have motions between the epochs greater than the 1" matching radius used by the WSA for GPS data. Additionally, the groups are mostly pairs in which the first match is a K1 detection only and the other is a K2 detection only (K1 being defined in the WSA as the K epoch contemporaneous with the J and H data).

I then matched to the J and H band FITS file catalogues taking into account the proper motion of the source to calculate the expected position of the target in these images.

Where the catalogue photometry might possibly be unsatisfactory (e.g. an IPHAS non-detection, or a high contrast binary with a small separation where significant PSF overlap was likely to have occured) and the target was deemed interesting (e.g. a UCD candidate), it was necessary to perform additional photometry. I used the IRAF DAOPHOT package in these cases and the targets in question are identified in their tables and/or text.

4.4.1 New High Proper Motion Sources

To identify those high proper motion sources already in the literature I cross checked against both SIMBAD and VizieR. Between them these services contain several catalogues of verified high proper motion sources (e.g. the LSPM catalogue, Lépine and Shara 2005; the search by Boyd et al., 2011a, 2011b) which are likely to have previously identified many of the same sources from the 617 that R. Bunce and I found.

I used the SIMBAD script service to compile a list of all stars in their database with $\mu > 100\ mas\ yr^{-1}$. To this I matched the epoch 2000 positions of the GPS high proper motion detections using a 15" matching radius, keeping only the closest match. I considered these matches genuine and the source known if the J, H, and K photometry taken from the 2MASS Point Source Catalogue (Skrutskie et al., 2006) did not differ by more than one magnitude. I note that most matches with differing photometry also had large proper motion differences. I identified 426 of the GPS proper motion sources in the SIMBAD database, leaving 191 unknown at this stage. I identified all catalogues in the VizieR database which contain any source within 15" of the position of each of the remaining high proper motion candidates. I dismissed identifications from the catalogues which were repeatedly identified but do not contain visually verified high proper motion source discoveries. These include proper motion catalogues such as the USNO-B1.0 Catalog, (Monet et al., 2003); the PPMXL Catalog (Roeser et al., 2010) and photometric catalogues such as the WISE All-Sky Data Release (Wright et al., 2010); the UKIDSS-DR6 Galactic Plane Survey (Lucas et al., 2008). Of the 191 sources checked, 29 were identified in other surveys (the majority identified by Boyd et al., 2011a, 2011b, which are not present in the SIMBAD database) and 162 had no corresponding sources in any VizieR catalogues other than non-verified proper motion catalogues and single epoch photometric catalogues. Subsequently I identified eight more sources in common with the search by Luhman (2014a) and another with Luhman and Sheppard (2014). The remaining 153 high proper motion sources I consider to be new discoveries and can be found in Table A.6. Figure 4.9 shows the proper motion and magnitude distribution of the new and known high proper motion sources. Figure 4.10 shows a reduced proper motion diagram of the sources with the white dwarf, subdwarf and main sequence loci highlighted according to Salim and Gould (2002). I note that the known high proper motion sources include twelve very recent WISE-based proper motion discoveries from Kirkpatrick et al. (2014), and Luhman (2014a) and Luhman and Sheppard (2014) which had relatively poor astrometric precision. In Table A.7 I provide GPS proper motions for these objects, which benefit from higher resolution data and longer time baselines.

4.4.2 New L Dwarf Candidates

Brown dwarfs have insufficient mass to support nuclear hydrogen burning. Since they lack a significant internal heating mechanism they cool over time through the brown

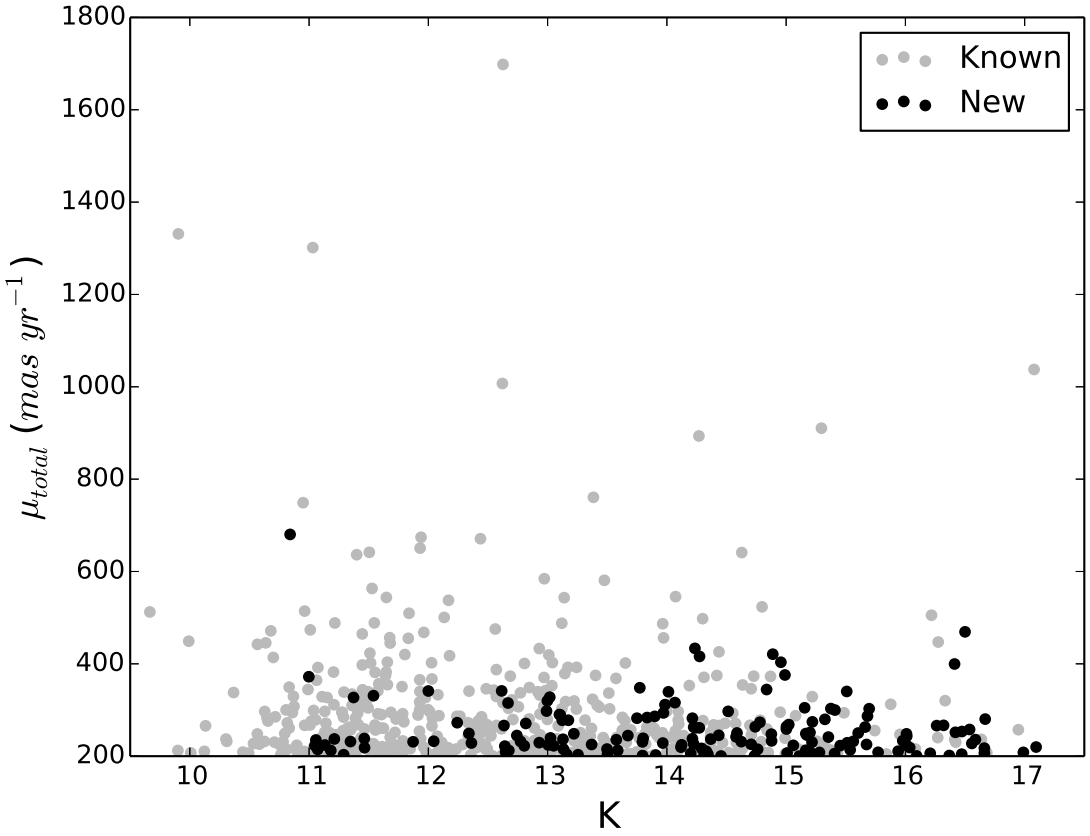

FIGURE 4.9: The distribution of known (grey) and newly discovered (black) high proper motion sources identified by this work.

dwarf sequence. The brown dwarf sequence begins with very young examples of late M type dwarfs and progresses on through L and T type dwarfs into Y dwarfs. An L type dwarf can also be either a low mass star or a brown dwarf depending on its mass and age (see e.g. Burrows et al. 2001). L dwarfs occupy the 2250 K to 1400 K temperature range (Kirkpatrick et al., 1999), which allows dust to form in their photospheres producing many spectral features not present in warmer objects. Almost a thousand L dwarfs have been identified to date but more discoveries of unusual L dwarfs are still needed to aid the development of evolutionary models and model atmospheres. For example relatively few L dwarfs are known in astrometric binaries, yet these are crucial for accurate mass determination. L dwarfs with unusual colours, low metallicity and halo kinematics, and low surface gravity (see e.g. Kirkpatrick et al. 2010, Faherty et al. 2012) are also poorly sampled.

Since detectable L dwarfs are relatively nearby and as such tend to exhibit large proper

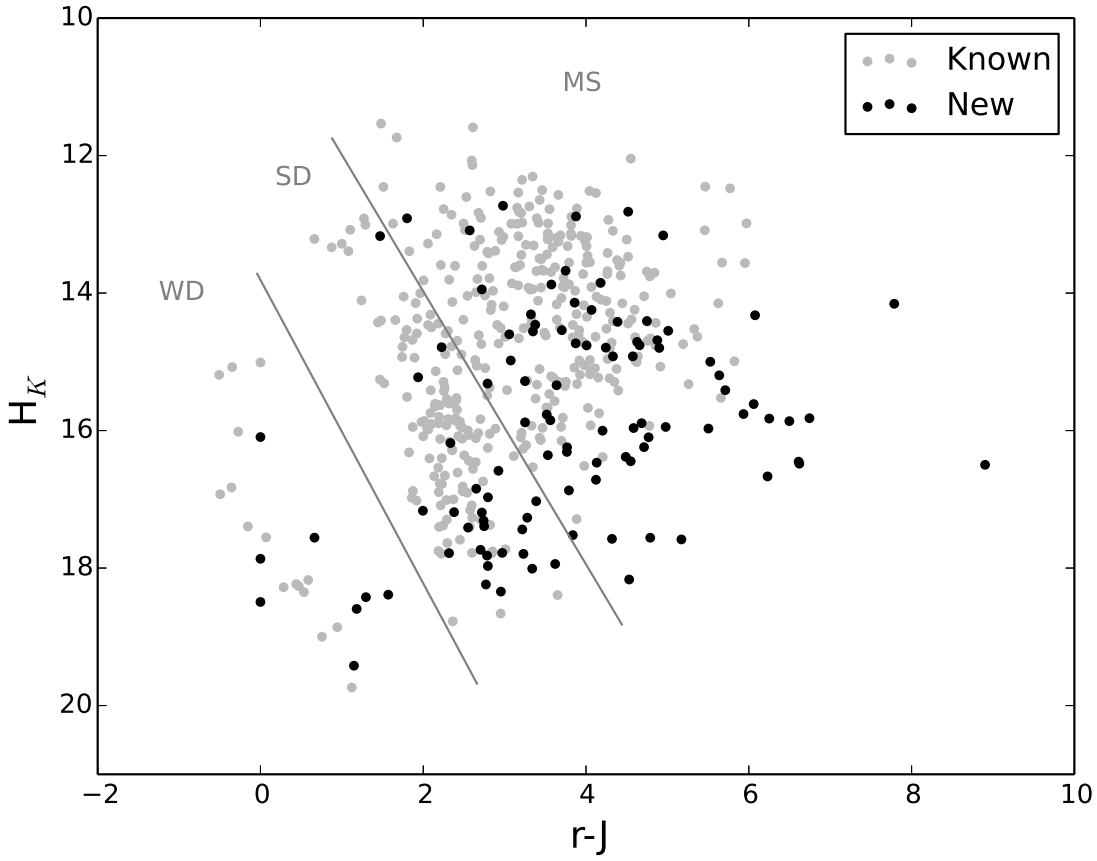

FIGURE 4.10: The K band reduced proper motion (H_K) distribution of known (grey) and newly discovered (black) high proper motion sources versus their r-J band colours. The main sequence, subdwarf and white dwarf loci are annotated.

motions, I searched the GPS high proper motion sample for previously undetected examples. I note however that many L dwarfs in the GPS will have proper motions smaller than this selection, this likely to be my primary source of incompleteness. Nonetheless, L dwarfs exhibit a range of near infrared colours dependant on a number of factors, and selections which do not rely on these colours are necessary to identify unusual examples. They are relatively faint in optical bandpasses and for this reason optical to infrared colours are very useful for identifying them.

I classified sources as L dwarf candidates if they displayed i-J > 4 (where the IPHAS i magnitude is on the Vega system), or had estimated L spectral types using the system of Skrzypek et al. (2015). The 13 candidate L dwarfs I identified are listed in Table 4.1. One candidate, UGPS J063333.37+100127.4, is unusually blue for an L dwarf, with J−K of 0.94. I note however that the IPHAS field containing this object was observed in poor weather, and the photometry is unreliable as a result. This object also falls

TABLE 4.1: GPS L dwarf candidates based on red optical to infrared colours and a minimum χ^2 fit of the available photometry to brown dwarf colour templates. The i band photometry is from the IPHAS survey and is on the Vega system.

RA	Dec	K	i−J	J−H	H−K	SpTy est.	Note
03:53:04.59	+47:55:45.6	14.59	3.8	0.61	0.58	L0	[a]
04:46:39.22	+40:54:52.9	15.60	∼4.0	0.63	0.61	L1	[d]
05:44:57.43	+37:05:04.1	12.36	4.1	0.80	0.74	L2.5	[a]
06:33:33.37	+10:01:27.4	14.21	4.1	0.43	0.51	L1	
06:47:12.29	+08:24:40.0	15.17	∼3.8	0.63	0.59	L0.5	[d]
19:55:30.48	+26:13:13.1	16.99	>2.2 [b]	0.82	0.67	L3.5	[a]
20:05:30.35	+36:35:50.7	16.01	>3.0 [b]	0.86	0.60	L9.5	[d]
20:17:31.27	+33:53:59.5	16.01	>3.1 [b]	0.74	0.60	L2	[d]
20:31:32.54	+43:03:19.4	14.27	4.4	0.83	0.75	L4	[a]
21:14:25.17	+50:10:15.9	14.51	3.9	0.78	0.79	L3	[a]
21:18:59.26	+43:38:01.3	13.50	∼3.1 [c]	0.6[c]	0.3[c]		[e]
21:19:52.83	+48:26:12.0	14.74	4.4	0.66	0.58	L1	[a]
22:07:06.47	+53:52:53.3	15.00	4.1	0.63	0.59	L1	[a]

[a] Spectral type based on a photometric typing by Skrzypek et al. (2015) using available optical and NIR photometry.
[b] Not visible in i band image, lower limit on i band photometry taken as the magnitude of a 3σ detection.
[c] Performed own photometry in i, J, H, and K. Near infrared colours have ±0.3 uncertainties.
[d] Spectral type based on a photometric typing by Skrzypek et al. (2015), though missing several bands.
[e] In a binary or triple system, see Section 4.4.3.

within the area of the Galactic plane covered by the SDSS. The SDSS i band magnitude of 19.08 gives the source an i-J colour of 3.9 which is roughly consistent with a late M dwarf and would match the relatively blue J-K colour. The WISE W1−W2 colour for this object is 0.29 ± 0.05 which is within the range seen for normal late M dwarfs (Kirkpatrick et al., 2011). I also note that it is the only candidate in the list with an H−K colour greater than its J−H colour. Another candidate, UGPS J054457.43+370504.1, is likely to be within the 25 pc volume limited sample. I estimate its distance at 16 to 23 pc assuming a spectral type of L2.5 ±1 subtype and using the spectral type to J band absolute magnitude relation of Dupuy and Liu (2012). I identified an additional L dwarf candidate which did not meet the original high proper motion candidate selection criteria, UGPS J065420.86+040056.5, see Section 4.4.3.2.

4.4.3 New Benchmark Ultracool Dwarf Candidates

Ultracool dwarfs as binary companions to other objects (e.g. main sequence stars or white dwarfs) offer an opportunity to test the properties predicted for them by atmospheric models and hence evaluate and refine the models themselves. Age and metallicity

are difficult to constrain observationally in UCDs and these properties can sometimes be measured for a companion and then adopted for the UCD since they will usually have formed from the same molecular cloud at a similar time (Pinfield et al., 2006).

I undertook a search for new benchmark UCD candidates using two methods: The first was a straightforward search of current proper motion catalogues for companions to the 153 previously unidentified high proper motion sources. The second method is a wide search of the full 167 million source results table for common proper motion companions to all 617 genuine high proper motion sources.

4.4.3.1 Existing Catalogue Search

For the search of existing proper motion catalogues I used the LSPM catalogue for the northern sources, which also contains proper motion sources from the Tycho-2 Catalogue of 2.5 Million Bright Stars (Tycho-2, Høg et al. 2000) and the All-sky Compiled Catalogue of 2.5 million stars (ASCC-2.5, Kharchenko 2001), and the catalogue created by Boyd et al. (2011a, 2011b) for the small number of the GPS proper motion objects in the south. I performed a 1000" sky match, returning all matches with proper motion difference significance in $\alpha \cos \delta$ and δ combined $< 2\sigma$. The Boyd et al. search yielded no results. Table 4.2 shows the seven candidate pairs identified in the LSPM search, two of which are matched to the same GPS source (UGPS J211859.26+433801.3) and are therefore a candidate triple system. Below I discuss the two systems in which the newly discovered high proper motion object may be an ultracool dwarf.

UGPS J211859.26+433801.3 is a close, faint ($\Delta_J \simeq 3.7$, J = 14.7, $\mu = 215 \pm 4\, mas\, yr^{-1}$) companion to the bright M dwarf LP 234-2220. LP 234-2220 was classified as an M3.5 dwarf with an estimated distance of 53.3±8.1 pc using spectroscopic observations by Reid et al. (2004). The pair are separated by 2.2" and the Reid et al. (2004) spectrum may be contaminated by flux from the companion, though the level of contamination should be small and the spectral classification still reasonably accurate.

Due to the high contrast and small separation between the pair I deemed it necessary to re-measure the full range of photometry from the original image files. In each case I used a background count level equal to the median counts in a one pixel wide annulus with a radius equal to the separation between the pair centred on LP 234-2220. The

TABLE 4.2: The seven candidate companions identified in a search of the LSPM catalogue, two of which are matched to the same GPS source and are therefore together a candidate triple system. The first three columns are those of the GPS source, the next four are of the LSPM candidate companion. The coordinates given are at epoch 2000.0. The proper motions of the candidate companion identified by an asterisk are those of the Tycho-2 catalogue (as indicated in the LSPM catalogue by the astrometric flag), otherwise they are those of the LSPM. All proper motions are in units of $mas\ yr^{-1}$. K_s is the 2MASS short K band magnitude obtained from the LSPM catalogue.

α	δ	K	i-J	Name	$\mu_\alpha \cos\delta$	μ_δ	K_s	Separation (")	Δ_μ Significance (σ)
04:02:29.42	+48:12:56.6	16.53	0.64	LSPM J0402+4812	139	-223	15.49	2.1	0.66
04:35:19.94	+43:06:09.4	11.13	1.94	LSPM J0435+4305*	155	-163	7.62	67.3	1.35
21:11:04.39	+48:00:21.9	11.87	1.89	LSPM J2109+4811	183	127	11.25	949.2[a]	0.84
21:18:59.26	+43:38:01.3	13.50	∼3.1	LSPM J2118+4338	177	116	10.23	2.2	1.62
21:18:59.26	+43:38:01.3	13.50	∼3.1	LSPM J2119+4352	170	139	10.03	931.2[a]	0.43
21:32:12.97	+44:52:29.3	15.67	1.58	LSPM J2132+4452	164	133	13.79	28.5	0.99
21:41:15.07	+56:40:12.9	14.01	3.02	LSPM J2141+5640	224	247	11.34	5.6	0.62

[a] Owing to their very large angular separations these are likely chance alignments, see Section 4.4.3.3.

uncertainties in the new photometry are relatively large, as much as 0.3 mag in each case. For this reason I relied more on the magnitude of the contrast than optical or infrared colours as an indicator of spectral type since the uncertainty on the contrast is dependant on the uncertainty of only one photometric measurement of the secondary, rather than colour which is dependent on two. A companion i−J colour of ∼3.1 suggests a spectral type around M6-7. A primary of type M3.5 ($M_J \sim 7.8$) and a $\Delta_J \simeq 3.7$ suggests a spectral type for the companion of around M9.5/L0.

I identified another very widely separated (15.5') common proper motion companion to this system: 2MASS J21193088+4352264 (2MASS J2119+4352 hereafter, see also Table 4.3). The IPHAS r-i colour of 2MASS J2119+4352 suggests a spectral type of M3.5 based on Drew et al. (2005) Table 2 and assuming the object is unreddened, which is not an unreasonable assumption given its high proper motion. The similar spectral types and IPHAS optical and GPS infrared magnitudes between LP 234-2220 and 2MASS J2119+4352 suggest a similar distance. The LSPM proper motions for 2MASS J2119+4352 and LP 234-2220 which do not suffer from the saturation seen in the GPS for these bright objects, differ by 1.5 σ. The angular separation gives a projected separation of order 50,000AU at 53pc. Such a system is unlikely to have survived for any significant length of time and the IPHAS narrow band photometry indicates that neither component has any excess Hα emission (which would have indicated youth). I find in Section 4.4.3.3 that I expect several pairs of sources in this GPS proper motion sample with large angular separations and similar proper motions that are not physically associated. I therefore conclude that the similar proper motions of LP 234-2220 and 2MASS J2119+4352 are most likely coincidental.

UGPS J214115.07+564012.9 (UGPS J2141+5640B hereafter) is a $\mu = 339 \pm 12\ mas\ yr^{-1}$ common proper motion companion to G 232-30 with a separation of ∼5.6". G232-30 appears to be an M0/M1 type dwarf based on its i-J and near infrared colours, which given the J band contrast (2.85) between the pair and assuming their genuine companionship and no unresolved multiplicity in either component suggests that UGPS J2141+5640B is approximately M5/M6. The i-J colour (3.02) of UGPS J2141+5640B suggests an approximate spectral type of M6.5 and this is also consistent with its J-H colour (0.57, although this changes very little across the M dwarf sequence). However, H-K = 0.47

for this object, which suggests a later type M dwarf (M7/M8). On balance it is most likely that UGPS J2141+5640B is an M6.5 dwarf.

4.4.3.2 Internal GPS Search

For the internal search of the full GPS proper motion results table I searched for candidate common proper motion ($\Delta_\mu < 20\ mas\ yr^{-1}$) companions to all 617 identified high proper motion GPS sources with separations up to 30'. I applied no further quality control or brightness selection criteria to the candidate list to prevent rejection of potentially valuable sources due to e.g. a profile misclassification at a single epoch, this selection returned 1032 candidates. A visual inspection yielded 41 genuine high proper motion objects within this sample after removal of 5 duplicate sources from frame overlap regions. Among these I find 11 instances where both components are among the original 617 GPS high proper motion sources and hence they produce a reversed pair (i.e. two instances with switched components), removal of these pairs left me with 19 candidate common proper motion pairs which I show in Table 4.3. Since all the companions did not meet the original high proper motion source candidate selection criteria their astrometry is likely compromised and the uncertainty on the proper motion will be underestimated, as a result the stated significance of the proper motion difference should be regarded as a lower limit.

Based on the i-J colours of the original GPS high proper motion sources from Table 4.3 and their K band contrasts I identified pairs 1, 2, and 12 as candidates for new UCD benchmark objects. Based on the positions of the three candidate primaries in a K band reduced proper motion (H_K) vs. i-J plot, the primary in pair 2 appears to be a white dwarf (faint in H_K, blue in i-J) while the remaining two candidate primaries appear to be main sequence stars with the primary of pair 12 just on the edge of the subdwarf locus (unremarkable i-J, faint in H_K). Inspection of the IPHAS i band images and catalogues showed that the secondary in pair 2 is equal in i band brightness to the primary (17.39) and it is therefore likely that they are a pair of equal mass white dwarfs given their almost identical i-K colour. The secondaries in pairs 1 and 12 are non-detections in the IPHAS i band images and are promising UCD candidates as a result.

TABLE 4.3: Internal GPS common proper motion companion candidates. Columns 2 to 4 refer to the original GPS high proper motion source and columns 5 to 8 refer to the GPS source which did not meet the original high proper motion candidate selection criteria. The coordinates given are at epoch 2000.0. The dropout note indicates the reason the companion was not selected as an initial high proper motion candidate. Dropout note key: a - flagged as saturated at either epoch; b - flagged as a galaxy at either epoch; c - bad pixel within 2" aperture flag at either epoch; d - ellipticity > 0.3 at either epoch; e - μ_{tot} just below original selection criteria (200 $mas\ yr^{-1}$); f - neither epoch K band magnitudes below 17. In the 'Known' column the left tick/cross corresponds to the original GPS source, the right tick/cross corresponds to the new GPS companion candidate.

Pair	α	δ	K	α	δ	K	Dropout Note	Ang. Sep. (")	Δ_μ Signif. (σ)	Known
1	03:42:14.85	+54:10:19.6	11.14	03:42:14.52	+54:10:18.8	15.69	bd	2.9	1.10	✓ ✗
2	04:02:29.42	+48:12:56.6	16.54	04:02:29.21	+48:12:56.8	16.57	b	2.1	0.47	✗ ✗[a]
3	04:33:14.79	+40:47:35.8	12.63	04:33:14.76	+40:47:37.8	13.02	b	2.0	0.10	✓ ✗[a]
4	04:39:15.47	+39:06:31.1	13.82	04:39:16.15	+39:06:36.4	12.52	e	9.4	1.48	✓ ✓
5	05:15:07.12	+45:13:00.6	11.80	05:15:06.99	+45:12:59.9	12.84	b	1.6	0.93	✓ ✗[a]
6	05:21:43.70	+33:22:05.5	10.01	05:21:43.46	+33:21:58.8	15.70	b	7.4	1.15	✓ ✓
7	05:27:46.10	+44:35:34.2	11.58	05:27:46.99	+44:36:11.4	9.62	a	38.4	0.39	✓ ✓
8	05:27:46.94	+44:36:13.9	10.87	05:27:46.99	+44:36:11.4	9.62	a	2.7	1.05	✓ ✓
9	05:34:21.85	+42:27:39.0	11.91	05:34:21.82	+42:27:37.3	13.29	b	1.8	0.68	✓ ✗[a]
10	05:47:33.08	+38:03:05.5	15.02	05:47:32.93	+38:03:05.2	16.91	b	1.8	0.44	✗ ✗
11	06:48:20.56	+05:40:33.5	11.20	06:48:20.30	+05:40:30.1	9.09	a	5.1	2.12	✓ ✓
12	06:53:11.66	+03:47:50.7	12.44	06:54:20.86	+04:00:56.5	17.11	cf	1300.1[b]	0.95	✓ ✗
13	20:40:04.51	+42:21:07.1	12.03	20:39:52.64	+42:20:33.8	10.91	d	135.7	0.64	✓ ✓
14	20:55:51.57	+43:27:48.1	13.22	20:56:56.34	+43:08:08.4	11.19	a	1375.4[b]	0.84	✓ ✓
15	21:18:59.26	+43:38:01.3	13.50	21:18:59.30	+43:38:03.5	10.04	a	2.2	1.83	✗ ✓
16	21:18:59.26	+43:38:01.3	13.50	21:19:30.94	+43:52:26.8	9.89	a	931.2[b]	1.27	✗ ✓
17	21:23:42.21	+44:19:17.1	12.76	21:23:43.45	+44:19:28.0	10.59	a	17.2	0.13	✓ ✓
18	22:21:29.14	+55:56:00.1	14.20	22:23:34.94	+56:10:05.1	10.39	a	1350.9[b]	1.61	✗ ✓
19	22:37:06.22	+55:54:40.8	10.82	22:37:05.95	+55:54:44.3	9.33	a	4.2	0.55	✓ ✓

[a] Known high proper motion object is actually a blend of both components, previously unresolved.
[b] Owing to their very large angular separations these are likely chance alignments, see Section 4.4.3.3.

UGPS J034214.85+541019.6 AB: - pair 1 in Table 4.3, UGPS J0342+5410 AB hereafter. UGPS J0342+5410 B is an $\mu = 240\pm12\ mas\ yr^{-1}$ IPHAS i band non-detection, the 3σ detection limit of the field is 21.2. The pair are separated by 2.9". Flux from the primary at this radius only increases the background count level by of order 30% in the i band image so the detection limit should still be reasonably accurate. UGPS J0342+5410 B has J=16.67±0.02 and H=16.12±0.02, this gives a lower limit on i-J of 4.5 which corresponds to a spectral type later than or equal to approximately L1. The infrared colours of UGPS J0342+5410 B (J-H = 0.55, H-K = 0.43) are somewhat bluer than expected for a typical L type dwarf and suggest a late M spectral type. The near infrared colours of UGPS J0342+5410 A suggest a spectral type of approximately M1.5 (± 1.5 subtypes, using 2MASS photometry as the GPS photometry is near saturation). Given the contrast ratio between the pair I can say the secondary is between M8 and L1 and could be either a red late M dwarf or a blue early L dwarf, follow up spectroscopy will be needed for confirmation.

UGPS J065311.66+034750.7 and UGPS J065420.86+040056.5: - pair 12 in Table 4.3, UGPS J0653+0347 ($\mu = 251\pm6\ mas\ yr^{-1}$) and UGPS J0654+0400 ($\mu = 258\pm15\ mas\ yr^{-1}$) hereafter. UGPS J0654+0400 is an IPHAS i band non-detection, the 3σ detection limit of the field is 20.3. It has J and H band magnitudes of 18.86±0.07 and 17.86±0.05 respectively giving a lower limit on i-J of approximately 1.4. The near infrared colours of UGPS J0654+0400 (J-H = 1.00, H-K = 0.75) indicate it is an L dwarf (see e.g. Day-Jones et al. 2013). The Dupuy and Liu (2012) spectral type to absolute magnitude relation for L0 to L9 dwarfs suggest a distance to UGPS J0654+0400 of 75 to 300 pc. This pair are separated by 21.7', and I find in Section 4.4.3.3 that I expect several pairs of sources in the GPS proper motion sample with large angular separations and similar proper motions that are not physically associated and therefore conclude that this likely to be a chance alignment.

4.4.3.3 Notes on Chance Alignment Probabilities

Here I evaluate the probability that the common proper motion companions discussed above are chance alignments. My estimates are drawn from large simulations made with the online Besançon synthetic stellar population tool (Robin et al., 2003). The catalogues

were generated with a K magnitude range equivalent to the GPS high proper motion sample, using the Galactic position of each candidate. I generated "small field" simulated catalogues with several million stars (equivalent to a 1500 deg^2 area but with properties fixed for the precise Galactic location) for each of the binary candidates discussed. The catalogue simulations generate realistic proper motions for each source but do not produce physically associated systems (such as moving groups or binaries). All common proper motion companions in the sample are therefore purely chance alignments. I then identified all sources within each simulated catalogue that have a proper motion consistent with the GPS component of the binary candidate within the 2σ uncertainty on the proper motion difference. The approximate probability of a source appearing within a given angular separation r and with a common proper motion to one of the GPS high proper motion sources is therefore the number of matches in the simulated catalogue multiplied by the area of a circle with radius r, divided by 1500 deg^2. I must also take into account that there are 617 high proper motion objects, and therefore 617 chances of finding such a chance alignment. For each binary candidate discussed above I treated this using a simple multiplicative factor. In fact there is some variation in the number of proper motion matches in the simulated catalogues, depending on Galactic coordinates and the direction of proper motion but tests indicate that this is less than a factor of 4. In the cases discussed above with separations < 1' the probability is always less than 10^{-3} so the factor of 4 is not significant. Note that for each candidate companion the Galactic coordinates, proper motions and angular separations are different and they require a unique calculation as a result.

In Tables 4.2 and 4.3 I list six very widely separated (>10') common proper motion companions to sources in the GPS proper motion sample, two of which contain a UCD candidate and are discussed in more detail. For these two systems the above calculation indicates that the expected number of chance alignments in the GPS proper motion sample is 8 and 13 respectively. Even allowing for the factor of 4 uncertainty I still expect to find a few examples in the sample so I conclude that these are chance alignments.

4.4.4 New T Dwarfs

T type brown dwarfs are later in the brown dwarf sequence than L dwarfs. As they age and cool through the brown dwarf sequence the dust present in L dwarf atmospheres

sinks below the photosphere and its effect on their spectra disappears. The cooler temperatures of T dwarfs allow molecules such as methane and water to form, which are responsible for the deep absorption features observed in their spectra. They emit most of their radiation in the near infrared and for this reason recent large scale near infrared sky surveys (e.g. 2MASS, Skrutskie et al. 2006; DENIS, Epchtein et al. 1997; CFBDS, Delorme et al. 2010; UKIDSS, Lawrence et al. 2007) are responsible for the majority of current T dwarf discoveries. Later type T dwarfs are cooler still and the WISE mission (Wright et al., 2010) in the mid infrared becomes more sensitive to them at around T6 and later. To date several hundred T dwarfs have been identified.

T dwarfs are extremely faint, even in the near infrared and are only detectable by the current generation of large scale NIR surveys out to of order 100pc. Due to the close proximity of detectable T dwarfs they tend to exhibit relatively large proper motions. For this reason proper motion searches such as this could be expected to identify many examples of T dwarfs. I have found two new examples of T dwarfs, which I describe below, among the 153 previously unidentified high proper motion sources due to their characteristic blue J-H and H-K colors. I also recover UGPS J0722-05 amongst the 617 high proper motion sources. The two GPS T dwarfs identified by Burningham et al. (2011a) are fainter than my $K = 17$ cut and were not recovered as a result. Two very nearby bright T dwarfs in the GPS footprint were identified by the WISE team recently. WISE J192841.35+235604.9 (Mace et al., 2013a) lies outside the area covered by this work and WISE J200050.19+362950.1 (Cushing et al., 2014) was excluded due to a high ellipticity and a profile misclassification in the second epoch K band observation. The GPS proper motion for WISE J200050.19+362950.1 is 75±7 and 415±9 $mas\ yr^{-1}$ in $\alpha \cos \delta$ and δ respectively.

UGPS J20480024+503821.9 (UGPS J2048+5038 hereafter) was identified as a J=16.30 $\mu = 267 \pm 11\ mas\ yr^{-1}$, IPHAS i band non-detection. The 3σ IPHAS i band detection limit of this field is 20.4±0.4, which is consistent with approximately M9 or later based on i-J (>4.1). The blue nature of this object in J−H and H−K (-0.07 and 0.05 respectively) and the H−W2 and W1−W2 colours (∼1.5 and ∼1.6 respectively) suggested that this was likely a mid T type dwarf. The source is not included in the WISE All Sky Catalogue nor the AllWISE catalogue but it is visible in the WISE images as a faint source in a crowded field and it is included in the WISE L1b source table, which includes

less reliable photometry. The H−W2 and W1−W2 colours (∼1.5 and ∼1.6 respectively) are bluer than expected for a mid T dwarf but the uncertainties should be assumed to be large.

D. Rodriguez [Universidad de Chile, Santiago, Chile] and J. Faherty [Carnegie Institution of Washington, USA] obtained a NASA Infrared Telescope Facility (IRTF) SpeX (Rayner et al., 2003) spectrum of UGPS J2048+5038 (see Figure 4.11) on the 30th of September 2013 using the 0.8" slit in prism mode with six AB nod cycles of 200s per nod, although the target drifted out of the slit for the final two and these were discarded as a result. This gave a total on source time of 1600s. They also observed the spectral standard HD199217 for use in removing telluric features from the target spectrum and flux calibration. I combined and reduced the spectrum using the standard reduction tool: SpeXTool (Cushing et al., 2004).
B. Burningham classified UGPS J2048+5038 following the spectral typing scheme laid out by Burgasser et al. (2006) for T dwarfs. In Figure 4.12 I show the SpeX YJHK spectrum of UGPS J2048+5038 compared to the T4 (2MASS J22541892+3123498) and T5 (2MASS J15031961+2525196) spectral templates of Burgasser et al. (2006). The new source matches the T5 template very closely in the J and H band flux peaks, but shows less flux in the Y band peak, and enhanced flux in the K band. In Table 4.4 I give the spectral flux ratios used for index based classification in the Burgasser et al. (2006) scheme. These values further support the classification of UGPS J2048+5038 as a T5, and I therefore adopt this classification for this object (T5±0.5). See Table 4.5 for a list of parameters. The Dupuy and Liu (2012) spectral type to MKO J band absolute magnitude relation gives an M_J of 14.44 for an isolated T5 dwarf, which puts UGPS J2048+5038 (J=16.30) at a distance of approximately 24pc.

An initial IPHAS DR2 match to UGPS J03553200+4743588 (UGPS J0355+4743 hereafter, $\mu = 469\pm16\ mas\ yr^{-1}$) found the closest match to have a separation >1" of the expected position of the target at the IPHAS epoch. Subsequent visual inspection of the IPHAS i band image confirmed a mismatch or blend with a background source. I attempted a subtraction of the PSF of the background source using the standard IRAF ALLSTAR program and subsequent inspection of the residual image showed no remaining sign of either the background source or the target. This suggested either the pair were so close they were completely unresolved, or more likely given the expected ∼1.1" (3.3

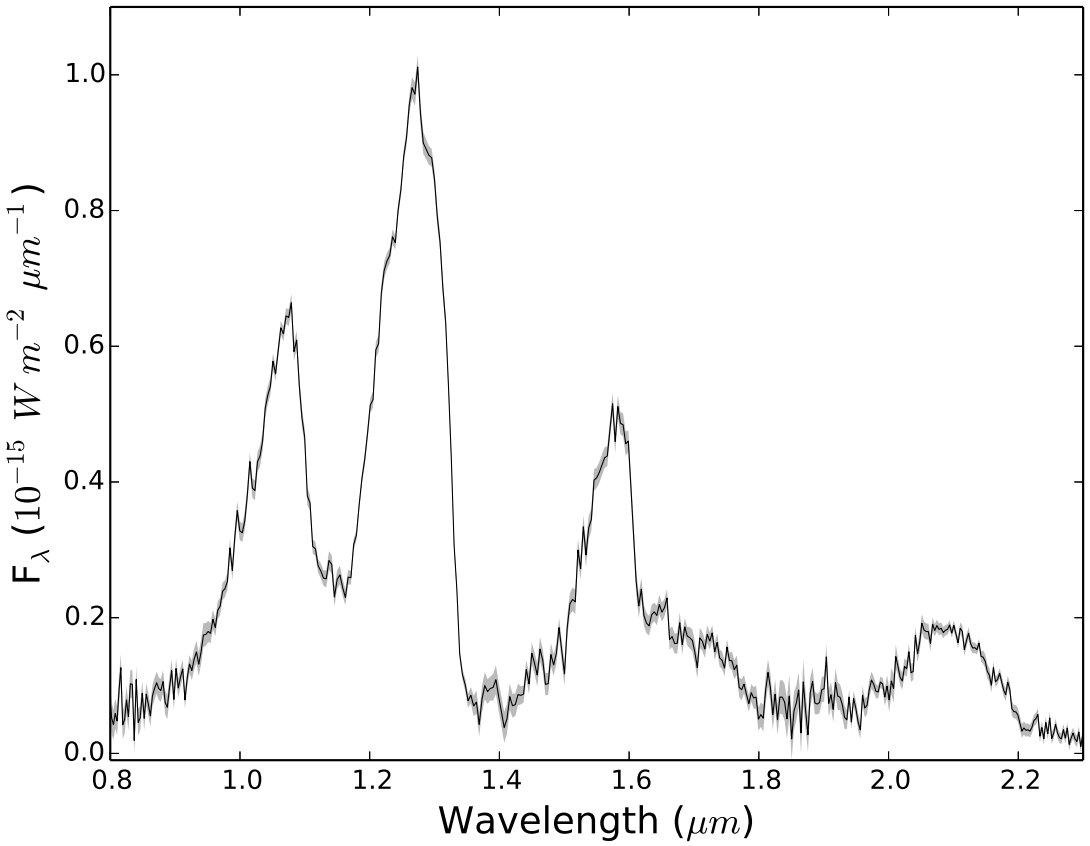

FIGURE 4.11: An IRTF SpeX spectrum of the previously unidentified T5 dwarf UGPS J2048+5038.

TABLE 4.4: The spectral flux ratios used for classifying UGPS J2048+5038.

Index	Ratio	Value	Type
H_2O-J	$\frac{\int_{1.14}^{1.165} f(\lambda)d\lambda}{\int_{1.26}^{1.285} f(\lambda)d\lambda}$	0.26 ± 0.01	T5
CH_4-J	$\frac{\int_{1.315}^{1.34} f(\lambda)d\lambda}{\int_{1.26}^{1.285} f(\lambda)d\lambda}$	0.41 ± 0.01	T5
H_2O-H	$\frac{\int_{1.48}^{1.52} f(\lambda)d\lambda}{\int_{1.56}^{1.60} f(\lambda)d\lambda}$	0.38 ± 0.01	T4/5
CH_4-H	$\frac{\int_{1.635}^{1.675} f(\lambda)d\lambda}{\int_{1.56}^{1.60} f(\lambda)d\lambda}$	0.42 ± 0.01	T5
CH_4-K	$\frac{\int_{2.215}^{2.255} f(\lambda)d\lambda}{\int_{2.08}^{2.12} f(\lambda)d\lambda}$	0.21 ± 0.01	T5

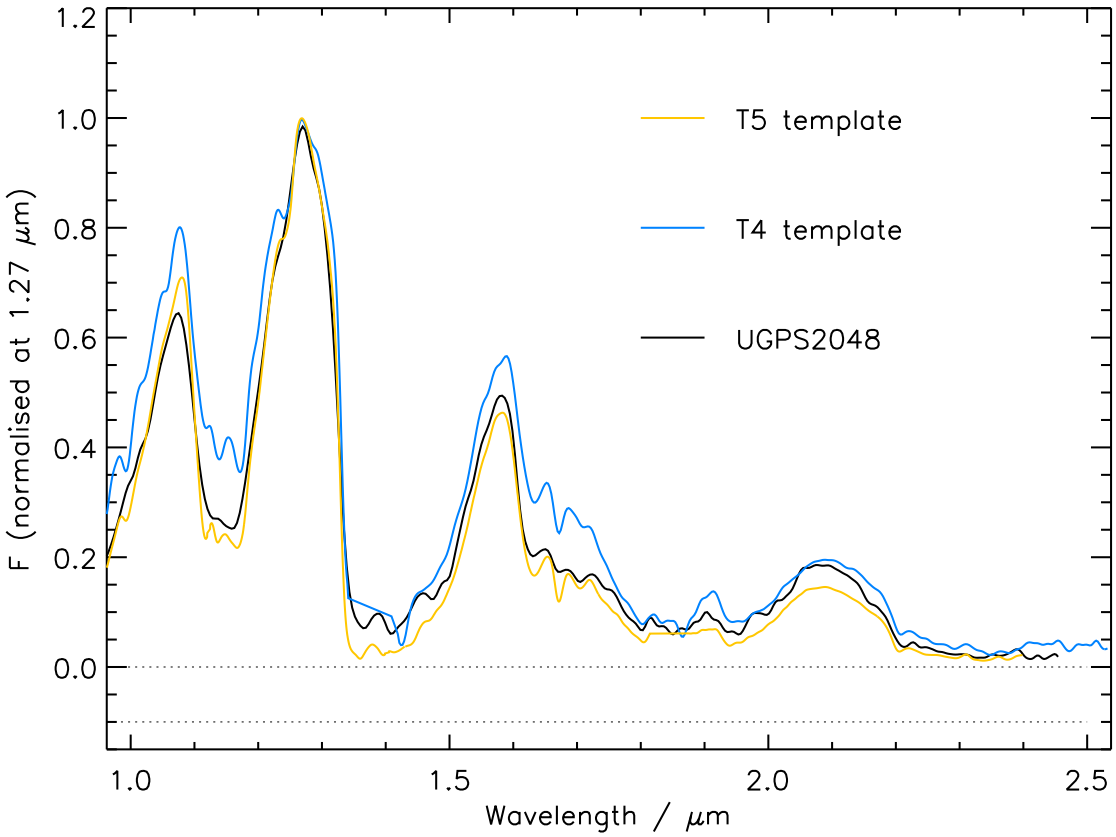

FIGURE 4.12: A $YJHK$ spectrum of UGPS J2048+5038 compared to the T4 (2MASS J15031961+2525196 and T5 (2MASS J15031961+2525196) spectral templates defined in Burgasser et al. (2006).

pixel) separation at the IPHAS epoch, the target is simply too faint in the i band to be detected.

An approximate 3σ IPHAS i band detection limit of this field is 20.5 magnitudes, suggesting the target is approximately L0 or later type. Given the blue nature of UGPS J0355+4743 in the near infrared, (J-H = -0.37 and H-K = 0.08), and H−W2 and W1−W2 of ∼2.67 and ∼1.12 respectively I regard it as a bona fide T dwarf and with an estimate type of T6 type dwarf.

The Dupuy and Liu (2012) spectral type to MKO J band absolute magnitude relation gives an M_J of 14.78 for an isolated T6 dwarf, which puts UGPS J0355+4743 (J = 16.20) at a distance of approximately 19pc. If the target is an unresolved binary or system of higher order multiplicity then this distance is an underestimate.

TABLE 4.5: Parameters of the two previously unidentified T dwarfs which I describe in Section 4.4.4.

	UGPS J2048+5038	UGPS J0355+4743
Right Ascension	20:48:00.24	03:55:32.00
Declination	+50:38:21.9	+47:43:58.8
Spectral Type	T5	∼T6
J	16.30	16.20
μ_{total}	267 $mas\ yr^{-1}$	469 $mas\ yr^{-1}$
Distance	∼24 pc	∼19 pc
J−H	-0.07	-0.37
H−K	0.05	0.08
W1−W2	∼1.6	1.12
H−W2	∼1.5	2.67

4.4.5 Other Objects of Note

UGPS J04514383+4549580 ($\mu = 680 \pm 7\ mas\ yr^{-1}$) is a faint companion to LHS 1708, a G1 type main sequence star, with a separation of 5.6" and a Δ_J of 5.9 magnitudes. It was identified in the search for new candidate UCD benchmark objects. The GPS proper motion differs by 2.1σ from the Hipparcos proper motion of LHS 1708 and as a result the pair did not show in the $< 2\sigma$ candidate companion list in Section 4.4.3.1. Given the K band brightness (10.8), the uncertainty on the GPS proper motion for UGPS J04514383+4549580 ($\pm$ 7 $mas\ yr^{-1}$) is likely underestimated by the pipeline and the significance of the similarity in the proper motion of this pair is therefore also underestimated. Based on its IPHAS optical and GPS infrared colours UGPS J04514383+4549580 is either a mid-M type main sequence star or a white dwarf. LHS 1708 does have an entry in the Washington Double star Catalogue (WDS, Mason et al. 2001), although the stated separations (101.6" and 85.80" for the 1909 and 1989 epochs respectively) are higher than for the object I identified. The position of the WDS secondary at the 1909 and 1989 epochs, which I calculated from the stated separations and position angles relative to the position of LHS 1708 at the two epochs, is consistent with a bright source on the GPS image which shows no proper motion. I conclude that the secondary given in the WDS does not share a proper motion with LHS 1708 and is therefore not a genuine binary companion. However, the object UGPS J04514383+4549580, is a genuine common proper motion companion to LHS 1708.

4.5 Summary

I present the results of a search for high proper motion objects in the UKIDSS Galactic Plane Survey. I selected 5,655 high proper motion ($\mu > 200\ mas\ yr^{-1}$) candidates from 900 deg^2 of sky at $l > 60°$ and K < 17 for visual verification and found 617 to be genuine, 153 of which were previously unidentified. Among the new high proper motion discoveries I identified two new mid T dwarfs that are likely to be within 25 pc, a further thirteen new L dwarf candidates and two ultracool dwarf binary candidates.

The large 24" matching radius I adopted in an effort to detect objects with very high proper motions at the expense of a large number of mismatches gave an overall ratio of false to genuine candidates of 9:1. At high galactic longitudes, where the source density is much lower, I found this to be less of a problem; the ratio of false to genuine candidates at l =180° is ∼1:1. The accuracy of the genuine high proper motions is good, the median uncertainty on the proper motions of sources at K < 16 is 6.6 $mas\ yr^{-1}$. These GPS proper motions for sources in common with existing long epoch baseline optical catalogues are in good agreement within their uncertainties.

Proper motions were calculated for 167 million sources in total and I plan to extend the search to objects with lower but not insignificant motions. I also plan to extend the selection presented here to data taken after March 31st 2013, search for brighter high proper motion objects at $l < 60°$, and search for high proper motion objects at K > 17 with the aid of colour selections.

Chapter 5

The VVV Astrometric Pipeline

5.1 Introduction

The VISTA VVV survey covers 560 deg^2 of the Galactic disc and bulge in 5 passbands, including typically between 50 and 150 times in the Ks passband over 5 years (2009 to 2014). This astrometric pipeline is restricted to using only the Ks band observations to try to limit the incidence of mismatches between epochs, which degrades the quality of the astrometric fits. The VVV also includes complete coverage in the Z, Y, J and H bandpasses at a single epoch at the start of the survey and another at the end. The relative few additional epochs these observations provide are not worth the added complications due to inter-band crossmatching for example, which is further complicated by interstellar reddening.

Definitions

In this document I adopt the following terms in the description of VVV data.

Tile - The VVV survey is split into 348 individual 1.5°×1° tiles, 196 in the bulge and 152 in the disk.

Pawprint - Each VVV tile is split into 6 separate pawprints. Each pawprint is overlapped by other pawprints such that each point is usually covered by two pawprints. Exceptions occur in which a point may be covered by up to six pawprints, or at

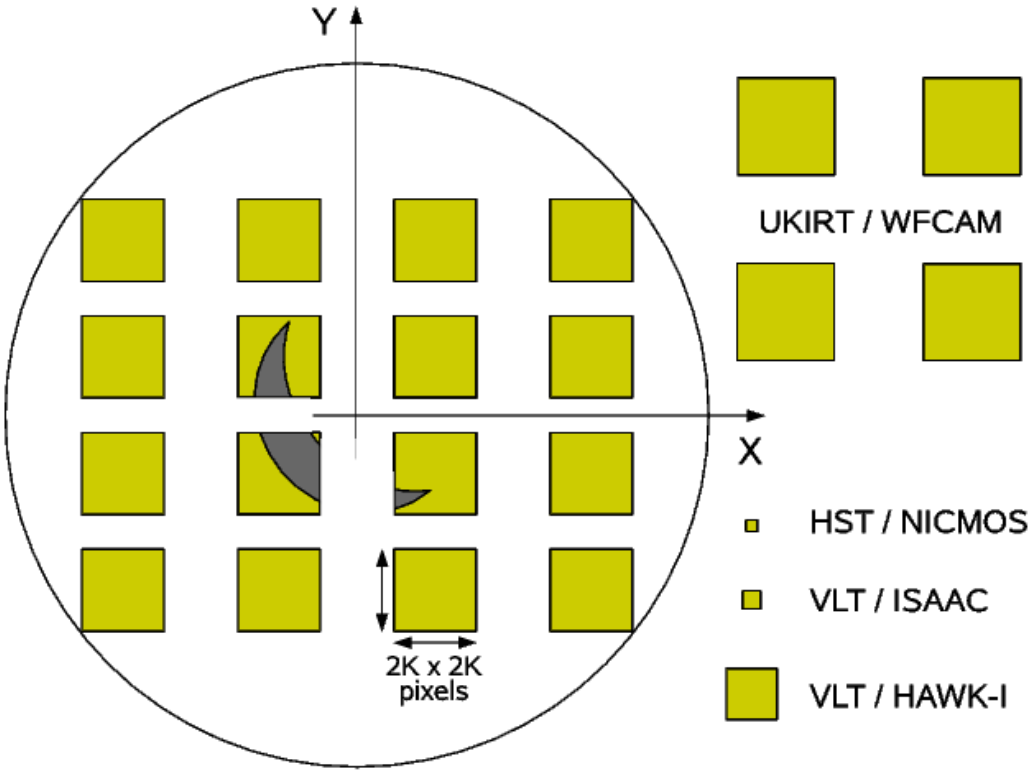

FIGURE 5.1: A VIRCAM pawprint compared to the Moon, WFCAM and other instruments. Adapted from Minniti et al. (2010).

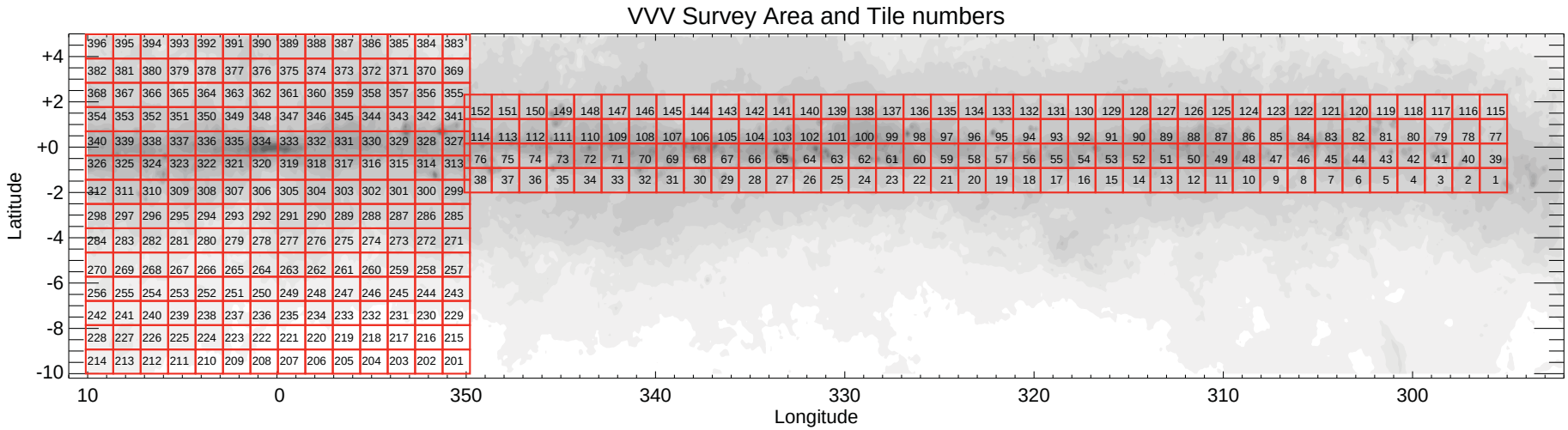

FIGURE 5.2: The VVV survey area with overlaid tile outlines and numbers. The axes are Galactic coordinates in degrees. Plot taken from Catelan et al. (2011).

the edges of the survey area as few as one pawprint. Each pawprint is made up of 16 arrays numbered 1-16 arranged in a 4×4 grid (i.e. a VIRCAM pawprint, see Figure 5.1).

5.2 The VIRCAM VVV Data

The VIRCAM is the largest near-infrared imager in astronomical use, consisting of sixteen 2048×2048 pixel mercury cadmium telluride arrays. Combined with VISTA optics this gives a total viewing area of 0.6 deg^2 (0.339" per pixel). Detectors are placed in a 4×4 gride spaced 0.9× the detector width in the y direction 0.425× the detector width in the x direction. VISTA and VIRCAM are described in great detail by Sutherland et al. (2015). Pipeline data reduction, catalogue generation and calibration of the photometry and astrometry for VISTA are provided by CASU and described by Lewis et al. (2010). The VSA facilitates further processing (bandmerging, pawprint merging, etc.) and curation of the VISTA data and makes it available to the user. The VSA is described in detail by Cross et al. (2012).

5.3 Data Acquisition

I wrote a BASH script to download successive VSA Archive Listing results pages producing an index of VVV Ks band observations. I then used a simple BASH FOR loop and WGET to download batches of FITS file catalogues. The catalogues acquired were based on observation taken between February 16^{th} 2009 and April 30^{th} 2014.

The raw VVV FITS file catalogues were fed through a modified fortran routine FITSIO_CAT_LIST originally provided by the CASU team. In a similar manner to the UKIDSS method (see Chapter 2), the modified FITSIO_CAT_LIST unpacks the binary tables for each individual chip in the FITS file, calculates calibrated magnitudes from the fluxes given, flags saturated sources, removes columns which are surplus to my requirements and outputs the resultant tables in ascii space delimited format. The modifications made to the UKIDSS FITSIO_CAT_LIST routine necessary to deal with VVV data were limited to a decrease in the flux/magnitude aperture size, from aperture magnitude (aperMag) 3 (radius = 1″) to aperMag 2 (radius = $1/\sqrt{2} \times 1''$). A smaller aperture produces more

reliable magnitudes in crowded fields (Lucas et al., 2008), and aperMag 2 benefits from a better calibration than aperMag 1 (radius = $1/2 \times 1''$). FITSIO_CAT_LIST deals with the increase in the number of arrays/binary tables, from 4 to 16, without the need for modification. An example processed catalogue, ready for the proper motion calculation pipeline is shown in Table 5.1.

I stripped a subset of the header information from each catalogue to be used for observation quality evaluation, including airmass, ESO grade, seeing for each chip and the source counts for each chip. I also retrieved the modified julian date of the observation and telescope pointing coordinates. I calculated an observation seeing value as the mean seeing of all 16 chips multiplied by the average VIRCAM pixel scale (0.339"/pixel). I initially rejected any "deprecated" (i.e. flagged as poor quality) pawprint, any with seeing > 1.2" (which corresponds to approximately 2% of the lowest quality data, see Figure 5.3) and any for which one or more of the 16 chips contained a factor of two more or fewer sources than the mean across the same chip from all coincident pawprints with adequate seeing (< 1.2"). I also rejected three observations for which the catalogue became corrupted.

Coincident pawprints were identified by matching the telescope pointing coordinates of all pawprints using an internal sky match with a 20" matching radius in TOPCAT. This yielded 2100 pawprint groups which corresponds to 6 pawprint groups for each of 346 VVV tiles and 12 pawprint groups for each of 2 VVV tiles for which the telescope pointing positions were > 1' from their usual positions at a number of epochs (specifically d015 and b390). These two tiles were subject to a change in pointing coordinates due to guiding problems caused by non-stellar profiles of guide stars used by the telescope guiding system. Because of this observations before and after the change in pointing coordinates are placed in separate pawprints, effectively doubling the number of pawprints for each at the expense of continuous epoch baseline.

5.4 Epoch Matching

Many factors needed to be considered when devising a suitable matching strategy. Previously with the two epoch UKIDSS data (see Chapter 2), the issue was simple enough with STILTS that only matching radius and a magnitude consistency requirement were

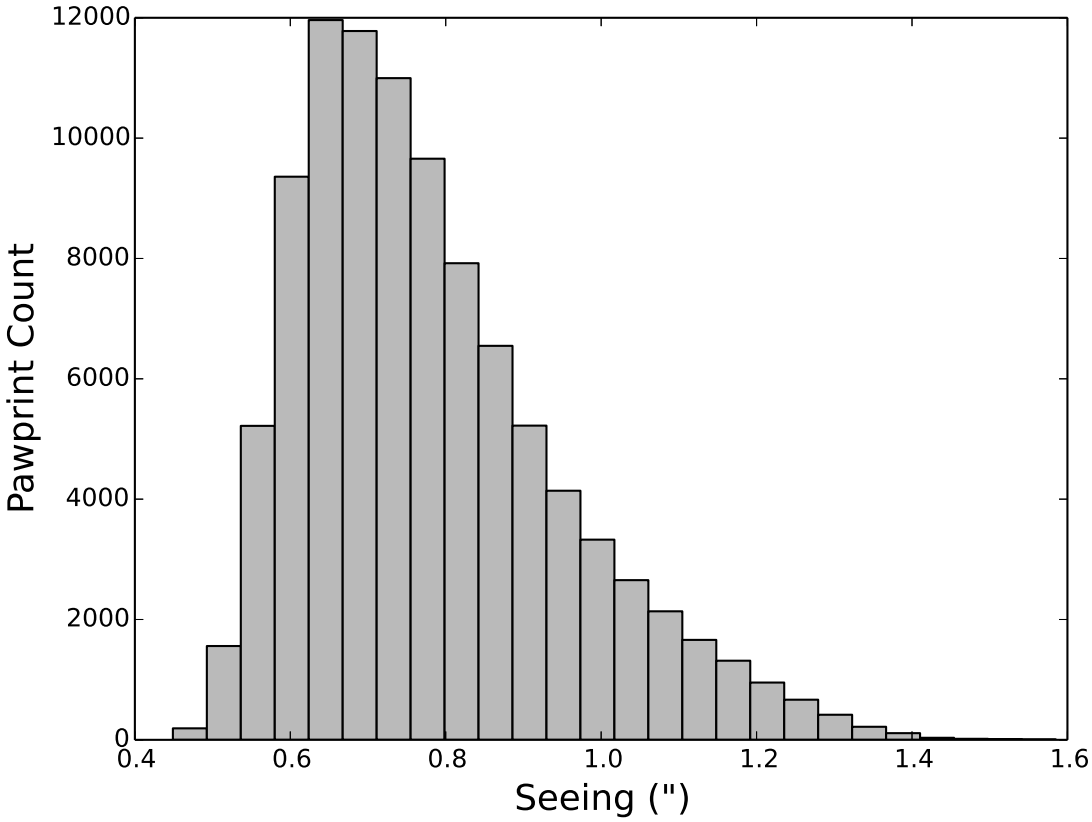

FIGURE 5.3: A histogram showing the distribution of seeing values across all VVV Ks band observations. The seeing values are the mean seeing value measured across the 16 arrays of each pawprint.

TABLE 5.1: A sample of a VVV pawprint table processed and ready for epoch matching. Ellipses indicate where values have been truncated for the purpose of this document. *Ks* is the Ks band magnitude derived from the AperFlux2 values in the raw FITS file catalogue. *eN* is the array extension number [1-16], *Clss* is the morphological classification flag (see description with Table A.1), *Ell* is the source ellipticity, *PA* is the position angle of the ellipticity, and *MJDObs* is the modified julian day of observation.

α	δ	X	Y	Ks	σ_{Ks}	eN	Clss	Ell	PA	σ_X	σ_Y	MJDObs
261.470...	-27.450...	2020.80...	1314.19...	16.16...	0.14...	2	1	0.19...	70.10...	0.24...	0.24...	56144.10...
261.759...	-27.730...	85.08...	327.39...	16.15...	0.15...	4	1	0.39...	5.70...	0.23...	0.23...	56144.10...
261.441...	-26.974...	1927.30...	1464.95...	15.86...	0.10...	5	1	0.09...	107.59...	0.16...	0.16...	56144.10...
261.901...	-27.359...	1935.59...	468.53...	16.67...	0.21...	7	1	0.07...	76.47...	0.33...	0.33...	56144.10...
262.193...	-27.429...	1723.05...	1350.67...	16.04...	0.12...	8	1	0.27...	90.77...	0.23...	0.23...	56144.10...
261.834...	-26.873...	1493.90...	506.11...	15.81...	0.09...	10	-1	0.12...	-18.79...	0.14...	0.14...	56144.10...
262.107...	-26.916...	972.41...	1548.98...	15.20...	0.06...	11	-2	0.25...	-0.12...	0.08...	0.08...	56144.10...
261.767...	-26.425...	1265.92...	226.14...	8.25...	0.01...	13	-9	0.03...	-25.08...	0.01...	0.01...	56144.10...
262.131...	-26.513...	1737.31...	1355.41...	12.83...	0.01...	14	-1	0.04...	46.13...	0.01...	0.01...	56144.10...
262.495...	-26.856...	778.63...	210.48...	13.88...	0.02...	16	-1	0.09...	20.30...	0.03...	0.03...	56144.10...

considered. With two epochs I had to accept that I was limited by the quality of the worst epoch. With many epochs I need to consider the possibility of sources not being detected in poor quality epochs and produce a trade off between efficient source retention and rejection of bad data. For simplicity I am using STILTS to perform the actual epoch matching.

In an ideal world, all observations would be of the same high quality, detecting the same sources at each epoch. The simplest and most complete matching method would then be to match consecutive epochs, no sources would be lost and the proper motion detection limit is determined by the longest time baseline between any two consecutive epochs and the matching radius. With epochs of variable quality however, matching all epochs consecutively (either back and/or forward) to the highest quality epoch will lose all detections of a source past the first epoch in which it is not detected.

Initially I simply performed a match of all epochs to the highest quality (i.e. best seeing) epoch with a 1" radius. I adopted a 1" radius as P.W. Lucas (*priv. comm.*) found that when performing an internal match of crowded UKIDSS/VISTA catalogues a 1" matching radius typically returned only self matches whereas > 1" matching radii returned significant numbers of additional matches. The disadvantages of the straightforward match to the highest quality epoch were: *1*) If a source was not detected in the highest quality epoch (e.g. blended with a background source at only this epoch due to a high proper motion) then it would not be retained and the motion not calculated. *2*) The further in time the highest quality epoch is from other epochs the smaller the upper limit of proper motion detection.

To overcome these limitations I split the observations into groups based on epoch. These groups have smaller epoch baselines than the survey as a whole and a match of each group member to the highest quality epoch of its group with a 1" match radius therefore has a higher upper limit of proper motion detection. Matching between the highest quality epochs of consecutive groups without requiring a detection in all groups means I am not reliant on a detection in any single epoch. The drawback of this method was that the lack of a requirement of detection in all groups retained many poor quality sources, which increased the overall proper motion and parallax computation time of the pawprint as well as the matching time.

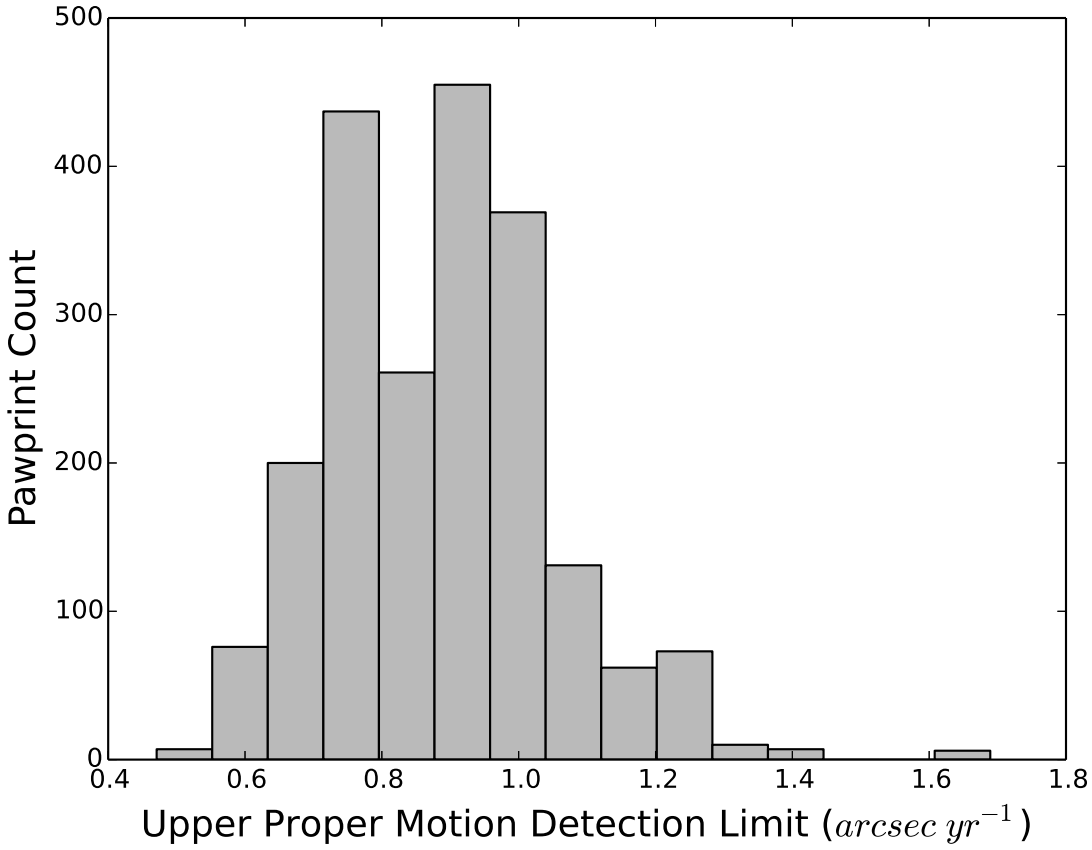

FIGURE 5.4: A histogram showing the distribution of the theoretical proper motion detection upper limits across all pawprints. Values are estimated as the matching radius (1") divided by the largest time separation between the highest quality epochs of consecutive epoch groups. This is an estimate since the random positional uncertainty of source detections varies the proper motion limit on a source by source basis.

I settled on a method which retains the group system, but requires a detection in the highest quality epoch of each group. This method, which is described in more detail below, sacrifices completeness for reliability. The lower completeness I plan to address through an alternate pipeline described in Section 5.10. Figure 5.4 shows the final upper limits on proper motion detection sensitivity obtained using this matching method.

In future it may be worth using initial proper motion results to attempt to recover sources in any missing epochs. It would then be possible to identify all unmatched sources and attempt to match between them and calculate a motion, perhaps including further iterations once well fitted motions are obtained and their detections removed from the pool.

5.4.1 Epoch Group Identification

I identify intervals between any two consecutive epochs greater than 90 days. These intervals define the start and end points of individual epoch groups. On occasion, groups containing few epochs are generated. Ultimately I require all sources to be detected in the highest quality observation of each group, the 'primary' epoch. The completeness of the catalogue is therefore limited by the quality of the worst primary epoch. Small groups are less likely to contain high quality primary epochs and may limit the completeness of the catalogue. To mitigate this, I require a minimum of 3 epochs per group. Any group containing fewer than 3 epochs is added to the nearest chronological group. This scenario most often occurs with the earlier observations. Epochs that are moved to the nearest group are flagged such that they should not be selected as the primary epoch of the new group, which could potentially lower the theoretical maximum proper motion detection. For example, if two 2010 observations are moved to the 2011 group and one of the two 2010 epochs were selected as the primary of the new group, this would leave an epoch baseline of approximately two years between the first (2010 + 2011) and second (2012) groups and would approximately halve the maximum possible proper motion detection.

5.4.2 Primary Epoch Selection

I select a primary epoch from each epoch group based on a number of criteria. First, a selection based on the ESO grade contained in the catalogue FITS header. Initially an ESO 'A' grade is required, however if fewer than 3 epochs have ESO 'A' grades then I accept 'B' grades in addition. I also reject epochs that have been included in the current group having being members of a rejected smaller group. If no epochs meet these two requirements then they are abandoned and I select from all epochs in the group. From here I identify any epochs with seeing equal to the best seeing in the current selection. Singular best seeing epochs are selected as the primary epoch.

An overall primary epoch is also selected following the same routine as above, independently of all epoch groups. For the purpose of this chapter the overall primary epoch will be referred to as P1, the individual epoch group primary epochs will be referred to as P2.

5.4.3 Epoch Match

Intra-group match I match all secondary epochs within an epoch group to their P2 epoch using successive 1" sky matches in STILTS. I require only that a source is present in the P2 epoch, a match to a secondary epoch source is not required and returns empty fields in the relevant secondary epoch columns.

Inter-group match I match each epoch group intra-matched table to the next chronological epoch group intra-matched table using 1" sky matches in STILTS. Each table is matched using the coordinates of its P2 epoch. I require each resultant row to contain a match only in every P2 epoch, matches in any secondary epoch are not required.

The match process essentially concatenates the relevant input catalogues (see Table 5.1 for an example) horizontally onto their P2 epoch catalogue and then horizontally concatenates the resultant intra-group matched tables. This process yields large fits tables consisting of many columns (specifically 13 $\times$ the epoch count). In cases of pawprints with large numbers of epochs I hit a 999 column limit for STILTS FITS files, where necessary I performed the intra-group matches using STILTS and the inter-group match within MATLAB to overcome this limitation.

5.5 Coordinate Transformation

5.5.1 Equatorial Tangent Plane Projection

In order to transform array coordinate positions on to the tangent plane of the equatorial system, the P1 epoch α and δ positions underwent a tangent plane projection conversion about the centre of the frame, producing ξ and η positions (2.2a and 2.2b).

5.5.2 Reference Source Selection

I select astrometric reference sources using the following criteria:

Position not within 6 pixels of the edge of the (dithered) array

$12.5 < Ks < 14.5$

Ks error < 0.05

Ellipticity < 0.3

Stellar morphological classification

I require a detection in every epoch and these criteria must be met by every epoch. The distribution of reference source counts is shown in Figure 5.5. If fewer than 200 sources in an array meet these criteria then I relax them somewhat. I still reject all sources within 6 pixels of the edge of the dithered array, but I require only the median magnitude and modal morphological classifications meet the same criteria as before. This also means a detection in every epoch is no longer necessary. If fewer than 200 sources meet these criteria then I reject the tile and queue for further analysis later, though in practice all arrays met these relaxed requirements. Where 200 or more sources meet the new relaxed criteria I grade sources based on the sum of the ellipticity rank and magnitude error rank. The rank is the sources position in the list of all sources, ellipticity and magnitude error for each source are the mean across all epochs. I then select the best 200 sources. In practice, 4.2% of arrays did not meet the stricter reference source criteria.

5.5.3 Coordinate Transformation

Array Coordinates I fit all P2 and secondary epoch array coordinate positions onto the P1 epoch array coordinate system using a second order polynomial (see Equation 2.1), the selected astrometric reference sources (Section 5.5.2) and the FITGEOTRANS function which is part of MATLAB's Image Processing Toolbox. I then transform all the P2 and secondary epoch array coordinates onto the P1 epoch array coordinate frame. In practice MATLAB does not allow a forward transformation from a 2D second order polynomial, so I actually fit the P1 epoch to the P2 and secondary epochs and use an inverse coordinate transformation provided by the TRANSFORMPOINTSINVERSE function (again, part of MATLAB's Image Processing Toolbox). I will refer to the new transformed array coordinates as X' and Y' hereafter.

To calculate the transformed X' & Y' uncertainties of an example source I add together in quadrature the RMS residual to the fit of the astrometric reference sources used and the original positional uncertainties of the example source.

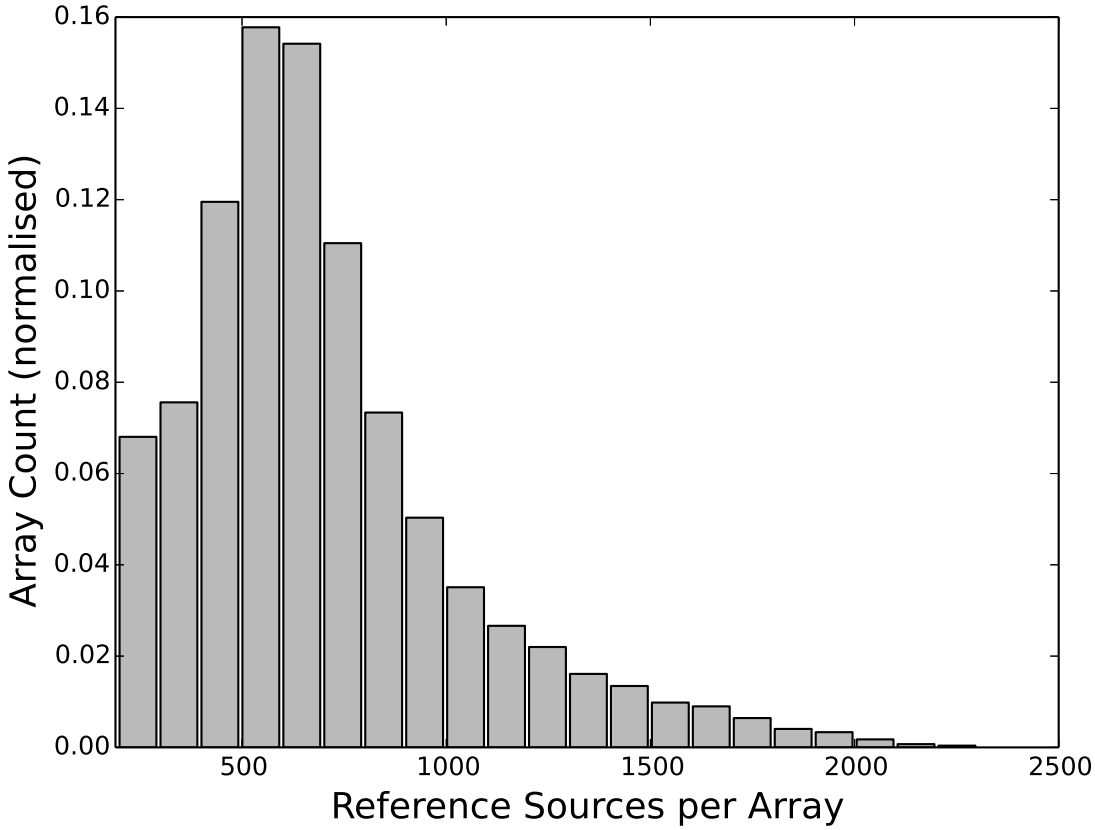

FIGURE 5.5: A histogram showing the distribution of the number of reference sources per array across all arrays that initially met the 200 reference source requirement (95.8% of all arrays).

Ideally, the procedure should remove the target source from its coordinate fit if it has been selected as an astrometric reference source, however, this greatly increases the number of fit and transformation procedures that must be made and hence the time to compute. In practice, the large number of reference sources (≥ 200, Figure 5.5) and low order polynomial fit means that any single source has a very limited affect on the fit. Ideally, I would also remove any reference sources which display a significant motion, but this requires two coordinate fit and transformation procedures, and crucially two motion calculation procedures. The motion calculation procedure is one of the most time consuming section of the pipeline so I did not want to have to run this twice if it were not necessary. I tested the removal of reference sources with significant motion ($> 1\sigma$) in the tile 'b389', which is a typical bulge tile containing a known high proper motion L dwarf with a measurable parallax (Beamín et al., 2013). I found a very slight increase in average proper motion and average uncertainty, but the difference was at the $\sim 0.04\sigma$ (few microarcsecond) level.

Equatorial Tangent Plane Coordinates I fit the array coordinates of all sources in the P1 epoch to their ξ and η coordinates calculated previously (Section 5.5.1) using the same images.geotrans.PolynomialTransformation2D function as before and a third order polynomial (see Equation 2.3). I then use the resultant fit to transform the P1 epoch array coordinates and the X' and Y' coordinates of all secondary epochs onto the P1 epoch equatorial tangent plane system.

Since the VVV observations are aligned to the Galactic plane there is a significant rotation angle to the equatorial plane (in contrast to the UKIDSS LAS and GPS observations). Propagation of array coordinate errors to equatorial tangent plane coordinate errors, even by transformation of the 1σ error box as in the UKIDSS pipeline (see Section 2.7) is not simple. It is also not hugely necessary, since ultimately the uncertainties on the proper motions come from the standard error of the robust regression (see Section 5.6). The coordinate error is used only for calculation of the χ^2 goodness of fit statistic. I therefore estimate the single dimensional tangent plane coordinate uncertainties as the mean of the X and Y transformed positional errors (in pixels) multiplied by the average pixel scale (0.339"/pixel).

5.6 Proper Motion Calculation

For every source I fit a linear model of the response in χ and η to time to measure the proper motions in $\alpha \cos \delta$ and δ respectively. I use the ROBUSTFIT function provided by the MATLAB Statistics Toolbox, a tool for performing a robust linear regression. ROBUSTFIT uses a least squares method of fitting with an iterative reweighting of the data points.

A standard least squares fit to a data set is ideal where the uncertainties on data points are known to be Gaussian. Our crowded field data are in some cases non Gaussian, for example blended stars and inhomogeneous observing conditions cause variations in the quality of each data point. For data with known non-Gaussian errors robust methods of fitting are useful. See e.g. 'Robust statistics: a method of coping with outliers' an Analytical Methods Committee Technical Brief from the Royal Society of Chemisty (2001) for more information. The improvement in accuracy for our data using a robust

regression technique over a standard least squares fit (in the context of a parallactic motion fit) is shown in Figure 5.6.

I use the default parameters for ROBUSTFIT, namely a bisquare weighting function, as described below:

$$w = (1 - r^2)^2 \text{ for } |r| < 1 \text{ else } w = 0$$

where:

$$r = \text{residual}/(\text{tune} \times s \times \sqrt{1 - h})$$

$$s = MAD/0.6745$$

$$\text{tune } = 4.685$$

MAD(median absolute deviation) is the median deviation from the median of the data

h is the epoch leverage value from a least-squares fit

see http://uk.mathworks.com/help/stats/robustfit.html

The proper motion of the source in each dimension is the linear gradient of the relevant fit. The uncertainty in the proper motion in each dimension is provided by ROBUSTFIT as a standard error and I calculate a χ^2 goodness of fit statistic in each dimension.

I also calculate more accurate χ and η coordinates at epoch 2012.0 from the fit coefficients. I then deproject these from the equatorial tangent plane to equatorial coordinates using the starlink code TP2S translated into MATLAB and the tangent point equatorial coordinates used for the original tangent plane projection.

5.7 Parallax Calculation

All sources with 5σ proper motion that are not within 6 pixels of the edge of the dithered array are selected as candidates for parallax ellipse fitting.

I deproject the source χ and η equatorial tangent plane coordinates to equatorial coordinates at every epoch using the starlink code TP2S translated into MATLAB and the tangent point equatorial coordinates used for the original tangent plane projection. I

then reproject all epoch equatorial coordinates to a new tangent plane using tangent point coordinates half way between largest and smallest α and δ source position. The new tangent plane coordinates of each point are equivalent to $\cos\delta_1(\alpha_i - \alpha_1)$ and $\delta_i - \delta_1$ (see Equation 5.1). The new tangent point equatorial coordinates are used for the calculations of $\widehat{N}$ and $\widehat{W}$ below.

Using the FIT function, part of MATLAB's Curve Fitting Toolbox, I perform a robust fit (bisquare weighting function, see Section 5.6) of parallactic motions in χ and η based on the equations from Kirkpatrick et al. (2011, Section 5.2, see Equations 5.1). The improvement in parallax fit accuracy using a robust regression technique over a standard least squares fit is evident in Figure 5.6.

$$\begin{aligned} \cos\delta_1(\alpha_i - \alpha_1) &= A + \mu_\alpha(t_i - t_1) + \pi_{trig}\overrightarrow{R}_i \cdot \widehat{W} \\ \delta_i - \delta_1 &= B + \mu_\delta(t_i - t_1) - \pi_{trig}\overrightarrow{R}_i \cdot \widehat{N} \end{aligned} \tag{5.1}$$

where:

$\widehat{N}$ is the local north unit vector

$\widehat{W}$ is the local west unit vector

$\overrightarrow{R}_i$ is the position vector of the observer (earth) at time i

A and B are constants

The CONFINT function, again part of the MATLAB Curve Fitting Toolbox, provides 1σ confidence intervals for the coefficients calculated by the fit function. The independent parallax values in χ and η are combined using a standard weighted average (Taylor, 1996):

$$\begin{aligned} x_{wav} &= \frac{\sum w_i x_i}{\sum w_i} \\ \text{and } \sigma_{wav} &= \frac{1}{\sqrt{\sum w_i}} \\ \text{where } w_i &= \frac{1}{\sigma_i^2} \end{aligned} \tag{5.2}$$

χ^2 goodness of fit statistics and improved epoch 2012.0 coordinates are calculated as in Section 5.6.

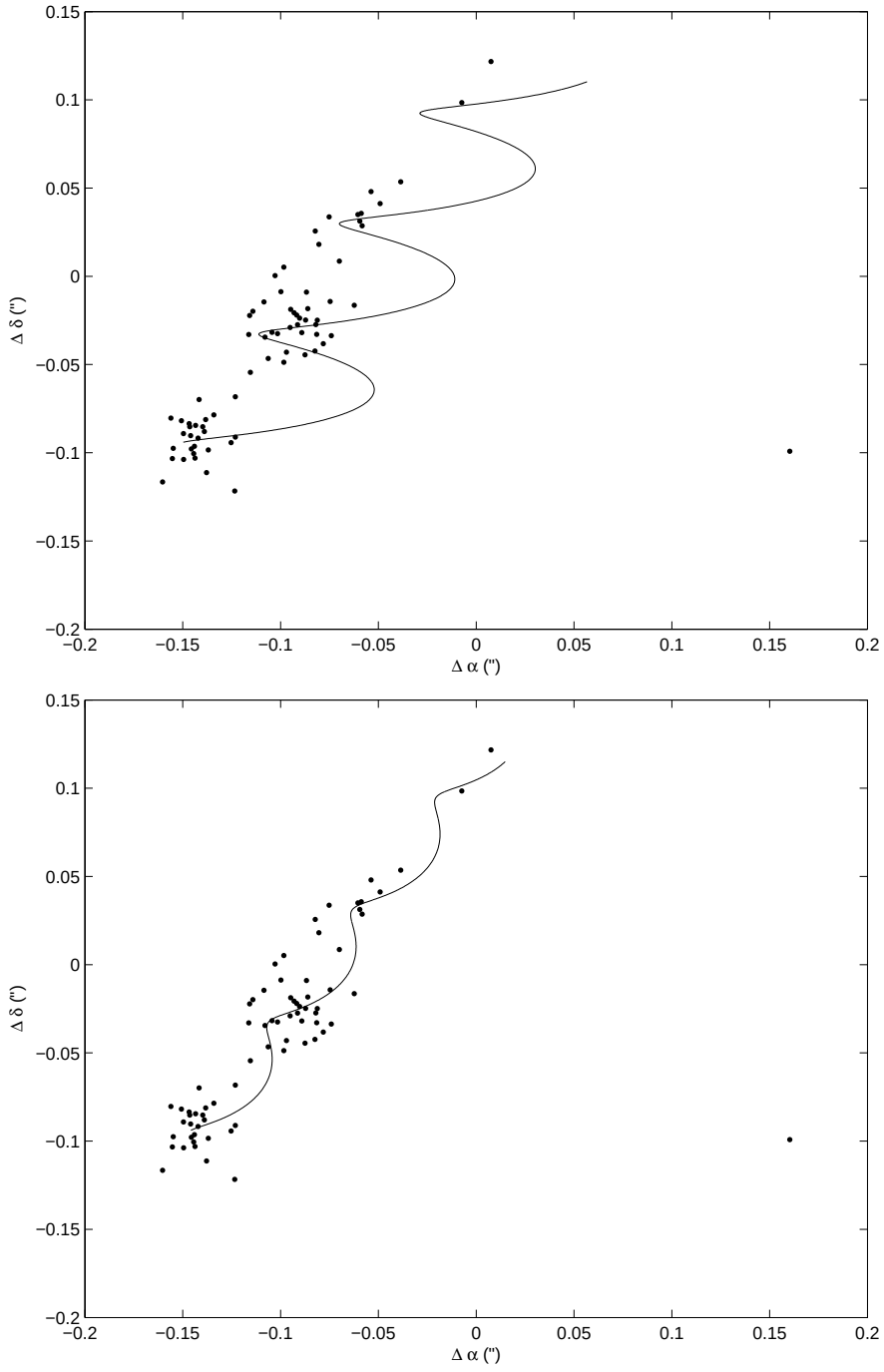

FIGURE 5.6: *Upper panel:* A standard linear least squares fit to all data points. An anomalous data point clearly carries more weight than it should, reducing the accuracy of the solution. *Lower panel:* A robust fit to all data points using a bisquare weighting function. The anomolous data point has a heavily reduced weight and does not greatly influence the solution. Note that this is an overall relatively poor quality, unremarkable parallax, it simply serves as a good example case for robust fitting methods.

5.8 Results Output

The pipeline outputs two results tables: one containing the proper motion fit results, effectively ignoring any results of the parallax fit; and a second containing results of the parallax fitting routine only, ie. only sources that were selected as parallax candidates and without proper motions from the proper motion only fit.

For both results tables I did not retain all columns (13 columns $\times$ the number of epochs plus columns calculated during the pipeline) in order to keep the final file sizes to a more manageable size. Columns created specifically to replace many removed from the output file are:

Median Ks band magnitude

Ks band magnitude error is standard deviation of the Ks magnitudes

A mean ellipticity

A modal morphological classification

The fraction of morphological classes equal to the mode

The X, Y and array extension numbers provided are of primary (P1) epochs only.

Tables 5.2 and 5.3 give example proper motion and parallax output tables respectively.

5.9 Pawprint Combination

Most of the ∼200 million VVV sources are contained within multiple pawprints. An average of the multiple measurements can be used to improve the final accuracy.

I group sources using STILTS, for example, using a 1" sky match marking groups of rows. Note that all source coordinates are provided at the same epoch, 2012.0. I reject all sources with poorly fit astrometry ($\chi^2_{red,\alpha} > 10$ and $\chi^2_{red,\delta} > 10$).

I then process each grouping, calculating new values of:

Equatorial coordinates: mean across all detections

TABLE 5.2: A sample of an output proper motion table, tile b201 pawprint 1. The table is split to fit to one page, line numbers are not present in the real output tables. Ellipses indicate where values have been truncated for the purpose of this document. α and δ are the equatorial coordinates of the source at epoch 2012.0 in decimal degrees. Ks is the median Ks band magnitude derived from the AperFlux2 values in the raw FITS file catalogue. σ_{Ks} is the standard deviation in Ks band magnitudes between observations. *Class* is the modal morphological classification flag (see description with Table A.1) between observations. *ClassFrac* is the fraction of observations which carry the *Class* value. *Ell* is the mean source ellipticity. *eNum*, X and Y are the array extension number [1-16], X coordinate and Y coordinate of the overall primary epoch frame. *ppID* is a pawprint identifier. *runNum* is a source identifier. *PM*, *PMRA*, *PMDE*, *ePM*, *etc* are the measured proper motions (total and individual) and their uncertainties, all are in units of *mas* yr^{-1}. *rX2RA* and *rX2DE* are the χ^2_{red} values in right ascension and declination respectively. *epochs* is the number of epochs for which the source has a measurement.

line	α	δ	Ks	σ_{Ks}	Class	ClassFrac	Ell	eNum	X	Y	ppID	runNum
1	270.757...	-42.324...	15.3...	0.1...	-1	0.8...	0.1...	2	1992.3...	1187.7...	12011	1829
2	271.391...	-42.623...	15.4...	0.1...	1	0.7...	0.1...	4	2034.2...	666.2...	12011	641
3	270.583...	-41.754...	15.5...	0.1...	-1	0.5...	0.1...	5	876.6...	1973.1...	12011	3767
4	271.202...	-42.096...	17.0...	0.1...	-1	0.7...	0.1...	7	1026.7...	1057.1...	12011	1880
5	270.853...	-41.600...	17.2...	0.1...	1	0.5...	0.1...	9	1991.4...	515.4...	12011	927
6	271.188...	-41.637...	15.8...	0.1...	-1	0.9...	0.1...	10	1593.6...	1406.1...	12011	2423
7	271.797...	-41.963...	16.3...	0.1...	-1	0.9...	0.1...	12	1602.7...	574.1...	12011	853
8	271.132...	-41.185...	16.9...	0.1...	1	0.7...	0.2...	13	1879.1...	1560.6...	12011	2881
9	271.670...	-41.505...	14.7...	0.0...	1	0.6...	0.3...	15	1410.4...	521.4...	12011	854
10	272.054...	-41.489...	15.8...	0.0...	-1	0.7...	0.1...	16	1128.4...	2103.3...	12011	2635

line	PM	PMRA	PMDE	ePM	ePMRA	ePMDE	rX2RA	rX2DE	epochs
1	8.2...	-2.7...	-7.7...	5.7...	3.5...	4.4...	0.8...	0.9...	42
2	6.7...	-4.7...	4.6...	8.0...	6.1...	5.2...	1.1...	0.7...	42
3	7.3...	-5.4...	4.9...	6.8...	5.5...	4.1...	1.4...	0.7...	43
4	27.6...	3.7...	27.3...	16.9...	12.2...	11.7...	0.9...	0.9...	39
5	8.6...	-1.4...	8.4...	16.6...	11.4...	12.1...	0.6...	0.8...	34
6	1.2...	1.2...	-0.3...	7.7...	5.3...	5.6...	1.0...	0.8...	43
7	11.7...	6.9...	-9.4...	6.6...	4.7...	4.6...	0.4...	0.5...	43
8	15.3...	0.3...	15.3...	25.7...	14.0...	21.5...	1.5...	4.1...	40
9	5.9...	3.5...	-4.7...	4.7...	2.7...	3.9...	0.6...	0.9...	43
10	4.8...	3.6...	3.2...	11.3...	8.9...	7.1...	0.9...	0.7...	41

TABLE 5.3: A sample of an output parallax table, tile b201 pawprint 1. The table is split to fit to one page, line numbers are not present in the real output tables. Ellipses indicate where values have been truncated for the purpose of this document. α and δ are the equatorial coordinates of the source at epoch 2012.0 in decimal degrees. Ks is the median Ks band magnitude derived from the AperFlux2 values in the raw FITS file catalogue. σ_{Ks} is the standard deviation in Ks band magnitudes between observations. *Class* is the modal morphological classification flag (see description with Table A.1) between observations. *ClassFrac* is the fraction of observations which carry the *Class* value. *Ell* is the mean source ellipticity. *eNum*, X and Y are the array extension number [1-16], X coordinate and Y coordinate of the overall primary epoch frame. *ppID* is a pawprint identifier. *runNum* is a source identifier. *PM*, *PMRA*, *PMDE*, *ePM*, *etc* are the measured proper motions (total and individual) and their uncertainties, all are in units of $mas\ yr^{-1}$. *plx*, *plxRA*, *plxDE*, *eplx*, *etc* are the measured parallaxes (total and individual) and their uncertainties, all in units of arc seconds. *rX2RA* and *rX2DE* are the χ^2_{red} values in right ascension and declination respectively. *epochs* is the number of epochs for which the source has a measurement.

line	α	δ	Ks	σ_{Ks}	Class	ClassFrac	Ell	eNum	X	Y	ppID	runNum	PM	PMRA	PMDE
1	270.563...	-42.245...	9.2...	0.6...	-9	0.7...	0.1...	2	265.5...	1203.4...	12011	1888	256.8...	-256.7...	6.5...
2	271.299...	-42.585...	14.4...	0.0...	1	0.7...	0.1...	4	1204.5...	695.8...	12011	682	24.6...	-4.7...	-24.1...
3	270.749...	-41.975...	13.9...	0.0...	-1	0.9...	0.0...	6	210.1...	532.8...	12011	831	14.4...	-8.9...	-11.3...
4	271.281...	-42.056...	17.1...	0.1...	1	0.9...	0.2...	7	1377.5...	1719.2...	12011	3084	714.4...	211.1...	682.5...
5	270.774...	-41.515...	12.4...	0.0...	-1	1.0...	0.1...	9	1014.3...	1018.9...	12011	1928	13.2...	8.9...	-9.7...
6	271.174...	-41.562...	15.6...	0.1...	-1	0.7...	0.1...	10	1127.1...	2054.1...	12011	3599	43.7...	-29.7...	-32.0...
7	271.682...	-41.915...	14.0...	0.0...	-1	1.0...	0.1...	12	565.7...	603.1...	12011	913	41.4...	-7.0...	-40.8...
8	271.106...	-41.146...	14.5...	0.0...	-1	0.9...	0.1...	13	1495.3...	1831.8...	12011	3388	28.3...	18.5...	-21.3...
9	271.630...	-41.502...	12.5...	0.0...	-1	1.0...	0.0...	15	1109.1...	409.6...	12011	651	24.0...	-7.0...	-23.0...
10	272.056...	-41.512...	12.8...	0.0...	-1	1.0...	0.0...	16	1261.5...	1886.7...	12011	2414	20.2...	20.1...	0.9...

line	ePM	ePMRA	ePMDE	plx	plxRA	plxDE	eplx	eplxRA	eplxDE	rX2RA	rX2DE	epochs
1	8.4...	5.4...	6.5...	0.036...	0.036...	0.018...	0.007...	0.007...	0.040...	4.8...	6.0...	43
2	3.7...	3.0...	2.2...	0.004...	0.001...	0.035...	0.003...	0.003...	0.013...	0.5...	0.3...	43
3	2.6...	1.8...	1.9...	0.002...	0.002...	0.002...	0.002...	0.002...	0.012...	0.3...	0.3...	43
4	94.9...	29.0...	90.3...	0.078...	0.076...	0.517...	0.037...	0.037...	0.614...	5.3...	59.7...	34
5	2.6...	1.5...	2.1...	0.001...	0.001...	0.014...	0.001...	0.002...	0.013...	0.5...	0.4...	43
6	7.1...	5.3...	4.6...	0.003...	0.002...	0.013...	0.006...	0.007...	0.029...	1.0...	0.7...	43
7	3.4...	3.0...	1.6...	0.003...	0.002...	0.011...	0.003...	0.003...	0.010...	0.7...	0.2...	43
8	3.2...	2.1...	2.4...	0.002...	0.001...	0.015...	0.002...	0.002...	0.016...	0.3...	0.6...	43
9	3.1...	2.2...	2.2...	0.006...	0.006...	0.000...	0.002...	0.002...	0.014...	0.4...	0.4...	43
10	3.7...	3.1...	2.0...	0.002...	0.001...	0.010...	0.003...	0.004...	0.013...	0.5...	0.3...	43

Ks magnitude: weighted average across all detections

Morphological classification: the classification of the pawprint with the highest modal fraction

Ellipticity: the mean ellipticity across all detections

The total number of epochs

Weighted average proper motions

Weighted average parallax measurements

I also return pawprint identifiers, array extension numbers, X and Y coordinates and $\chi^2_{reduced}$ values of all pawprints, the number of allocated columns in the output file allows for a detection in up to 6 pawprints. All weighted averages and associated uncertainties were calculated using Equation 5.2.

Creation of a proper motion catalogue using pawprints combined in this way which reaches down to 0 $mas\ yr^{-1}$ is not trivial. An initial internal match of a single table containing all 446,219,025 output rows is quite a job even for STILTS. Such a large match is not entirely necessary if it can be split into many smaller matches of only overlapping pawprints. In principle this is straightforward but consideration must also be given to the fact that two opposite edges of each tile overlap with a different tile so a list of all overlapping pawprints across all tiles is needed. Currently I am only able to create smaller catalogues based on a subset of the full results set. For example, an area of the sky of particular interest, or a subset containing proper motions above some minimum value.

5.10 High Proper Motion Extension

5.10.1 Rationale

The requirement that all sources be detected in every P2 epoch means that the detection of faint sources is limited by the quality of the worst P2 epoch. Also, high proper motion sources will go undetected if their motion brings them in front of a background source in any of the P2 epochs. The chance of this occurring increases with the proper motion

and hence the method described above (referred to as the LPM method hereafter) is less sensitive to the highest proper motion sources.

5.10.2 High Proper Motion Method

To regain some sensitivity to very high proper motion sources I use a modified method (hereafter referred to as the HPM method), which relies on the ability to measure a motion based on a subset of the epochs with a baseline of only a few months. Clearly, such a measurement is much less precise than using all epochs and will yield many false positives. However, multiple such groups of epochs are available across the 4-5 years of VVV observations and this is compounded when multiple overlapping pawprints are also taken into account. A low precision, low reliability detection becomes more trustworthy if it can be identified in multiple groups.

To generate groups of epochs I again identify intervals between consecutive epochs greater than 90 days, I then place a number of further requirements on each epoch group. Initial testing indicated that groups with very short epoch baselines or small numbers of epochs were too unreliable, so I reject groups containing fewer than 5 epochs or with an epoch baseline less than 2 months (1/6th of 1 year in practice). I also split groups of epochs that are much larger than necessary, since more groups of epochs mean a greater chance of detection. If a group has an epoch baseline greater than 1/2 of a year, it is split into two groups down the chronological midpoint. In order to retain these two groups I require them both to have epoch baselines greater than 1/4 of a year and also contain 5 or more epochs. If these requirements aren't met then the two groups are rejoined.

From this point on I select a primary (P2) epoch as before, which in this case also functions as the overall primary (P1). I then source match the epochs in the group independently of any other epoch groups, using only the intra-group match as described above. The coordinate transformation and proper motion measurement methods remain the same and I do not attempt a parallax calculation at this stage.

From the proper motion results I select the most promising candidates:

$\mu > 200\ mas\ yr^{-1}$

$\chi^2_{red} < 3$ in α and δ

$\mu > 3\sigma$

and save these for further analysis. I now have *relatively* low precision positions and proper motions, which I use to attempt a recovery of the source (the closest detection within 1" of the expected position) in every epoch of the relevant pawprint. I now add the source to the matched catalogue used for the low proper motion run and measure a more precise proper motion and parallax using the same low proper motion method.

Section 6.4 shows the efficacy of this high proper motion detection procedure. Of order 120 sources with $\mu > 200$ $mas\ yr^{-1}$ have been identified that were missed by the low proper motion pipeline.

5.11 Improved Astrometry

5.11.1 Rationale

The standard single pawprint proper motion and parallax pipeline is a trade off between reliability and accuracy, and speed. A number of techniques could have been implemented which would have improved the astrometric precision to a degree ('local' solutions for example, see Figure 2.2). However, implementation of these would require a considerable amount of extra processor time.

5.11.2 A More Accurate Pipeline

I wrote a routine to calculate proper motions and parallaxes which benefits from a number of improvements over the standard method, but which is much slower to run and hence is not suitable for survey scale implementation. This method is run on a single source basis; this description uses an example target source. First I identify the two pawprints in which the target source is furthest from the edge of its array. A source may be present in more than two pawprints, but in these it will typically be close to the edge of the array, where the astrometry is less precise. To recover the source reliably in each epoch of the two pawprints I require a position, a proper motion, a pawprint identifier for each of the two pawprints and their corresponding array extension numbers.

I recover the source by searching in each epoch for the closest object (within 1") of the expected position of the target, taking into account its proper motion. The main advantage of this method is that no single epoch is required in order to calculate a solution. This is more reliable than the standard LPM pipeline matching method for example, which requires a detection in each 'P2' primary epoch.

To produce a table of reference sources I match together the two relevant pawprint catalogues generated during the LPM run using their P1 epoch coordinates. Since I ultimately want to reject reference sources with large motions, it does not matter if the two P1 epochs are separated by a large time baseline though this is unlikely. I still require an overall primary epoch for use as the standard reference epoch, for this I use the P1 epoch of the pawprint in which the target is furthest from the edge of the array.

I perform the standard tangent plane projection of the overall primary epoch and make an initial rejection of reference sources. I relaxed the initial reference source selection criteria based on some preliminary testing on tile b389, which indicated that relaxed cuts (and hence a larger reference source pool) produced marginally more accurate motions.

Position not within 6 pixels of the edge of the (dithered) array

$12.5 <$ median $Ks < 16.0$

Ks standard deviation < 0.15

Mean ellipticity < 0.3

Stellar in $> 75\%$ of detections

Detected in every epoch

After applying these cuts I then select reference sources from a radius sufficient to ensure there were at least 50 in each quadrant, or 60", whichever is largest. If any quadrant contains fewer than 50 reference sources total, as can be the case if the target is close to the edge of an array, I proceed with the parallax measurement only on the condition that there are at least 50 reference sources in total. Relaxing photometric and morphological criteria provided a larger pool of initial reference sources. Ultimately my only concern is that a reference source is reasonably static and well centroided. To ensure this I employ a method of reference source rejection based on iterative coordinate fitting and

transformation and robust proper motion calculation. I reject reference sources that are poorly fit ($\chi^2_{red} > 1.5$ in α or δ), exhibit large proper motion ($\mu > 2\sigma$) or large proper motion uncertainty ($\sigma_\mu > 20\ mas\ yr^{-1}$) until the total number of reference sources remains the same between two iterations.

Once I have made a suitable selection of reference sources I perform a final coordinate transformation and then perform a robust fit to Equations 5.1 to produce a proper motion, parallax and epoch 2012.0 position. Figure 5.7 shows the improvements in parallax accuracy for 1,065 sources (see Section 6.2.3) over the best LPM based parallax (i.e. the one from the pawprint with the lowest uncertainty) and the weighted average of parallax measurements across all pawprints. For these sources the mean parallax uncertainties are 1.5, 3.0 and 2.2 *mas* for the improved parallax measurements, best LPM measurements and average LPM measurements respectively.

5.11.3 Further Improvements to Parallax Pipeline

Improvement in compute time can be achieved through a more efficient production of reference source candidates (eg. match independently of STILTS at the target recovery stage). The current pipeline was intended for use on a relatively small number of single objects and hence reading the entire matched catalogue every time. It now appears it would be worth running on several thousand (perhaps tens of thousands of) objects, i.e. many per pawprint. This means a great improvement in speed could be obtained by implementing a more efficient batch processing system.

Despite the use of robust fitting methods it would still be advantageous to reject bad data wherever possible. Blended detections or even simple misidentifications could be removed from the fit by rejecting individual epoch detections with significant deviation from the target median magnitude.

A more robust reference source pool may be generated by rejecting sources based on a parallax solution as well as proper motion. Sources with large parallaxes but low proper motions could negatively influence the final parallax solution, although in practice these will be uncommon and overwhelmed by the larger number of distant sources. It may be possible to reject reference sources with photometric distance estimates which place them nearby.

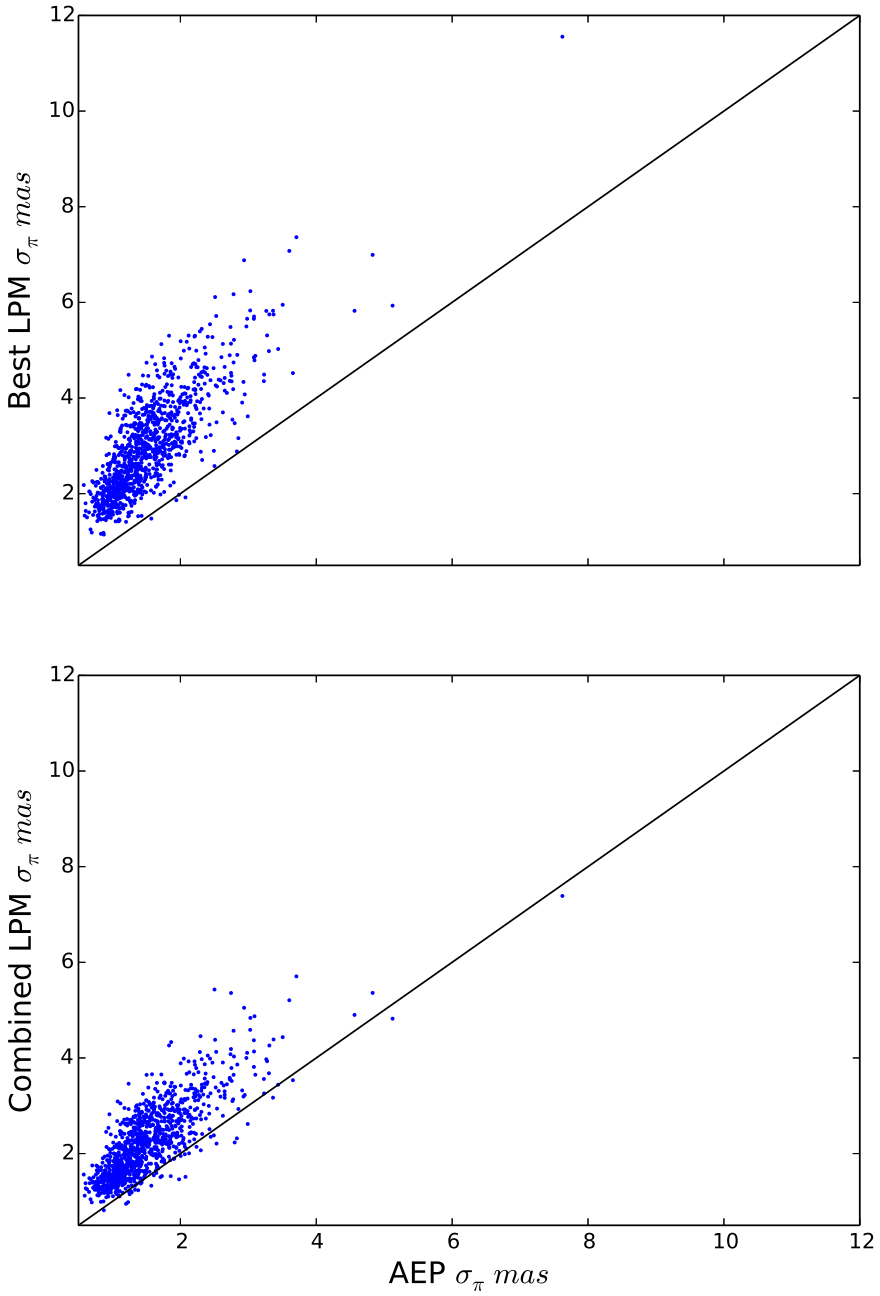

FIGURE 5.7: *Upper panel:* Five σ parallaxes from the more accurate pipeline (*AEP*, 1,065 sources, see also Section 6.2.3) compared to the best *LPM* measurement from any single pawprint. *Lower panel:* The same *AEP* parallaxes compared to the weighted average *LPM* parallax measurement from all pawprints. This pipeline produces parallaxes with lower statistical uncertainties.

Overall accuracy may be improved by producing a parallax measurement using the improvements made to the reference source selection in all (up to 6) pawprints separately and then combining them with a weighted average. A source will be in very different positions in the focal plane between pawprints and a simple second order polynomial

may not be sufficient to correct non-uniformity between these positions. However, one big advantage of one solution from all pawprints is a larger number of data points allows the robust fit to more reliably identify outliers.

I should investigate the effect of resizing the reference source selection radius based on the results of the iterative removal of reference sources with large residuals.

It may be the case that a well fit or accurate parallax measurement is not possible for a source due to one of a number of factors (e.g. significantly sub-optimal epoch distribution). For these sources it will still be possible to improve on the LPM proper motion measurement using all the reference source selection methods of the better parallax pipeline if it is fit independently of the parallax.

Chapter 6

The VVV Proper Motion and Parallax Catalogues

6.1 Introduction

The VVV is a public ESO near-infrared survey of 560 deg^2 of the southern Galactic plane and bulge using the wide-field VIRCAM on the VISTA telescope at Paranal observatory in Chile. The high source density in the Galactic plane complicates the identification of sources which have moved in between observations. The VVV data are multi-epoch, each source is observed between 50 and 150 times in the space of the ∼5 year survey. This means that high proper motion sources can be tracked over the relatively short baselines between epochs (days-months), but the overall ∼5 year epoch baseline allows accurate motion calculation. While the science goals of the VVV survey are dominated by the study of variable stars it is the identification of high proper motion objects in which I am interested, as well as the general production of proper motion data useful in pursuing other science goals.

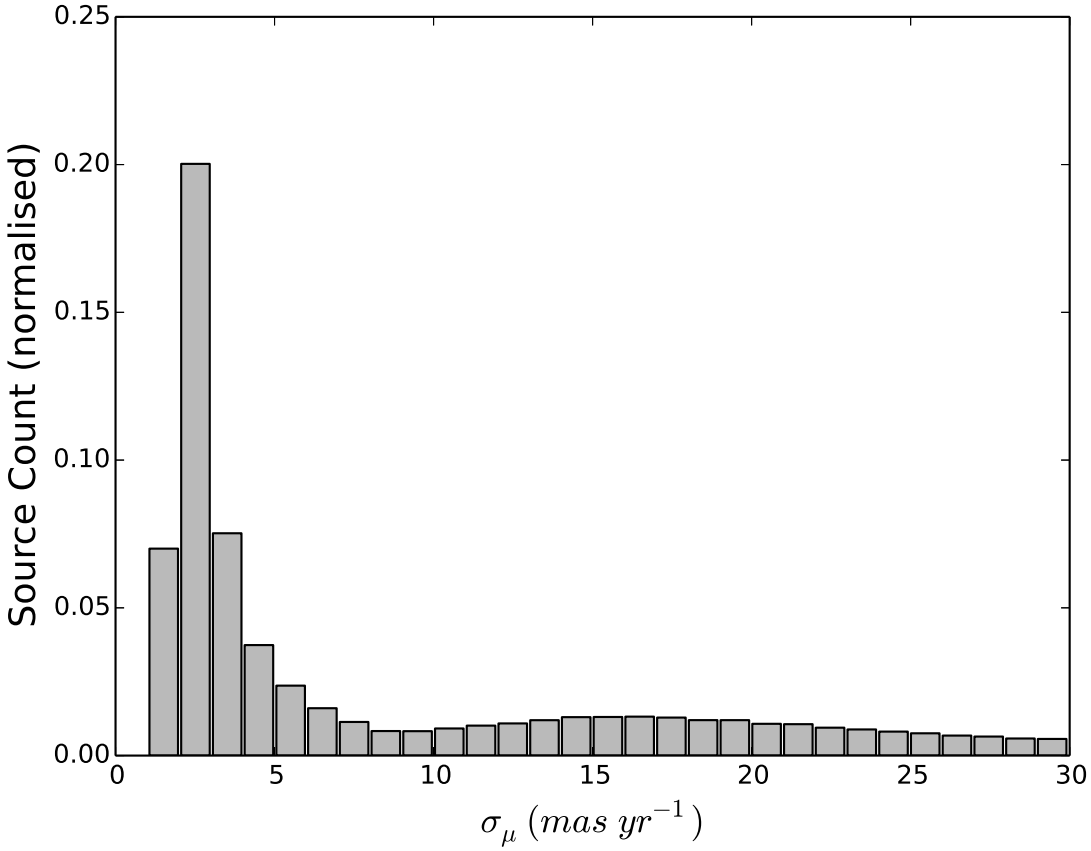

FIGURE 6.1: A histogram showing the distribution of weighted average proper motion uncertainties for sources with proper motion greater than 30 $mas\ yr^{-1}$. These are results of the LPM pipeline only. The trough at approximately 8 $mas\ yr^{-1}$ suggested a convenient maximum proper motion uncertainty cut at 10 $mas\ yr^{-1}$ was reasonable to limit the number of spurious proper motion entries. Note that the histogram was truncated at $\sigma_\mu = 30\ mas\ yr^{-1}$, the tail extends to 826 $mas\ yr^{-1}$. The lowest σ_μ is 1.07 $mas\ yr^{-1}$

6.2 Results

6.2.1 Proper Motion Catalogue

I generated a proper motion catalogue containing 62,536 sources from the standard 'LPM' pipeline detected in multiple pawprints. I require each detection have $\chi^2_{red,\alpha} < 10$, $\chi^2_{red,\delta} < 10$, and $\mu - \sigma_\mu > 30\ mas\ yr^{-1}$ and consistent proper motion and Ks magnitude. I also require weighted average proper motion greater than 30 $mas\ yr^{-1}$ and the uncertainty on the weighted average proper motion less than 10 $mas\ yr^{-1}$, see Figures 6.1 and 6.2.

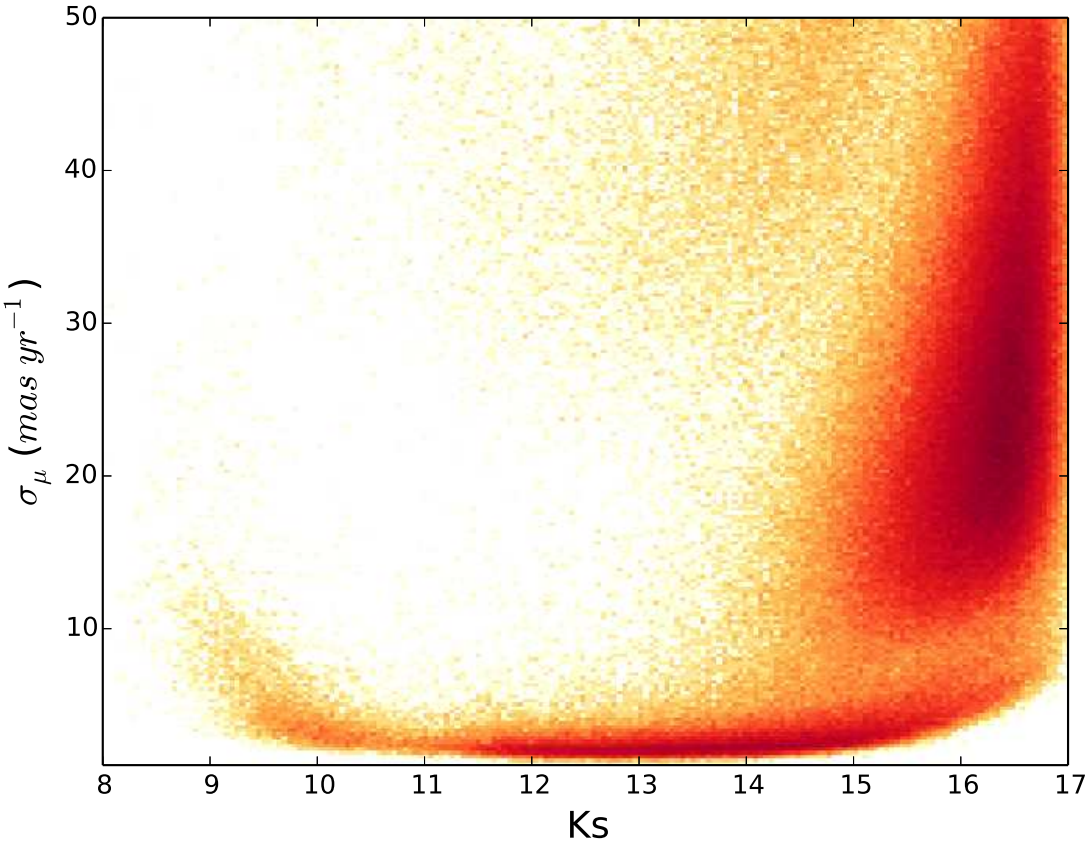

FIGURE 6.2: A density map of the distribution of weighted average proper motion uncertainties for sources with proper motion greater than 30 $mas\ yr^{-1}$ versus their Ks band magnitudes. Dark red indicates regions of higher density. These are results of the LPM pipeline only. Two distinct groups are visible separated at around 8 $mas\ yr^{-1}$, though a cut at 10 $mas\ yr^{-1}$ includes more of the better data at the faint end.

The Ks band magnitude vs. proper motion distribution of the $\mu > 30\ mas\ yr^{-1}$ catalogue is shown in Figure 6.3.

I note that this selection suffers from a number of incompletenesses, both inherent to the LPM proper motion pipeline and to the method of calculating the weighted averages of multiple pawprints. However, due to the requirement of a detection in multiple pawprints it is also a reliable sample. Incompleteness introduced as a result of the LPM pipeline will be reduced in due course by the HPM pipeline.

6.2.2 Photometry Acquisition

I acquired the VVV DR2 photometry for the $\mu > 30\ mas\ yr^{-1}$ sources via the VSA CrossID tool. I requested the nearest object only from the VVV source table within 5”

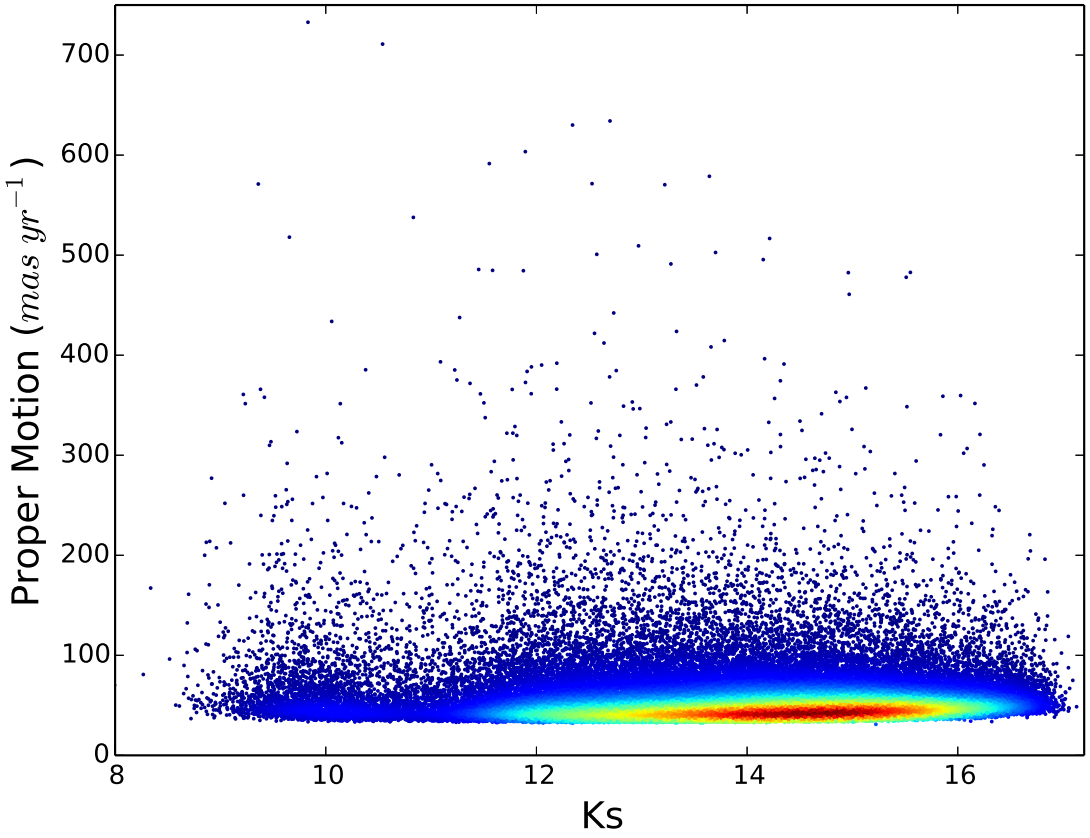

FIGURE 6.3: The Ks band magnitude versus proper motion distribution of the $\mu > 30\ mas\ yr^{-1}$ sample. These are results of the LPM pipeline only. The colour of the points indicates density, where redder means higher density.

of the epoch 2011.0 position of each proper motion source. Epoch 2011.0 is closer to the Y, J, and H band observations made near the start of the survey but usually before 2012.0. The VVV source table is crossmatched between passbands using a 1" matching radius. The highest proper motion source in this selection is 733 $mas\ yr^{-1}$ and should therefore be identified well between the observations.

6.2.3 Accurate Parallaxes

I ran a $\mu > 100\ mas\ yr^{-1}$ selection of 3,970 sources through the more accurate parallax routine. This yielded 1,065 parallaxes with $\chi^2_{red,\alpha} < 1.5$, $\chi^2_{red,\delta} < 1.5$, and $\pi > 5\sigma$. Figure 6.4 shows the proper motion versus parallax distribution of this sample and suggests that many more could be obtained by extending the selection to lower proper motions. Running the entire $\mu > 30\ mas\ yr^{-1}$ may yield a few thousand more.

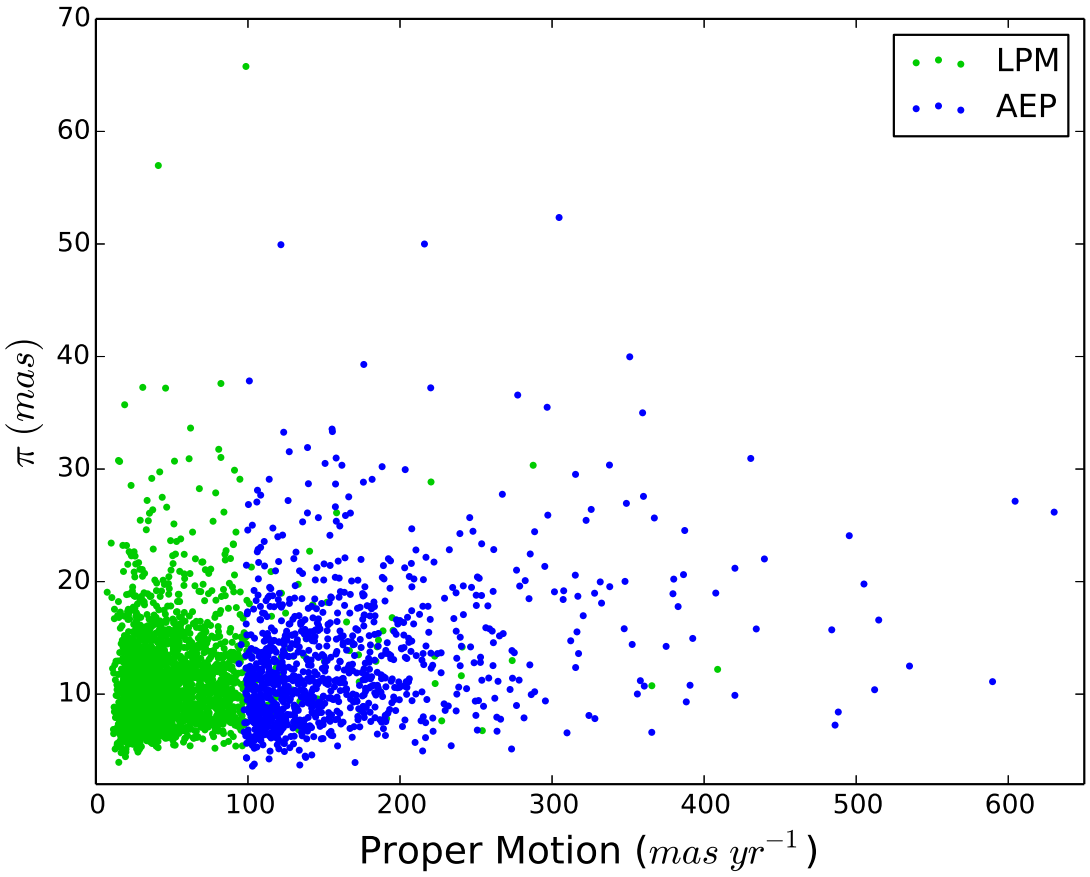

FIGURE 6.4: Proper motion versus parallax for the 1,065 well fitted 5σ parallaxes from the more accurate $\mu > 100$ *mas* yr^{-1} selection (*AEP*, blue) and the 2,338 5σ parallaxes obtained by combination of the LPM pipeline pawprint parallaxes (*LPM*, green).

6.2.4 Low Proper Motion Parallaxes

Single pawprint parallaxes for any source with a 5σ proper motion are also measured as part of the LPM pipeline (see Section 5.7). Combination of the multiple pawprints covering each source using a method similar to the one described in Section 5.9 yielded 2,338 5σ parallaxes in addition to the 1,065 5σ parallaxes obtained from the $\mu > 100$ *mas* yr^{-1} selection run through the more accurate parallax pipeline (Section 6.2.3). Figure 6.5 shows the distribution of parallaxes versus absolute Ks band magnitudes for the 3,403 5σ parallaxes.

6.2.5 Validating the Parallaxes

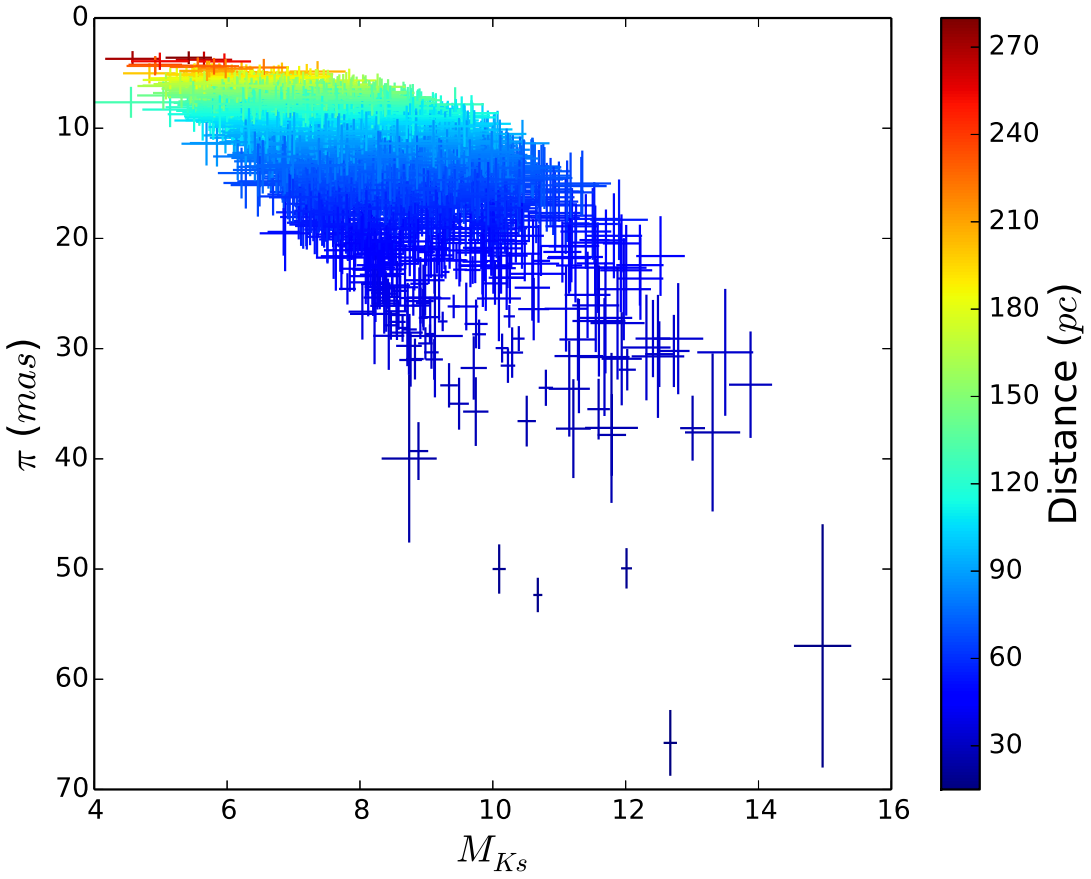

FIGURE 6.5: Absolute Ks magnitude versus parallax for the 3,403 5σ parallaxes from the AEP parallax pipeline and through combination of the LPM pipeline pawprint parallaxes.

Rojas-Ayala et al. (2014) identified 23,245 M dwarfs in VVV tile b201 at a range of distances using well calibrated M dwarf selections, and provide a reasonably accurate subtype calibration based on VVV near infrared colours. Their table 2 also provides absolute Ks magnitudes for each spectral subtype M0 through M9.

Using the Rojas-Ayala et al. (2014) M dwarf selection critera:

$0.336 < (Y - J) < 0.929$;

$0.952 < (Y - H) < 1.544$;

$1.100 < (Y - Ks) < 1.969$;

$0.432 < (J - H) < 0.727$;

$0.642 < (J - Ks) < 1.051$;

$0.045 < (H - Ks) < 0.438$.

I find 1,740 M dwarf candidates among the 2,909 sources with 5σ VVV parallaxes and DR2 photometry in the Y, J, H and Ks bands. From these I select only those 817 with parallaxes which place them within 100pc, to reject sources with possible reddening.

I estimated M subtypes for the M dwarf candidates using Rojas-Ayala et al. (2014) equation 1:

$$\begin{aligned} M_{subtype} = {} & 5.394(Y-J) + 4.370(Y-J)^2 \\ & + 24.325(Y-K) - 7.614(Y-K)^2 \\ & + 7.063(H-K) - 20.779 \end{aligned} \tag{6.1}$$

I then used Rojas-Ayala et al. (2014) table 2 to provide absolute Ks band magnitudes for the candidates. I performed a standard linear least squares fit to model the M spectral subtype to absolute Ks magnitude relation, see Figure 6.6. I note that there is some deviation from a straight line but the relation is still approximated well enough for my purposes, especially given the inherent uncertainty in spectral subtypes inferred photometrically.

Figure 6.7 compares the resultant absolute Ks band magnitudes of the sample based on the photometric estimation and VVV parallax based direct measurement. The Pearson product-moment correlation coefficient (Pearson's r) of these data is 0.40, which indicates only a mild correlation. This is perhaps unsurprising given the inherent uncertainty in the photometric spectral types of this sample and that there has been no treatment of multiple systems. There has also been no attempt to correct for Lutz-Kelker bias (Lutz and Kelker, 1973). These parallaxes are technically relative to the reference stars used though this is unlikely to contribute greatly to the scatter due to the large distances to most objects (and hence the reference stars) in the Galactic plane. The selections of sources with $> 10\sigma$ parallaxes and the extended rejection of sources within 2° of the Galactic plane are more encouraging, with Pearson's r values of 0.65 and 0.71 respectively. Sources in the plane are known to suffer from a relatively poor Z and Y calibration due to interstellar extinction[1], though Z is not used for this exercise.

[1] see http://www.eso.org/sci/observing/phase3/data_releases/vvv_dr4.pdf

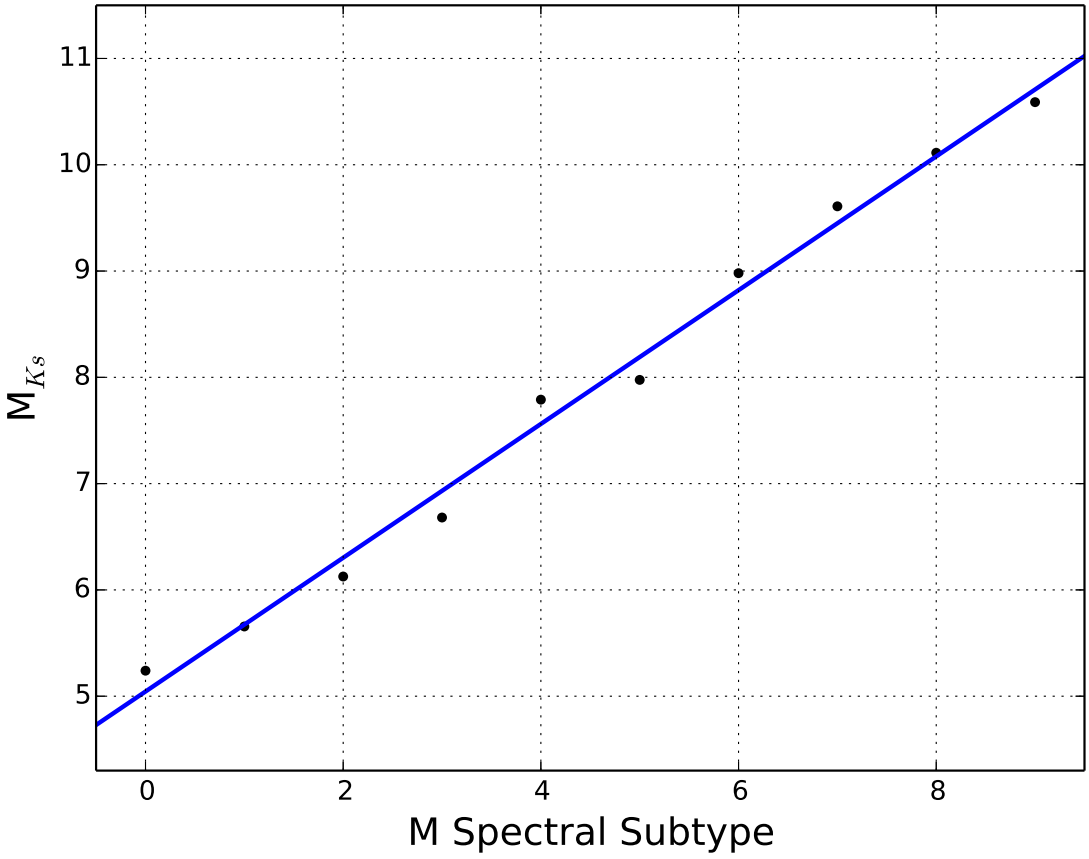

FIGURE 6.6: The straight line fit between the values of M dwarf spectral subtype and M_{Ks} given in table 2 of Rojas-Ayala et al. (2014).

6.3 Discoveries

6.3.1 Solar Neighbourhood Objects

Table 6.1 shows four objects initially placed at a distance of less than 25 parsecs. A fifth object was also placed within 25pc by the lower precision LPM parallax results but further analysis placed it at over 25pc (see below). Here I present further details and analysis of these five objects. Figure 6.8 shows these four sources on a near infrared HR diagram.

VVV J141159.32-592045.7

VVV J141159.32-592045.7 (J1411-5920 hereafter, 14.8 ± 0.3 *pc*) falls in the white dwarf locus of Figure 6.8. There are no entries in the SIMBAD database within 2' of the

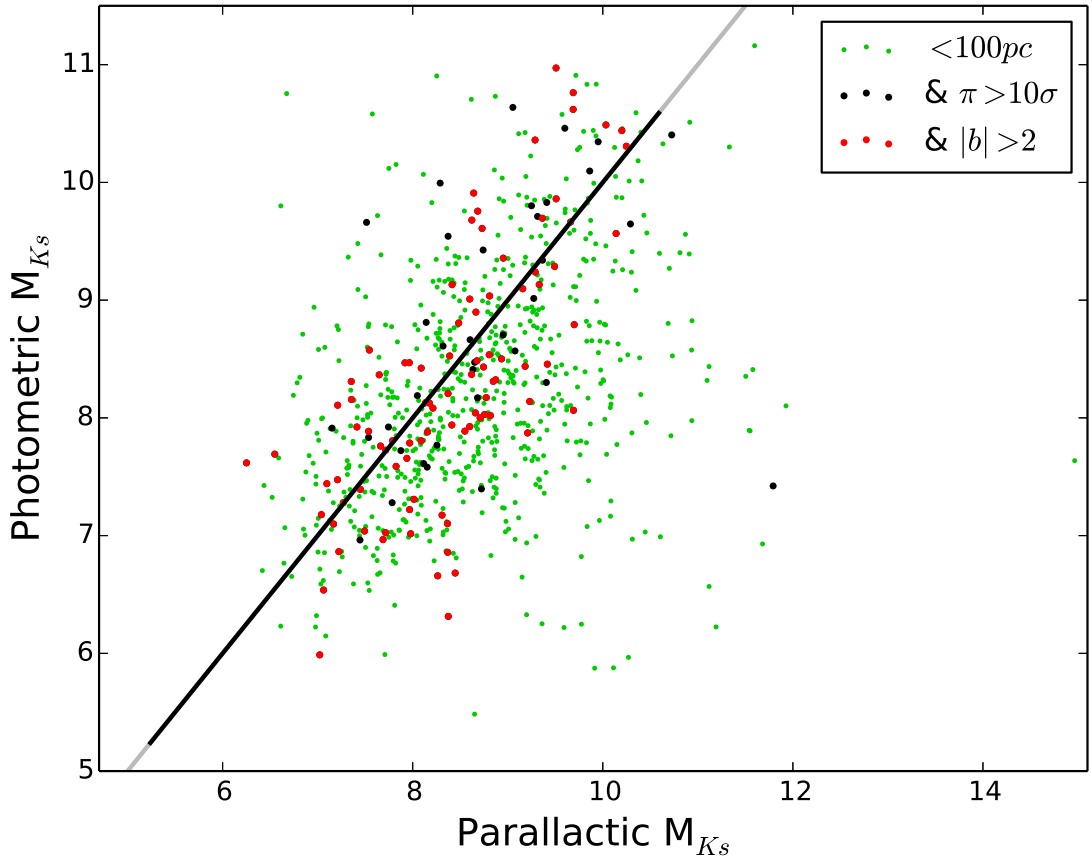

FIGURE 6.7: A comparison of absolute Ks band magnitude based on the VVV parallax measurement and a photometric estimation of spectral type using the method descibed in Rojas-Ayala et al. (2014). I have included the $X = Y$ line for clarity, which is black in the M_{Ks} range covered by Rojas-Ayala et al. (2014) and grey outside it. Green points are the 817 M dwarf candidates within 100pc, blue points are the selection within 100pc with 10σ parallaxes and red points are the selection within 100pc with 10σ parallaxes and more than 2° from the Galactic plane.

position of J1411-5920 but I have confirmed its proper motion through visual inspection of a sample of the VVV images. This source is consistent with a pure-H white dwarf of between 6000 and 9000 Kelvin, or a pure-He white dwarf of between 5000 and 7500 Kelvin based on tables of absolute magnitudes and near infrared colours for pure-H and pure-He white dwarfs (tables 13 and 14 respectively) of Hewett et al. (2006). For a pure-H white dwarf, a 6000-6500 Kelvin object is the best fit, with Y-J, H-K and absolute K mag in agreement. For a pure-He white dwarf a 7000 Kelvin object is the best fit, with J-H, H-K and absolute K mag in agreement. Z-Y is also close. The discrepancies in the remaining colours of either flavour of white dwarf could be explained if the object is of mixed composition, or indeed differs in surface gravity to that used to generate the model spectra from which these colours were derived ($log\ g = 8$). A fit of the available

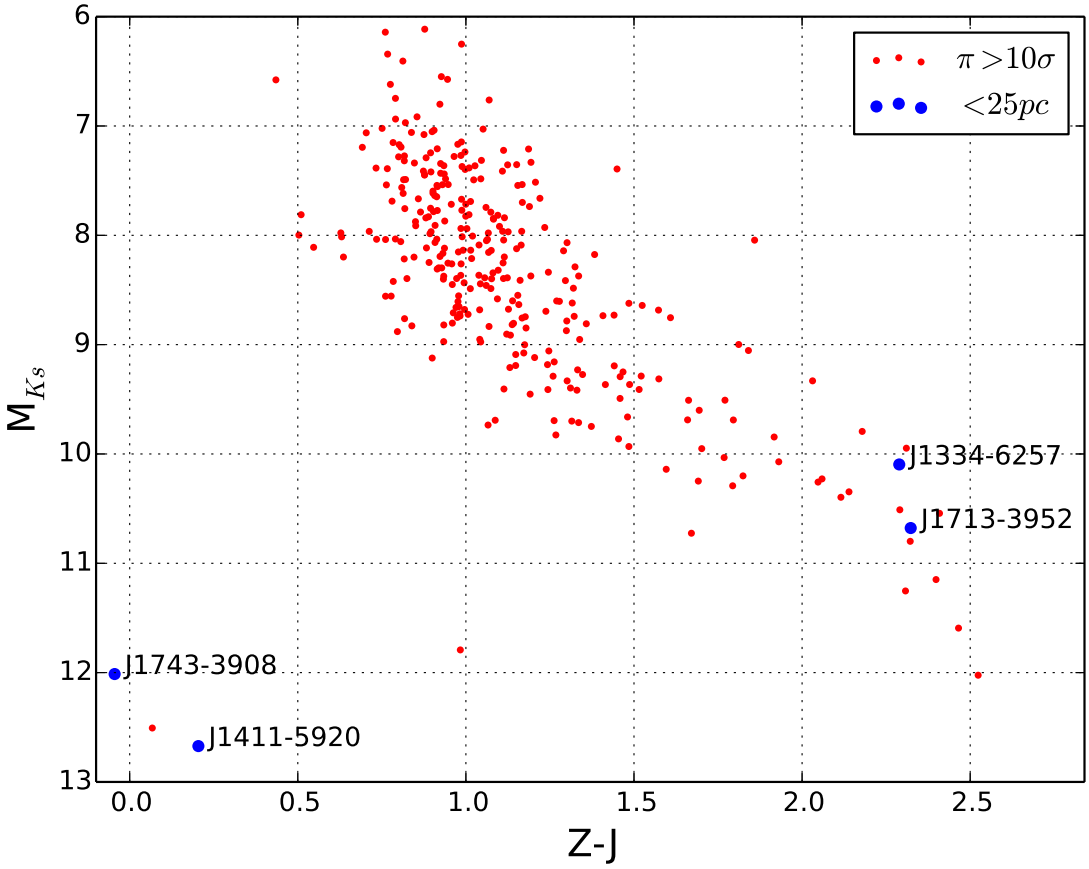

FIGURE 6.8: A near infrared HR diagram of all sources with 10σ parallaxes and the four sources with initial parallaxes that placed them within 25pc.

TABLE 6.1: The four sources from the low proper motion pipeline and accurate parallax samples with parallaxes that place them within 25pc. Positions are given at epoch 2012.0, proper motions are in units of $mas\ yr^{-1}$ and parallaxes are in units of mas. Photometry is that of the WSA VVV DR2 source table. Distances (d) are in units of parsecs. I adopt 0.02 magnitudes as a baseline uncertainty on all photometry.

	1411-5920	1713-3952	1334-6257	1743-3908
α	14 11 59.32	17 13 40.61	13 34 27.66	17 43 49.16
δ	-59 20 45.7	-39 52 15.2	-62 57 35.9	-39 08 25.4
$\mu_\alpha \cos\delta$	82.8±1.1	112.3±0.8	-214.4±1.4	-110.9±1.1
μ_δ	-52.2±1.2	-283.2±1.0	-27.2±1.2	50.1±1.1
π	67.4±1.5	52.4±1.6	50.0±2.2	49.9±1.8
Z	13.94±0.00	15.60±0.01	14.75±0.00	13.52±0.00
Y	13.96±0.00	14.43±0.00	13.58±0.00	13.51±0.00
J	13.74±0.00	13.28±0.00	12.46±0.00	13.57±0.00
H	13.64±0.00	12.61±0.00	12.52±0.00	13.63±0.00
Ks	13.58±0.01	12.08±0.00	11.60±0.00	13.52±0.01
M_{Ks}	12.72±0.10	10.68±0.07	10.10±0.10	12.01±0.08
d	14.8±0.3	19.1±0.6	20.0±0.9	20.0±0.7

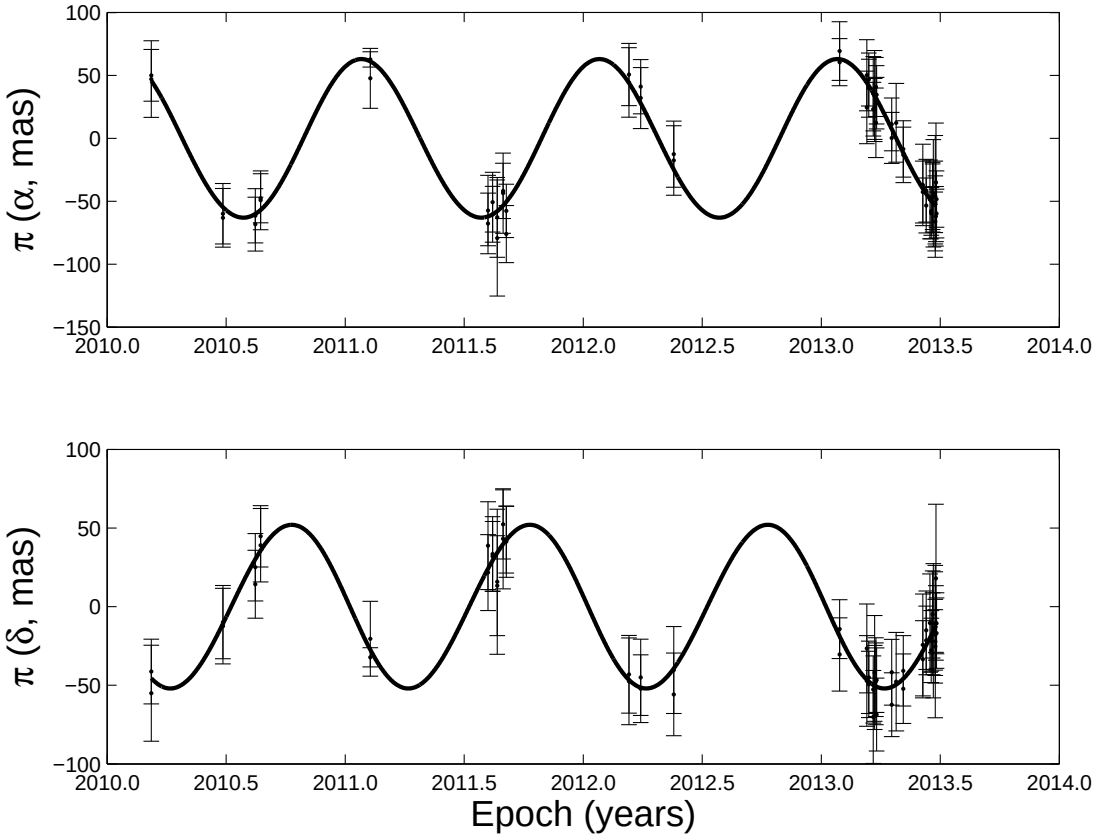

FIGURE 6.9: The parallax fit of VVV J141159.32-592045.7.

photometry to model spectra tailored for this object is necessary to accurately estimate its physical paramaters, but this analysis at least suggests that the VVV parallax is trustworthy. The parallax itself (Figure 6.9) is well sampled at critical points (i.e. the peaks and troughs of both fits) and also through the whole of the 2013.0-2013.5 season.

VVV J171340.61-395215.2

VVV J171340.61-395215.2 (J1713-3952 hereafter, 19.1±0.6 *pc*) falls at the bottom of the main sequence in Figure 6.8. There is no corresponding source in the SIMBAD database and I have confirmed the proper motion through visual inspection of a selection of the VVV images. The VVV parallax based measurement of the absolute Ks magnitude of J1713-3952 (M_{Ks} = 10.67) corresponds to a spectral type of M9 based on the M spectral subtype to absolute VISTA Ks magnitudes given in table 2 of Rojas-Ayala et al. (2014). The NIR colours of J1713-3952 agree with this based on plots of synthetic VISTA colours compared versus spectral type (M7-T8, M. Gromadzki *priv. comm.*).

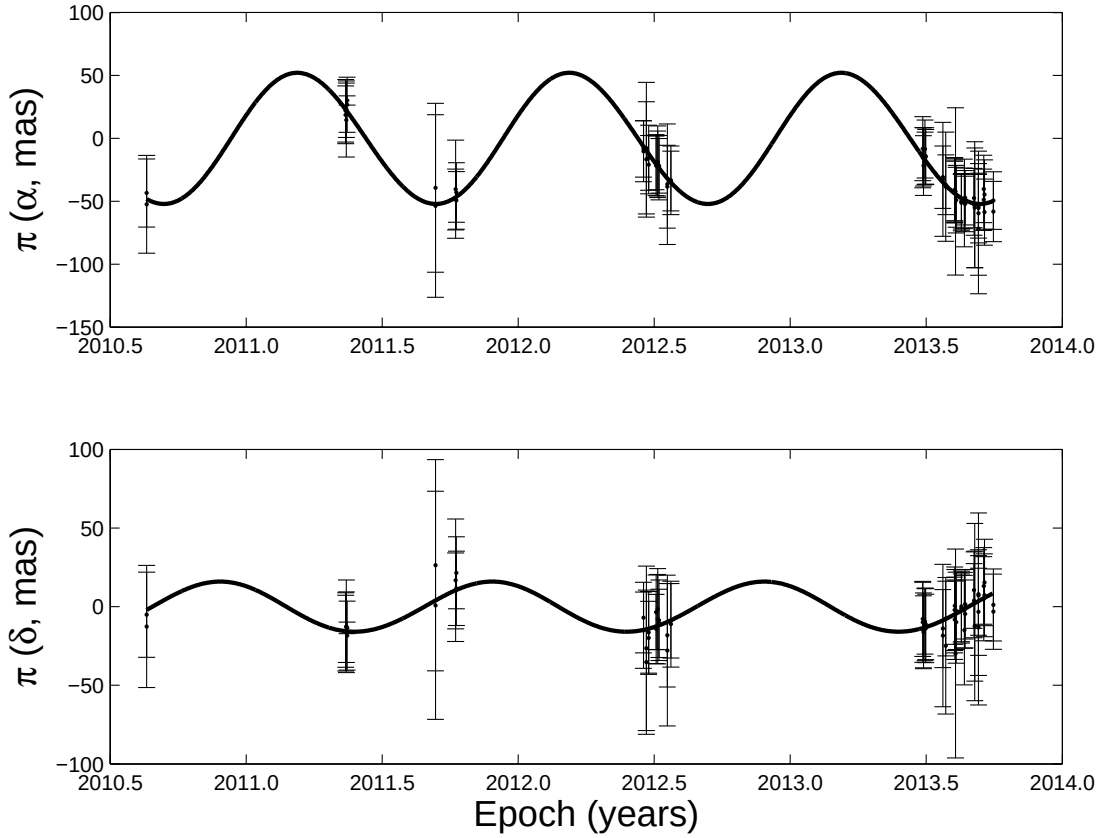

FIGURE 6.10: The parallax fit of VVV J171340.61-395215.2.

However, the equivalent relations in Faherty et al. (2012) and Dupuy and Liu (2012) suggest it is an L0 dwarf. These are all assuming J1713-3952 is a single object. J1713-3952 is redder than all but the J-H colour selection criteria given in Section 6.2.5 which supports an L0 spectral type. The parallax fit is shown in Figure 6.10.

VVV J133427.66-625735.9

VVV J133427.66-625735.9 (J1334-6257 hereafter, 20.0±0.9 *pc*) falls at the bottom of the main sequence in Figure 6.8. There is no corresponding source in the SIMBAD database and I have confirmed the proper motion through visual inspection of a selection of the VVV images. Placing J1334-6257 in several plots of synthetic VISTA colours compared to spectral type (M7-T8, M. Gromadzki *priv. comm.*) suggests it is a late M/early L type dwarf (∼M7-L0). The absolute Ks band magnitude of J1334-6257 ($M_{Ks} = 10.09$) corresponds to a spectral type of M8 assuming it is a single object (Dupuy and Liu, 2012; Rojas-Ayala et al., 2014). Interestingly, while the Z, Y, J and Ks band photometry

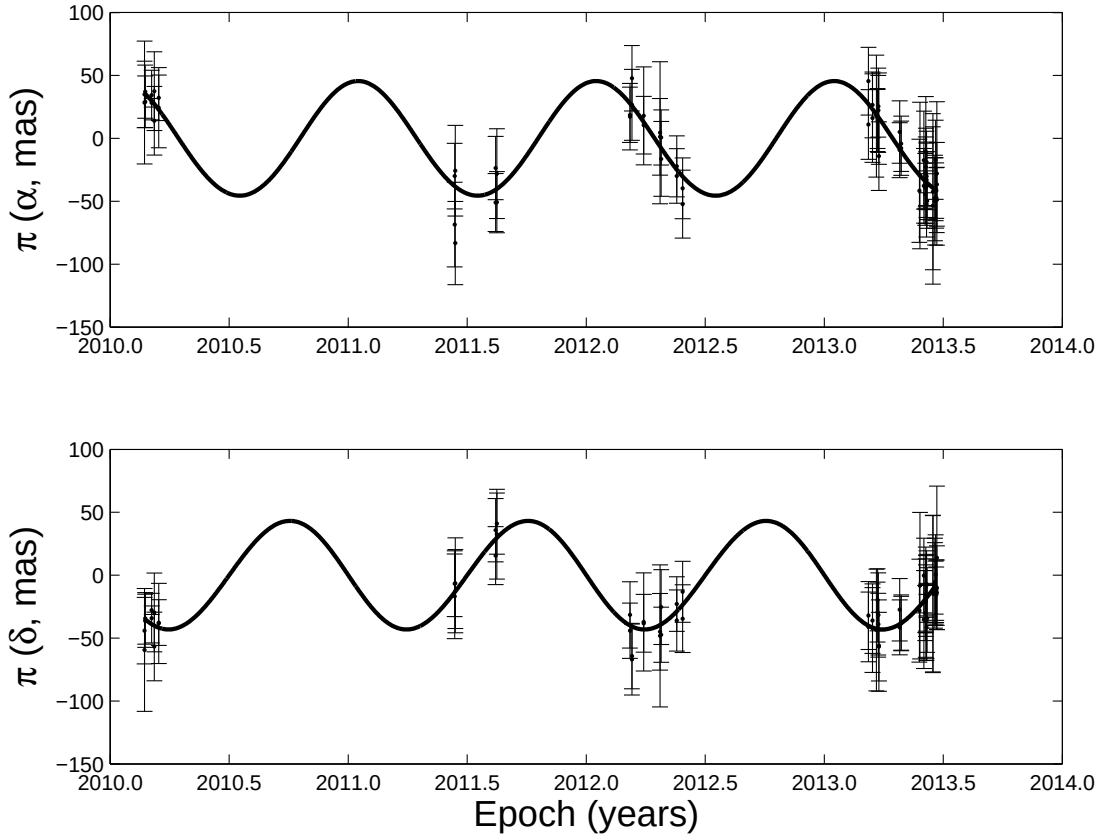

FIGURE 6.11: The parallax fit of VVV J133427.66-625735.9.

support a late M spectral type, the DR2 H band is approximately half a magnitude fainter than expected for such an object. Visual inspection of the VVV images does not indicate a problem with the observation, though J. Alonso performed profile fitting photometry and this does not reproduce the suppressed H band. The reasonably well sampled parallax fit is shown in Figure 6.11.

VVV J174349.16-390825.4

VVV J174349.16-390825.4 (J1743-3908 hereafter, 20.0 ± 0.7 *pc*) appears in the white dwarf locus of the NIR HR diagram (Figure 6.8). I have visually inspected a selection of the VVV images and can confirm that the proper motion is genuine. There are no entries in the SIMBAD database within 2' of the position of J1743-3908. The absolute magnitude of J1743-3908 may be consistant with a white dwarf of T_{eff} slightly above 10000K, though the Hewett et al. (2006) synthetic photometry for white dwarfs do not extend past this. Between the pure-H and pure-He synthetic photometry tables

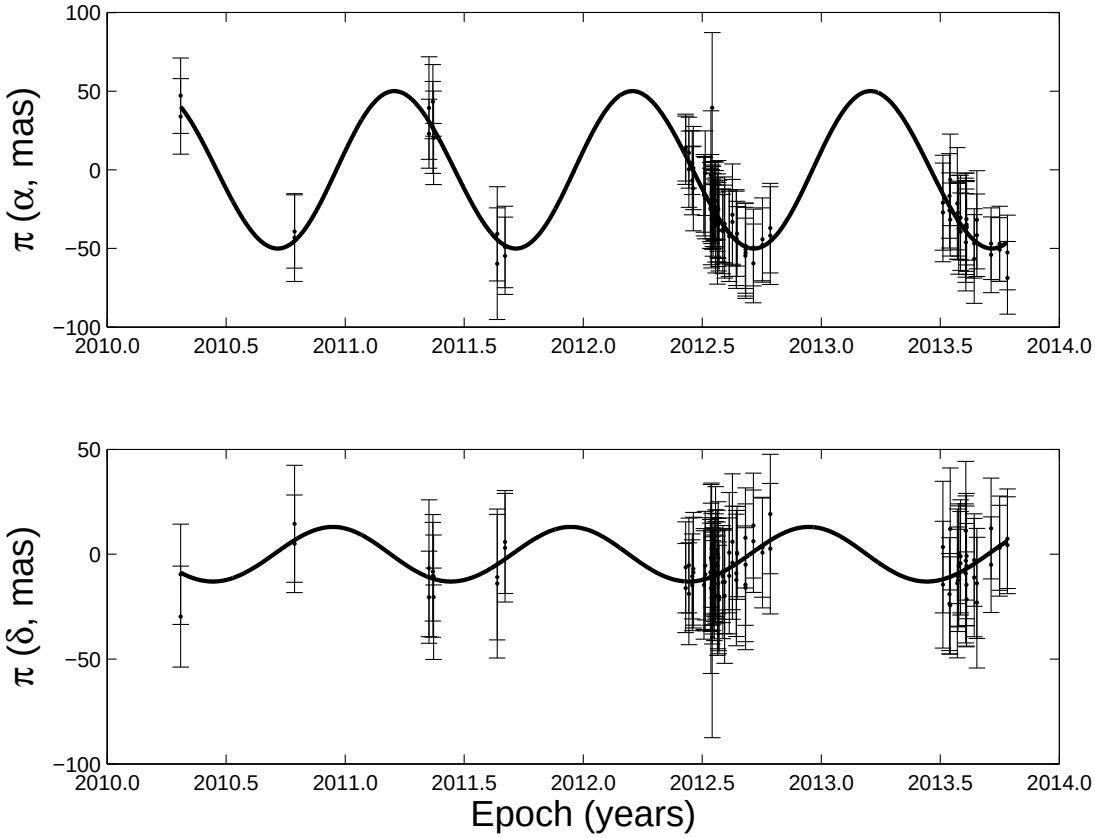

FIGURE 6.12: The parallax fit of VVV J174349.16-390825.4.

the Z-Y and H-K colours of J1743-3908 place it somewhat cooler, at between 5500 and 7500 Kelvin, which corresponds to an absolute K magnitude between 12.5 and 13.0 and a distance between ∼15.8 and ∼12.6 parsecs (i.e. still within the 25pc limit of this sample). If the higher T_{eff} trends towards bluer Z-Y, Y-J, J-H and H-K colours with increasing temperature continue then the Y-J and J-H colours of J1743-3908 should match those of the models at just over 10000K, confirming the VVV parallax. The Z-Y and H-K discrepancy might be due to the appearance of spectral lines though it is also possible that it may have a different surface gravity than that used to produce the model spectra ($log\ g = 8$). This is of course purely speculative. Testing this will require a spectrum and/or synthetic colours for hotter white dwarfs using the VISTA filter profiles and a range of surface gravities. Figure 6.12 shows the well sampled parallax fit.

VVV J170947.23-400555.3

An initial LPM parallax (57 ± 11 mas) placed VVV J170947.24-400555.3 at 17.6pc. Reprocessing with the more accurate pipeline gave a revised parallax of 39 ± 10 mas, placing it at a distance of 25.4pc. The faintness of this source ($Ks = 16.2 \pm 0.1$) has contributed to a relatively inaccurate parallax. Given its position in Z-J compared to the main locus of main sequence dwarfs in a Z-J versus M_{Ks} HR diagram it is most likely to be a later type M dwarf. If this is the case then to place it in the main locus it would need to be at a distance of around 100pc or greater taking into account its Ks band magnitude. The proper motion fit of this source is much better than that of the parallax, and is just about visible during blinking $\mu = 41 \pm 7$ $mas\ yr^{-1}$. At 25pc it would have an unusually low tangential velocity of 4.9 $km\ s^{-1}$, at 100pc however it would have a tangential velocity of 19.4 $km\ s^{-1}$ which is closer to what could expected for a standard field population object. It seems most likely then that this is a more distant (>100pc) late M type dwarf. There is no corresponding source in the SIMBAD database. Figure 6.13 shows the updated parallax fit.

6.3.2 L Dwarfs

I used the parallax and proper motion catalogues to search for new brown dwarfs. I produce an initial pool of sources with $Ks < 15$ and either distance $< 100pc$ from the 5σ parallax catalogue or $\mu > 100$ $mas\ yr^{-1}$ from the proper motion catalogue. Where sources are present in both the parallax and proper motion catalogues I use the astrometry from the parallax catalogue in preference. The aim of the distance and proper motion cuts is to restrict the sample to nearby sources. In principle, with a $Ks = 15$ limit I should not find any sources later than ∼M9 at around 75pc. Similar mass brown dwarf binaries could be brighter, detectable out to of order 100pc. The 100pc limit also means I do not need to take extinction into account, though it is likely that extinction would not be a problem out to a much larger distance for the majority of the survey. The search methods employed are detailed below. Figures 6.14 and 6.15 show the resultant candidates in $Y - J$, $Z - J$, $J - Ks$ and M_{Ks} space.

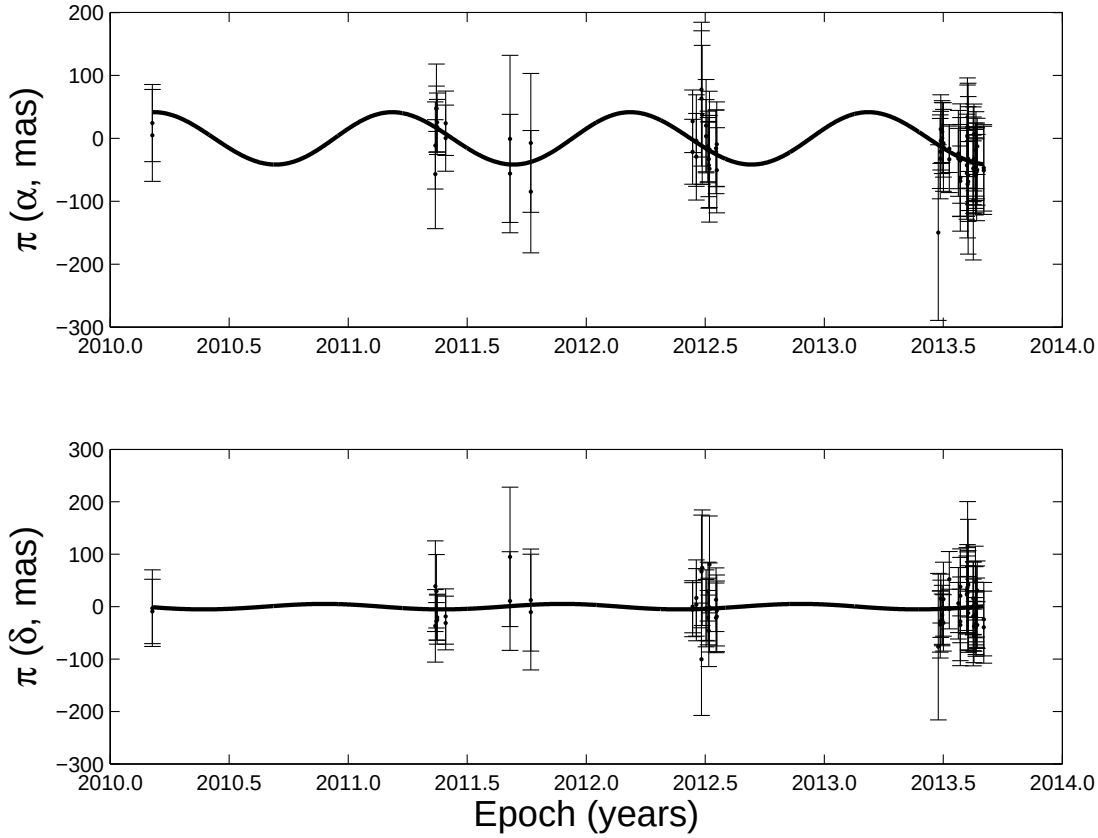

FIGURE 6.13: The parallax fit to VVV J170947.23-400555.3.

6.3.2.1 Colour Selection

I looked at the NIR colours of the L dwarf sample of Faherty et al. (2012) with well measured J, H and K photometry ($\sigma < 0.1$) that aren't flagged as peculiar (i.e. a subdwarf or with gravity class). Y, J, H and K photometry for their targets are provided on the MKO system. VISTA uses the MKO short K band which is similar to the Faherty et al. (2012) MKO K band. Stephens and Leggett (2004) show that for MKO K is very similar to 2MASS Ks for early L dwarfs. The CASU VISTA photometric properties web page[2] shows that 2MASS/WFCAM - VISTA photometric offsets are at the few hundreths of a magnitude level up to the 0.1 magnitude level in $Z/Y_{VISTA} - Z/Y_{WFCAM}$ for early L dwarfs. It is also important to note that the VISTA Z and Y band calibration is less accurate in the mid-plane by up to about 0.1 magnitudes due to extinction. The $Y - J > 1.0$ selection criteria is somewhat stringent and is likely to miss the bluest

[2]http://apm49.ast.cam.ac.uk/surveys-projects/vista/technical/photometric-properties

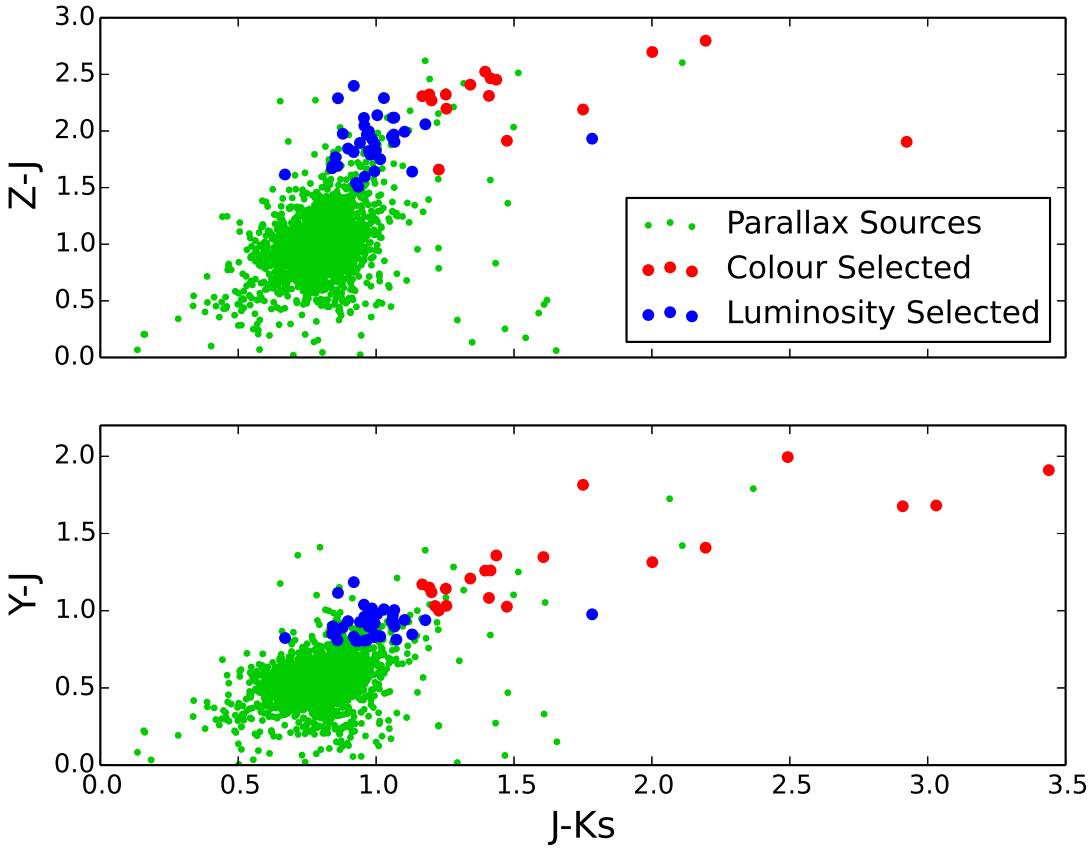

FIGURE 6.14: *Upper panel:* A J-Ks versus Z-J colour-colour diagram. *Lower panel:* A J-Ks versus Y-J colour-colour diagram. Both panels show the 5σ parallax sources and L dwarf candidates from the two selection methods.

examples (e.g. subdwarfs), but the luminosity based selection (Section 6.3.2.2) should identify any missed candidates.

The Faherty et al. (2012) L dwarfs have the following NIR colours:

$Y - J > 1.0$

$Y - H > 1.7$

$Y - K > 2.2$

$J - H > 0.5$

$J - K > 0.9$

$H - K > 0.3$

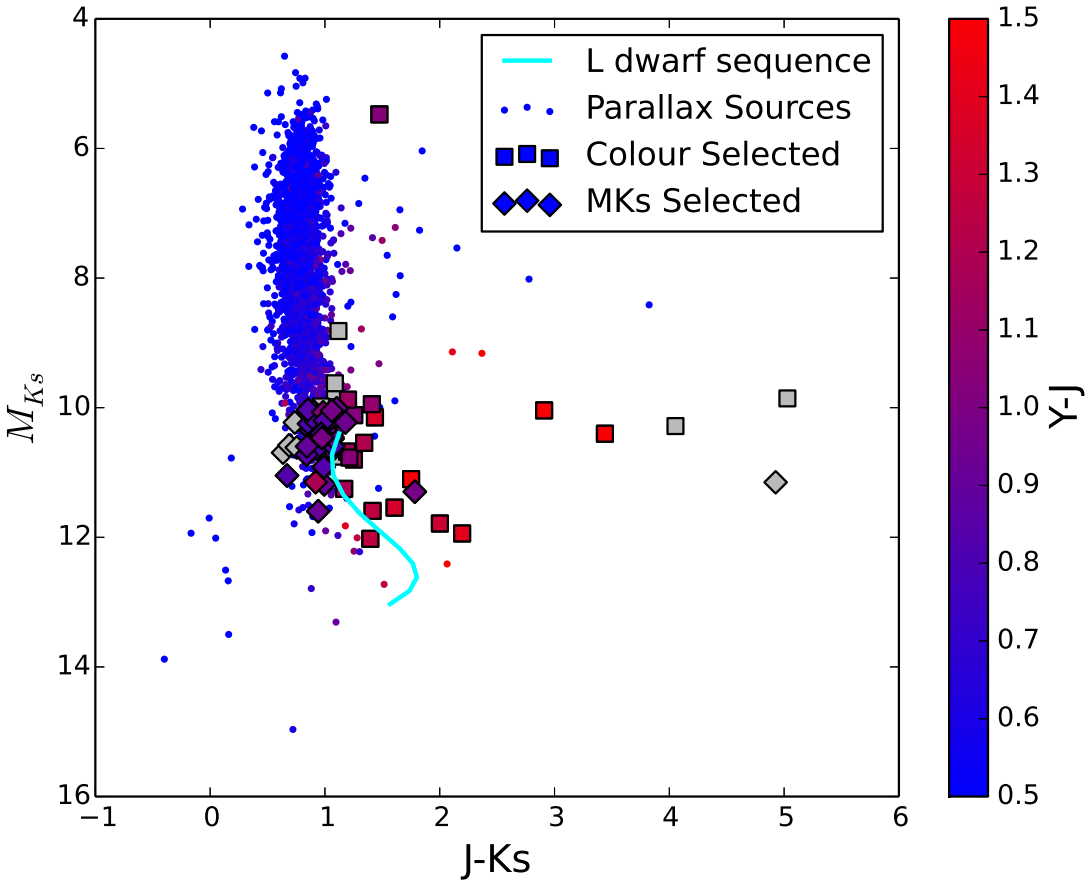

FIGURE 6.15: A J-Ks versus absolute Ks magnitude plot of the 5σ parallax sources and L dwarf candidates from the two selection methods. Y-J is on the colour axis, grey indicates no Y data. The cyan line shows the expected L dwarf locus (L0 at the top, T0 at the bottom) (Dupuy and Liu, 2012).

Using these criteria I select 59 L dwarf candidates from the nearby/high proper motion pool. I allowed a non-detection in the Y band, allowing for objects to either be too red for a detection or not covered by the VVV DR2 source table. Detections in J, H and Ks are required. I ran any sources with either no parallax or a parallax based on the relatively inaccurate LPM pipeline results through the more accurate parallax pipeline. There were 10 sources for which a parallax was not produced, usually due to an inadequate number of reference sources. I rejected any sources with luminosity (including uncertainty) not within the bounds of typical L dwarfs, approximately $10 < M_{Ks} < 14$ based on Faherty et al. (2012). In some cases the uncertainties on the parallaxes and hence the absolute Ks magnitudes are significant. The position of any given source on a chip and its epoch distribution can vary significantly meaning that in some cases an accurate parallax determination is simply not possible. In these cases the source

is retained as a candidate. Forty candidates either fall within $10 < M_{Ks} < 14$ within their uncertainties or do not have a parallax measurement. The candidates are shown in Table 6.2.

6.3.2.2 Luminosity Selection

A number of L dwarfs have been identified with colours outside normal values for such objects. These peculiar L dwarfs are of particular interest since they usually represent the extremes of the L dwarf parameter space. L subdwarfs for example are usually bluer than a typical L dwarf of the same subtype due to decreased flux in the H and K bandpasses (Kirkpatrick et al., 2014) (see eg. their figure 8) and can be overlooked by standard photometric searches. Indeed, for the photometric search above many of the L type subdwarfs from Faherty et al. (2012) would not be selected using those criteria. I select any source with a 5σ parallax, $Ks < 15$ and $10 < M_{Ks} < 14$ as an L dwarf candidate based on the absolute K band magnitude range of L dwarfs in Faherty et al. (2012) table 5. This selection produces 153 candidates, 137 of which were not selected as part of the colour based search. Colours derived from Z, Y and J photometry appear similar between normal L dwarfs and L subdwarfs, so I also require candidates to have $Z-J > 1.5$ and $Y-J > 0.8$ (which are fairly relaxed criteria) or non detections in the Z and/or Y bandpasses. This colour requirement should remove white dwarfs and all but the latest M dwarfs scattered in by Lutz-Kelker and Malmquist (Malmquist, 1922) biases and reduced the selection to the 52 candidates shown in Table 6.3. The least luminous object in the 5σ parallax $Ks < 15$ sample has $M_{Ks} = 12.3$. The absolute K magnitudes of Faherty et al. (2012) suggest that T dwarfs can be as bright as $M_{Ks} = 12.3$, though this is unusual, objects at this luminosity are L dwarfs more often than not.

6.3.2.3 Binary Search

Between the colour and luminosity selections I have 91 L dwarf candidates. To search for L dwarf candidates which are part of a binary (or higher order) system I matched them to a list of SIMBAD objects with $\mu > 100\ mas\ yr^{-1}$ (SIMBAD match) and the $\mu > 30\ mas\ yr^{-1}$ VVV proper motion catalogue (internal match). I used a 300" matching radius and allow up to 20 $mas\ yr^{-1}$ difference independently in proper motion in right ascension and declination. I removed sources from the internal match with

TABLE 6.2: The astrometry and photometry for the L dwarf candidates identified in Section 6.3.2.1. Coordinates are J2012.0, proper motions are in units of $mas\ yr^{-1}$, parallaxes are in units of mas. The photometry are from the VVV DR2 source table, missing values are indicative of a either a non-detection or a deprecation of the relevant observation. Missing DR2 Ks photometry are replaced with the median Ks magnitude of all the detections used for the proper motion and parallax calculations from the FITS files. I adopt 0.02 magnitudes as a baseline uncertainty on all photometry.

Object	α	δ	$\mu_\alpha \cos\delta$	μ_δ	π	M_{Ks}	Z	Y	J	H	Ks
Lc1	13:08:25.18	-63:20:39.7	-276.2±2.0	-108.6±1.6	35.5±2.8	11.6±0.2	17.72±0.02	16.52±0.01	15.26±0.01	14.43±0.01	13.84±0.02
Lc2	13:14:19.22	-63:03:12.8	-131.0±2.4	-4.0±2.0	12.0±2.6	10.1±0.5	18.18±0.02	17.01±0.02	15.98±0.01	15.26±0.01	14.73±0.02
Lc3	13:36:47.45	-61:46:48.5	128.2±1.4	54.2±1.4	31.9±1.9	12.0±0.1	18.42±0.03	17.16±0.02	15.90±0.01	15.14±0.01	14.50±0.02
Lc4	13:56:04.89	-63:34:24.2	-156.3±2.5	-12.5±2.8	15.0±3.0	10.8±0.4			16.01±0.01	15.39±0.01	14.87±0.02
Lc5	14:01:52.79	-61:59:27.9	64.7±2.8	-184.7±6.7			19.43±0.08		17.53±0.03	16.10±0.02	14.60±0.02
Lc6	15:17:21.46	-58:51:31.5	-90.1±1.0	-126.5±1.2	33.6±1.6	10.8±0.1	16.74±0.01	15.57±0.01	14.42±0.00	13.71±0.00	13.17±0.02
Lc7	15:53:15.37	-55:13:24.2	-16.8±1.4	23.0±2.0	15.7±2.5	10.4±0.3		19.77±0.24	17.86±0.05	15.58±0.02	14.42±0.02
Lc8	16:04:24.93	-52:13:38.2	17.4±1.7	-17.3±2.6	17.7±2.6	10.0±0.3		18.38±0.07	16.71±0.03	14.98±0.01	13.80±0.02
Lc9	16:18:02.56	-50:48:41.9	-53.7±2.2	-148.0±2.3	20.4±3.4	11.5±0.4		17.95±0.03	16.60±0.02	15.71±0.02	15.00±0.02
Lc10	16:39:53.35	-48:04:40.4	37.0±2.3	-26.9±2.2	17.1±3.3	10.1±0.4	17.87±0.02	16.78±0.02	15.42±0.01	14.55±0.01	13.98±0.02
Lc11	16:57:16.93	-42:55:49.5	-55.3±1.8	-181.4±2.5	5.9±5.7	8.8±2.1			16.08±0.01	15.26±0.01	14.96±0.02
Lc12	17:00:53.35	-40:48:18.5	-98.9±1.4	-18.4±2.1	1.3±3.5	5.5±5.8	18.24±0.03	17.36±0.02	16.33±0.01	15.26±0.01	14.86±0.02
Lc13	17:13:40.61	-39:52:15.2	112.3±0.8	-283.2±1.0	52.4±1.6	10.7±0.1	15.60±0.01	14.43±0.00	13.28±0.00	12.61±0.00	12.08±0.02
Lc14	17:19:00.54	-38:48:05.7	-45.8±3.8	-0.8±2.0	37.2±6.8	11.8±0.4	18.63±0.04	17.25±0.02	15.94±0.02	14.57±0.01	13.93±0.02
Lc15	17:22:09.88	-35:14:54.4	52.4±2.2	89.2±3.0				19.56±0.20	17.87±0.07	16.28±0.05	14.84±0.02
Lc16	17:28:09.77	-26:40:20.3	-112.1±1.5	-21.5±1.6			16.55±0.02	15.90±0.01	14.90±0.01	14.14±0.01	13.67±0.02
Lc17	17:32:29.01	-31:47:11.5	-80.9±3.1	-85.8±4.1				19.05±0.22	17.06±0.11	15.37±0.06	14.56±0.05
Lc18	17:44:55.45	-29:13:14.6	62.9±3.4	81.1±4.1					17.70±0.07	14.77±0.03	12.47±0.02
Lc19	17:45:03.31	-29:01:36.5	164.0±6.2	-116.7±3.7					17.15±0.04	14.96±0.03	12.78±0.02
Lc20	17:45:12.62	-28:54:34.8	-58.4±3.3	-87.5±4.5					19.19±0.26	15.19±0.04	12.97±0.02
Lc21	17:45:24.03	-29:16:14.7	-99.3±5.9	-133.7±8.0	20.6±5.1	9.9±0.5			18.32±0.12	15.33±0.05	13.29±0.02
Lc22	17:45:26.36	-29:15:50.2	64.4±4.1	-128.5±4.5					17.45±0.05	14.48±0.02	12.57±0.02
Lc23	17:45:28.56	-29:03:47.7	115.8±8.4	5.9±4.4					17.52±0.06	14.28±0.02	12.33±0.02
Lc24	17:45:46.34	-28:58:15.7	126.9±5.2	24.4±3.0					17.53±0.06	14.83±0.03	12.87±0.02
Lc25	17:46:01.53	-28:39:19.1	179.7±6.5	-36.4±2.8	1.7±6.5	5.1±8.4			18.29±0.15	15.77±0.06	13.91±0.04
Lc26	17:48:14.52	-28:13:56.7	-60.1±4.0	11.9±2.9	30.9±4.2	11.9±0.3	19.48±0.18	18.09±0.08	16.68±0.03	15.55±0.05	14.49±0.06
Lc27	17:48:26.19	-28:20:45.0	78.0±4.5	-99.4±4.6	0.5±5.2	2.6±22.9			18.03±0.11	15.46±0.05	14.11±0.04
Lc28	17:48:56.57	-28:26:11.5	88.1±5.6	52.0±3.1	14.0±8.2	10.3±1.3			18.61±0.19	16.17±0.09	14.56±0.06
Lc29	17:50:24.24	-27:49:40.3	37.4±3.7	0.7±1.6	26.4±3.9	11.1±0.3	17.94±0.05	17.56±0.05	15.75±0.02	14.73±0.02	14.00±0.04
Lc30	17:53:25.19	-20:37:37.1	7.7±3.3	-132.1±2.5	8.9±4.4	9.7±1.1			16.08±0.03	15.46±0.03	14.99±0.04

Table 6.2 continued.

Object	α	δ	$\mu_\alpha \cos\delta$	μ_δ	π	M_{Ks}	Z	Y	J	H	Ks
Lc31	17:59:02.14	-22:33:18.4	-19.3±1.9	-56.2±2.3	10.8±1.9	9.9±0.4	18.18±0.04	17.03±0.03	15.91±0.01	15.27±0.03	14.71±0.04
Lc32	17:59:55.41	-30:50:14.6	58.1±1.8	-105.6±1.9	14.6±1.9	10.8±0.3		17.18±0.16	16.15±0.10	15.45±0.09	14.94±0.06
Lc33	18:01:33.73	-36:23:14.8	111.5±1.3	-46.1±1.6	19.0±1.4	10.5±0.2	17.90±0.08	16.70±0.04	15.50±0.01	14.71±0.01	14.15±0.02
Lc34	18:08:04.70	-30:49:48.2	1.2±1.9	-154.5±1.7	18.6±1.7	11.3±0.2	18.38±0.17	17.24±0.08	16.07±0.04	15.44±0.03	14.90±0.02
Lc35	18:09:31.94	-26:50:26.8	-27.9±1.6	-84.0±1.9	22.1±1.3	10.0±0.1			14.23±0.01	13.66±0.01	13.26±0.02
Lc36	18:20:43.81	-32:15:54.3	-52.1±1.5	-124.2±1.7	16.4±1.7	10.2±0.2			15.09±0.01	14.50±0.01	14.11±0.02
Lc37	18:22:50.57	-31:25:40.0	-19.5±1.0	-112.3±1.1	29.1±1.1	10.4±0.1			14.07±0.00	13.51±0.00	13.07±0.02
Lc38	18:24:40.62	-26:39:30.1	-12.6±1.8	-28.8±1.7	10.5±2.1	9.6±0.4			15.61±0.01	15.07±0.01	14.52±0.02
Lc39	18:26:33.50	-33:41:38.1	-47.6±1.2	-95.7±1.0	20.2±1.2	9.9±0.1	17.14±0.02	15.91±0.01	14.83±0.01	14.08±0.01	13.42±0.02

TABLE 6.3: The astrometry and photometry for the L dwarf candidates identified in Section 6.3.2.2. Coordinates are J2012.0, proper motions are in units of $mas\ yr^{-1}$, parallaxes are in units of mas. The photometry are from the VVV DR2 source table, missing values are indicative of a either a non-detection or a deprecation of the relevant observation. Missing DR2 Ks photometry are replaced with the median Ks magnitude of all the detections used for the proper motion and parallax calculations from the FITS files. I adopt 0.02 magnitudes as a baseline uncertainty on all photometry.

Object	α	δ	$\mu_\alpha \cos\delta$	μ_δ	π	M_{Ks}	Z	Y	J	H	Ks
Ll1	11:49:49.64	-61:58:05.2	93.4±1.3	-98.8±1.5	20.7±3.3	11.2±0.3	17.48±0.02	16.51±0.02	15.60±0.02		14.60±0.02
Ll2	11:58:55.23	-61:45:34.2	-320.4±1.2	-5.6±1.2	17.0±2.8	10.3±0.4	17.06±0.02	15.97±0.02	15.08±0.02	14.50±0.01	14.20±0.02
Ll3	12:20:58.22	-63:43:54.1	-115.8±1.0	-94.3±1.3	17.3±2.1	10.4±0.3	17.16±0.02	16.14±0.02	15.19±0.02	14.62±0.01	14.23±0.02
Ll4	12:34:56.06	-64:19:24.0	-254.7±1.4	109.9±1.4	36.6±2.3	10.5±0.1	16.01±0.02	14.73±0.02	13.72±0.02	13.36±0.00	12.69±0.02
Ll5	12:50:33.50	-61:01:30.0	-129.5±1.4	1.5±2.0	16.7±3.1	10.1±0.4	16.69±0.02	15.78±0.02	14.84±0.02	14.27±0.00	13.95±0.02
Ll6	13:26:57.62	-61:18:18.1	-198.8±1.4	-64.5±1.4	16.2±2.0	10.0±0.3	17.05±0.02	16.00±0.02	15.06±0.02	14.42±0.00	13.96±0.02
Ll7	13:34:27.66	-62:57:35.9	-214.4±1.4	-27.2±1.2	50.0±2.2	10.1±0.1	14.75±0.02	13.58±0.02	12.46±0.02	12.52±0.00	11.60±0.02
Ll8	13:38:10.84	-63:33:29.8	-137.1±1.7	2.7±1.3	15.3±2.6	10.0±0.4				14.28±0.01	14.10±0.07
Ll9	14:04:51.99	-61:33:30.5	106.3±2.1	57.0±1.3	17.9±2.5	10.7±0.3	17.35±0.02	16.35±0.02	15.45±0.02	14.89±0.01	14.38±0.02
Ll10	14:19:51.11	-59:40:29.6	-110.9±1.9	-3.8±2.0	21.4±2.5	10.5±0.3	17.01±0.02	15.90±0.02	14.90±0.02	14.35±0.01	13.83±0.02
Ll11	15:55:44.39	-54:51:27.6	-25.7±1.5	-36.0±2.4	14.3±2.6	10.4±0.4	17.15±0.02	16.36±0.02	15.55±0.02	14.96±0.01	14.60±0.02
Ll12	15:56:15.07	-53:28:47.5	-10.5±1.4	-22.1±2.5	14.6±2.6	10.7±0.4			15.51±0.02		14.87±0.02
Ll13	16:01:01.36	-52:45:23.6	-9.5±1.4	-25.6±1.7	13.6±2.7	10.6±0.4			15.59±0.02		14.91±0.02
Ll14	16:03:15.85	-50:46:30.1	-31.0±1.4	-73.8±2.4	13.5±2.2	10.6±0.4	17.45±0.02	16.72±0.02	15.91±0.02	15.37±0.02	14.99±0.02
Ll15	16:28:36.14	-46:52:53.3	38.3±1.2	-118.5±1.4	15.2±2.2	10.3±0.3	17.13±0.02	16.34±0.02	15.49±0.02	14.86±0.01	14.36±0.02
Ll16	16:57:45.14	-43:25:06.4	243.9±1.6	44.6±1.2	24.5±3.0	10.6±0.3		15.54±0.02	14.73±0.02	14.10±0.01	13.65±0.02
Ll17	17:02:15.65	-38:28:22.7	-43.4±2.7	-4.0±1.8	27.5±5.0	11.6±0.4	17.24±0.02	16.27±0.02	15.34±0.02	14.81±0.01	14.40±0.02
Ll18	17:10:02.98	-40:40:05.1	-14.9±3.0	4.7±1.6	30.7±5.2	11.3±0.4	17.58±0.02	16.62±0.02	15.65±0.02	14.50±0.01	13.86±0.02
Ll19	17:10:07.71	-36:46:11.4	-76.3±0.9	-124.9±1.0	16.7±3.0	10.5±0.4	17.37±0.02	16.33±0.02	15.41±0.02	14.80±0.01	14.34±0.02
Ll20	17:20:44.76	-35:26:23.9	59.6±1.3	-127.3±1.4	22.7±2.3	10.1±0.2	15.79±0.02	15.08±0.02	14.28±0.02	13.73±0.01	13.34±0.02
Ll21	17:21:17.02	-29:16:07.1	-91.9±1.5	-58.4±1.6	13.7±2.1	10.1±0.3	17.22±0.04	16.30±0.03	15.40±0.02	14.87±0.02	14.43±0.02
Ll22	17:25:21.19	-29:52:22.7	99.8±1.0	35.3±0.9	27.1±1.0	10.2±0.1	15.64±0.02	14.75±0.02	13.95±0.02	13.44±0.01	13.09±0.02
Ll23	17:29:16.50	-31:18:13.6	-53.0±1.6	1.3±2.4	23.6±2.4	10.3±0.2	16.40±0.02	15.31±0.02	14.35±0.02	13.77±0.01	13.40±0.02
Ll24	17:33:42.34	-31:56:39.8	-155.9±1.3	-112.7±1.2	22.0±1.4	10.7±0.1	16.52±0.02	15.70±0.02	14.85±0.02	14.32±0.01	14.01±0.02
Ll25	17:44:45.00	-29:15:24.2	25.3±4.4	44.6±4.1	25.1±3.9	11.4±0.3					14.43±0.07
Ll26	17:44:53.35	-28:46:31.0	-70.1±5.4	58.2±6.2	29.9±4.8	12.3±0.4					14.93±0.10
Ll27	17:45:20.03	-29:24:02.3	81.9±3.5	-87.9±6.0	21.8±3.2	11.1±0.3					14.46±0.07
Ll28	17:45:47.38	-25:52:51.0	-28.8±1.9	-71.2±2.1	13.5±2.6	10.6±0.4	17.48±0.05	16.68±0.05	15.78±0.04	15.37±0.07	14.94±0.08
Ll29	17:45:51.52	-28:56:19.6	-51.4±4.9	-35.1±5.6	33.6±4.3	11.2±0.3			18.44±0.13	15.29±0.04	13.52±0.13
Ll30	17:46:39.31	-28:40:05.8	87.0±2.7	-68.4±2.6	23.6±2.9	10.2±0.3				15.59±0.05	13.35±0.02

Table 6.3 continued.

Object	α	δ	$\mu_\alpha \cos\delta$	μ_δ	π	M_{Ks}	Z	Y	J	H	Ks
Ll31	17:47:27.40	-25:03:22.8	-29.0±1.5	24.4±2.0	12.4±2.2	10.1±0.4	17.30±0.02	16.49±0.03	15.66±0.03	14.98±0.04	14.66±0.05
Ll32	17:47:43.58	-28:14:15.8	-101.7±4.8	-37.4±4.6	27.7±5.1	11.9±0.4				16.13±0.08	14.67±0.07
Ll33	17:48:06.77	-28:16:18.1	-42.6±3.9	-39.5±4.4	20.7±4.1	11.2±0.4				16.42±0.11	14.59±0.06
Ll34	17:48:17.81	-25:22:58.5	17.0±2.0	-202.4±1.2	21.2±2.8	11.0±0.3	16.70±0.02	15.91±0.02	15.08±0.02	14.69±0.03	14.41±0.04
Ll35	17:55:22.43	-18:46:06.8	-70.5±2.4	-101.5±2.8	13.7±2.4	10.3±0.4	17.37±0.03	16.45±0.02	15.62±0.02	15.06±0.02	14.60±0.02
Ll36	17:56:02.73	-36:27:55.2	-103.2±1.7	-181.9±1.2	20.2±2.0	10.3±0.2	16.96±0.03	15.80±0.02	14.82±0.02	14.16±0.01	13.82±0.02
Ll37	17:57:29.20	-36:28:50.9	14.4±1.7	-136.7±1.3	16.6±1.8	10.2±0.2	16.83±0.03	15.85±0.02	15.02±0.02	14.47±0.01	14.10±0.02
Ll38	18:02:05.29	-23:17:36.5	-120.0±1.3	-116.1±1.4	17.2±1.3	10.4±0.2	17.29±0.02	16.21±0.02	15.17±0.02	14.68±0.01	14.22±0.02
Ll39	18:06:22.65	-39:58:35.2	-207.7±1.7	-449.8±1.9	24.1±1.9	10.0±0.2	15.75±0.02	14.82±0.02	13.98±0.02	13.46±0.00	13.12±0.02
Ll40	18:06:28.06	-35:20:06.7	43.7±2.0	-40.3±1.9	15.5±2.1	10.9±0.3	17.78±0.04	16.78±0.03	15.95±0.02	15.37±0.01	14.96±0.02
Ll41	18:09:15.34	-22:15:42.2	-77.0±2.2	-82.2±3.5	13.9±1.6	10.2±0.3	17.45±0.02	16.43±0.02	15.50±0.02	15.00±0.02	14.44±0.02
Ll42	18:12:45.97	-21:02:06.5	31.8±1.9	-48.7±2.3	17.3±1.4	10.1±0.2	16.80±0.02	15.89±0.02	14.87±0.02	14.33±0.01	13.89±0.02
Ll43	18:12:51.63	-31:04:50.9	108.0±1.2	-67.1±1.1	31.5±1.6	10.2±0.1	15.97±0.02	14.85±0.02	13.91±0.02	13.23±0.00	12.73±0.02
Ll44	18:17:00.00	-26:34:37.2	-134.6±1.3	-93.0±1.4	17.9±1.3	10.2±0.2	16.76±0.04	15.78±0.03	14.94±0.02	14.33±0.01	13.94±0.02
Ll45	18:17:36.84	-30:26:18.5	-254.1±1.5	-130.5±1.4	22.5±2.0	11.1±0.2	17.71±0.08	16.50±0.03	15.31±0.02	14.81±0.01	14.39±0.02
Ll46	18:22:09.32	-32:35:18.9	27.8±2.1	-20.8±2.2	13.0±2.3	10.1±0.4			15.39±0.02	14.89±0.01	14.55±0.02
Ll47	18:23:19.40	-28:20:04.6	16.4±1.7	-96.8±2.1	15.0±2.1	10.4±0.3		16.30±0.03	15.49±0.02	14.93±0.01	14.52±0.02
Ll48	18:27:10.47	-33:06:29.4	5.9±1.8	-56.1±1.9	12.5±2.1	10.2±0.4			15.48±0.02	14.94±0.01	14.74±0.02
Ll49	18:29:34.53	-28:58:14.1	23.9±2.1	-17.5±2.2	13.6±2.6	10.5±0.4	17.57±0.04	16.67±0.02	15.78±0.02	15.24±0.01	14.80±0.02
Ll50	18:32:23.59	-28:31:04.8	18.5±1.8	8.9±1.6	14.6±2.0	10.0±0.3	17.40±0.03	16.25±0.02	15.28±0.02	14.62±0.01	14.22±0.02
Ll51	18:32:38.23	-30:46:21.5	-242.0±2.3	-218.0±2.5	26.4±2.8	10.6±0.2			14.26±0.02	13.83±0.00	13.51±0.02
Ll52	18:33:26.21	-28:32:43.6	-42.4±1.8	-106.0±2.0	14.8±2.0	10.5±0.3	17.59±0.04	16.58±0.02	15.60±0.02	15.05±0.01	14.62±0.02

TABLE 6.4: Binary candidates generated via a match of the VVV L dwarf candidates to the SIMBAD database. Proper motions are in units of $mas\ yr^{-1}$, K band photometry is that of 2MASS.

L Dwarf Candidate	Name	$\mu_\alpha \cos\delta$ $mas\ yr^{-1}$	μ_δ $mas\ yr^{-1}$	K	Separation arcsec	$\Delta\mu$ $mas\ yr^{-1}$
Lc6	β Circini	-97.74±0.28	-134.15±0.22	3.88±0.18	217.8	10.8
Ll24	NLTT 45014	-167±20	-109±20	12.50±0.07	109.5	12

separations <1" to remove instances where the source matched to itself. The results of the two matches are shown in Tables 6.4 and 6.5. At first glance most of the internal binary candidates have a fairly low probability of being genuine, i.e. they have relatively large separations and significant differences in proper motion. One internal match pair which stands out as being most likely genuine is discussed below along with the two pairs from the SIMBAD match.

Lc6/β Circini

β Circini (β Cir hereafter) is an A3 type main sequence star (Gray et al., 2006) with well measured radial velocity, rotational velocity and metallicity. Crucially β Cir has a constrained age: $166^{+212}_{-116}\ Myr$ based on Schaller et al. (1992) evolutionary grids (Song et al., 2001); $245^{+110}_{-119}\ Myr$ based on Bertelli et al. (1994) isochrones (Lachaume et al., 1999). Nielsen et al. (2013) give a 1σ age of between 272 and 458 Myr based on a Bayesian analysis, and rule out a companion with $\Delta mag \sim 15$ separated by between and 1.5" and 7" to 2σ (this falls to $\Delta mag = 11$ at 0.36"). Lagrange et al. (2009) present a high precision radial velocity analysis using HARPS which rules out 1.1, 1.5 and 2.5 M_{Jup} companions at 3, 10 and 100 days respectively to 1σ. Nakajima and Morino (2012) conclude β Cir is a candidate member of the TW Hydra stellar kinematic group, their TW Hydra age ($8Myr$) clearly disagrees with the estimates of the age of β Cir in literature.

The VVV proper motion of Lc6 (of Table 6.2, VVV J151721.49-585131.5, J1517-5851 hereafter, -90.1 ± 1.0 and $-126.5 \pm 1.2\ mas\ yr^{-1}$ in $\alpha\cos\delta$ and δ respectively) has some agreement with the Hipparcos proper motion of β Cir (-97.74 ± 0.28 and $-134.15 \pm 0.22\ mas\ yr^{-1}$ in $\alpha\cos\delta$ and δ respectively). The Hipparcos parallax of β Cir ($32.73 \pm 0.19\ mas$) is consistent with the VVV parallax of J1517-5851 ($33.6 \pm 1.6\ mas$) within the uncertainties, which greatly strengthens the case for a genuine binary pair despite the 6.7σ disagreement in proper motion. It is likely that some of the disagreement in proper

motion ($\delta\mu = 10.8 \pm 1.6\ mas\ yr^{-1}$) can be accounted for by the lack of an absolute VVV proper motion correction. The remainder may be due to orbital motion. If the orbital velocity of J1517-5851 happens to be perpendicular to the line of sight it could present as a 3.5 to 4.0 $mas\ yr^{-1}$ proper motion relative to β Cir assuming a primary mass of order 2.0 to 2.5 solar masses and a circular orbit. A more elliptical orbit would increase the relative proper motion. Increase in the inclination of the system relative to the line of sight or decrease in the inclination of the orbital velocity vector relative to the line of sight will decrease the relative proper motion.

J1517-5851 is one of the more compelling L dwarf candidates since it has the full range of photometry and measured luminosity, all of which point to an early L type dwarf. If I assume a T_{eff} in the region of 2000K and the age of β Cir the AMES-Dusty isochrones (Allard et al., 2001) suggest a mass of $0.04 - 0.06\ M_{\odot}$ for 150 and 500 Myr respectively. This is likely to be a valuable young, low gravity benchmark at an age greater than that of Pleiades brown dwarfs.

Ll24/NLTT 45014

Ll24 (of Table 6.3, VVV J173342.34-315639.8, J1733-3156 hereafter) meets all the Rojas-Ayala et al. (2014) M dwarf selection criteria and their equation 1 gives it a spectral type of M8.5. An M8.5 dwarf should have an absolute Ks magnitude of 10.4. Given the uncertainty in the Rojas-Ayala et al. (2014) based M type ($\pm$1 subtype) and the absolute Ks magnitude of J1733-3156 (10.7 ± 0.1), it is likely that J1733-3156 is slightly later at around M9$-$M9.5. NLTT 45014 is one of the 167 proper motion targets located in VVV images by Ivanov et al. (2013), a search for companions to known high proper motion stars. Ivanov et al. did not identify a companion for NLTT 45014, though J1733-3156 should have been visible on their 3.6' image centered on NLTT 45014, perhaps even the edge of the 1.8' image depending on the rotation angle. I have confirmed the motion of J1733-3156 is visible between the reddest POSS-II image (IR) and the 2MASS and VVV J band images. Add to this that this pair was not also identified in the internal search is a sign of a problem. My own measurement of the proper motion of NLTT 45014 based on 117 epochs of VVV Ks band observations is -105.2 ± 1.4 and $-245.4 \pm 1.5\ mas\ yr^{-1}$ in $\alpha \cos\delta$ and δ respectively compared to the Salim and Gould (2003) proper motion of -167 ± 20 and $-109 \pm 20\ mas\ yr^{-1}$ in $\alpha \cos\delta$ and δ respectively. The motion of J1733-3156 is -155.9 ± 1.3 and $-112.7 \pm 1.2\ mas\ yr^{-1}$ in $\alpha \cos\delta$ and δ respectively, in

fact the difference in proper motion of the two sources is clear in the images, which rules this out as a genuine binary pair.

Internal Candidate 4

Internal binary candidate 4 is the only internal match pair which seems likely to be genuine. The L dwarf candidate, VVV J172117.02-291607.1 (J1721-2916 B hereafter) meets all the Rojas-Ayala et al. (2014) M dwarf selection criteria. The M dwarf subtype equation they present places J1721-2916 B at ∼M9.5, though the VVV parallax based $M_{Ks} = 10.1 \pm 0.3$ places it at around M8. It is therefore unlikely that J1721-2916 B is an L dwarf, unless again it is a particularly blue example. The proper motion of J1721-2916 B differs from that of the candidate primary (VVV J172116.98-291615.7, J1721-2916 A hereafter) by 9.2 $mas\ yr^{-1}$ (2.6σ). The parallaxes of the pair also do not agree within their uncertainties, 22.5 ± 2.9 mas and 13.7 ± 2.1 mas for A and B respectively. This difference in proper motion and parallax could be explained if the uncertainties on these values for J1721-2916 A are underestimated due to saturation. Visual inspection of a selection of the VVV Ks band images for this pair confirms their proper motion. The relatively small angular separation strengthens the argument that these are a genuine binary pair. Indeed, using a method similar to that of Section 4.4.3.3 I estimate that I expect to find 8.9×10^{-7} sources within 10" of J1721-2916 B with proper motion consistent to within three times the uncertainties on the proper motions of J1721-2916 A and B. It is clearly improbable then that this is a chance alignment, even taking into account that there are 91 L dwarf candidates and therefore 91 chances of finding such an alignment.

6.4 High Proper Motion Results

From results of the high proper motion pipeline (see Section 5.10) based on proper motions of the short epoch baseline groups I have identified 862 candidate high proper motion sources with $\mu > 200\ mas\ yr^{-1}$. I required each to be detected in a minimum of two epoch group results tables (including contemporaneous epoch groups from overlapping pawprints) with $\sigma_\mu < 50\ mas\ yr^{-1}$ and low χ^2_{red} in α and δ. Until the sources are identified in all epochs and an accurate proper motion calculated I use the short epoch group proper motion measurement with the lowest uncertainty for each source. Of these,

TABLE 6.5: Binary candidates generated via a match of the VVV L dwarf candidates to the VVV $\mu > 30$ $mas\ yr^{-1}$ catalogue.

	Companion Name	$\mu_\alpha \cos\delta$ $mas\ yr^{-1}$	μ_δ $mas\ yr^{-1}$	Ks	L Dwarf Candidate	L Dwarf Name	Separation arcsec	$\Delta\mu$ $mas\ yr^{-1}$	$\Delta\mu$ Signif. σ
1	VVV J155544.75-545508.3	-18.4±1.9	-46.5±3.6	15.73±0.05	Ll11	VVV J155544.39-545127.6	220.8	12.7	2.6
2	VVV J155633.99-532939.8	-24.1±3.6	-36.4±4.1	16.44±0.08	Ll12	VVV J155615.07-532847.5	176.8	19.8	3.2
3	VVV J170957.96-364228.6	-87.2±2.1	-110.4±2.3	11.11±0.40	Ll19	VVV J171007.71-364611.4	251.8	18.2	5.4
4	VVV J172116.98-291615.7	-99.0±2.0	-52.5±1.9	9.93±0.29	Ll21	VVV J172117.02-291607.1	8.7	9.2	2.6
5	VVV J174444.20-291229.3	35.9±3.0	29.9±2.9	13.64±0.12	Ll25	VVV J174445.00-291524.2	175.2	18.1	2.5
6	VVV J174457.63-284242.1	-71.9±7.2	41.8±5.7	14.51±0.12	Ll26	VVV J174453.35-284631.0	235.7	16.5	1.3
7	VVV J174534.81-290010.0	105.7±4.8	21.3±2.5	13.79±0.22	Lc23	VVV J174528.56-290347.7	232.7	18.4	1.7
8	VVV J174549.15-290111.1	-37.0±4.5	-44.9±4.9	14.48±0.14	Ll29	VVV J174551.52-285619.6	293.2	17.4	1.8
9	VVV J174542.52-285637.4	-59.7±5.3	-21.3±3.0	12.48±0.15	Ll29	VVV J174551.52-285619.6	119.4	16.1	1.7
10	VVV J174713.95-250157.0	-44.4±4.7	12.7±2.8	15.07±0.07	Ll31	VVV J174727.40-250322.8	201.9	19.3	3.2
11	VVV J174743.33-281150.8	-86.3±1.7	-28.1±2.2	12.74±0.07	Ll32	VVV J174743.58-281415.8	145.0	18.0	2.5
12	VVV J174802.39-281524.9	-54.6±2.5	-30.1±2.3	13.17±0.06	Ll33	VVV J174806.77-281618.1	78.6	15.3	2.3
13	VVV J174814.15-281803.2	-57.7±7.7	28.6±4.8	15.55±0.21	Lc26	VVV J174814.52-281356.7	246.5	16.8	1.6
14	VVV J182211.01-323546.6	16.7±2.0	-36.8±2.0	11.66±0.23	Ll46	VVV J182209.32-323518.9	35.0	19.5	4.7
15	VVV J182437.39-264225.0	2.8±2.0	-37.9±1.6	14.99±0.05	Lc38	VVV J182440.62-263930.1	180.2	18.0	5.1
16	VVV J182714.33-330548.7	2.7±2.5	-42.8±2.1	15.26±0.06	Ll48	VVV J182710.47-330629.4	63.3	13.6	3.2
17	VVV J182722.41-330858.1	7.7±2.2	-37.5±2.9	14.60±0.05	Ll48	VVV J182710.47-330629.4	211.3	18.6	4.1

337 were identified as part of the low proper motion pipeline leaving 525 sources identified using the high proper motion pipeline alone. It is important to note that most of these new sources will be false (see Figure 6.16). Motions calculated using data over such a short epoch baseline are much less reliable. Nearby sources could also be affected by parallactic motion.

Figure 6.17 compares total proper motion from the LPM pipeline and the most accurate short epoch group results of the HPM pipeline for the 337 sources with measurements available from both. Once taken into account that these HPM pipeline proper motions are not final and have considerably larger proper motion uncertainties than the LPM pipeline as a result, the general agreement in proper motion is encouraging.

The next stage in the HPM pipeline is to attempt to recover every candidate from the short time groups in each epoch of their respective pawprints and produce a more accurate final proper motion, on par with the final accuracy of the LPM pipeline. This next step is complete for approximately 80% of the VVV tiles. From these preliminary results I have identified 415 high proper motion candidates. I select sources with $\sigma_\mu < 20\ mas\ yr^{-1}$ (note that these proper motion are much more accurate than those of the short epoch groups), and low χ^2_{red} in α and δ. I then identify sources detected in more than one epoch group (again including contemporaneous epoch groups from overlapping pawprints) within 1" and with proper motion consistent within 20 $mas\ yr^{-1}$ in each dimension. Next I run these multiple detections of individual sources through a routine which produces weighted averages of their proper motions (see Section 5.9) and retain only those with a weighted average proper motion uncertainty less than 10 $mas\ yr^{-1}$. Of the 415 sources that pass these criteria 365 were also identified by the LPM pipeline, leaving 50 which were only identified as part of the HPM pipeline.

Of the 525 $\mu > 200\ mas\ yr^{-1}$ candidates identified among the short epoch group results only 50 remain after further processing. Even taking into account that only $\sim$ 80% of tiles have currently undergone the further processing I must conclude that the short epoch group results alone are not enough. Attempted recovery of the candidates through all epochs is necessary for a confident detection.

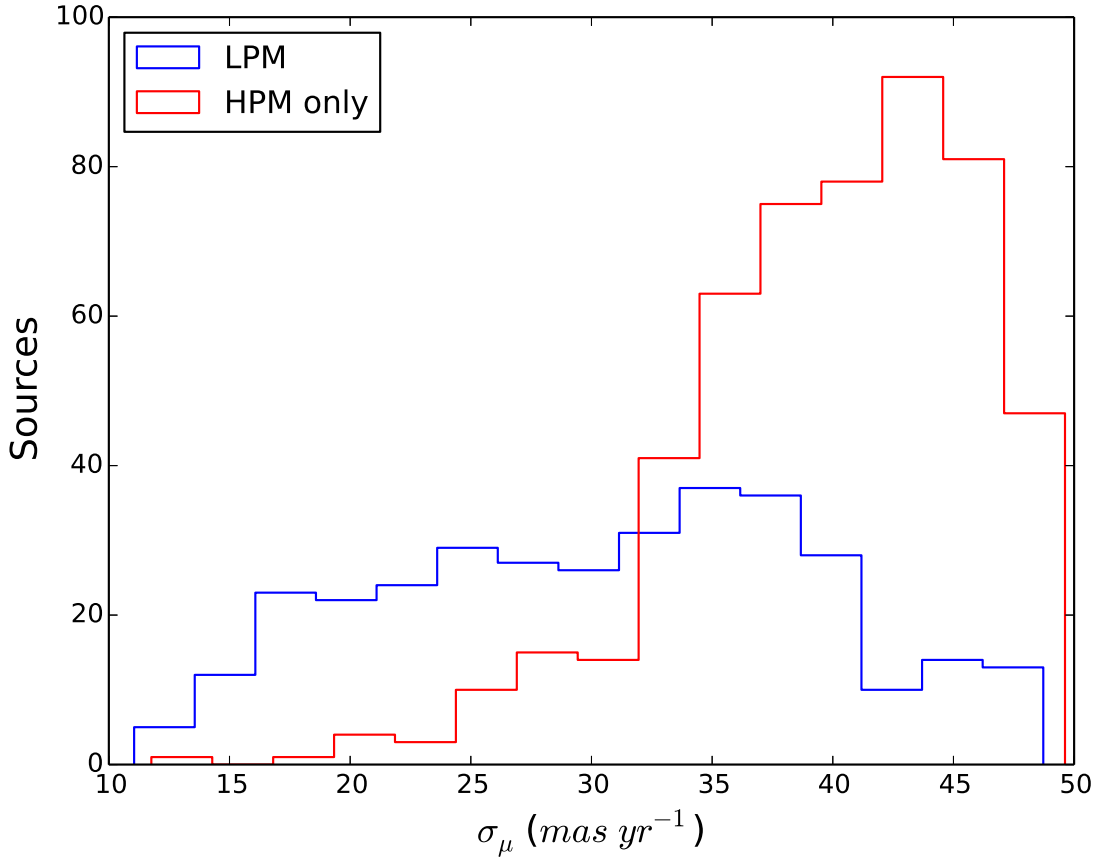

FIGURE 6.16: The distribution of short time group proper motion uncertainties for high proper motion ($\mu > 200\ mas\ yr^{-1}$) candidates identified in Section 6.4. The candidates are split based on whether or not they are also identified by the much more reliable LPM pipeline. The sharp increase of HPM only sources past $\sigma_\mu \sim 30\ mas\ yr^{-1}$ suggests that many are not genuine.

6.5 Summary

Here I present preliminary results of proper motion and parallax reductions of the Ks band observations of the VVV survey. I have produced an accurate and reliable catalogue of 62,536 sources with proper motion in excess of 30 $mas\ yr^{-1}$. Combining this with preliminary results of a variant of the pipeline designed to identify additional high proper motion sources I find 554 sources with $\mu > 200\ mas\ yr^{-1}$, 504 and 50 from the results of the LPM and HPM pipelines respectively (with 10-15 more to come from the HPM pipeline). I have currently produced parallaxes at $> 5\sigma$ for over 3,400 sources, the accuracy and volume of which I expect to improve with a number of planned alterations to the parallax pipeline and candidate pool. The derived absolute Ks magnitudes of a

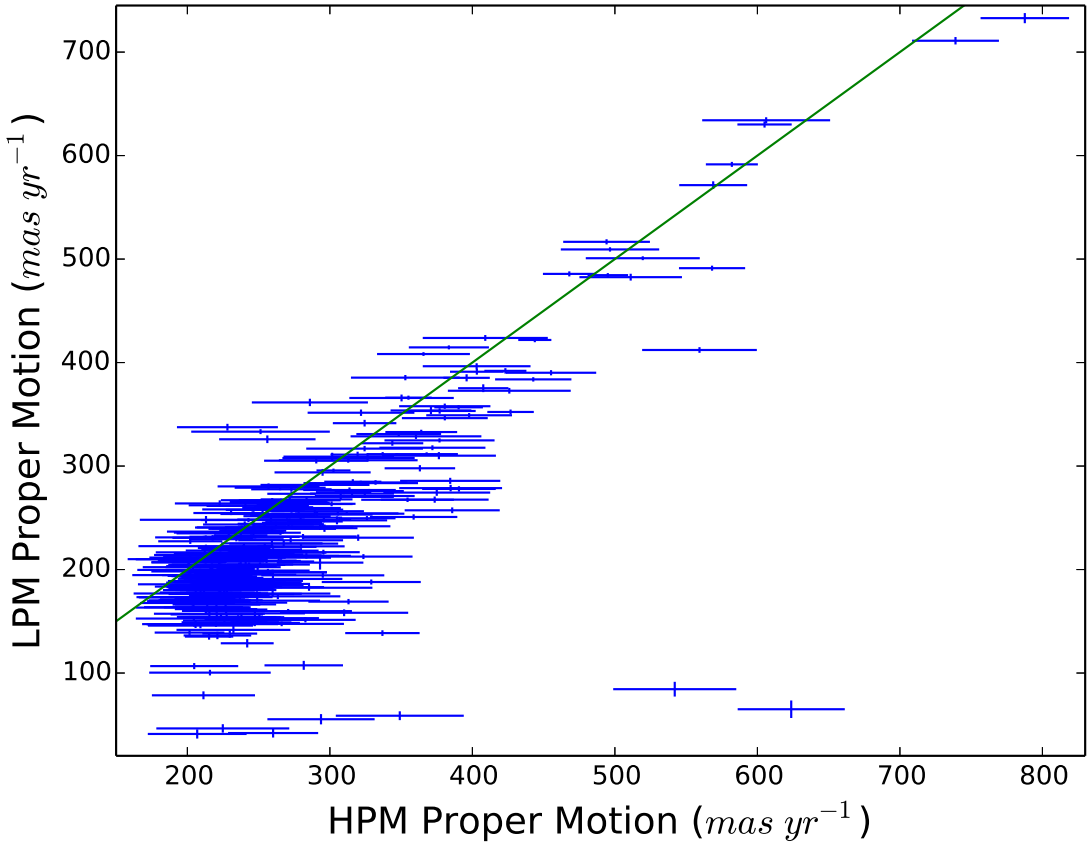

FIGURE 6.17: A comparison of the total proper motions for some sources of the LPM proper motion pipeline and their most accurate short epoch group total proper motions of the HPM pipeline. Proper motions are reasonably consistent between the two within their uncertainties. The $x = y$ line has been included for clarity. Note the much smaller uncertainties on the LPM pipeline results, as is to be expected. I suspect that the apparent worsening of the agreement at around HPM $\mu = 200\ mas\ yr^{-1}$ is a selection effect due to the cutoff in the HPM results at that point that isn't mirrored by the LPM results.

colour based selection of M dwarf candidate objects compare favourably to estimates of absolute Ks magnitudes based on VVV photometry.

I have identified approximately 90 L dwarf candidates based on NIR colour and luminosity selections. One of these is a clearly established companion to a very well studied early type main sequence star and will be invaluable in the future study of such objects. Two of the L dwarf candidates (Lc13 and Ll7) and an additional two objects which are most likely white dwarfs, are within the 25pc volume limited sample.

The low proper motion pipeline has generated 446,219,025 proper motion measurements for of order 200 million stars. Examples of what these could prove useful for include: Identifying or ruling out members of Galactic clusters; Measuring kinematic properties

of globular clusters (e.g. space motion, kinematic dispersion); Constraining distances to VVV sources either through a direct proper motion measurement or by placing upper limits if an approximate tangential motion is known (e.g. Galactic disc membership).

While motions are currently relative to the reference stars used in the fit, an approximate relative to absolute correction can be performed using PPMXL. A much more accurate solution will be possible using Gaia in 2017, which will enable study of the streaming motions of stars in the Galactic bulge, for example.

Chapter 7

Conclusions and Future Work

Large scale proper motion catalogues are not new. Catalogues based on data from photographic sky surveys are numerous and date back many decades. Only relatively recently have high resolution near infrared sky surveys been undertaken, and for this reason proper motion catalogues in the near infrared are few. Optical surveys are sub-optimal for the study of intrinsically red objects, such as ultracool dwarfs, and distant objects in regions of high extinction. It is therefore important that proper motion catalogues are provided at longer wavelengths. The UKIDSS and VISTA surveys offer superb high resolution near infrared data, ideal for the task of proper motion catalogue production. I sought to generate and exploit such proper motion catalogues using these data.

In Chapter 2 I present details of a proper motion pipeline designed with UKIDSS LAS and GPS data in mind. The pipeline is cabable of providing proper motions with typical 1σ uncertainties of about 10 $mas\ yr^{-1}$ for bright sources in the UKIDSS data. The reliability of generated catalogues is heavily dependent on matching parameters and has proven to be good for the LAS and in less crowded GPS fields, especially when additional information such as ellipticity and morphological classification (which are provided) are used as selection criteria.

The LAS proper motion catalogue described in Chapter 3 covers approximately 1500 deg^2 of northern sky and is of order 15 million sources. The motions provided correlate well with existing optical catalogues where there is overlap.

The GPS proper motion catalogue described in Chapter 4 also covers approximately 1500 deg^2 of the northern Galactic plane and is of order 400 million sources. High proper motion candidates with $K < 17$ from the $l > 60°$ area, approximately 900 deg^2, were visually inspected resulting in 617 genuine high proper motion source identifications, of which 153 are new detections.

The LAS proper motion catalogue has enabled the identification of a variety of scientifically interesting high proper motion sources. The brightest pure-H ultracool white dwarf LSR J0745+2627 was identified by Catalán et al. (2012). Burningham et al. (2013) identified two T dwarf - main sequence star binaries, for which the LAS proper motion catalogue was crucial: LHS 6176B, a sub-solar metallicity T8 dwarf; and HD 118865B, a solar metallicity T5 dwarf. These important benchmark objects indicated that $H - 4.5\mu m$ and $J - W2$ colours were more sensitive to metallicity and surface gravity than the atmospheric models predicted. Burningham et al. (2014) identified ULAS J131610.28+075553.0, a T6p subdwarf, one of only two confirmed T type subdwarfs, the other being Wolf 1130b (Mace et al., 2013b).

Among the GPS $l > 60°$, $K < 17$ high proper motion discoveries I identified two new mid T dwarfs that are likely to be within 25 pc, a further thirteen new L dwarf candidates and two ultracool dwarf binary candidates. Additionally, four T dwarfs identifications are the product of searches still in progress, two from a search of sources with $\mu < 200\ mas\ yr^{-1}$ and one each from WISE and GLIMPSE360 cross matches of high proper motion candidates at $K > 17$. The T dwarf product of the WISE cross match exhibits unusual photometric properties suggestive of Galactic thick disc/halo membership. A proposal for spectroscopic follow up has been submitted. Searches for brown dwarf benchmarks are also coming to fruition, with several candidates currently being followed up spectroscopically.

Chapter 5 describes an astrometric pipeline, measuring proper motions and parallaxes, for multi-epoch VISTA data. In development it became clear that reliability and completeness are heavily reliant on the specific details of the source matching where multi-epoch data are concerned, I am confident improvements to both can be made through further revision of the method. The overall accuracy of the proper motions and parallaxes are excellent, of order $1 - 2\ mas\ yr^{-1}$ for standard pipeline proper motions and

parallaxes with uncertainties below 1 mas are not unusual for bright sources. Selections of sources with low uncertainties and low χ^2_{red} have also proven to be extremely reliable.

The low proper motion variant of the VVV pipeline has generated 446,219,025 proper motion measurements for of order 200 million stars once pawprint overlaps are taken into account. I produced a preliminary catalogue of 62,536 sources with $\mu > 30\ mas\ yr^{-1}$. From those a selection of sources with $\mu > 200\ mas\ yr^{-1}$ yields 504 high proper motion sources. A second pipeline which aims to improve on the completeness at the high proper motion end adds another 50 or so sources to the high proper motion source list. Over 3400 parallaxes have been measured for a variety of VVV sources with distances up to 300 pc, and more will be produced in the coming months. Among these I find four new members of the $< 25pc$ volume limited sample: two L dwarf candidates and two white dwarf candidates. I have also produced a list of 90 further L dwarf candidates from colour and luminosity based selections, one of which is a very promising age benchmark: β Circini B.

For the GPS, extension of searches for scientifically valuable objects (e.g. cool white and brown dwarfs) to lower proper motions, for brighter high proper motion objects at $l < 60°$, and for high proper motion objects at $K > 17$ with the aid of colour selections are all underway. There are also plans to incorporate the GPS proper motion catalogue into the final GPS data release. For the LAS, several groups are working on characterising the brown dwarf content of the LAS using the catalogue presented here. I am involved in ongoing projects to characterise the white dwarf content of the LAS including a spectroscopic follow up campaign of cool white dwarfs.

There is still much that should be done with the VVV pipeline and catalogue. Inclusion of the most recent data and further optimisation of pipeline should provide a significant improvement in astrometric precision. While the current sample of 5σ parallaxes is already significant there are still more to come. It might prove valuable to target a selection (e.g. ultracool dwarf candidates) with multi-object spectroscopy to aid spectral type to luminosity relations. Certainly β Circini B will be the subject of spectroscopic follow up. Searches for T dwarfs are still to be undertaken, as are searches for white dwarfs in conjunction with VPHAS. White dwarfs in particular might benefit from a large sample of parallaxes to improve current mass-radius relations. Looking further

ahead, the study of bulk motions of stars in the bulge and beyond should be possible, aided by the Gaia absolute reference frame calibration.

In the next few years Gaia will provide astrometric information for of order 10^9 stars of unprecedented accuracy, although there are caveats. Gaia performs astrometry in the optical and as a result sources reddened by interstellar dust and those that are intrinsically red will be missed. It is for this reason that the proper motion catalogues in the near infrared which are presented here will retain their value well into the post-Gaia era. In fact, Gaia will aid such catalogues by providing a very precise astrometric reference grid on which to anchor their own astrometry. The release of Gaia proper motion data which can be used for this is expected during 2017. I plan to update all three proper motion catalogues at that time in order to benefit from the improvement in precision and provide accurate absolute proper motions for the GPS and VVV.

Høg and Knude (2014) discuss a proposed successor to Gaia operating in the near infrared, they conclude that such an instrument is not worth the required effort due to the relative loss of accuracy in the K band. Ground based proper motion surveys with some infrared capability will be further strengthened in the near term with the large scale results from Pan-STARRS expected this year and LSST from 2020. Large scale proper motion surveys in the near infrared such as these are therefore unlikely to be rendered obselete in the near future.

Appendix A

Additional Tables

Table A.1 gives a sample of ten rows from the catalogue, the column headers correspond to the following:

Line - Links the same line across the splits in this sample table.

RA - Right Ascension of first epoch J band detection.

Dec - Declination of first epoch J band detection.

Y - UKIDSS DR10 Y magnitude.

e_Y - Uncertainty on UKIDSS DR10 Y magnitude.

J1 - UKIDSS FITS File first epoch J band magnitude.

e_J1 - Uncertainty on UKIDSS FITS File first epoch J band magnitude.

J2 - UKIDSS FITS File second epoch J band magnitude.

e_J2 - Uncertainty on UKIDSS FITS File second epoch J band magnitude.

H - UKIDSS DR10 H magnitude.

e_H - Uncertainty on UKIDSS DR10 H magnitude.

K - UKIDSS DR10 K magnitude.

e_K - Uncertainty on UKIDSS DR10 K magnitude.

J1ell - Ellipticity of first epoch J band detection.

J1PA - Position angle of ellipticity of first epoch J band detection.

J2ell - Ellipticity of second epoch J band detection.

J2PA - Position angle of ellipticity of second epoch J band detection.

J1class - Morphological classification of first epoch J band detection.

J2class - Morphological classification of second epoch J band detection.

RAPM_rel - Relative proper motion in Right Ascension ($\times \cos\delta$).

DecPM_rel - Relative proper motion in Declination.

e_RAPM_rel - Uncertainty on relative proper motion in Right Ascension ($\times \cos\delta$).

e_DecPM_rel - Uncertainty on relative proper motion in Declination.

RAPM - Proper motion in Right Ascention ($\times \cos\delta$).

DecPM - Proper motion in Declination.

e_RAPM - Uncertainty on proper motion in Right Ascention ($\times \cos\delta$).

e_DecPM - Uncertainty on proper motion in Declination.

J1MJDobs - Modified Julian Date of first epoch observation.

EpochBaseline - Epoch baseline in decimal years.

SourceID - UKIDSS DR10 sourceID (for WSA crossmatching).

local - Local/Global transformation flag ('true' indicates a local transform was used).

Right Ascension, Declination and position angles are in units of decimal degrees. All UKIDSS magnitudes are AperMag3 values (2" aperture). Proper motions and uncertainties are in units of $mas\ yr^{-1}$. Morphological classification flags are as follows:

1 - Galaxy

0 - Noise

-1 - Star

-2 - Probable star

TABLE A.1: Sample rows from the LAS proper motion catalogue.

Line	RA	Dec	Y	e_Y	J1	e_J1	J2	e_J2	H	e_H
1	0.00606	-0.673361	15.473	0.0050	14.969	0.01	14.987	0.01	14.43	0.0050
2	0.012379	-0.605281			19.708	0.219	19.429	0.179	18.809	0.195
3	0.016784	-0.799593			19.2	0.142	19.294	0.159		
4	0.025975	-0.702338	13.481	0.0020	13.081	0.01	13.088	0.01	12.545	0.0020
5	0.028177	-1.142162	16.55	0.0090	16.095	0.01	16.116	0.01	15.497	0.01
6	0.062918	15.916086	14.303	0.0030	13.892	0.01	13.785	0.01	13.156	0.0020
7	0.070539	15.928027	15.103	0.0040	14.555	0.01	14.591	0.01	14.074	0.0040
8	0.102226	15.828653	16.047	0.0070	15.565	0.014	15.561	0.01	15.067	0.0090
9	0.108392	15.845481	19.093	0.082	18.358	0.153	18.559	0.077	18.3	0.152
10	0.1466	15.906866	18.214	0.038	18.086	0.122	17.719	0.037	17.216	0.057

Line	K	e_K	J1ell	J1PA	J2ell	J2PA	J1class	J2class	RAPM_rel	DecPM_rel	e_RAPM_rel
1	14.162	0.0060	0.08	-72.6	0.08	-26.81	-1	-1	-15.44	-21.9	3.98
2			0.4	63.01	0.24	61.0	1	-1	44.66	-112.37	12.0
3			0.41	-17.6	0.25	-88.07	-7	-1	175.51	164.84	13.45
4	12.329	0.0020	0.05	-78.73	0.06	-17.92	-1	-1	-78.6	-52.84	6.89
5	15.258	0.014	0.03	151.43	0.08	153.55	-1	-1	43.49	-22.88	6.94
6	12.906	0.0030	0.34	106.41	0.06	122.9	1	-1	-158.3	39.32	7.94
7	13.827	0.0050	0.02	77.86	0.04	126.85	-1	-1	81.27	32.61	7.81
8	14.778	0.011	0.03	70.5	0.04	108.77	-1	-1	-63.07	-30.77	6.96
9	17.535	0.123	0.12	127.78	0.42	124.2	-1	1	115.6	-68.38	15.74
10	17.106	0.084	0.33	42.7	0.06	160.08	-7	-1	67.12	-55.98	11.44

Line	e_DecPM_rel	RAPM	DecPM	e_RAPM	e_DecPM	J1MJDobs	EpochBaseline	SourceID	local
1	4.89	-22.33	-27.04	3.98	4.89	53634.42578	6.069462286	433867580351	true
2	11.59	37.78	-117.51	12.0	11.59	53634.42578	6.069462286	433867580667	false
3	13.14	168.63	159.7	13.45	13.14	53634.42578	6.069462286	433867580597	false
4	4.06	-85.49	-57.98	6.89	4.06	53634.42578	6.069462286	433867580292	true
5	5.85	36.72	-28.0	6.94	5.85	53634.42578	6.069462286	433870019429	true
6	7.03	-163.67	31.52	7.94	7.03	54398.37891	3.999807474	433804633469	true
7	5.89	75.9	24.81	7.81	5.89	54398.37891	3.999807474	433804633507	true
8	7.26	-68.44	-38.57	6.96	7.26	54398.37891	3.999807474	433804633203	true
9	15.89	110.23	-76.18	15.74	15.89	54398.37891	3.999807474	433804633253	true
10	11.87	61.75	-63.78	11.44	11.87	54398.37891	3.999807474	433804633434	false

-7 - Bad pixel within 2" aperture

-9 - Saturated.

The CASU standard source extraction documentation contains more information on these morphological classifications.

TABLE A.2: The 12 common proper motion systems identified within the LAS proper motion catalogue from section 3.5.3.2. I adopt 0.02 magnitudes as a baseline uncertainty on all photometry.

α	δ	i	z	J	H	K	$\mu_\alpha \cos\delta$ $mas\ yr^{-1}$	μ_δ $mas\ yr^{-1}$	i-J	SIMBAD entry	Spectral type	Known binary
09:53:24.13	+05:27:01.3	15.64 ± 0.00	14.68 ± 0.00	13.13 ± 0.01	12.58 ± 0.00	12.24 ± 0.00	-185 ± 8	38 ± 7	2.51	y	M4	[b]
09:53:24.45	+05:26:58.7	20.20 ± 0.04	18.21 ± 0.02	15.74 ± 0.01	15.05 ± 0.01	14.47 ± 0.01	-188 ± 9	39 ± 6	4.46	y	M9.5	
09:56:14.81	+01:44:57.5	14.12 ± 0.00	13.49 ± 0.00	12.11 ± 0.01	11.65 ± 0.00	11.40 ± 0.00	-105 ± 11	-182 ± 9	2.01	y	M2	[b]
09:56:13.07	+01:45:13.1	20.29 ± 0.04	18.50 ± 0.04	16.35 ± 0.01	15.92 ± 0.01	15.48 ± 0.02	-109 ± 11	-177 ± 9	3.94	y	M9	
11:58:25.59	-01:22:58.9	15.34 ± 0.00	14.49 ± 0.00	12.95 ± 0.01	12.49 ± 0.00	12.18 ± 0.00	-201 ± 8	-74 ± 7	2.39	y	*M4*[a]	
11:58:24.04	-01:22:45.5	20.31 ± 0.04	18.69 ± 0.04	16.64 ± 0.01	16.12 ± 0.01	15.66 ± 0.02	-208 ± 10	-75 ± 7	3.67	y	M8	
11:59:48.15	+07:06:59.1	18.49 ± 0.01	17.16 ± 0.01	15.30 ± 0.01	14.80 ± 0.01	14.40 ± 0.01	-160 ± 12	101 ± 10	3.19	y	M7	[c]
11:59:48.47	+07:07:09.1	17.81 ± 0.01	18.01 ± 0.02	17.52 ± 0.04	17.58 ± 0.06	17.49 ± 0.10	-159 ± 12	102 ± 10	0.29	y	WD?	
12:08:16.83	+08:45:27.6	17.67 ± 0.01	16.08 ± 0.01	13.94 ± 0.01	13.37 ± 0.00	12.90 ± 0.00	-122 ± 7	-68 ± 9	3.73	y	M9	
12:08:15.55	+08:45:42.7	17.77 ± 0.01	17.64 ± 0.01	16.75 ± 0.02	16.51 ± 0.02	16.40 ± 0.03	-123 ± 8	-66 ± 9	1.02	y	WD	
13:25:13.86	+12:30:13.3	17.96 ± 0.01	16.85 ± 0.01	15.11 ± 0.01	14.56 ± 0.00	14.21 ± 0.01	-95 ± 8	-41 ± 8	2.85	n	*M5/6*[a]	
13:25:12.44	+12:30:22.0	20.37 ± 0.04	18.70 ± 0.04	16.42 ± 0.01	15.79 ± 0.01	15.31 ± 0.01	-98 ± 8	-38 ± 8	3.95	n	*M8.5/9*[a]	
13:28:35.49	+08:08:19.5	18.34 ± 0.01	17.06 ± 0.01	15.27 ± 0.01	14.74 ± 0.01	14.35 ± 0.01	-145 ± 8	-60 ± 9	3.07	n	*M6*[a]	
13:28:34.69	+08:08:18.9	20.52 ± 0.04	18.62 ± 0.03	16.45 ± 0.01	15.86 ± 0.01	15.33 ± 0.01	-145 ± 8	-60 ± 9	4.07	y	M8.5	
14:04:40.20	-00:40:19.8	15.52 ± 0.00	14.63 ± 0.00	13.06 ± 0.01	12.56 ± 0.00	12.24 ± 0.00	-135 ± 8	-79 ± 10	2.46	n	*M4*[a]	
14:04:40.39	-00:40:26.9	17.17 ± 0.01	16.03 ± 0.01	14.25 ± 0.01	13.72 ± 0.00	13.35 ± 0.00	-136 ± 8	-81 ± 10	2.92	n	*M6*[a]	
14:20:16.86	+12:07:38.9	16.18 ± 0.00	15.21 ± 0.01	13.55 ± 0.01	13.09 ± 0.00	12.71 ± 0.00	-108 ± 7	-21 ± 8	2.64	n	*M5*[a]	
14:20:17.83	+12:07:53.5	20.76 ± 0.07	18.86 ± 0.05	16.54 ± 0.01	15.89 ± 0.01	15.35 ± 0.01	-113 ± 8	-20 ± 8	4.22	n	*L0*[a]	
14:24:38.98	+09:17:09.4	20.53 ± 0.06	18.46 ± 0.03	15.68 ± 0.01	14.80 ± 0.00	14.07 ± 0.00	-221 ± 7	-156 ± 4	4.85	y	L4	[d]
14:24:39.04	+09:17:13.1	14.91 ± 0.01	14.89 ± 0.01	14.52 ± 0.01	14.52 ± 0.00	14.58 ± 0.01	-211 ± 7	-156 ± 4	0.39	y	DA	
14:59:41.64	+08:35:07.7	18.69 ± 0.01	17.63 ± 0.02	15.83 ± 0.01	15.31 ± 0.01	14.98 ± 0.01	43 ± 7	-85 ± 5	2.86	n	*M5/6*[a]	
14:59:41.92	+08:35:13.5	20.28 ± 0.04	19.13 ± 0.05	17.18 ± 0.02	16.71 ± 0.04	16.37 ± 0.04	50 ± 6	-85 ± 5	3.10	n	*M6*[a]	
15:49:51.57	+08:57:29.6	15.45 ± 0.00	14.70 ± 0.00	13.20 ± 0.01	12.68 ± 0.00	12.40 ± 0.00	-55 ± 3	-100 ± 5	2.25	n	*M4*[a]	
15:49:51.88	+08:57:30.7	20.03 ± 0.03	18.50 ± 0.03	16.29 ± 0.01	15.76 ± 0.01	15.28 ± 0.01	-57 ± 4	-101 ± 5	3.74	n	*M8*[a]	

[a] Indicates an estimated spectral type based on $i - J$ colour using Hawley et al. (2002).
[b] Zhang et al. (2010)
[c] Deacon et al. (2009b)
[d] Becklin and Zuckerman (1988)

TABLE A.3: The 24 probable common proper motion systems from section 3.5.3.2 identified using the LAS proper motion catalogue and SIMBAD.

Primary		*Secondary*							*Pair*		
Name	Spectral type	α	δ	J	$\mu_\alpha \cos\delta$ $mas\ yr^{-1}$	μ_δ $mas\ yr^{-1}$	i-J	Spectral type	Separation "	μ_{diff} σ	Known binary
NLTT 21820		09:27:53.47	+01:49:13.9	17.95 ± 0.03	-26 ± 8	-138 ± 8	3.17 ± 0.10	*M6*[a]	111	1.7	
LP 488-31		09:46:12.09	+11:16:31.0	15.66 ± 0.01	-187 ± 6	-25 ± 6	3.33 ± 0.01	*M7*[a]	10	0.5	[b]
2MASS J10084007+0150537		10:09:04.17	+01:58:46.5	17.99 ± 0.05	34 ± 7	-163 ± 10	> 3.3	> *M6.5*[a]	595	1.5	
2MASS J12020964+0742538		12:01:59.65	+07:35:53.6	14.97 ± 0.01	127 ± 7	-136 ± 7	3.69 ± 0.01	M8	446	1.4	
2MASS J12020933+0742477		12:01:59.65	+07:35:53.6	14.97 ± 0.01	127 ± 7	-136 ± 7	3.69 ± 0.01	M8	438	1.4	
SDSS J120331.33-005332.8		12:02:53.30	-00:56:08.3	15.87 ± 0.01	-216 ± 5	-22 ± 4	4.05 ± 0.03	*M9*[a]	591	3.3	
10 Vir	K3III	12:09:49.00	+01:52:38.3	14.65 ± 0.01	57 ± 8	-192 ± 4	3.32 ± 0.01	*M7*[a]	137	2.2	
DT Vir	M2Ve	13:00:41.73	+12:21:14.7	16.68 ± 0.01	-639 ± 9	-24 ± 10	6.60 ± 0.57	T8.5	105	1.8	[c]
HD 115151	G5	13:15:13.10	+10:41:57.6	15.85 ± 0.01	-154 ± 7	-20 ± 6	3.64 ± 0.02	*M8*[a]	39	0.7	
G 63-23	K5	13:20:41.49	+09:57:49.7	13.65 ± 0.01	-251 ± 8	-142 ± 6	3.81 ± 0.01	M8	169	0.1	[d]
LHS 2722	K2V	13:20:43.97	+04:09:06.4	15.18 ± 0.01	-498 ± 9	199 ± 10	4.71 ± 0.03	L3	68	0.8	[d]
2MASS J13272850+0916323		13:27:26.77	+09:16:05.6	14.52 ± 0.01	-143 ± 5	-67 ± 4	3.43 ± 0.01	*M7*[a]	37	0.3	[b]
2MASS J13284331+0758378		13:28:34.69	+08:08:18.9	16.45 ± 0.01	-145 ± 8	-60 ± 9	4.07 ± 0.04	M8.5	595	1.3	
2MASS J13284331+0758378		13:28:35.49	+08:08:19.5	15.27 ± 0.01	-145 ± 8	-60 ± 9	3.07 ± 0.01	*M6*[a]	593	1.3	
BD+13 2724	G5	13:54:41.14	+12:47:47.5	18.29 ± 0.05	-103 ± 9	10 ± 11	3.68 ± 0.15	*M8*[a]	574	1.3	
LHS 2875	M2.5	14:12:11.72	-00:35:14.3	13.03 ± 0.01	-705 ± 8	221 ± 6	3.63 ± 0.01	M6	14	1.1	[e]
2MASS J14493646+0533379		14:49:46.20	+05:36:53.4	17.79 ± 0.04	-107 ± 10	-135 ± 10	4.35 ± 0.39	*L1*[a]	243	1.0	
2MASS J14511622+0922464		14:51:24.61	+09:20:05.0	14.35 ± 0.01	-156 ± 5	-33 ± 4	3.28 ± 0.01	*M6.5*[a]	204	1.3	
G 66-40		14:54:08.08	+00:53:25.6	15.07 ± 0.01	-270 ± 9	35 ± 9	3.84 ± 0.01	*M8.5*[a]	23	0.3	
2MASS J14552241+0419361		14:55:23.27	+04:19:48.6	16.12 ± 0.01	-137 ± 11	-39 ± 10	3.24 ± 0.02	*M6.5*[a]	18	1.4	
USNO-B1.0 0988-00251407		14:59:35.25	+08:57:51.2	17.92 ± 0.03	-172 ± 10	-83 ± 7	> 3.4	T4.5	386	1.4	[f]
LHS 3020	K8V	15:04:57.66	+05:38:00.8	16.59 ± 0.02	-616 ± 11	-523 ± 9	7.26 ± 0.51	T6.5	64	1.4	[c]
G 151-59	K0	15:25:57.45	-02:04:56.4	17.85 ± 0.05	179 ± 9	-158 ± 10	4.43 ± 0.16	*L1*[a]	46	0.6	
TYC 2032-546-1		15:32:52.33	+28:51:28.5	18.39 ± 0.06	-142 ± 9	-131 ± 9	> 2.9	> *M6*[a]	10	1.5	

[a] Indicates an estimated spectral type based on $i - J$ colour using Hawley et al. (2002).
[b] Deacon et al. (2009b)
[c] Scholz (2010)
[d] Faherty et al. (2010)
[e] Luyten (1979a)
[f] Day-Jones et al. (2011)

TABLE A.4: Astrometry for 41 genuine high proper motion ($> 300 mas\ yr^{-1}$) sources from the LAS proper motion catalogue. Coordinates are those of the UKIDSS LAS (J1 epoch), converted to 2000.0 epoch using the measured proper motion values. Proper motions are given in units of $mas\ yr^{-1}$.

Name	α_{J2000}	δ_{J2000}	$\mu_\alpha \cos\delta$	μ_δ	alternate $\mu_\alpha \cos\delta$	alternate μ_δ	alternate μ source
LP 365-11	07:28:25.75	+24:31:51.9	136 ± 6	-315 ± 6	148 ± 8	-321 ± 8	LSPM
LP 65-25	07:35:02.85	+24:57:04.4	201 ± 5	-251 ± 6	199 ± 8	-238 ± 8	LSPM
2MASS J07414920+2351275	07:41:49.18	+23:51:27.8	-262 ± 11	-212 ± 9	-250 ± 12	-116 ± 13	[a]
LSR J0745+2627	07:45:08.95	+26:27:06.4	527 ± 12	-719 ± 13	496 ± 8	-744 ± 8	LSPM
2MASS J07474639+2605167	07:47:46.39	+26:05:17.5	-189 ± 9	-245 ± 10	-253 ± 49	-170 ± 50	[b]
LP 366-18	07:49:17.18	+21:03:35.8	69 ± 9	-304 ± 9	65 ± 8	-299 ± 8	LSPM
LHS 1953	07:52:08.12	+27:00:01.5	609 ± 7	-658 ± 8	604 ± 8	-667 ± 8	LSPM
LP 366-27	07:56:40.85	+23:36:35.6	74 ± 7	-305 ± 7	93 ± 8	-307 ± 8	LSPM
2MASS J08044064+2239502	08:04:40.63	+22:39:49.7	12 ± 10	-320 ± 11	4 ± 8	-336 ± 8	LSPM
LP 424-14	08:09:40.24	+19:32:04.3	-396 ± 7	-109 ± 6	-398 ± 8	-110 ± 8	LSPM
ULAS J081045.24+222841.9	08:10:45.25	+22:28:44.1	-20 ± 10	-306 ± 8			
ULAS J081127.84+203925.7	08:11:27.82	+20:39:28.4	40 ± 8	-460 ± 8			
LHS 6139	08:11:27.90	+20:39:26.2	32 ± 8	-461 ± 8	37 ± 8	-467 ± 8	LSPM
G 40-12	08:13:24.20	+26:57:10.6	351 ± 11	-253 ± 7	340 ± 8	-259 ± 8	LSPM
LP 367-56	08:16:36.29	+23:06:16.1	96 ± 8	-344 ± 5	84 ± 8	-350 ± 8	LSPM
EGGR 531	08:16:42.05	+21:37:36.0	-93 ± 9	-397 ± 6	-104 ± 8	-392 ± 8	LSPM
ULAS J082155.56+250939.8	08:21:55.79	+25:09:40.2	-448 ± 11	-62 ± 14			
LHS 2006	08:23:47.97	+24:56:57.7	237 ± 6	-479 ± 7	235 ± 8	-471 ± 8	LSPM
2MASS J08253258+2359306	08:25:32.59	+23:59:30.6	-6 ± 7	-327 ± 7	15 ± 8	-320 ± 8	LSPM
LP 311-21	08:28:35.05	+26:45:33.1	193 ± 11	-251 ± 11	199 ± 8	-239 ± 8	LSPM
2MASS J08332144+2300120	08:33:21.45	+23:00:11.8	65 ± 7	-314 ± 10	72 ± 8	-319 ± 8	LSPM
LSPM J0836+2432	08:36:18.07	+24:32:56.7	238 ± 10	-499 ± 13	231 ± 8	-496 ± 8	LSPM
LP 321-30	08:46:01.27	+27:23:07.5	-108 ± 11	-447 ± 5	-103 ± 8	-443 ± 8	LSPM
ULAS J085335.33+285902.4	08:53:35.59	+28:59:07.0	-471 ± 20	-629 ± 11			
LP 260-3	09:16:06.52	+32:56:03.0	-229 ± 8	-238 ± 7	-236 ± 8	-229 ± 8	LSPM
LP 313-36	09:17:43.21	+30:56:50.9	-23 ± 8	-304 ± 6	-21 ± 8	-306 ± 8	LSPM
WD 0921+315	09:24:30.86	+31:20:33.6	-204 ± 13	-369 ± 10	-193 ± 8	-378 ± 8	LSPM
2MASS J15052821+3115037	15:05:28.21	+31:15:02.9	-20 ± 6	-512 ± 7	-37	-529	[c]
LP 272-48	15:10:38.43	+33:10:16.9	-43 ± 7	-361 ± 7	-45 ± 8	-365 ± 8	LSPM
LP 327-24	15:11:51.21	+30:33:06.2	-397 ± 8	-283 ± 8	-393 ± 8	-265 ± 8	LSPM
ULAS J151354.98+303543.9	15:13:54.91	+30:35:46.2	156 ± 8	-421 ± 9			
LHS 3042	15:14:26.02	+30:23:34.0	-583 ± 9	-9 ± 7	-603 ± 8	-5 ± 8	LSPM
LHS 3063	15:21:51.72	+30:48:26.2	-412 ± 8	341 ± 8	-413 ± 8	339 ± 8	LSPM
2MASS J15593876+2550362	15:59:38.80	+25:50:36.3	-358 ± 10	108 ± 10	-328 ± 37	119 ± 37	[b]
ULAS J160036.59+284305.7	16:00:36.70	+28:43:04.2	-228 ± 13	228 ± 12			
NLTT 41963	16:05:52.82	+25:11:38.8	-337 ± 7	-5 ± 7	-339 ± 8	-4 ± 8	LSPM
NLTT 42004	16:06:35.73	+24:28:40.9	-93 ± 5	-309 ± 4	-86 ± 8	-325 ± 8	LSPM
NLTT 42650	16:22:40.15	+29:19:13.0	-298 ± 8	-226 ± 9	-296 ± 8	-218 ± 8	LSPM
LP 330-15	16:26:24.56	+28:56:26.0	-151 ± 9	-304 ± 9	-152 ± 8	-298 ± 8	LSPM
LHS 3198	16:27:40.18	+29:27:15.1	-173 ± 7	-532 ± 8	-156 ± 8	-537 ± 8	LSPM
LSPM J1641+3210	16:41:43.41	+32:10:39.0	-350 ± 6	29 ± 6	-370 ± 8	37 ± 8	LSPM

[a] Casewell et al. (2008)
[b] Zhang et al. (2010)
[c] Sheppard and Cushing (2009), stated total proper motion uncertainty is about 10%

TABLE A.5: SDSS optical and UKIDSS near infrared photometry for 41 high proper motion ($> 300\ mas\ yr^{-1}$) sources from the LAS proper motion catalogue. J band magnitude is first epoch UKIDSS LAS. I adopt 0.02 magnitudes as a baseline uncertainty on all photometry.

Name	u	g	r	i	z	Y	J	H	K
LP 365-11	20.59 ± 0.05	17.98 ± 0.01	16.59 ± 0.01	16.02 ± 0.01	15.73 ± 0.01	14.980 ± 0.004	14.525 ± 0.010	14.043 ± 0.004	13.865 ± 0.004
LP 65-25	20.17 ± 0.05	17.62 ± 0.01	16.24 ± 0.00	15.67 ± 0.00	15.34 ± 0.01	14.581 ± 0.003	14.178 ± 0.010	13.673 ± 0.003	13.448 ± 0.004
2MASS J07414920+2351275	25.44 ± 0.63	24.31 ± 0.43	24.34 ± 0.52	24.85 ± 0.41	19.56 ± 0.06	17.129 ± 0.013	15.880 ± 0.010	16.104 ± 0.023	16.277 ± 0.037
LSR J0745+2627	22.65 ± 0.24	19.99 ± 0.02	18.69 ± 0.01	18.23 ± 0.01	17.96 ± 0.02	17.389 ± 0.014	17.122 ± 0.013	17.087 ± 0.051	17.184 ± 0.080
2MASS J07474639+2605167	25.35 ± 0.68	25.37 ± 0.56	23.86 ± 0.42	20.68 ± 0.04	18.86 ± 0.03	17.547 ± 0.016	16.679 ± 0.011	16.182 ± 0.020	15.778 ± 0.025
LP 366-18	21.78 ± 0.14	19.49 ± 0.01	18.07 ± 0.01	17.51 ± 0.01	17.17 ± 0.01	16.448 ± 0.008	15.965 ± 0.010	15.531 ± 0.009	15.375 ± 0.012
LHS 1953	20.29 ± 0.04	17.50 ± 0.01	15.93 ± 0.00	15.27 ± 0.00	14.88 ± 0.01	14.106 ± 0.002	13.648 ± 0.010	13.228 ± 0.002	13.027 ± 0.003
LP 366-27	21.79 ± 0.16	19.24 ± 0.01	17.79 ± 0.01	16.46 ± 0.00	15.75 ± 0.01	14.896 ± 0.004	14.376 ± 0.010	13.934 ± 0.004	13.652 ± 0.005
2MASS J08044064+2239502	19.78 ± 0.03	18.28 ± 0.01	17.60 ± 0.01	17.39 ± 0.01	17.31 ± 0.01	16.818 ± 0.011	16.693 ± 0.010	16.832 ± 0.034	17.238 ± 0.072
LP 424-14	20.72 ± 0.06	18.07 ± 0.01	16.62 ± 0.00	15.08 ± 0.00	14.26 ± 0.01	13.332 ± 0.002	12.761 ± 0.010	12.365 ± 0.001	11.997 ± 0.002
ULAS J081045.24+222841.9	25.41 ± 0.72	22.20 ± 0.09	20.28 ± 0.03	18.82 ± 0.01	18.02 ± 0.02	17.189 ± 0.013	16.605 ± 0.010	16.185 ± 0.016	15.952 ± 0.023
ULAS J081127.84+203925.7	22.67 ± 0.56	18.48 ± 0.02	17.49 ± 0.01	17.76 ± 0.02	16.98 ± 0.02	15.999 ± 0.007	15.519 ± 0.010	15.110 ± 0.008	14.908 ± 0.012
LHS 6139	17.77 ± 0.01	15.84 ± 0.00	15.73 ± 0.01	14.25 ± 0.00	13.98 ± 0.00	12.874 ± 0.001	12.448 ± 0.010	11.996 ± 0.001	11.778 ± 0.001
G 40-12	18.15 ± 0.01	15.82 ± 0.00	14.69 ± 0.00	14.83 ± 0.01	13.97 ± 0.00	13.218 ± 0.002	12.812 ± 0.010	12.292 ± 0.001	12.111 ± 0.002
LP 367-56	21.56 ± 0.12	18.81 ± 0.01	17.33 ± 0.01	16.76 ± 0.01	16.40 ± 0.01	15.674 ± 0.005	15.217 ± 0.010	14.776 ± 0.006	14.613 ± 0.008
EGGR 531	17.95 ± 0.01	17.18 ± 0.00	16.84 ± 0.00	16.71 ± 0.00	16.70 ± 0.01	16.168 ± 0.006	15.954 ± 0.010	15.728 ± 0.009	15.665 ± 0.016
ULAS J082155.56+250939.8						18.610 ± 0.043	17.226 ± 0.015	17.290 ± 0.065	17.232 ± 0.095
LHS 2006	21.78 ± 0.14	18.72 ± 0.01	17.08 ± 0.00	16.08 ± 0.00	15.54 ± 0.01	14.739 ± 0.003	14.254 ± 0.010	13.791 ± 0.003	13.534 ± 0.004
2MASS J08253258+2359306	22.68 ± 0.26	19.79 ± 0.02	18.31 ± 0.01	16.53 ± 0.00	15.59 ± 0.01	14.604 ± 0.003	14.068 ± 0.010	14.14 ± 0.03 [a]	13.336 ± 0.004
LP 311-21	21.30 ± 0.10	18.62 ± 0.01	17.15 ± 0.00	16.52 ± 0.00	16.13 ± 0.01	15.359 ± 0.005	14.934 ± 0.010	14.430 ± 0.006	14.210 ± 0.008
2MASS J08332144+2300120	21.95 ± 0.16	19.03 ± 0.01	17.52 ± 0.01	15.80 ± 0.00	14.88 ± 0.01	13.903 ± 0.002	13.359 ± 0.010	12.923 ± 0.002	12.614 ± 0.002
LSPM J0836+2432	20.30 ± 0.05	19.51 ± 0.01	18.90 ± 0.01	18.74 ± 0.01	18.69 ± 0.03	18.197 ± 0.026	17.985 ± 0.028	17.909 ± 0.096	17.968 ± 0.162
LP 321-30	21.93 ± 0.16	19.01 ± 0.01	17.33 ± 0.00	16.44 ± 0.00	15.95 ± 0.01	15.136 ± 0.004	14.643 ± 0.010	14.176 ± 0.004	13.906 ± 0.006
ULAS J085335.33+285902.4	23.16 ± 0.50	24.12 ± 0.43	24.09 ± 0.62	22.17 ± 0.20	20.33 ± 0.13	18.930 ± 0.129	17.705 ± 0.031	16.936 ± 0.123	16.425 ± 0.044
LP 260-3	22.84 ± 0.28	19.81 ± 0.02	18.20 ± 0.01	17.26 ± 0.01	16.69 ± 0.01	15.891 ± 0.006	15.403 ± 0.010	14.931 ± 0.010	14.670 ± 0.012
LP 313-36	21.86 ± 0.13	19.20 ± 0.01	17.61 ± 0.01	16.80 ± 0.01	16.33 ± 0.01	15.537 ± 0.004	15.041 ± 0.010	14.591 ± 0.005	14.323 ± 0.007
WD 0921+315	20.66 ± 0.06	18.73 ± 0.01	17.93 ± 0.01	17.64 ± 0.01	17.50 ± 0.02	16.927 ± 0.009	16.631 ± 0.010	16.408 ± 0.022	16.401 ± 0.038
2MASS J15052821+3115037	23.27 ± 0.42	20.77 ± 0.03	19.09 ± 0.01	17.71 ± 0.01	16.96 ± 0.01	16.131 ± 0.007	15.547 ± 0.010	15.115 ± 0.007	14.810 ± 0.010
LP 272-48	20.91 ± 0.06	18.15 ± 0.01	16.67 ± 0.01	15.35 ± 0.01	14.62 ± 0.01	13.768 ± 0.002	13.239 ± 0.010	12.811 ± 0.002	12.555 ± 0.002
LP 327-24	21.62 ± 0.11	19.18 ± 0.01	17.81 ± 0.01	15.81 ± 0.00	14.63 ± 0.00	13.479 ± 0.002	12.843 ± 0.010	12.259 ± 0.001	11.854 ± 0.001
ULAS J151354.98+303543.9	24.60 ± 0.76	21.44 ± 0.04	20.05 ± 0.02	17.31 ± 0.01	15.79 ± 0.01	14.543 ± 0.003	13.850 ± 0.010	13.343 ± 0.002	12.911 ± 0.002
LHS 3042	23.30 ± 0.42	20.36 ± 0.02	18.72 ± 0.01	16.90 ± 0.01	15.92 ± 0.01	14.973 ± 0.004	14.401 ± 0.010	14.015 ± 0.003	13.697 ± 0.004
LHS 3063	20.25 ± 0.05	18.01 ± 0.01	16.52 ± 0.00	15.03 ± 0.00	14.21 ± 0.00	13.260 ± 0.001	12.763 ± 0.010	12.344 ± 0.001	12.043 ± 0.001
2MASS J15593876+2550362	24.86 ± 0.59	24.38 ± 0.33	23.71 ± 0.30	20.43 ± 0.03	18.57 ± 0.03	17.293 ± 0.017	16.442 ± 0.010	16.099 ± 0.014	15.647 ± 0.018
ULAS J160036.59+284305.7	23.95 ± 0.79	23.82 ± 0.35	23.51 ± 0.38	21.89 ± 0.16	21.49 ± 0.42	18.856 ± 0.060	17.650 ± 0.029	16.833 ± 0.025	16.136 ± 0.031
NLTT 41963	20.42 ± 0.05	18.12 ± 0.01	16.66 ± 0.01	15.17 ± 0.00	14.37 ± 0.01	13.393 ± 0.002	12.897 ± 0.010	12.481 ± 0.001	12.179 ± 0.002
NLTT 42004	22.35 ± 0.17	19.46 ± 0.01	17.83 ± 0.01	16.96 ± 0.01	16.45 ± 0.01	15.596 ± 0.005	15.131 ± 0.010	14.638 ± 0.004	14.406 ± 0.008
NLTT 42650	21.99 ± 0.16	19.85 ± 0.01	18.88 ± 0.01	18.49 ± 0.01	18.33 ± 0.02	17.743 ± 0.022	17.462 ± 0.022	17.355 ± 0.039	17.305 ± 0.083
LP 330-15	24.10 ± 0.76	20.04 ± 0.02	18.39 ± 0.01	17.11 ± 0.01	16.47 ± 0.01	15.579 ± 0.005	15.050 ± 0.010	14.612 ± 0.005	14.312 ± 0.006
LHS 3198	19.73 ± 0.04	17.10 ± 0.00	15.62 ± 0.00	15.06 ± 0.00	14.71 ± 0.00	13.923 ± 0.002	13.498 ± 0.010	13.016 ± 0.002	12.837 ± 0.002
LSPM J1641+3210	23.22 ± 0.38	20.74 ± 0.03	19.22 ± 0.01	16.95 ± 0.01	15.71 ± 0.01	14.642 ± 0.003	14.012 ± 0.010	13.574 ± 0.003	13.223 ± 0.003

[a] No LAS H band data available, 2MASS H magnitude given.

TABLE A.6: Previously unidentified high proper motion sources in the GPS. The coordinates given are at epoch 2000.0

α	δ	$\mu_\alpha \cos\delta$	μ_δ	r	i	J	H	K
03:20:43.87	+59:18:23.2	146±7	-137±9		19.64±0.14	16.20±0.02	15.60±0.02	15.11±0.02
03:28:47.25	+59:10:56.0	176±5	-102±7	18.64±0.03	16.89±0.02	15.08±0.02	14.63±0.02	14.31±0.02
03:39:05.89	+59:35:42.0	318±6	-294±6		19.26±0.11	15.34±0.02	14.79±0.02	14.23±0.02
03:46:24.92	+54:36:26.5	128±6	-162±7	18.78±0.02	17.52±0.02	15.85±0.02	15.27±0.02	15.01±0.02
03:46:57.15	+56:40:33.5	17±5	-225±5		17.91±0.05	15.04±0.02	14.63±0.02	14.23±0.02
03:49:02.69	+55:34:19.8	186±7	-235±8	19.49±0.03	17.98±0.02	16.25±0.02	15.71±0.02	15.41±0.02
03:53:04.59	+47:55:45.6	-81±6	-237±5		19.54±0.18	15.78±0.02	15.17±0.02	14.59±0.02
03:55:31.53	+47:44:00.6	438±12	-168±11			16.20±0.02	16.58±0.02	16.50±0.04
04:02:29.42	+48:12:56.6	127±10	-224±10	18.00±0.02	17.46±0.02	16.82±0.02	16.57±0.02	16.54±0.04
04:06:21.18	+47:47:57.1	114±8	-199±8	19.12±0.02	17.94±0.03	16.38±0.02	15.79±0.02	15.51±0.02
04:06:33.73	+47:15:16.7	71±7	-220±7	21.09±0.14	17.94±0.03			13.80±0.02
04:07:29.52	+58:38:55.9	81±7	-318±7	19.61±0.03	16.57±0.02			13.02±0.02
04:08:23.65	+47:05:03.0	88±8	-337±6	21.30±0.14	18.12±0.03	14.68±0.02	14.27±0.02	13.77±0.02
04:13:22.06	+44:44:36.6	162±7	-183±4	20.75±0.27	17.66±0.03	14.69±0.02	14.15±0.02	13.67±0.02
04:22:28.37	+45:17:39.8	273±7	-13±6		17.80±0.03	15.53±0.02	15.14±0.02	14.78±0.02
04:30:46.79	+49:55:49.7	157±8	-170±9	19.92±0.04	17.47±0.02	15.37±0.02	14.95±0.02	14.62±0.02
04:31:21.84	+47:07:38.3	403±7	-121±9	19.06±0.04	17.45±0.03	15.72±0.02	15.16±0.02	14.89±0.02
04:34:03.07	+49:53:40.0	91±8	-183±8	19.10±0.03	16.61±0.02			13.50±0.02
04:35:19.94	+43:06:09.4	148±4	-168±5	15.86±0.02	13.92±0.02	11.98±0.02	11.44±0.02	11.13±0.02
04:43:30.77	+46:45:34.4	236±6	-105±5		18.74±0.10[a]	15.85±0.02	15.44±0.02	15.00±0.02
04:44:21.20	+42:02:36.2	110±4	-170±4	18.92±0.04	16.70±0.02			13.91±0.02
04:46:39.22	+40:54:52.9	191±4	-162±5		20.90±0.51[a]	16.84±0.02	16.21±0.02	15.60±0.02
04:51:43.83	+45:49:58.0	365±5	-574±5		13.22±0.02	11.67±0.02[b]	11.43±0.02[b]	10.65±0.02[b]
04:54:09.74	+46:16:09.4	195±13	-133±13		19.48±0.11	17.38±0.02	16.94±0.02	16.59±0.04
05:07:19.98	+34:58:52.6	60±3	-277±4	19.45±0.03	16.99±0.02	14.68±0.02	14.23±0.02	13.83±0.02
05:15:37.00	+44:48:20.1	58±5	-280±5	16.93±0.02	15.83±0.02	14.60±0.02	14.13±0.02	13.90±0.02
05:18:17.90	+42:11:31.9	-15±5	-238±3			14.89±0.02	14.31±0.02	13.80±0.02

[a] Based on my own aperture photometry due to the source being a dropout in IPHAS i band catalogue but visible in image.
[b] Based on my own aperture photometry, survey photometry was deemed unreliable due to nearby bright companion.
[c] Undetected in IPHAS source identification. Profile fit photometry performed to measure this magnitude.
[d] Undetected in IPHAS i band, 3σ limit of field given.

Table A.6 continued.

α	δ	$\mu_\alpha \cos\delta$	μ_δ	r	i	J	H	K
05:21:24.85	+39:08:14.1	121±4	-237±4	18.50±0.02	17.60±0.03	16.93±0.02	16.45±0.02	16.26±0.03
05:22:49.68	+43:51:57.7	103±4	-208±5	16.58±0.02	15.09±0.02	13.53±0.02	13.05±0.02	12.77±0.02
05:22:50.00	+39:41:28.6	205±3	-119±3	14.54±0.02	13.31±0.02	11.97±0.02	11.47±0.02	11.21±0.02
05:25:55.61	+37:22:11.9	129±7	-175±7		19.48±0.10	17.43±0.03	17.01±0.04	16.66±0.05
05:25:59.58	+33:06:06.3	85±6	-193±7	20.17±0.08	17.52±0.02	15.19±0.02	14.74±0.02	14.33±0.02
05:27:21.68	+42:58:36.5	155±5	-304±5	16.59±0.02	14.94±0.02	13.34±0.02	12.89±0.02	12.61±0.02
05:33:01.65	+37:38:20.0	44±4	-245±4		>20.54[d]	16.79±0.02	15.94±0.02	15.16±0.02
05:34:49.33	+40:37:01.4	-40±4	-277±4	20.84±0.08	18.28±0.04	16.05±0.02	15.63±0.02	15.32±0.02
05:35:42.81	+26:49:20.4	173±7	-364±8		18.49±0.05	15.77±0.02	15.35±0.02	14.96±0.02
05:40:41.35	+34:00:24.1	142±6	-172±6	16.07±0.02	15.09±0.02	13.85±0.02	13.28±0.02	13.05±0.02
05:41:47.12	+30:20:16.2	177±6	-97±6	17.42±0.02	16.09±0.02	14.63±0.02	14.07±0.02	13.80±0.02
05:44:14.33	+34:55:42.9	64±4	-205±4	21.31±0.13	18.56±0.04			14.76±0.02
05:44:57.43	+37:05:04.1	-10±3	-228±4	21.69±0.41	18.01±0.04	13.90±0.02	13.10±0.02	12.36±0.02
05:45:02.32	+33:58:31.6	66±6	-206±6	20.62±0.09	17.56±0.02	15.11±0.02	14.68±0.02	14.29±0.02
05:47:25.11	+35:42:43.0	134±4	-190±3	19.05±0.03	17.72±0.03	16.30±0.02	15.83±0.02	15.56±0.02
05:47:33.08	+38:03:05.5	198±5	-181±4	17.72±0.02	16.79±0.02	15.73±0.02	15.20±0.02	15.02±0.02
05:49:02.26	+22:23:30.5	10±9	-249±9	19.51±0.03	16.57±0.02	13.43±0.02	12.81±0.02	12.34±0.02
05:54:03.58	+20:28:36.8	209±6	-221±7	20.17±0.20	18.23±0.20	15.85±0.02	15.44±0.02	15.15±0.02
05:54:07.07	+21:18:20.0	126±11	-189±11	20.21±0.06	18.80±0.06	17.25±0.02	16.81±0.03	16.56±0.04
05:54:46.14	+19:31:13.6	174±8	-168±8	19.39±0.04	17.68±0.02	16.11±0.02	15.65±0.02	15.35±0.02
05:55:39.76	+22:52:55.3	18±10	-243±9	20.42±0.07	18.64±0.06	16.80±0.02	16.31±0.02	16.01±0.02
05:57:17.90	+34:37:14.1	-69±3	-197±3		19.34±0.09	16.09±0.02	15.66±0.02	15.20±0.02
06:02:31.77	+22:15:53.3	19±13	-280±13		>20.57[d]	17.82±0.03	17.29±0.04	16.67±0.05
06:03:45.45	+20:16:44.8	39±10	-200±10		19.92±0.27[a]	17.29±0.02	16.82±0.02	16.47±0.04
06:05:18.50	+19:48:49.9	60±5	-216±6	18.46±0.02	16.02±0.02	13.80±0.02	13.37±0.02	13.01±0.02
06:10:37.22	+12:58:48.6	14±9	-228±6	20.82±0.15	17.69±0.03	14.88±0.02	14.38±0.02	13.97±0.02
06:21:09.24	+08:23:15.6	164±7	-115±8	19.19±0.02	17.29±0.02	15.42±0.02	14.99±0.02	14.73±0.02
06:24:40.48	+06:48:22.3	94±5	-197±5	19.48±0.03	18.26±0.04	16.78±0.02	16.34±0.02	16.04±0.03
06:27:27.79	+05:15:37.5	119±6	-319±6	20.75±0.32	18.16±0.04	16.22±0.02	15.81±0.02	15.51±0.02
06:27:50.06	+01:43:29.6	213±4	-154±5		>20.35[d]	16.89±0.02	16.30±0.02	15.66±0.02
06:30:50.26	-00:10:49.7	-43±4	-291±4	18.48±0.04	16.56±0.02	14.71±0.02	14.25±0.02	13.97±0.02
06:32:32.21	+01:53:49.8	55±4	-216±4	18.85±0.05	17.59±0.03	16.13±0.02	15.69±0.02	15.45±0.02
06:32:35.71	+03:14:03.7	-167±5	166±6		17.93±0.03	14.61±0.02	14.06±0.02	13.58±0.02

Table A.6 continued.

α	δ	$\mu_\alpha \cos\delta$	μ_δ	r	i	J	H	K
06:33:33.37	+10:01:27.4	184±15	-214±12	19.28±0.20	19.21±0.20	15.15±0.02	14.72±0.02	14.21±0.02
06:43:16.71	-06:10:10.3	239±4	-109±4			14.96±0.02	14.52±0.02	14.23±0.02
06:44:16.75	+03:16:17.9	101±3	-280±3		17.25±0.18[a]	14.06±0.02	13.47±0.02	12.99±0.02
06:45:04.23	-02:52:49.3	149±5	-231±4	18.55±0.02	17.37±0.03	16.00±0.02	15.50±0.02	15.22±0.02
06:45:33.53	-05:30:47.2	58±4	-218±3			14.28±0.02	13.72±0.02	13.37±0.02
06:45:49.25	-05:22:19.9	297±4	-61±5			16.44±0.02	15.90±0.02	15.70±0.02
06:47:12.29	+08:24:40.0	150±5	-195±6		20.22±0.22[a]	16.39±0.02	15.76±0.02	15.17±0.02
06:47:24.04	-03:38:38.7	63±4	-203±4			15.85±0.02	15.41±0.02	15.16±0.02
06:50:05.51	-03:03:32.8	34±3	-270±3	17.49±0.20	15.45±0.20	13.10±0.02	12.52±0.02	12.24±0.02
06:52:10.42	-01:20:35.5	194±6	-233±9	18.49±0.02	17.55±0.02	16.17±0.02	15.64±0.02	15.38±0.02
06:53:27.95	+02:39:43.8	-15±3	210±4	16.91±0.02	16.58±0.02	16.24±0.02	16.00±0.02	15.94±0.02
06:54:12.55	-06:27:31.0	260±4	-271±3					14.99±0.02
06:55:37.37	-06:38:04.2	66±3	-281±4			14.01±0.02	13.48±0.02	13.11±0.02
06:56:17.02	+04:21:05.7	35±4	-228±4	19.35±0.02	17.61±0.02	15.97±0.02	15.51±0.02	15.22±0.02
06:58:45.22	-01:15:52.6	271±9	-293±8	17.72±0.02	17.15±0.02	16.57±0.02	16.32±0.02	16.41±0.06
07:01:52.79	-13:02:31.2	39±5	-230±4	19.47±0.04	18.27±0.02	16.68±0.02	16.21±0.02	15.98±0.03
07:05:18.20	+01:29:10.4	167±3	-268±3		17.85±0.02	14.99±0.02	14.48±0.02	14.07±0.02
07:06:52.01	-17:05:19.1	-334±4	-71±4			12.75±0.02	12.37±0.02	12.00±0.02
07:07:29.26	-02:49:48.6	61±3	194±4			12.06±0.02	11.52±0.02	11.29±0.02
07:09:35.53	-15:08:08.1	-113±4	-294±4			13.38±0.02	12.95±0.02	12.67±0.02
07:09:39.72	-12:38:46.4	-47±6	-267±5	16.60±0.02	15.12±0.02	13.53±0.02	13.08±0.02	12.82±0.02
07:12:18.30	-07:59:33.7	61±3	-213±3			13.35±0.02	12.79±0.02	12.64±0.02
07:12:44.28	-12:58:02.4	151±5	-309±5	19.48±0.03	17.72±0.02	15.64±0.02	15.15±0.02	14.84±0.02
07:17:12.18	-14:55:13.8	-16±6	-244±8			13.48±0.02	13.02±0.02	12.74±0.02
07:17:28.15	-15:05:17.6	62±4	-223±5	13.40±0.02	12.85±0.02	11.93±0.02	11.35±0.02	11.35±0.02
07:22:22.47	-14:51:22.4	-347±6	133±4	15.95±0.02	13.92±0.02	11.77±0.02	11.79±0.02	11.00±0.02
07:24:15.02	-12:47:31.2	174±5	-228±5	19.16±0.02	17.90±0.02	16.37±0.02	15.90±0.02	15.68±0.02
07:28:53.82	-14:01:10.2	-270±4	-67±3			13.95±0.02	13.51±0.02	13.17±0.02
07:29:45.63	-07:33:49.1	208±4	-114±4				14.57±0.02	14.21±0.02
07:40:28.99	-13:00:44.1	31±4	221±5			11.77±0.02	10.74±0.02	11.05±0.02
19:55:30.48	+26:13:13.1	-185±10	-96±10		>20.69[d]	18.48±0.05	17.66±0.04	16.99±0.07
19:59:24.81	+39:31:56.1	-62±9	321±7	13.74±0.02	12.75±0.02	11.02±0.02	10.17±0.02	11.37±0.02
20:04:09.96	+24:26:35.3	-109±5	-168±5		20.04±0.22	16.90±0.02	16.48±0.02	16.09±0.03

Table A.6 continued.

α	δ	$\mu_\alpha \cos\delta$	μ_δ	r	i	J	H	K
20:05:30.35	+36:35:50.7	-126±6	-184±6			17.47±0.02	16.61±0.02	16.01±0.04
20:05:35.97	+30:09:24.8	96±3	-216±3	19.45±0.04	16.50±0.02	13.92±0.02	13.53±0.02	13.13±0.02
20:06:11.93	+24:07:53.3	226±3	226±3		16.98±0.02	13.96±0.02	13.42±0.02	13.00±0.02
20:08:37.94	+39:20:56.1	-45±11	-199±12	19.85±0.06	17.39±0.02	15.17±0.02	14.69±0.02	14.34±0.02
20:09:12.58	+37:12:12.5	-137±4	-199±5	24.63±3.30	19.50±0.11	15.73±0.02	15.11±0.02	14.58±0.02
20:14:39.96	+38:50:23.4	-218±6	-249±6	16.09±0.02	14.16±0.02	12.23±0.02	11.71±0.02	11.54±0.02
20:16:08.23	+42:00:32.8	237±6	152±6	18.67±0.02	16.50±0.02	14.46±0.02	14.11±0.02	13.75±0.02
20:16:44.23	+41:40:43.5	-23±7	-211±7	16.21±0.02	15.39±0.02	14.27±0.02	13.76±0.02	13.59±0.02
20:17:31.27	+33:53:59.5	-247±4	24±4		>20.44[d]	17.35±0.02	16.61±0.03	16.01±0.03
20:19:02.41	+44:53:16.3	-173±6	-140±5	17.21±0.02	15.35±0.02	13.51±0.02	13.06±0.02	12.80±0.02
20:21:12.34	+37:25:05.9	-171±3	-234±3	19.69±0.05	16.64±0.02	13.98±0.02	13.46±0.02	13.10±0.02
20:25:28.30	+40:13:19.7	184±6	106±7	16.74±0.02	15.07±0.02	13.42±0.02	12.95±0.02	12.68±0.02
20:28:02.85	+42:05:51.6	-169±23	-189±20					16.47±0.06
20:28:10.47	+41:01:19.0	177±4	123±4	18.90±0.02	16.37±0.02	14.00±0.02	13.51±0.02	13.13±0.02
20:31:32.54	+43:03:19.4	259±5	326±7		20.29±0.17	15.85±0.02	15.02±0.02	14.27±0.02
20:32:53.25	+36:38:17.0	28±7	200±7		19.32±0.12	17.03±0.02	16.67±0.02	16.37±0.04
20:33:46.52	+37:50:58.3	197±4	49±5	18.35±0.02	16.23±0.02	14.11±0.02	13.59±0.02	13.26±0.02
20:43:14.92	+50:46:22.5	170±7	199±7			15.12±0.02	14.65±0.02	14.24±0.02
20:48:00.13	+50:38:19.3	99±8	248±8			16.30±0.02	16.37±0.02	16.32±0.03
20:53:10.56	+36:27:37.6	95±4	219±4			12.29±0.02	11.33±0.02	11.46±0.02
20:55:07.49	+38:46:44.4	139±5	155±5	19.81±0.07	17.83±0.02	16.02±0.02	15.56±0.02	15.28±0.02
20:55:25.17	+45:06:10.4	40±3	-236±3	18.16±0.02	15.97±0.02	13.83±0.02	13.37±0.02	13.02±0.02
20:55:27.42	+38:12:17.1	176±4	193±5	18.53±0.04	16.76±0.02	15.00±0.02	14.55±0.02	14.27±0.02
20:59:58.64	+41:25:13.7	-78±7	193±6		>20.54[d]	16.91±0.02	16.38±0.02	15.77±0.02
21:04:53.81	+41:46:28.3	154±4	141±4	17.50±0.02	15.40±0.02	13.43±0.02	12.98±0.02	12.65±0.02
21:05:57.74	+47:01:44.5	126±4	174±3	14.82±0.02	13.37±0.02	11.84±0.02	11.20±0.02	11.07±0.02
21:06:04.96	+50:19:54.9	-140±7	-174±7		19.69±0.12	15.95±0.02	15.52±0.02	15.06±0.02
21:07:35.11	+48:13:43.6	170±6	181±7	19.76±0.12	16.80±0.02	14.12±0.02	13.62±0.02	13.22±0.02
21:09:29.87	+50:24:34.5	132±5	-158±6	19.80±0.07	18.29±0.05	16.83±0.02	16.41±0.02	16.21±0.03
21:11:04.39	+48:00:21.9	193±3	127±3		14.60±0.02	12.72±0.02	12.21±0.02	11.87±0.02
21:11:54.34	+43:17:54.1	143±3	140±3	19.85±0.07	17.53±0.02	15.26±0.02	14.77±0.02	14.45±0.02
21:14:25.17	+50:10:15.9	296±5	30±4		20.00±0.19	16.08±0.02	15.30±0.02	14.51±0.02
21:18:59.25	+43:38:01.3	169±3	134±3		17.80±0.20[c]	14.74±0.20[b]	14.13±0.20[b]	13.81±0.20[b]

Table A.6 continued.

α	δ	$\mu_\alpha \cos\delta$	μ_δ	r	i	J	H	K
21:19:52.83	+48:26:12.0	151±4	216±3		20.37±0.26	15.98±0.02	15.32±0.02	14.74±0.02
21:20:11.58	+51:14:15.9	46±4	220±4	18.10±0.02	16.46±0.02	14.85±0.02	14.42±0.02	14.12±0.02
21:28:05.25	+56:34:16.6	155±8	135±8	18.95±0.02	17.61±0.02	16.16±0.02	15.65±0.02	15.41±0.02
21:29:19.99	+51:46:42.4	-92±4	214±4	21.59±0.17	18.37±0.04	17.47±0.02	17.27±0.04	14.88±0.02
21:30:48.11	+57:12:36.8	298±4	91±6	21.51±0.21	17.93±0.03	14.90±0.02	14.42±0.02	13.98±0.02
21:32:12.97	+44:52:29.3	172±6	145±7	19.61±0.06	17.97±0.03	16.39±0.02	15.92±0.02	15.67±0.02
21:41:15.07	+56:40:12.9	234±8	246±9	21.28±0.15	18.07±0.03	15.05±0.02	14.48±0.02	14.01±0.02
21:44:46.49	+50:52:26.6	-99±5	-203±4		18.62±0.05	15.62±0.02	15.12±0.02	14.71±0.02
21:52:50.45	+55:12:52.9	228±4	28±4	17.57±0.02	15.60±0.02	13.69±0.02	13.25±0.02	12.93±0.02
21:53:12.31	+53:51:49.6	243±4	30±4	19.67±0.07	17.33±0.02	15.19±0.02	14.76±0.02	14.44±0.02
22:00:15.74	+51:09:45.5	123±13	182±13			17.78±0.03	17.38±0.04	17.10±0.07
22:00:44.34	+54:21:55.6	218±4	126±4		20.07±0.24	16.32±0.02	15.71±0.02	15.20±0.02
22:01:56.74	+51:08:19.7	206±6	74±6	17.30±0.02	14.80±0.02	12.35±0.02	11.90±0.02	11.47±0.02
22:07:06.47	+53:52:53.3	154±4	215±3		20.31±0.22	16.22±0.02	15.59±0.02	15.00±0.02
22:07:15.68	+52:14:05.1	103±4	225±4	18.19±0.02	17.01±0.02	15.54±0.02	15.10±0.02	14.88±0.02
22:10:32.97	+52:55:51.2	206±6	112±7	13.69±0.02	11.82±0.02	11.89±0.02	11.28±0.02	11.06±0.02
22:11:49.28	+55:02:06.2	-121±3	-237±3	17.36±0.02	15.35±0.02	13.35±0.02	12.93±0.02	12.63±0.02
22:13:07.90	+52:55:08.7	-201±6	-38±6	18.65±0.02	16.27±0.02	14.02±0.02	13.49±0.02	13.16±0.02
22:17:30.73	+51:39:32.5	217±5	32±4	21.36±0.16	18.06±0.03	15.11±0.02	14.56±0.02	14.12±0.02
22:18:00.59	+56:02:15.1	108±4	227±4	17.88±0.02	17.21±0.02	16.58±0.02	16.40±0.02	16.42±0.04
22:18:17.08	+56:12:28.9	236±3	21±3	19.84±0.04	17.29±0.02	15.12±0.02	14.71±0.02	14.37±0.02
22:21:29.14	+55:56:00.1	106±5	176±4	18.47±0.02	16.68±0.02	14.95±0.02	14.48±0.02	14.20±0.02
22:21:35.00	+54:09:52.5	215±3	176±4	17.45±0.02	15.67±0.02	13.81±0.02	13.40±0.02	13.12±0.02
22:23:04.16	+54:28:00.8	166±6	124±6	20.13±0.12	18.78±0.10	17.36±0.02	16.92±0.03	16.66±0.05
22:32:30.30	+55:15:24.3	202±5	69±6	18.73±0.03	17.78±0.03	16.35±0.02	15.78±0.02	15.54±0.02
22:32:33.83	+52:35:22.5	229±5	38±5	16.34±0.02	14.49±0.02	12.77±0.02	12.34±0.02	12.05±0.02
22:33:16.60	+52:27:22.3	212±5	8±6	16.58±0.02	14.26±0.02	12.06±0.02	11.59±0.02	11.18±0.02

TABLE A.7: UKIDSS GPS proper motions and epoch 2000.0 coordinates for twelve recent WISE proper motion discoveries.

α	δ	$\mu_\alpha \cos\delta$	μ_δ	K	Discoverer
03:23:01.53	+56:26:00.8	289±6	-279±6	13.65±0.02	Luhman (2014a)
04:54:25.04	+40:04:10.4	388±4	-177±4	14.44±0.02	Luhman and Sheppard (2014)
05:32:52.18	+41:43:39.6	226±4	-274±4	11.66±0.02	Kirkpatrick et al. (2014)
06:48:37.95	+07:37:02.1	-54±6	-378±7	11.55±0.02	Luhman (2014a)
07:01:24.23	-13:34:13.8	215±3	166±3	11.14±0.02	Luhman (2014a)
20:06:17.71	+38:11:48.9	107±5	-309±6	11.98±0.02	Kirkpatrick et al. (2014)
20:28:59.19	+45:09:51.9	182±5	360±7	11.66±0.02	Luhman (2014a)
20:45:44.35	+50:53:48.1	254±5	286±5	11.65±0.02	Luhman (2014a)
21:10:06.33	+46:15:36.4	-199±3	-370±3	11.80±0.02	Luhman (2014a)
21:44:42.19	+47:44:05.5	-201±3	-231±3	13.43±0.02	Luhman (2014a)
22:22:33.43	+58:57:09.0	394±5	75±5	12.81±0.02	Luhman (2014a)
22:42:00.46	+58:16:40.3	18±3	-311±3	11.21±0.02	Kirkpatrick et al. (2014)

Bibliography

Abad, C., Vieira, K., Bongiovanni, A., et al., 2003. An extension of Herschel's method for dense and extensive catalogues. Application to the determination of solar motion. *A&A*, 397:345.

Abell, G.O., 1959. The National Geographic Society-Palomar Observatory Sky Survey. *Leaflet of the Astronomical Society of the Pacific*, 8:121.

Allard, F., Hauschildt, P.H., Alexander, D.R., et al., 2001. The Limiting Effects of Dust in Brown Dwarf Model Atmospheres. *ApJ*, 556:357.

Andrei, A.H., Smart, R.L., Penna, J.L., et al., 2011. Parallaxes of Southern Extremely Cool Objects. I. Targets, Proper Motions, and First Results. *AJ*, 141:54.

Andrei, A.H., Souchay, J., Zacharias, N., et al., 2009. The large quasar reference frame (LQRF). An optical representation of the ICRS. *A&A*, 505:385.

Artigau, É., Radigan, J., Folkes, S., et al., 2010. DENIS J081730.0-615520: An Overlooked Mid-T Dwarf in the Solar Neighborhood. *ApJ*, 718:L38.

Bakos, G.Á., Sahu, K.C., and Németh, P., 2002. Revised Coordinates and Proper Motions of the Stars in the Luyten Half-Second Catalog. *ApJ*, 141:187.

Barentsen, G., Farnhill, H.J., Drew, J.E., et al., 2014. The second data release of the INT Photometric Hα Survey of the Northern Galactic Plane (IPHAS DR2). *MNRAS*, 444:3230.

Beamín, J.C., Minniti, D., Gromadzki, M., et al., 2013. One more neighbor: The first brown dwarf in the VVV survey. *A&A*, 557:L8.

Becklin, E.E. and Zuckerman, B., 1988. A low-temperature companion to a white dwarf star. *Nature*, 336:656.

Bertelli, G., Bressan, A., Chiosi, C., et al., 1994. Theoretical isochrones from models with new radiative opacities. *A&A Supp.*, 106:275.

Boyd, M.R., Henry, T.J., Jao, W.C., et al., 2011a. The Solar Neighborhood. XXVII. Discovery of New Proper Motion Stars with $\mu \geq 0.18$" yr^{-1} in the Southern Sky with $16.5 < \mathrm{R}_{59F} \leq 18.0$. *AJ*, 142:92.

Boyd, M.R., Winters, J.G., Henry, T.J., et al., 2011b. The Solar Neighborhood. XXV. Discovery of New Proper Motion Stars with 0.40" yr^{-1} $> \mu \geq$ 0.18" yr^{-1} between Declinations -47° and 00°. *AJ*, 142:10.

Burgasser, A.J., 2004. T Dwarfs and the Substellar Mass Function. I. Monte Carlo Simulations. *ApJ*, 155:191.

Burgasser, A.J., Cushing, M.C., Kirkpatrick, J.D., et al., 2011. Fire Spectroscopy of Five Late-type T Dwarfs Discovered with the Wide-field Infrared Survey Explorer. *ApJ*, 735:116.

Burgasser, A.J., Geballe, T.R., Leggett, S.K., et al., 2006. A Unified Near-Infrared Spectral Classification Scheme for T Dwarfs. *ApJ*, 637:1067.

Burgasser, A.J., Gillon, M., Melis, C., et al., 2015. WISE J072003.20-084651.2: an Old and Active M9.5 + T5 Spectral Binary 6 pc from the Sun. *AJ*, 149:104.

Burningham, B., Cardoso, C.V., Smith, L., et al., 2013. 76 T dwarfs from the UKIDSS LAS: benchmarks, kinematics and an updated space density. *MNRAS*, 433:457.

Burningham, B., Leggett, S.K., Homeier, D., et al., 2011a. The properties of the T8.5p dwarf Ross 458C. *MNRAS*, 414:3590.

Burningham, B., Leggett, S.K., Lucas, P.W., et al., 2010. The discovery of a very cool binary system. *MNRAS*, 404:1952.

Burningham, B., Lucas, P.W., Leggett, S.K., et al., 2011b. The discovery of the T8.5 dwarf UGPS J0521+3640. *MNRAS*, 414:L90.

Burningham, B., Smith, L., Cardoso, C.V., et al., 2014. The discovery of a T6.5 subdwarf. *MNRAS*, 440:359.

Burrows, A., Hubbard, W.B., Lunine, J.I., et al., 2001. The theory of brown dwarfs and extrasolar giant planets. *Reviews of Modern Physics*, 73:719.

Casali, M., Adamson, A., Alves de Oliveira, C., et al., 2007. The UKIRT wide-field camera. *A&A*, 467:777.

Casali, M., Lunney, D., Henry, D., et al., 2001. The UKIRT IR Wide-Field Camera (WFCAM). In R. Clowes, A. Adamson, and G. Bromage, editors, *The New Era of Wide Field Astronomy*, volume 232 of *Astronomical Society of the Pacific Conference Series*, page 357.

Casewell, S.L., Jameson, R.F., and Burleigh, M.R., 2008. Proper motions of field L and T dwarfs - II. *MNRAS*, 390:1517.

Castro, P.J. and Gizis, J.E., 2012. Discovery of a Late L Dwarf: WISEP J060738.65+242953.4. *ApJ*, 746:3.

Castro, P.J., Gizis, J.E., Harris, H.C., et al., 2013. Discovery of Four High Proper Motion L Dwarfs, Including a 10 pc L Dwarf at the L/T Transition. *ApJ*, 776:126.

Catalán, S., Tremblay, P.E., Pinfield, D.J., et al., 2012. The brightest pure-H ultracool white dwarf. *A&A*, 546:L3.

Catelan, M., Minniti, D., Lucas, P.W., et al., 2011. The Vista Variables in the Vía Láctea (VVV) ESO Public Survey: Current Status and First Results. In A. McWilliam, editor, *RR Lyrae Stars, Metal-Poor Stars, and the Galaxy*, page 145.

Chen, E.Y. and Hansen, B.M.S., 2011. Cooling curves and chemical evolution curves of convective mixing white dwarf stars. *MNRAS*, 413:2827.

Collins, R. and Hambly, N., 2012. Calculating Proper Motions in the WFCAM Science Archive for the UKIRT Infrared Deep Sky Surveys. In P. Ballester, D. Egret, and N.P.F. Lorente, editors, *Astronomical Data Analysis Software and Systems XXI*, volume 461 of *Astronomical Society of the Pacific Conference Series*, page 525.

Contreras Peña, C., Lucas, P.W., Froebrich, D., et al., 2014. Extreme infrared variables from UKIDSS - I. A concentration in star-forming regions. *MNRAS*, 439:1829.

Cross, N.J.G., Collins, R.S., Mann, R.G., et al., 2012. The VISTA Science Archive. *A&A*, 548:A119.

Crossfield, I.J.M., Biller, B., Schlieder, J.E., et al., 2014. A global cloud map of the nearest known brown dwarf. *Nature*, 505:654.

Cruz, K.L., Reid, I.N., Liebert, J., et al., 2003. Meeting the Cool Neighbors. V. A 2MASS-Selected Sample of Ultracool Dwarfs. *AJ*, 126:2421.

Cushing, M.C., Kirkpatrick, J.D., Gelino, C.R., et al., 2011. The Discovery of Y Dwarfs using Data from the Wide-field Infrared Survey Explorer (WISE). *ApJ*, 743:50.

Cushing, M.C., Kirkpatrick, J.D., Gelino, C.R., et al., 2014. Three New Cool Brown Dwarfs Discovered with the Wide-field Infrared Survey Explorer (WISE) and an Improved Spectrum of the Y0 Dwarf WISE J041022.71+150248.4. *AJ*, 147:113.

Cushing, M.C., Roellig, T.L., Marley, M.S., et al., 2006. A Spitzer Infrared Spectrograph Spectral Sequence of M, L, and T Dwarfs. *ApJ*, 648:614.

Cushing, M.C., Vacca, W.D., and Rayner, J.T., 2004. Spextool: A Spectral Extraction Package for SpeX, a 0.8-5.5 Micron Cross-Dispersed Spectrograph. *PASP*, 116:362.

Cutri, R.M., Wright, E.L., Conrow, T., et al., 2012. Explanatory Supplement to the WISE All-Sky Data Release Products. Technical report.

Cutri, R.M., Wright, E.L., Conrow, T., et al., 2013. Explanatory Supplement to the AllWISE Data Release Products. Technical report.

Day-Jones, A.C., Marocco, F., Pinfield, D.J., et al., 2013. The sub-stellar birth rate from UKIDSS. *MNRAS*, 430:1171.

Day-Jones, A.C., Pinfield, D.J., Ruiz, M.T., et al., 2011. Discovery of a T dwarf + white dwarf binary system. *MNRAS*, 410:705.

de Bruijne, J.H.J., Rygl, K.L.J., and Antoja, T., 2015. Gaia astrometric science performance - post-launch predictions. *ArXiv e-prints: 1502.00791.*

Deacon, N.R., Groot, P.J., Drew, J.E., et al., 2009a. The IPHAS-POSS-I proper motion survey of the Galactic plane. *MNRAS*, 397:1685.

Deacon, N.R., Hambly, N.C., and Cooke, J.A., 2005. Southern infrared proper motion survey. I. Discovery of new high proper motion stars from first full hemisphere scan. *A&A*, 435:363.

Deacon, N.R., Hambly, N.C., King, R.R., et al., 2009b. The UKIDSS-2MASS proper motion survey - I. Ultracool dwarfs from UKIDSS DR4. *MNRAS*, 394:857.

Deacon, N.R., Liu, M.C., Magnier, E.A., et al., 2011. Four New T Dwarfs Identified in Pan-STARRS 1 Commissioning Data. *AJ*, 142:77.

Delorme, P., Albert, L., Forveille, T., et al., 2010. Extending the Canada-France brown dwarfs survey to the near-infrared: first ultracool brown dwarfs from CFBDSIR. *A&A*, 518:A39.

Dierickx, M., Klement, R., Rix, H.W., et al., 2010. Observational Evidence from SDSS for a Merger Origin of the Milky Way's Thick Disk. *ApJ*, 725:L186.

Drew, J.E., Greimel, R., Irwin, M.J., et al., 2005. The INT Photometric Hα Survey of the Northern Galactic Plane (IPHAS). *MNRAS*, 362:753.

Dupuy, T.J. and Liu, M.C., 2012. The Hawaii Infrared Parallax Program. I. Ultracool Binaries and the L/T Transition. *ApJ*, 201:19.

Dye, S., Warren, S.J., Hambly, N.C., et al., 2006. The UKIRT Infrared Deep Sky Survey Early Data Release. *MNRAS*, 372:1227.

Epchtein, N., de Batz, B., Capoani, L., et al., 1997. The deep near-infrared southern sky survey (DENIS). *The Messenger*, 87:27.

Faherty, J.K., Burgasser, A.J., Cruz, K.L., et al., 2009. The Brown Dwarf Kinematics Project I. Proper Motions and Tangential Velocities for a Large Sample of Late-Type M, L, and T Dwarfs. *AJ*, 137:1.

Faherty, J.K., Burgasser, A.J., Walter, F.M., et al., 2012. The Brown Dwarf Kinematics Project (BDKP). III. Parallaxes for 70 Ultracool Dwarfs. *ApJ*, 752:56.

Faherty, J.K., Burgasser, A.J., West, A.A., et al., 2010. The Brown Dwarf Kinematics Project. II. Details on Nine Wide Common Proper Motion Very Low Mass Companions to Nearby Stars. *AJ*, 139:176.

Feast, M. and Whitelock, P., 1997. Galactic kinematics of Cepheids from HIPPARCOS proper motions. *MNRAS*, 291:683.

Folkes, S.L., Pinfield, D.J., Jones, H.R.A., et al., 2012. Identifying ultra-cool dwarfs at low Galactic latitudes: a southern candidate catalogue. *MNRAS*, 427:3280.

Folkes, S.L., Pinfield, D.J., Kendall, T.R., et al., 2007. Discovery of a nearby L-T transition object in the Southern Galactic plane. *MNRAS*, 378:901.

Gizis, J.E., Burgasser, A.J., Faherty, J.K., et al., 2011. WISEP J180026.60+013453.1: A nearby late-L Dwarf near the Galactic Plane. *AJ*, 142:171.

Goldman, B., Marsat, S., Henning, T., et al., 2010. A new benchmark T8-9 brown dwarf and a couple of new mid-T dwarfs from the UKIDSS DR5+ LAS. *MNRAS*, 405:1140.

Gomes, J.I., Pinfield, D.J., Marocco, F., et al., 2013. Two new ultracool benchmark systems from WISE+2MASS. *MNRAS*, 431:2745.

Gray, R.O., Corbally, C.J., Garrison, R.F., et al., 2006. Contributions to the Nearby Stars (NStars) Project: Spectroscopy of Stars Earlier than M0 within 40 pc-The Southern Sample. *AJ*, 132:161.

Greenstein, J.L., 1980. Degenerate stars. XII - Recognition of hot nondegenerates. *ApJ*, 242:738.

Hambly, N.C., Collins, R.S., Cross, N.J.G., et al., 2008. The WFCAM Science Archive. *MNRAS*, 384:637.

Hambly, N.C., Davenhall, A.C., Irwin, M.J., et al., 2001a. The SuperCOSMOS Sky Survey - III. Astrometry. *MNRAS*, 326:1315.

Hambly, N.C., Irwin, M.J., and MacGillivray, H.T., 2001b. The SuperCOSMOS Sky Survey - II. Image detection, parametrization, classification and photometry. *MNRAS*, 326:1295.

Hambly, N.C., MacGillivray, H.T., Read, M.A., et al., 2001c. The SuperCOSMOS Sky Survey - I. Introduction and description. *MNRAS*, 326:1279.

Hawley, S.L., Covey, K.R., Knapp, G.R., et al., 2002. Characterization of M, L, and T Dwarfs in the Sloan Digital Sky Survey. *AJ*, 123:3409.

Hewett, P.C., Warren, S.J., Leggett, S.K., et al., 2006. The UKIRT Infrared Deep Sky Survey ZY JHK photometric system: passbands and synthetic colours. *MNRAS*, 367:454.

Høg, E., Fabricius, C., Makarov, V.V., et al., 2000. The Tycho-2 catalogue of the 2.5 million brightest stars. *A&A*, 355:L27.

Høg, E. and Knude, J., 2014. A Gaia successor with NIR Sensors. *ArXiv e-prints: 1408.3305*.

Irwin, M.J., 1985. Automatic analysis of crowded fields. *MNRAS*, 214:575.

Ivanov, V.D., Minniti, D., Hempel, M., et al., 2013. Discovery of new companions to high proper motion stars from the VVV Survey. *A&A*, 560:A21.

Ivezic, Z., Tyson, J.A., Abel, B., et al., 2008. LSST: from Science Drivers to Reference Design and Anticipated Data Products. *ArXiv e-prints*.

Kharchenko, N.V., 2001. All-sky compiled catalogue of 2.5 million stars. *Kinematika i Fizika Nebesnykh Tel*, 17:409.

Kilic, M., Burrows, A., Kuchner, M., et al., 2006. Resolving Mysteries: Ultra-Cool White Dwarfs and the Age of the Galaxy. In *Spitzer Proposal ID #30208*, page 30208.

Kilic, M., Leggett, S.K., Tremblay, P.E., et al., 2010. A Detailed Model Atmosphere Analysis of Cool White Dwarfs in the Sloan Digital Sky Survey. *ApJ*, 190:77.

Kilic, M., Munn, J.A., Harris, H.C., et al., 2005. Discovery of 282 Cool White Dwarfs ($T_{eff} \lesssim 8000$ K) in the Sloan Digital Sky Survey. In D. Koester and S. Moehler, editors, *14th European Workshop on White Dwarfs*, volume 334 of *Astronomical Society of the Pacific Conference Series*, page 131.

Kirkpatrick, J.D., 2005. New Spectral Types L and T. *Annual Review of Astronomy and Astrophysics*, 43:195.

Kirkpatrick, J.D., 2011. New Surveys for Brown Dwarfs and Their Impact on the IMF. In C. Johns-Krull, M.K. Browning, and A.A. West, editors, *Astronomical Society of the Pacific Conference Series*, volume 448 of *Astronomical Society of the Pacific Conference Series*, page 323.

Kirkpatrick, J.D., Cushing, M.C., Gelino, C.R., et al., 2011. The First Hundred Brown Dwarfs Discovered by the Wide-field Infrared Survey Explorer (WISE). *ApJ*, 197:19.

Kirkpatrick, J.D., Gelino, C.R., Cushing, M.C., et al., 2012. Further Defining Spectral Type "Y" and Exploring the Low-mass End of the Field Brown Dwarf Mass Function. *ApJ*, 753:156.

Kirkpatrick, J.D., Looper, D.L., Burgasser, A.J., et al., 2010. Discoveries from a Near-infrared Proper Motion Survey Using Multi-epoch Two Micron All-Sky Survey Data. *ApJ*, 190:100.

Kirkpatrick, J.D., Reid, I.N., Liebert, J., et al., 1999. Dwarfs Cooler than "M": The Definition of Spectral Type "L" Using Discoveries from the 2 Micron All-Sky Survey (2MASS). *ApJ*, 519:802.

Kirkpatrick, J.D., Schneider, A., Fajardo-Acosta, S., et al., 2014. The AllWISE Motion Survey and the Quest for Cold Subdwarfs. *ApJ*, 783:122.

Lachaume, R., Dominik, C., Lanz, T., et al., 1999. Age determinations of main-sequence stars: combining different methods. *A&A*, 348:897.

Lagrange, A.M., Desort, M., Galland, F., et al., 2009. Extrasolar planets and brown dwarfs around A-F type stars. VI. High precision RV survey of early type dwarfs with HARPS. *A&A*, 495:335.

Latham, D.W., Stefanik, R.P., Torres, G., et al., 2002. A Survey of Proper-Motion Stars. XVI. Orbital Solutions for 171 Single-lined Spectroscopic Binaries. *AJ*, 124:1144.

Lawrence, A., Warren, S.J., Almaini, O., et al., 2007. The UKIRT Infrared Deep Sky Survey (UKIDSS). *MNRAS*, 379:1599.

Leggett, S.K., Burningham, B., Saumon, D., et al., 2010. Mid-Infrared Photometry of Cold Brown Dwarfs: Diversity in Age, Mass, and Metallicity. *ApJ*, 710:1627.

Leggett, S.K., Cushing, M.C., Saumon, D., et al., 2009. The Physical Properties of Four ˜600 K T Dwarfs. *ApJ*, 695:1517.

Leggett, S.K., Lodieu, N., Tremblay, P.E., et al., 2011. Cool White Dwarfs Found in the UKIRT Infrared Deep Sky Survey. *ApJ*, 735:62.

Leggett, S.K., Saumon, D., Marley, M.S., et al., 2012. The Properties of the 500 K Dwarf UGPS J072227.51-054031.2 and a Study of the Far-red Flux of Cold Brown Dwarfs. *ApJ*, 748:74.

Lépine, S. and Shara, M.M., 2005. A Catalog of Northern Stars with Annual Proper Motions Larger than 0.15" (LSPM-NORTH Catalog). *AJ*, 129:1483.

Lépine, S., Shara, M.M., and Rich, R.M., 2002. New High Proper Motion Stars from the Digitized Sky Survey. I. Northern Stars with 0.5" yr^{-1}<μ<2.0" yr^{-1} at Low Galactic Latitudes. *AJ*, 124:1190.

Lewis, J.R., Irwin, M., and Bunclark, P., 2010. Pipeline Processing for VISTA. In Y. Mizumoto, K.I. Morita, and M. Ohishi, editors, *Astronomical Data Analysis Software and Systems XIX*, volume 434 of *Astronomical Society of the Pacific Conference Series*, page 91.

Liu, M.C., Magnier, E., Deacon, N., et al., 2011. Surveying the Extended Solar Neighborhood with Pan-STARRS-1. In *American Astronomical Society Meeting Abstracts 218*, page 113.14.

Looper, D.L., Kirkpatrick, J.D., and Burgasser, A.J., 2007. Discovery of 11 New T Dwarfs in the Two Micron All Sky Survey, Including a Possible L/T Transition Binary. *AJ*, 134:1162.

Lucas, P.W., Hoare, M.G., Longmore, A., et al., 2008. The UKIDSS Galactic Plane Survey. *MNRAS*, 391:136.

Lucas, P.W., Tinney, C.G., Burningham, B., et al., 2010. The discovery of a very cool, very nearby brown dwarf in the Galactic plane. *MNRAS*, 408:L56.

Luhman, K.L., 2013. Discovery of a Binary Brown Dwarf at 2 pc from the Sun. *ApJ*, 767:L1.

Luhman, K.L., 2014a. A Search for a Distant Companion to the Sun with the Wide-field Infrared Survey Explorer. *ApJ*, 781:4.

Luhman, K.L., 2014b. Discovery of a ˜250 K Brown Dwarf at 2 pc from the Sun. *ApJ*, 786:L18.

Luhman, K.L. and Sheppard, S.S., 2014. Characterization of High Proper Motion Objects from the Wide-field Infrared Survey Explorer. *ApJ*, 787:126.

Lutz, T.E. and Kelker, D.H., 1973. On the Use of Trigonometric Parallaxes for the Calibration of Luminosity Systems: Theory. *PASP*, 85:573.

Luyten, W.J., 1979a. *LHS catalogue. A catalogue of stars with proper motions exceeding 0”5 annually.*

Luyten, W.J., 1979b. *NLTT catalogue. Volume_I. +90__to_+30_. Volume._II. +30__to_0_.*

Mace, G.N., Kirkpatrick, J.D., Cushing, M.C., et al., 2013a. A Study of the Diverse T Dwarf Population Revealed by WISE. *ApJ*, 205:6.

Mace, G.N., Kirkpatrick, J.D., Cushing, M.C., et al., 2013b. The Exemplar T8 Subdwarf Companion of Wolf 1130. *ApJ*, 777:36.

Malmquist, K.G., 1922. . *Lund Medd.*, 100:1.

Mamajek, E.E., Barenfeld, S.A., Ivanov, V.D., et al., 2015. The Closest Known Flyby of a Star to the Solar System. *ApJ*, 800:L17.

Marocco, F., Smart, R.L., Jones, H.R.A., et al., 2010. Parallaxes and physical properties of 11 mid-to-late T dwarfs. *A&A*, 524:A38.

Mason, B.D., Wycoff, G.L., Hartkopf, W.I., et al., 2001. The 2001 US Naval Observatory Double Star CD-ROM. I. The Washington Double Star Catalog. *AJ*, 122:3466.

Meng, X.C., Yang, W.M., and Li, Z.M., 2010. The cooling time of white dwarfs produced from type Ia supernovae. *Research in Astronomy and Astrophysics*, 10:927.

Michalik, D., Lindegren, L., Hobbs, D., et al., 2014. Joint astrometric solution of HIPPARCOS and Gaia. A recipe for the Hundred Thousand Proper Motions project. *A&A*, 571:A85.

Minniti, D., Lucas, P.W., Emerson, J.P., et al., 2010. VISTA Variables in the Via Lactea (VVV): The public ESO near-IR variability survey of the Milky Way. *NewA*, 15:433.

Monet, D.G., Levine, S.E., Canzian, B., et al., 2003. The USNO-B Catalog. *AJ*, 125:984.

Morley, C.V., Marley, M.S., Fortney, J.J., et al., 2014. Water Clouds in Y Dwarfs and Exoplanets. *ApJ*, 787:78.

Murray, D.N., Burningham, B., Jones, H.R.A., et al., 2011. Blue not brown: UKIRT Infrared Deep Sky Survey T dwarfs with suppressed K-band flux. *MNRAS*, 414:575.

Nakajima, T. and Morino, J.I., 2012. Potential Members of Stellar Kinematic Groups within 30 pc of the Sun. *AJ*, 143:2.

Nielsen, E.L., Liu, M.C., Wahhaj, Z., et al., 2013. The Gemini NICI Planet-Finding Campaign: The Frequency of Giant Planets around Young B and A Stars. *ApJ*, 776:4.

Noll, K.S., Geballe, T.R., Leggett, S.K., et al., 2000. The Onset of Methane in L Dwarfs. *ApJ*, 541:L75.

Perryman, M.A.C. and ESA, editors, 1997. *The HIPPARCOS and TYCHO catalogues. Astrometric and photometric star catalogues derived from the ESA HIPPARCOS Space Astrometry Mission*, volume 1200 of *ESA Special Publication*.

Phan-Bao, N., Bessell, M.S., Martín, E.L., et al., 2008. Discovery of new nearby L and late-M dwarfs at low Galactic latitude from the DENIS data base. *MNRAS*, 383:831.

Pinfield, D.J., Burningham, B., Lodieu, N., et al., 2012. Discovery of the benchmark metal-poor T8 dwarf BD +01° 2920B. *MNRAS*, 422:1922.

Pinfield, D.J., Burningham, B., Tamura, M., et al., 2008. Fifteen new T dwarfs discovered in the UKIDSS Large Area Survey. *MNRAS*, 390:304.

Pinfield, D.J., Jones, H.R.A., Lucas, P.W., et al., 2006. Finding benchmark brown dwarfs to probe the substellar initial mass function as a function of time. *MNRAS*, 368:1281.

Rayner, J.T., Toomey, D.W., Onaka, P.M., et al., 2003. SpeX: A Medium-Resolution 0.8-5.5 Micron Spectrograph and Imager for the NASA Infrared Telescope Facility. *PASP*, 115:362.

Reid, I.N., 2003. Meeting the Cool Neighbors. VI. A Search for Nearby Ultracool Dwarfs in the Galactic Plane. *AJ*, 126:2449.

Reid, I.N., Brewer, C., Brucato, R.J., et al., 1991. The second Palomar Sky Survey. *PASP*, 103:661.

Reid, I.N., Cruz, K.L., Allen, P., et al., 2004. Meeting the Cool Neighbors. VIII. A Preliminary 20 Parsec Census from the NLTT Catalogue. *AJ*, 128:463.

Reid, I.N. and Gizis, J.E., 2005. Probing the LHS Catalog. II. Faint Proper-Motion Stars. *PASP*, 117:676.

Robin, A.C., Reylé, C., Derrière, S., et al., 2003. A synthetic view on structure and evolution of the Milky Way. *A&A*, 409:523.

Roeser, S., Demleitner, M., and Schilbach, E., 2010. The PPMXL Catalog of Positions and Proper Motions on the ICRS. Combining USNO-B1.0 and the Two Micron All Sky Survey (2MASS). *AJ*, 139:2440.

Rojas-Ayala, B., Iglesias, D., Minniti, D., et al., 2014. M dwarfs in the b201 tile of the VVV survey. Colour-based selection, spectral types and light curves. *A&A*, 571:A36.

Royal Society of Chemistry, 2001. Robust statistics: a method of coping with outliers. AMC Technical Brief, The Analytical Methods Committee, The Royal Society of Chemistry, Burlington House, Piccadilly, London W1J 0BA.

Salim, S. and Gould, A., 2002. Classifying Luyten Stars Using an Optical-Infrared Reduced Proper-Motion Diagram. *ApJ*, 575:L83.

Salim, S. and Gould, A., 2003. Improved Astrometry and Photometry for the Luyten Catalog. II. Faint Stars and the Revised Catalog. *ApJ*, 582:1011.

Sayres, C., Subasavage, J.P., Bergeron, P., et al., 2012. A Multi-survey Approach to White Dwarf Discovery. *AJ*, 143:103.

Schaller, G., Schaerer, D., Meynet, G., et al., 1992. New grids of stellar models from 0.8 to 120 solar masses at Z = 0.020 and Z = 0.001. *A&A Supp.*, 96:269.

Scholz, R.D., 2010. Hip 63510C, Hip 73786B, and nine new isolated high proper motion T dwarf candidates from UKIDSS DR6 and SDSS DR7. *A&A*, 515:A92.

Scholz, R.D., 2014. Neighbours hiding in the Galactic plane, a new M/L dwarf candidate for the 8 pc sample. *A&A*, 561:A113.

Sheppard, S.S. and Cushing, M.C., 2009. An Infrared High Proper Motion Survey Using the 2MASS and SDSS: Discovery of M, L, and T Dwarfs. *AJ*, 137:304.

Skrutskie, M.F., Cutri, R.M., Stiening, R., et al., 2006. The Two Micron All Sky Survey (2MASS). *AJ*, 131:1163.

Skrzypek, N., Warren, S.J., Faherty, J.K., et al., 2015. Photometric brown-dwarf classification. I. A method to identify and accurately classify large samples of brown dwarfs without spectroscopy. *A&A*, 574:A78.

Smart, R.L., Jones, H.R.A., Lattanzi, M.G., et al., 2010. The distance to the cool T9 brown dwarf ULAS J003402.77-005206.7. *A&A*, 511:A30.

Smith, L., Lucas, P., Burningham, B., et al., 2013. The Kinematic Age of the Coolest T Dwarfs. *ArXiv e-prints: 1303.5288*.

Song, I., Caillault, J.P., Barrado y Navascués, D., et al., 2001. Ages of A-Type Vega-like Stars from uvbyβ Photometry. *ApJ*, 546:352.

Stephens, D.C. and Leggett, S.K., 2004. JHK Magnitudes for L and T Dwarfs and Infrared Photometric Systems. *PASP*, 116:9.

Sutherland, W., Emerson, J., Dalton, G., et al., 2015. The Visible and Infrared Survey Telescope for Astronomy (VISTA): Design, technical overview, and performance. *A&A*, 575:A25.

Taylor, J.R., 1996. *An Introduction to Error Analysis: The Study of Uncertainties in Physical Measurements*. University Science Books.

Taylor, M.B., 2005. TOPCAT & STIL: Starlink Table/VOTable Processing Software. In P. Shopbell, M. Britton, and R. Ebert, editors, *Astronomical Data Analysis Software and Systems XIV*, volume 347 of *Astronomical Society of the Pacific Conference Series*, page 29.

Taylor, M.B., 2006. STILTS - A Package for Command-Line Processing of Tabular Data. In C. Gabriel, C. Arviset, D. Ponz, and S. Enrique, editors, *Astronomical Data Analysis Software and Systems XV*, volume 351 of *Astronomical Society of the Pacific Conference Series*, page 666.

van Leeuwen, F., 2007. Validation of the new Hipparcos reduction. *A&A*, 474:653.

Vick, A., Folger, M., McLay, S., et al., 2004. The WFCAM instrument software. In F. Ochsenbein, M.G. Allen, and D. Egret, editors, *Astronomical Data Analysis Software and Systems (ADASS) XIII*, volume 314 of *Astronomical Society of the Pacific Conference Series*, page 732.

Warren, S., 2002. Scientific goals of the UKIRT Infrared Deep Sky Survey. In J.A. Tyson and S. Wolff, editors, *Society of Photo-Optical Instrumentation Engineers (SPIE) Conference Series*, volume 4836 of *Society of Photo-Optical Instrumentation Engineers (SPIE) Conference Series*, pages 313–320.

West, A.A., Hawley, S.L., Bochanski, J.J., et al., 2008. Constraining the Age-Activity Relation for Cool Stars: The Sloan Digital Sky Survey Data Release 5 Low-Mass Star Spectroscopic Sample. *AJ*, 135:785.

Wright, E.L., Eisenhardt, P.R.M., Mainzer, A.K., et al., 2010. The Wide-field Infrared Survey Explorer (WISE): Mission Description and Initial On-orbit Performance. *AJ*, 140:1868.

Zhang, Z.H., Pinfield, D.J., Day-Jones, A.C., et al., 2010. Discovery of the first wide L dwarf + giant binary system and eight other ultracool dwarfs in wide binaries. *MNRAS*, 404:1817.